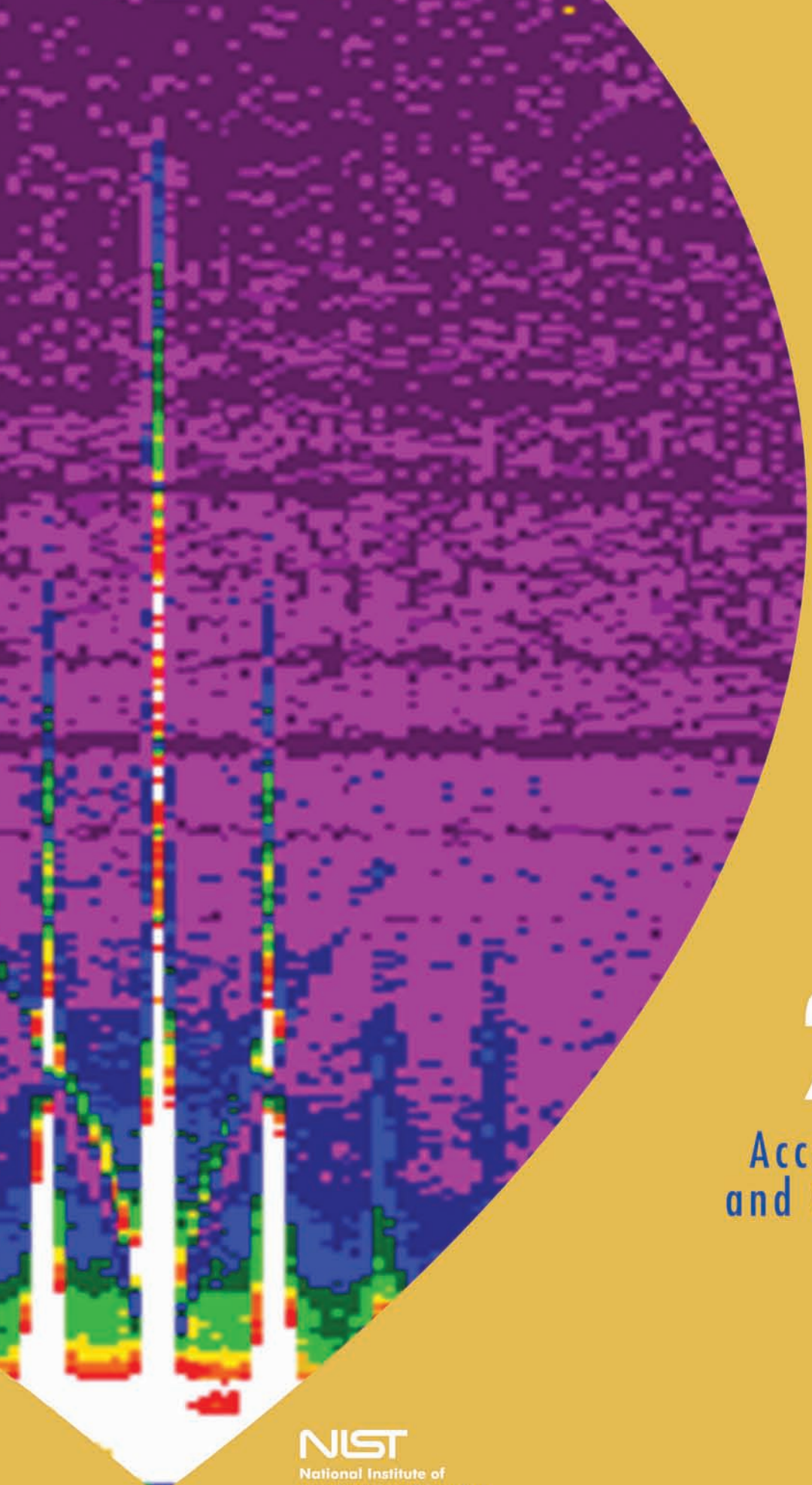

NIST Center for Neutron Research

2009

Accomplishments and Opportunities

NIST
National Institute of Standards and Technology

NIST SP 1105

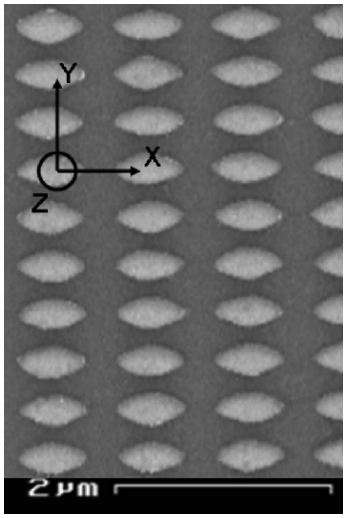

ON THE COVER

On-specular (z direction) and off-specular (over the in-plane x-axis) neutron scattering measured with the AND/R reflectometer using a position-sensitive detector. In this experiment, columnar spin-valves having layers in the z-direction and an ellipsoidal cross-section (image, left) were made in a regular rectangular array on a silicon substrate. The in-plane Bragg peaks (sharp features) come from the repeat distance of the array, while the broader feature comes from a more local real-space structure, i.e., the micromagnetic structure of the individual spin valves averaged over many spin-valves.
K. Krycka, *et al.*, J. of Appl. Phys. 105, 07C120 (2009).

2009 NIST Center for Neutron Research

Accomplishments and Opportunities

NIST Special Publication 1105

Robert M. Dimeo, Deputy Director

Ronald L. Cappelletti, Editor

December 2009

National Institute of Standards and Technology
Patrick Gallagher, Director

U.S. Department of Commerce
Gary Locke, Secretary

DISCLAIMER

Certain commercial entities, equipment, or materials may be identified in this document in order to describe an experimental procedure or concept adequately. Such identification is not intended to imply recommendation or endorsement by the National Institute of Standards and Technology, nor is it intended to imply that the entities, materials, or equipment are necessarily the best available for the purpose.

National Institute of Standards and Technology
Special Publications 1105

Natl. Inst. Stand. Technol. Spec. Publ. 1105, 88 pages
(December 2009)

CODEN: NSPUE2

U.S. GOVERNMENT PRINTING OFFICE-WASHINGTON: 2009

For sale by the Superintendent of Documents,
U.S. Government Printing Office

Internet: bookstore.gpo.gov Phone: 1.866.512.1800
Fax: 202.512.2104 Mail: Stop SSOP, Washington, DC 20402-0001

Table of Contents

Foreword

It is my pleasure to present to you the research accomplishments and opportunities for the NIST Center for Neutron Research for 2009. This has been a very exciting year and one of change. Pat Gallagher, NCNR Director since 2004, was appointed to NIST Deputy Director in September 2008, and sworn in as NIST Director in November 2009. We have all watched with great interest as Pat has taken on these new responsibilities where his significant leadership talents, which have been known well to all of us here at the NCNR, are now appreciated by a much broader population.

It is particularly exciting for me to witness daily the progress towards our Expansion Project. Since our last annual report in 2008 our site has changed its appearance substantially with a great deal of the construction of our expanded cold neutron guide hall (GH) and technical support/administrative building (TSB) underway. As of this writing, much of the steel and concrete work is complete in the TSB and the steel work is ready to begin on the expanded GH. I invite you to look at the photographs of the site as of August 2009 in this report. More details regarding progress on the Expansion Project can be found in the section on Facility Developments.

This was an outstanding year for reactor operations and engineering. The reactor operated for 242 days out of 246 scheduled, with a reliability factor better than 98 %. The cold source availability during 2009 was more than 99 %. This availability is a testimony to our dedicated operations and engineering staff responsible for the day-to-day operations and maintenance of the plant. Reliability has always been one of the most essential ingredients in running a successful user program. Perhaps the biggest news this year from reactor operations and engineering is on our re-licensing efforts. On July 2nd, the Nuclear Regulatory Commission presented us with a license to operate for another 20 years. Receipt of this license is the culmination of NCNR efforts that began over ten years ago. The successful conclusion of this multi-year effort is due to numerous individuals and I am delighted that we have achieved this significant milestone.

I am also delighted that Tawfik Raby, who retired this year, is being recognized by having his photograph placed in the NIST portrait gallery for his contributions for NBS/NIST. As Chief of Reactor Operations for many years, Tawfik left the NCNR with a legacy of safe, reliable, and highly economical reactor operations. We all are indebted to him for his leadership and setting the highest standards for reactor operations.

As always, the reason for our operations is the neutron measurement capability that we offer to the scientific community. Our success as a national user facility is measured by scientific output enabled by these capabilities. The highlights found here are representative of the continued outstanding research performed at the NCNR. I have greatly enjoyed reading these highlights and I think that you will agree that the productivity and quality of the scientific output continues to be exemplary.

I wish to extend my thanks to all who have contributed to an outstanding year!

The NIST Center for Neutron Research

Neutrons provide a uniquely effective probe of the structure and dynamics of materials ranging from water adhering to clefts within proteins to magnetic domains in memory storage materials. The properties of neutrons (outlined below) can be exploited using a variety of measurement techniques to provide information not otherwise available. The positions of atomic nuclei in crystals, especially those of light atoms, can be determined precisely. Atomic motion can be directly measured and monitored as a function of temperature or pressure. Neutrons are especially sensitive to hydrogen, so that hydrogen motion can be followed in new H-storage materials and water take-up can be monitored as cement sets. Residual stresses such as those deep within oil pipelines or in highway trusses can be mapped. Neutron-based measurements contribute to a broad spectrum of activities including in engineering, materials development, polymer dynamics, chemical technology, medicine, and physics.

The NCNR's neutron source provides the intense, conditioned beams of neutrons required for these types of measurements. In addition to the thermal neutron beams from the heavy water or graphite moderators, the NCNR has a large area liquid hydrogen moderator, or cold source, that provides long wavelength guided neutron beams for the major cold neutron facility in the U.S.

There are currently 29 experiment stations: four provide high neutron flux positions for irradiation, and 25 are beam facilities most of which are used for neutron scattering research. The subsequent pages provide a schematic description of our instruments. More complete descriptions can be found at www.ncnr.nist.gov/instruments/. The NCNR is currently adding a second guide hall with five new instruments in a major expansion (see pp. 4–5).

The Center supports important NIST measurement needs, but is also operated as a major national user facility with merit-based access made available to the entire U.S. technological community. Each year, more than 2000 research participants from government, industry, and academia from all areas of the country use the facility. Beam time for research to be published in the open literature is without cost to the user, but full operating costs are recovered for proprietary research. Access is gained mainly through a web-based, peer-reviewed proposal system with user time allotted by a beamtime allocation committee twice a year. For details see www.ncnr.nist.gov/beamtime.html. The National Science Foundation and NIST co-fund the Center for High Resolution Neutron Scattering (CHRNS) that operates six of the world's most advanced instruments. Time on CHRNS instruments is made available through the proposal system. Some access to beam time for collaborative measurements with the NIST science staff can also be arranged on other instruments.

Why Neutrons?

Neutrons reveal properties not readily probed by photons or electrons. They are electrically neutral and therefore easily penetrate ordinary matter. They behave like microscopic magnets, propagate as waves, can set particles into motion losing or gaining energy and momentum in the process, and they can be absorbed with subsequent emission of radiation to uniquely fingerprint chemical elements.

WAVELENGTHS – in practice range from ≈ 0.01 nm (thermal) to ≈ 1.5 nm (cold) (1 nm = 10 Å), allowing the formation of observable interference patterns when scattered from structures as small as atoms to as large as cells.

ENERGIES – of millielectronvolts, the same magnitude as atomic motions. Exchanges of energy as small as nanoelectronvolts and as large as tenths of electronvolts can be detected between samples and neutrons, allowing measurements in folding proteins, melting glasses and diffusing hydrogen.

Cold neutron Guide Hall and instruments. A second Guide Hall is under construction.

SELECTIVITY – in scattering power varies from nucleus to nucleus somewhat randomly. Specific isotopes can stand out from other isotopes of the same kind of atom. Specific light atoms, difficult to observe with x-rays, are revealed by neutrons. Hydrogen, especially, can be distinguished from chemically equivalent deuterium, allowing a variety of powerful contrast techniques.

MAGNETISM – makes the neutron sensitive to the magnetic moments of both nuclei and electrons, allowing the structure and behavior of ordinary and exotic magnetic materials to be detailed precisely.

NEUTRALITY – of the uncharged neutrons allows them to penetrate deeply without destroying samples, passing through walls that condition a sample's environment, permitting measurements under extreme conditions of temperature and pressure.

CAPTURE – characteristic radiation emanating from specific nuclei capturing incident neutrons can be used to identify and quantify minute amounts of elements in samples as diverse as ancient pottery shards and lake water pollutants.

NIST Center for Neutron Research Instruments

[1] BT-5 Perfect Crystal Ultra-Small Angle Neutron Scattering (USANS) Diffractometer for microstructure up to 10^4 nm, part of CHRNS.

[2] BT-4 Filter Analyzer Neutron Spectrometer with cooled Be/Graphite filter analyzer for chemical spectroscopy.

[3] BT-2 Neutron Imaging Facility for imaging hydrogenous matter in large components such as water in fuel cells and lubricants in engines, in partnership with General Motors.

[4] BT-1 Powder Diffractometer with 32 detectors; incident wavelengths of 0.208 nm, 0.154 nm, and 0.159 nm, with highest resolution of $\delta d/d = 8 \times 10^{-4}$.

[5] BT-9 Thermal Triple Axis Spectrometer for measurements of excitations and structure in condensed matter.

[6] BT-8 Residual Stress Diffractometer optimized for depth profiling of residual stresses in large components.

[7] VT-5 Thermal Neutron Capture Prompt Gamma-ray Activation Analysis Instrument with a neutron fluence rate of 3 x $10^8/cm^2/s$ used for quantitative elemental analysis of bulk materials. Generally used for the analysis of highly hydrogenous materials (≈ 1 % H) such as foods, oils, and biological materials.

[8] BT-7 Thermal Triple Axis Spectrometer with large double focusing monochromator, and interchangeable analyzer/detectors systems.

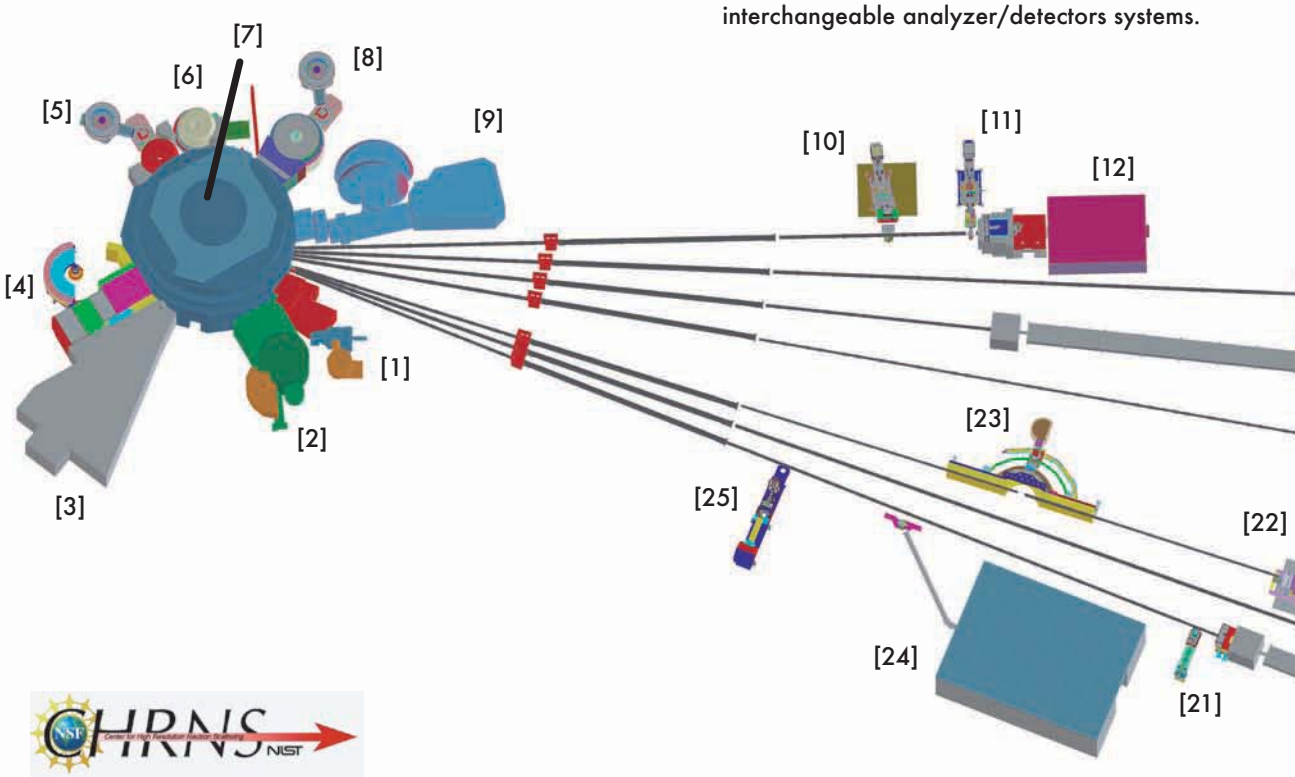

The Center for High Resolution Neutron Scattering (CHRNS) is a partnership between NIST and the National Science Foundation that develops and operates neutron scattering instrumentation for use by the scientific community. The following instruments are part of the Center: 1 (USANS), 13 (HFBS), 14 (NG-3 SANS), 15 (DCS), 22 (NSE), and 23 (SPINS).

[9] NG-0 MACS cold neutron triple axis crystal spectrometer (being commissioned) with double focusing monochromator and multiple crystal analyzer/detectors that can be flexibly configured for several energies simultaneously or for high throughput at one energy.

[10] NG-1 Advanced Neutron Diffractometer / Reflectometer (AND/R) a vertical sample reflectometer with polarization analysis and off-specular reflection capabilities for measuring reflectivities down to 10^{-8}.

[11] NG-1 Vertical Sample Reflectometer instrument with polarization analysis capability for measuring reflectivities down to 10^{-8} to determine subsurface structure.

[12] NG-1 Cold Neutron Depth Profiling instrument for quantitative profiling of subsurface impurities.

[13] NG-2 Backscattering Spectrometer (HFBS) high intensity inelastic scattering instrument with energy resolution < 1 μeV, for studies of motion in molecular and biological systems, part of CHRNS.

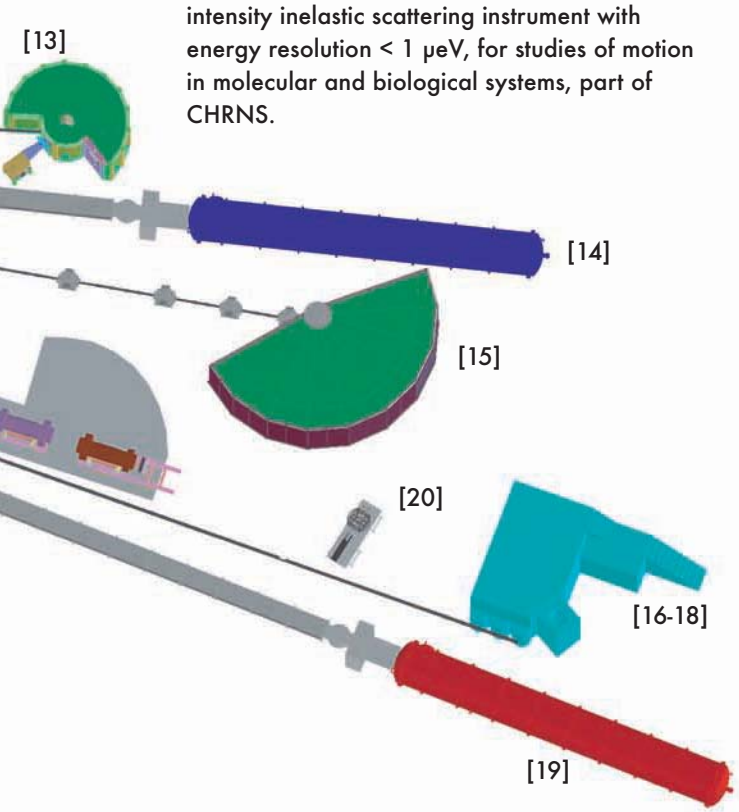

[14] NG-3 30 m SANS for microstructure measurements, part of CHRNS.

[15] NG-4 Disk Chopper Time-of-Flight Spectrometer for studies of diffusive motions and low energy dynamics of materials. Wavelengths from ≈ 0.18 nm to 2.0 nm give corresponding energy resolutions from ≈ 2 μeV to < 10 μeV, part of CHRNS.

[16-18] NG-6 Neutron Physics Station offering three cold neutron beams having wavelengths of 0.5 nm, 0.9 nm, and "white" that are available for fundamental neutron physics experiments.

[19] NG-7 30 m SANS for microstructure measurements, in partnership with NIST and ExxonMobil.

[20] NG-6 Neutron Physics Test Bed for developing measurement techniques and detectors.

[21] NG-7 Prompt Gamma Activation Analysis, cold neutron fluxes allow detection limit for H of 1 μg to 10 μg, depending on the matrix. Focused beams are available for profiling.

[22] NG-5 Neutron Spin-Echo Spectrometer (NSE) for measuring dynamics from 100 ns to 10 ps, in partnership with ExxonMobil, part of CHRNS.

[23] NG-5 Spin-Polarized Triple Axis Spectrometer (SPINS) using cold neutrons with position sensitive detector capability for high-resolution studies, part of CHRNS.

[24] NG-7 Neutron Interferometry and Optics Station with perfect crystal silicon interferometer. A vibration isolation system provides exceptional phase stability and fringe visibility.

[25] NG-7 Horizontal Sample Reflectometer allows reflectivity measurements of free surfaces, liquid/vapor interfaces, as well as polymer coatings.

NCNR Expansion

A multi-year plan to meet strong U.S. demand for cold neutron measurement capability by creating new beamlines and instruments.

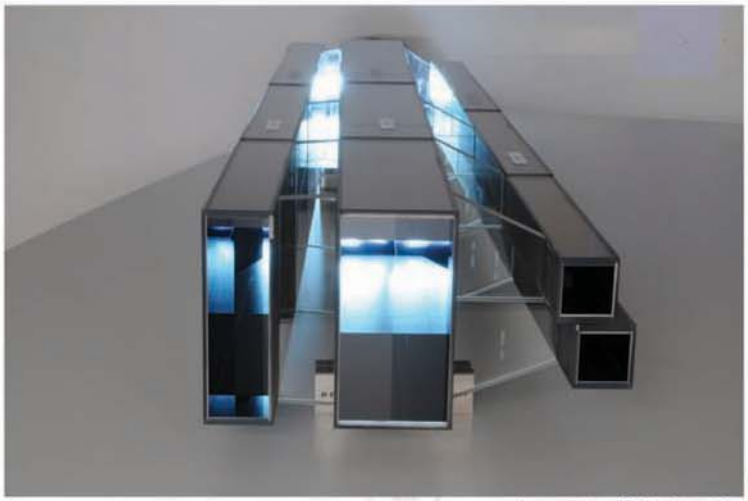

photo courtesy of Swiss Neutronics

New guides section

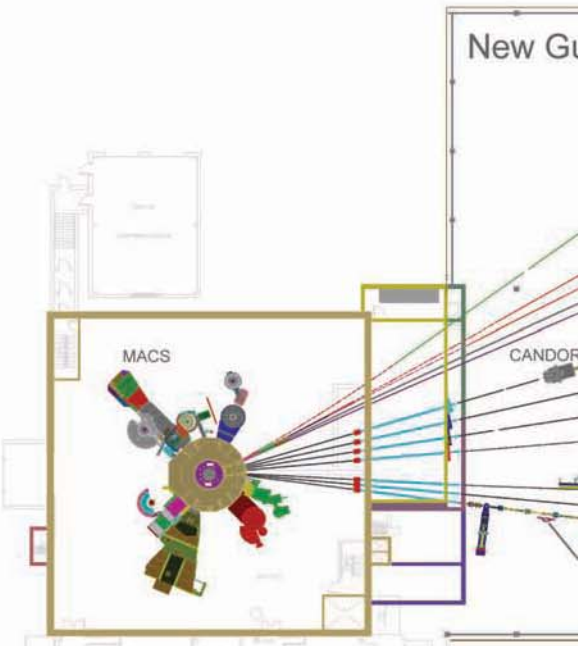

Panoramic view of New Guide Hall construction

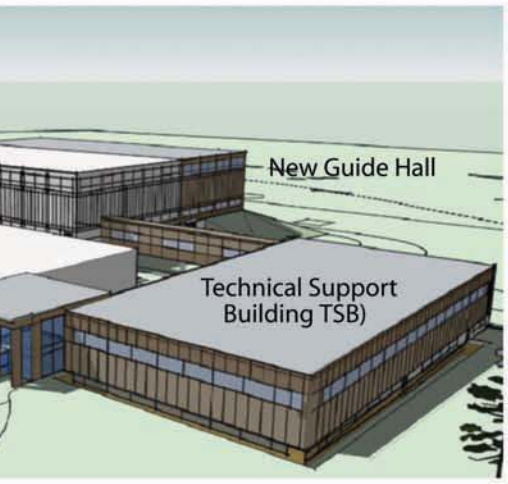

2009 Activities

- Groundbreaking and construction of Technical Support Building and New Guide Hall
- Instrumentation design and engineering in progress
- Guides procured and delivery underway
- Control Room upgrade procurement in progress

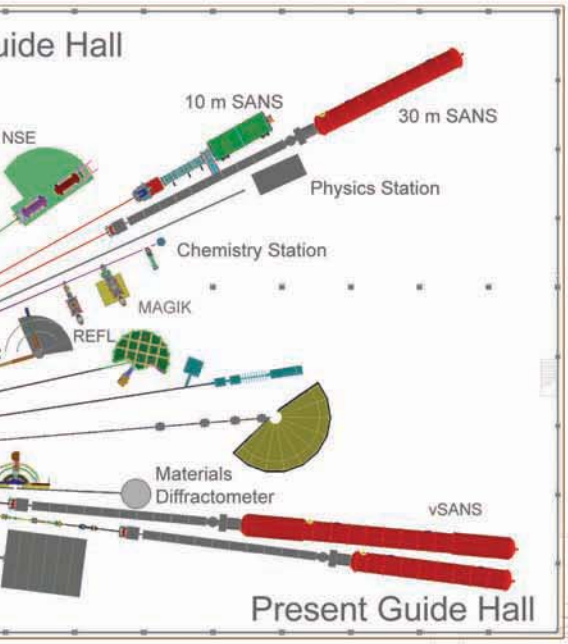

New cold source

Panoramic view of Technical Support Building construction

NCNR Images 2009

Groundbreaking
Celebration
October 1, 2008

Inauguration gathering of the MACS team in front of their instrument

NRC renews NCNR operating license for another 20 years

NCNR's Steve Kline discusses a point with NCNR alumnus Mu-Ping Nieh

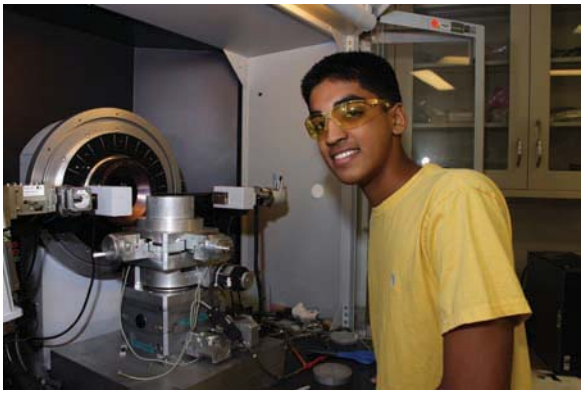

Summer intern Pavan Bhargava setting up an x-ray measurement

Construction, August 21, 2009

Huagen Peng of NIST Polymers Div. at a NG-7 reflectometry tutorial

NCNR's Paul Butler points out a SANS result to Liliana Polo, Carlos Rinaldi, and Adriana Herrera, all from UPRM

NCNR's Bill Clow and Elisabeth Carpenter place a sample into a top-loading ^{3}He cryostat

JHU student Vivek Thampy at the MAC console with NCNR's Jose Rodriguez

NCNR Dep. Dir. Robert Dimeo and NIST Dir. Patrick Gallagher at groundbreaking for NCNR expansion construction

Antiferromagnetic Exchange Coupling in the Dilute Ferromagnetic Semiconductor GaMnAs

J.-H. Chung[1], S.J. Chung[1], and S.Lee[1], B.J. Kirby[2], J.A. Borchers[2], Y.J. Cho[3], X. Liu[3], and J.K. Furdyna[3]

Magnetic data storage is a critical component of modern electronic devices such as personal computers and MP3 players. Current magnetic hard drives that are based on metallic magnets can only hold data. Data must be sent on to a semiconductor device for processing. In principle, use of a ferromagnetic semiconductor would make it possible for a single device to store data and process it, facilitating faster and smaller electronic gadgets. Unfortunately, no suitable ferromagnetic semiconductors are found in nature, causing researchers to focus on artificial dilute magnetic semiconductors, most notably semiconducting GaAs doped with magnetic Mn ions at Ga sites.

GaMnAs has been widely studied, and it has been convincingly established that it exhibits ferromagnetism mediated by itinerant holes. For thin layers of metallic ferromagnets separated by non-magnetic layers, carrier-mediated magnetic exchange can lead to spontaneous, anti-parallel alignment of the magnetizations of neighboring ferromagnetic layers. This phenomenon is known as antiferromagnetic exchange coupling, and is an extremely useful property in multilayer devices. If the layers spontaneously align antiparallel, they can be switched into parallel alignment via an applied magnetic field, which in turn can drastically affect the electrical conductivity of the stack (*i.e.*, the giant magnetoresistive effect). It has long been theoretically predicted that its carrier-mediated ferromagnetism should also make antiferromagnetic interlayer exchange coupling possible for GaMnAs [3], but it had never previously been experimentally demonstrated. Neutron scattering has been used to demonstrate for the first time that thin layers of the dilute magnetic semiconductor GaMnAs can exhibit antiferromagnetic interlayer exchange coupling [1,2], a discovery that helps pave the way for novel new "spintronic" devices, and deepens our understanding of this important class of materials.

To study this phenomenon, we used molecular beam epitaxy to grow two different multilayer samples, both comprised of ten layers of 6.95 nm $Ga_{0.97}Mn_{0.03}As$, each separated by a 3.47 nm non-magnetic spacer layer, with an extra GaAs capping layer at the top. For the control sample, the spacer layers were pure GaAs. For the other sample, the spacer layers were GaAs doped with $1.2x10^{20}$ cm^{-3} of Be. The Be is non-magnetic but adds holes to the spacer layer, and thus plays a role in the carrier-mediated ferromagnetism of the GaMnAs layers. A cartoon depicting the Be-doped sample is shown in Fig. 1.

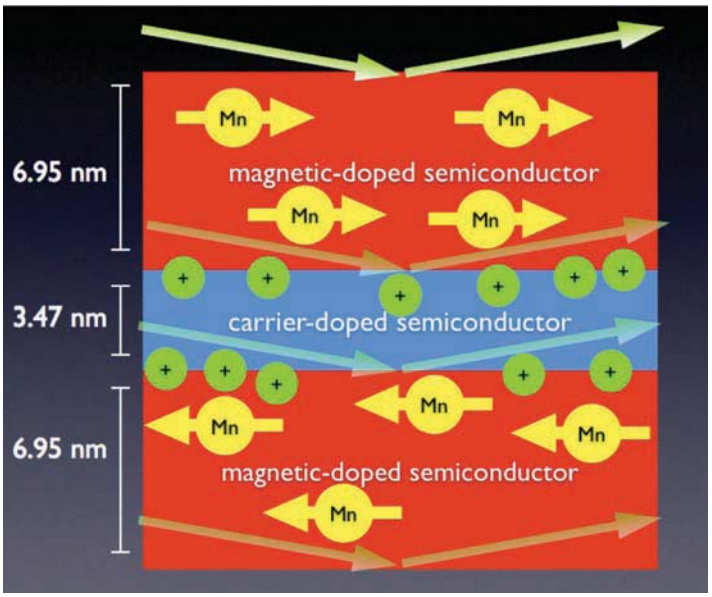

FIGURE 1: Cartoon depicting the Be-doped sample. Polarized neutron beams (long arrows) are sensitive to the properties of the individual layers in the multilayer stack, allowing us to demonstrate hole-mediated, antiferromagnetic interlayer exchange coupling among the GaMnAs layers.

The temperature-dependent magnetizations of the two samples were measured in the presence of several different magnetic fields using superconducting quantum interference device magnetometry (Fig. 2). For the undoped spacer sample (Fig. 2a), a smooth reduction in magnetization with temperature is observed for all fields studied. This is also the case for the Be-doped spacer sample (Fig. 2b) at higher fields (10 mT to 50 mT). However, for very small fields, (< 4 mT) a "hitch" is observed at about 40 K. This feature is consistent with a competition between an interlayer exchange coupling that promotes anti-parallel alignment of the GaMnAs magnetizations, and the applied magnetic field that promotes parallel alignment. However, this conjecture cannot be

[1]Korea University, Seoul 136-713, Korea
[2]NIST Center For Neutron Research, National Institute of Standards and Technology, Gaithersburg, Maryland 20899
[3]University of Notre Dame, Notre Dame, Indiana 46556

proven through magnetometry alone, which is sensitive only to the collective magnetic response of the entire multilayer sample.

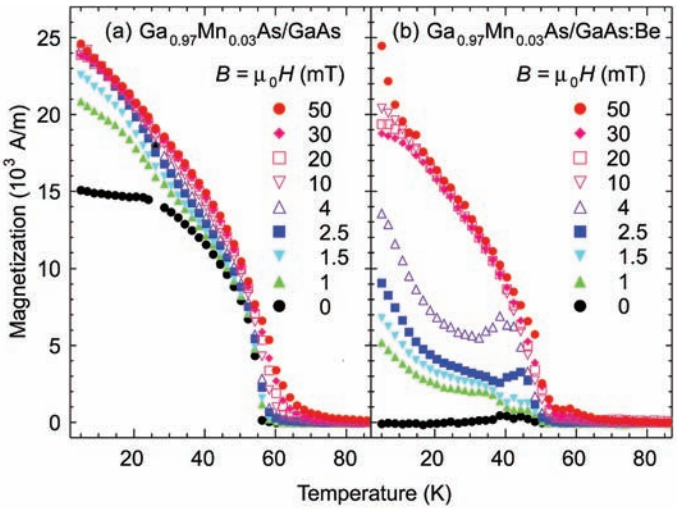

FIGURE 2: Temperature-dependent magnetizations for the undoped spacer sample (a) and the Be-doped spacer sample (b). From Ref. 1.

Thus, to study the samples we used polarized neutron reflectometry (PNR), a technique sensitive to the structural and magnetic depth profiles of thin films and multilayers. Figure 3 shows reflectivities as a function of scattering vector Q for the samples taken at characteristic conditions after cooling from room temperature in zero field. Unpolarized beam reflectivity for the Be-doped sample, taken in zero field at 100 K is shown at top (black). As 100 K is well above the ferromagnetic transition temperature, these data corresponds purely to the nuclear depth profile of the multilayer stack. A superlattice Bragg feature can be seen at 0.062 Å^{-1}, indicative of the repeating {6.97 nm GaMnAs / 3.47 nm GaBeAs} structure (note, the presence of an S-shaped "Bragg feature" instead of a classic Bragg peak is consequence of symmetry-breaking due to the capping layer). The second set of data from the top is of polarized beam, non spin-flip, spin-up (blue) and spin-down (red) reflectivities taken after cooling to 7 K and applying a 1.5 mT field. The structural Bragg feature is present in the same first order position in both channels, but an additional spin-split feature is also present at the half order position of the superlattice (*i.e.,* at ≈ 0.03 Å^{-1}, corresponding to two GaMnAs/GaBeAs repeats). Model fitting confirms that this feature is evidence of antiparallel alignment of alternating GaMnAs layer magnetizations, and is therefore evidence of antiferromagnetic exchange coupling among the layers.

When the applied field is increased to 100 mT (Fig. 3, third set of curves from the top), the half order Bragg feature disappears, and the first order Bragg feature becomes spin-split, indicating that the applied field dominates the intrinsic interlayer coupling and pulls the GaMnAs layer magnetizations into parallel alignment. At these low temperatures, crystalline anisotropy prevents a return to anitferromagnetic order when the field is reduced back to 1.5 mT.

However, if the anisotropy is weakened by raising the temperature to 30 K, exchange coupling can dominate, and antiferromagnetic order does return after field cycling (not shown), demonstrating the robustness of this effect. The bottom of Fig. 3 shows polarized beam data for the un-doped spacer sample, after cooling from room temperature to 7 K in zero field and then applying 1.5 mT. For this sample we see no half order Bragg feature, and a spin-split first order Bragg feature, indicating spontaneous parallel alignment of the GaMnAs layer magnetizations. Since the nature of the coupling is observed to be dependent on the Be concentration, and thereby dependent on the hole concentration, we can conclude that the exchange coupling between GaMnAs layers is indeed a carrier mediated effect.

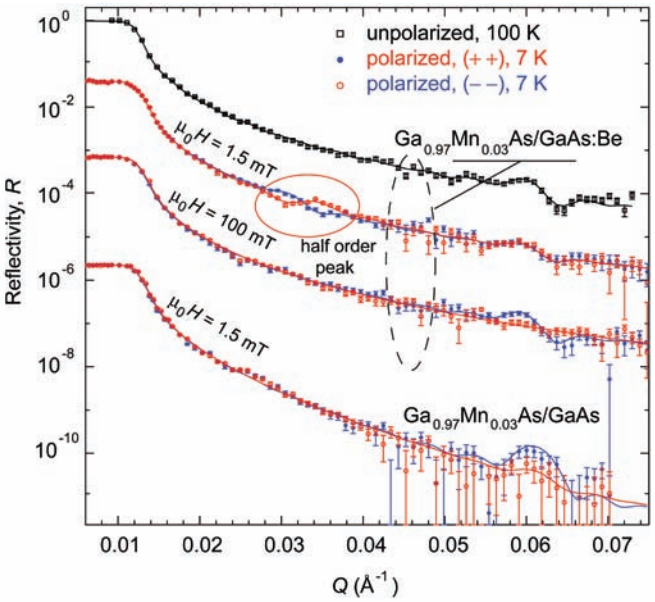

FIGURE 3: Neutron reflectivities for the the undoped and Be-doped samples taken under selected conditions. Different data sets are offset for clarity.

This work demonstrates that structures comprised of this important ferromagnetic semiconductor can be made to exhibit ferromagnetic/antiferromagnetic switching in response to an applied magnetic field, a property that should prove important in potential device applications.

References

[1] J.-H. Chung, S. J. Chung, Sanghoon Lee, B.J. Kirby, J.A. Borchers, Y.J. Cho, X. Liu, and J.K. Furdyna, Phys. Rev. Lett. **101**, 237202 (2008).

[2] S. Lee, J.-H. Chung, X. Liu, J.K. Furdyna, and B.J. Kirby, Materials Today **12**, 14 (2009).

[3] T. Jungwirth, W.A. Atkinson, B.H. Lee, and A.H. MacDonald, Phys. Rev. B **59**, 9818 (1999).

Observation of Magnetic Monopoles in Spin Ice

H. Kadowaki,[1] N. Doi,[1] Y. Aoki,[1] Y. Tabata,[2] T.J. Sato,[3] J.W. Lynn,[4] K. Matsuhira,[5] Z. Hiroi[6]

From the symmetry of Maxwell's equations of electromagnetism, magnetic charges or monopoles would be expected to exist in parallel with electric charges. Moving electric charges produce magnetic fields, and moving magnetic charges would then produce electric fields. The quantum mechanical hypothesis of the existence of magnetic monopoles was originally proposed by Dirac [1], and in current theories monopoles are predicted in grand unified theories as topological defects in the energy range of the order 10^{16} GeV [3]. These enormous energies preclude all hope of creating them in laboratory experiments, and magnetic monopoles have never been observed despite longstanding experimental searches [2]. Consequently, attention has turned to condensed matter systems where tractable analogs of magnetic monopoles might be found, and one prediction is for an emergent elementary excitation in the spin ice compound $Dy_2Ti_2O_7$, where the strongly competing magnetic interactions exhibit the same type of frustration as water ice [3]. We have successfully observed the signature of magnetic monopoles in spin ice using neutron scattering, and find that they interact via the magnetic inverse-square law force. In addition, specific heat measurements show that the density of monopoles can be controlled by temperature and magnetic field, with the density following the expected Arrhenius law [4].

In H_20 ice, the protons are disordered even at absolute zero temperature and thus retain finite entropy, and spin ice is a magnetic material that exhibits the same type of disordered ground state. Here the Dy spins occupy a cubic pyrochlore lattice, which is a corner sharing network of tetrahedra. The strongly competing magnetic interactions cannot all be satisfied, resulting in a frustrated magnetic ground state as shown in Fig. 1a, where each spin is parallel to a local [111] easy axis and interacts with neighboring spins via an effective ferromagnetic coupling. Then the lowest energy spin configurations on each tetrahedron follow the ice rule, in which two spins point inward and two point outward. There are six equivalent ways of arranging this "2-in, 2-out" ground state spin structure on each tetrahedron, and the possible ground states of the entire tetrahedral network are macroscopically degenerate in the same way as the disordered protons in ice. In addition to this remarkable observation, there is the more intriguing possibility that the excitations from these highly degenerate ground states are topological in nature and mathematically equivalent to magnetic monopoles [3].

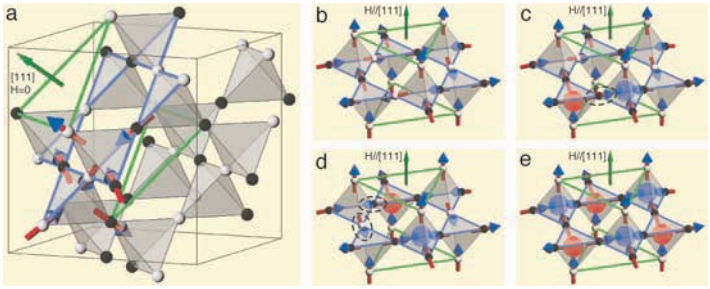

FIGURE 1: Magnetic moments of $Dy_2Ti_2O_7$ reside on the corners of tetrahedra of the cubic pyrochlore lattice. They are represented by arrows pointing inward or outward from centers of the tetrahedra. Four magnetic moments on each tetrahedron obey the ice rule (2-in, 2-out) to minimize the effective ferromagnetic interaction. The resulting spin ice state consists of a macroscopic number of disordered configurations, an example of which is shown in (a). The pyrochlore lattice consists of stacked triangular and kagomé lattices, shown by green and blue lines, respectively, along a [111] direction. (b) Under small [111] magnetic fields, spins on the triangular lattices become parallel to the field and drop out of the problem, while the spins on the kagomé lattice remain in the disordered kagomé ice state. (c) An excited state is induced by flipping a spin from (b), enclosed by a dashed circle, where neighboring tetrahedra have 3-in, 1-out and 1-in, 3-out configurations. These ice-rule-breaking tetrahedra are represented by magnetic monopoles with opposite charges depicted by blue and red spheres. (d) By consecutively flipping two spins from (c), the monopoles are fractionalized. (e) At high magnetic fields ($H \gg Hc$) spins realize a fully ordered, staggered arrangement of monopoles.

The macroscopic degeneracy of the spin ice state can be simplified by applying a small magnetic field along a [111] direction, producing the kagomé ice state (Fig. 1b) that serves as our initial "vacuum" state for the creation of magnetic monopoles. An excitation then is generated by flipping a spin on the kagomé lattice, which results in ice-rule-breaking "3-in, 1-out" (magnetic monopole) and "1- in, 3-out" (anti-monopole) tetrahedral neighbors, as shown in Fig. 1c. The ice-rule-breaking tetrahedra simulate magnetic monopoles, with net positive and negative charges sitting on the centers of tetrahedra. The monopoles should

[1]Tokyo Metropolitan University, Hachioji-shi, Tokyo 192-0397, Japan
[2]Kyoto University, Kyoto 606-8501, Japan
[3]NSL, Institute for Solid State Physics, University of Tokyo, Tokai, Ibaraki 319-1106, Japan
[4]NIST Center for Neutron Research, National Institute of Standards and Technology, Gaithersburg, MD 20899
[5]Kyushu Institute of Technology, Kitakyushu 804-8550, Japan
[6]Institute for Solid State Physics, University of Tokyo, Kashiwa 277-8581, Japan

interact via the magnetic inverse-square law force, which is brought about by the dipolar interaction between spins. The monopoles can move and separate by consecutively flipping spins, but are confined to the two-dimensional kagomé layer (*e.g.,* Fig. 1d). This possibility of separating the local excitation into its constituent parts is a novel fractionalization in a frustrated system, and enables many new aspects of these emergent excitations to be studied experimentally, such as pair creation and interaction, individual motion, currents of monopoles and their concomitant electric field, correlations, and cooperative phenomena.

In the neutron measurements, one challenge is to distinguish the relatively weak monopole scattering from the very strong magnetic scattering of the ground state 'vacuum'. The best temperature and field region to observe monopoles in $Dy_2Ti_2O_7$ is close to the liquid-gas type critical point (T_c, H_c) shown in the inset of Fig. 2. The data in Fig. 2 show the field dependence of the magnetic intensity of the (2,-2,0) Bragg reflection at $T = T_c + 0.05 = 0.43$ K. The intensity plateau for $\mu_0 H < 0.8$ T corresponds to the kagomé ice state with a low density of monopoles (Fig. 1b). The deviation from the plateau as $\mu_0 H$ exceeds 0.8 T indicates that monopoles are being created gradually, while the saturation of the intensity for $H \gg H_c$ denotes the staggered monopole state (Fig. 1e) where every tetrahedron contains a monopole. The Bragg intensity data are compared with (MC) simulations for the dipolar spin ice model to quantify our observations, and the overall agreement is very good.

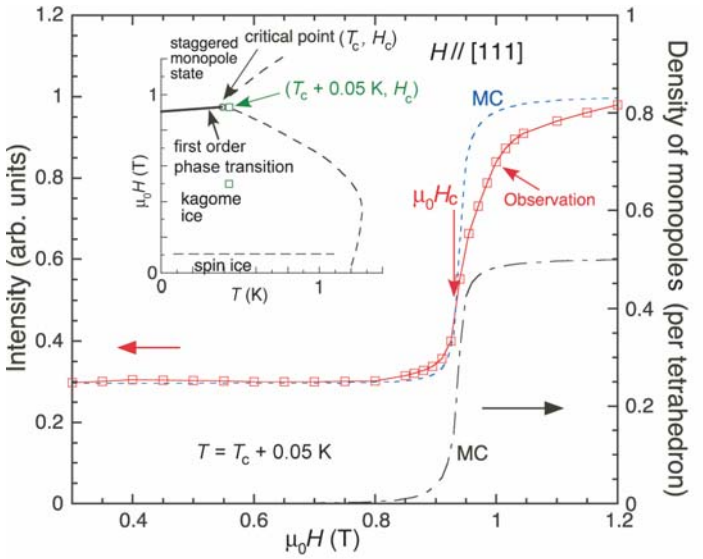

FIGURE 2: The magnetic Bragg intensity at $T = T_c + 0.05$ K is plotted as a function of the [111] magnetic field strength. The open squares and dashed curves represent the neutron scattering measurements at (2,-2,0) and corresponding MC simulations, respectively. The dot-dashed curve is the density of positively charged monopoles obtained by the MC simulation. (Inset) The *H,T* phase diagram for a [111] magnetic field. The solid line represents the first-order phase transition with the critical point shown by an open circle. The dashed lines are crossovers. The intensity maps shown in Fig. 3 were measured at the two points depicted by open squares.

Intensity maps for the diffuse monopole scattering and for the kagomé ice state at $T = T_c + 0.05$ K and $\mu_0 H = 0.5$ T are shown in Fig. 3. The observed scattering pattern of the kagomé ice state (Fig. 3a) is in excellent agreement with the MC simulations (Fig. 3c), showing the peaked structure at (2/3,-2/3,0) and the pinch point at (4/3,-2/3,-2/3). These structures reflect the vacuum kagomé ice state. The intensity map for the diffuse scattering around (2,-2,0) associated with the scattering by the separated monopoles is shown in Fig. 3b. The data agree quite well with the MC simulation shown in Fig. 3d. An interesting experimental fact is that correlations of the monopoles in the high-density regime are three dimensional in space, although the monopoles can only move in the two dimensional layers (Fig. 1d). The three dimensional correlations provide strong evidence that the magnetic inverse-square law interaction really acts between monopoles in all three dimensions.

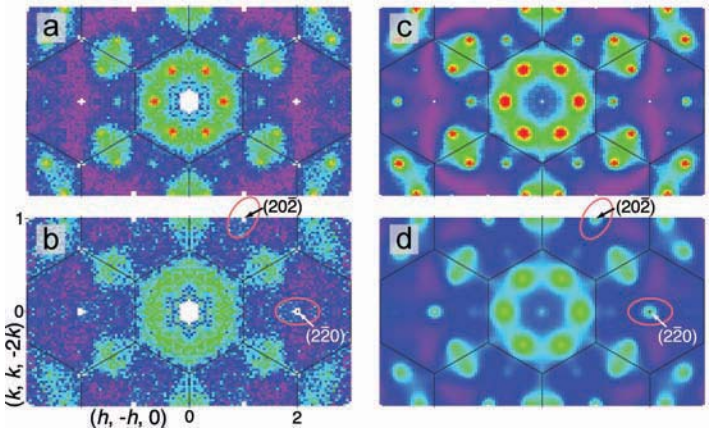

FIGURE 3: Intensity maps of neutron scattering measured at $T = T_c + 0.05$ K are shown for the two field-temperature values indicated in the inset of Fig. 2. The kagomé ice state at $\mu_0 H = 0.5$ T (a) compared with the MC simulations (c), and the weakened kagomé ice state scattering plus the diffuse monopole scattering (b) and MC simulations (d) $H = H_c$.

Typical elementary excitations in condensed matter, such as acoustic phonons and (gapless) magnons, are Nambu-Goldstone modes where a continuous symmetry is spontaneously broken when the ordered state is formed. This behavior contrasts with the monopoles in spin ice, which are point defects that can be fractionalized in the frustrated ground states. Such excitations are unprecedented in condensed matter, and will now enable conceptually new emergent phenomena to be explored experimentally.

References

[1] P. A. M. Dirac, Proc. Royal Soc. **133**, 60 (1931).

[2] K. A. Milton, Rep. Prog. Phys. **69**, 1637 (2006).

[3] C. Castelnovo, R. Moessner, and S. L. Sondhi, Nature **451**, 42 (2008).

[4] H. Kadowaki, N. Doi, Y. Aoki, Y. Tabata, T.J. Sato, J.W. Lynn, K. Matsuhira and Z. Hiroi, J. Phys. Soc. Jpn. **78**, 103706 (2009).

Magnetic and Structural Phase Diagram for the $CeFeAsO_{1-x}F_x$ High Temperature Superconductors

J. Zhao[1], Q. Huang[2], C. de la Cruz[1,3], S. Li[1], J.W. Lynn[2], Y. Chen[2,4], M.A. Green[2,4], G.F. Chen[5], G. Li[5], Z. Li[5], J. L. Luo[5], N.L. Wang[5], and P. Dai[1,3]

The nature of the magnetic order and spin fluctuations in superconductors has had a rich and interesting history, and has been a topic of special interest ever since the parent materials of the high T_c cuprates were found to be antiferromagnetic (AFM) Mott insulators that exhibit huge exchange energies within the Cu-O planes. The parent materials of the newly discovered iron-based superconductors are also energetic antiferromagnets with a layered crystal structure like the cuprates. However, they are not nearly as two-dimensional in character, which is an important advantage for applications such as power transmission lines and energy storage. In the superconducting regime, both classes of high T_c superconductors retain these energetic spin correlations, and it is clear that they are involved in an intimate way in the formation of the superconducting state [1]. Therefore it is critically important to understand how this transformation from magnet to high T_c superconductor is accomplished. We have carried out a systematic investigation of the magnetic and structural properties of $CeFeAsO_{1-x}F_x$ as the system is doped with fluorine (F) into the superconducting regime to elucidate these issues [2].

The parent iron oxypnictide materials such as LaFeAsO [3] and CeFeAsO are metals and have a tetragonal crystal structure at room temperature, but undergo a structural distortion to an orthorhombic phase around 155 K and develop long range antiferromagnetic order of the Fe spins below 140 K [3]. As oxygen is replaced by fluorine, electrons are doped into the parent compound, and both the structural and magnetic transitions decrease with increasing F concentration, x. The magnetic structure remains commensurate and long range in nature with doping, while the ordered moment and Néel temperature T_N(Fe) decrease rapidly with increasing x and vanish near $x = 0.06$, before the emergence of superconductivity for $x > 0.06$. This indicates that the superconducting and magnetic order parameters compete with each other, and the overall behavior is remarkably similar to that of the electron-doped high-T_c copper oxides. The phase diagram as a function of fluorine doping is shown in Fig. 1.

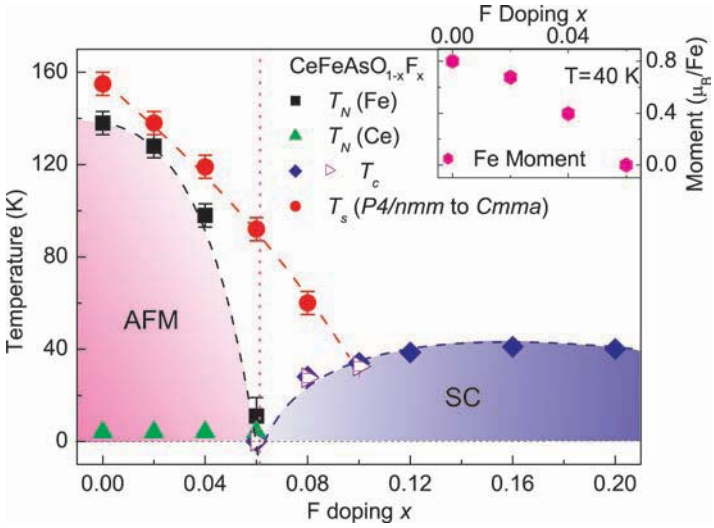

FIGURE 1: The structural and magnetic phase diagram determined from the neutron diffraction measurements on $CeFeAsO_{1-x}F_x$. The red circles indicate the onset temperature T_s of the tetragonal *P4/nmm* to orthorhombic *Cmma* phase transition. The black squares and green triangles designate the Néel temperatures of Fe T_N(Fe) and Ce T_N(Ce), respectively. The superconducting transition temperatures are from the onset T_c of the resistivity measurements. The open triangles are T_c determined from susceptibility measurements. The inset shows the ordered antiferromagnetic moment as a function of F doping.

The structural phase transition temperature decreases more gradually with increasing F doping and disappears around $x = 0.1$ when superconductivity is already well developed. It is important to establish unambiguously that the superconducting state can form equally in the tetragonal to orthorhombic structural phases in $CeFeAsO_{1-x}F_x$. We therefore carried out additional measurements on the $x = 0.08$, 0.10 samples, above x = 0.06, which have superconducting transitions of 27 K and 33 K, respectively. The tetragonal to orthorhombic phase transition temperature was determined to be 60 K for $x = 0.08$, making it clear that the orthorhombic phase is superconducting. No indication of a structural transition was evident for the $x = 0.10$ sample, indicating that this composition is at the terminus of the T-O structural phase boundary. Therefore, superconductivity in $CeFeAsO_{1-x}F_x$ can take place in either the low-temperature tetragonal or orthorhombic crystal structure. No evidence of static long range AFM Fe ordering was evident in either of these samples.

[1]University of Tennessee, Knoxville, Tennessee 37996-1200
[2]NIST Center for Neutron Research, National Institute of Standards and Technology, Gaithersburg, Maryland 20899
[3]Oak Ridge National Laboratory, Oak Ridge, Tennessee 37831
[4]University of Maryland, College Park, Maryland 20742
[5]Institute of Physics, Chinese Academy of Sciences, Beijing 100080, China

Undoped CeFeAsO has an orthorhombic low-temperature structure with $c > a > b$. Doping with F gradually reduces both the a (the long Fe-Fe nearest-neighbor distance) and c-axis lattice constants while leaving the b-axis (the short Fe-Fe nearest-neighbor distance) essentially unchanged. The orthorhombic distortion is quite small for $x = 0.08$, while the c-axis lattice constant decreases systematically with increasing doping for $x > 0.10$. The reduction in the c-axis lattice constant is achieved via a large reduction of the Ce-As distance, while the Ce-O/F and As-Fe-As block distances actually increase with increasing F-doping. This suggests that the effect of F doping is to bring the Ce-O/F charge transfer layer closer to the superconducting As-Fe-As block, thereby facilitating electron transfer. The Fe-As distance (2.405 Å) is found to be essentially independent of x, so that the strong hybridization between the Fe 3d and the As 4p orbitals is not affected by electron-doping. On the other hand, the Fe-Fe nearest-neighbor (J_1) and next-nearest-neighbor (J_2) effective exchange couplings are mediated through the electron Fe-As-Fe hopping and are controlled by the Fe-As-Fe angles, which are strongly x dependent.

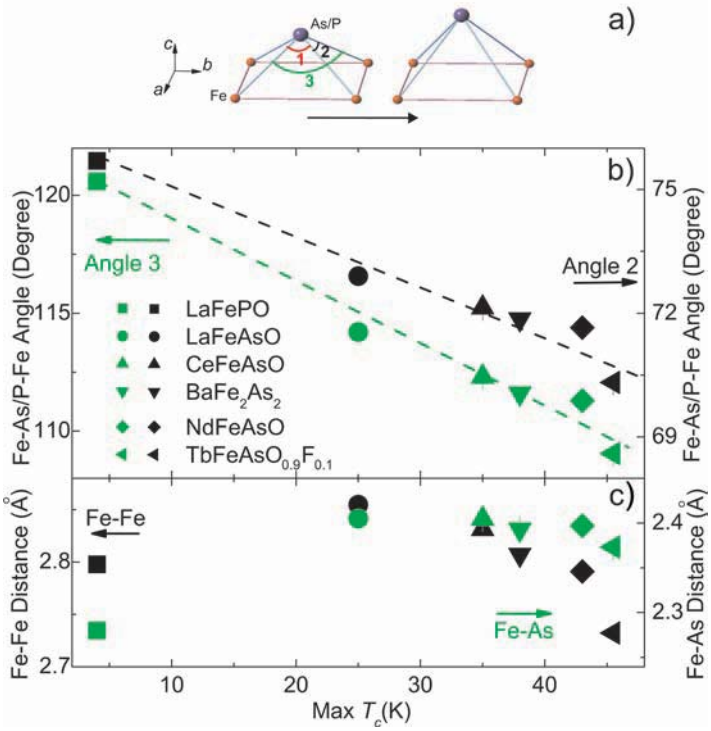

FIGURE 2: Fe-As(P)-Fe bond angles, Fe-Fe, and Fe-As(P) distances for different Fe-based superconductors. There is a systematic decrease in the Fe-As(P)-Fe bond angle for Fe-based superconductors with higher T_c, suggesting that the lattice effects are important. a) Schematic illustration of what happens to the Fe-As-Fe tetrahedron for Fe-based superconductors as a function of increasing T_c. b,c) Dependence of the maximum-T_c on Fe-As(P)-Fe angle and Fe-Fe/Fe-As(P) distance. The maximum T_c is obtained when the Fe-As(P)-Fe bond angle reaches the ideal value of 109.47° for the perfect Fe-As tetrahedron.

Comparison of the structural evolution of $CeFeAsO_{1-x}F_x$ with other rare-earth Fe pnictides and with $(Ba_{1-x}K_x)Fe_2As_2$ has revealed a general trend that the Fe-As-Fe bond angle decreases systematically for materials with increasing T_c. This result suggests that the structural perfection of the Fe-As tetrahedron plays a crucial role for the superconducting pairing in these high-T_c Fe pnictides. In particular, the exchange couplings (J_1 and J_2) are directly related to the Fe-As-Fe bond angles, shown in Fig. 2a. Figures 2b and 2c plot the Fe-As(P)-Fe angles and Fe-Fe/Fe-As(P) distances versus the maximum T_c for different Fe-based rare-earth oxypnictides and $Ba_{1-x}K_xFe_2As_2$ superconductors. While the Fe-Fe/Fe-As(P) distances don't appear to have a clear trend amongst different Fe-based superconductors, we find the remarkable result that the maximum T_c is directly related to the Fe-As(P)-Fe angles for a variety of materials as shown in Fig. 2c. In particular, the highest T_c is obtained when the Fe-As(P)-Fe angle reaches the ideal value of 109.47° for the perfect Fe-As tetrahedron. This suggests that the general way to increase T_c in the Fe-based superconductors is to reduce the deviation of the Fe-As(P)-Fe bond angle from the ideal Fe-As tetrahedron.

In summary, we have mapped out the structural and magnetic phase transitions of $CeFeAsO_{1-x}F_x$ and found that the Fe long range antiferromagnetic order vanishes before the appearance of superconductivity. The phase diagram of $CeFeAsO_{1-x}F_x$ is therefore remarkably similar to that of the electron-doped high-T_c copper oxides. The superconducting state, on the other hand, can form in both the orthorhombic and tetragonal structures. In addition to suppressing the static antiferromagnetism and inducing superconductivity, F doping also reduces the long-axis of the orthorhombic structure and decreases the Fe-As-Fe bond angles. We found that the Fe-As(P)-Fe bond angle plays a key role for the superconductivity, with T_c reaching its maximum value for the ideal Fe-As tetrahedral angle. Thus the distortion from the ideal Fe-As tetrahedron must be taken into account as we consider a mechanism for the high-T_c superconductivity in these Fe-based materials.

References

[1] J.W. Lynn and P. Dai, Physica C **469**, 469 (2009).

[2] J. Zhao, Q. Huang, C. de al Cruz, S. Li, J. W. Lynn, Y. Chen, M. A. Green, G. F. Chen, G. Li, Z. C. Li, J. L. Luo, N. L. Wang, and P. Dai, Nature Materials **7**, 953 (2008).

[3] C. de la Cruz, Q. Huang, J. W. Lynn, J. Li, W. Ratcliff II, J. L. Zarestky, H. A. Mook, G. F. Chen, J. L. Luo, N. L. Wang, and P. Dai, Nature **453**, 899 (2008).

Formulas Matter - Stoichiometry and Superconductivity in $Fe_{1+\delta}Se$

T.M. McQueen[1], Q. Huang[2], V. Ksenofontov[3], C. Felser[3], Q. Xu[4], H. Zandbergen[4], Y.S. Hor[1], J. Allred[1], A.J. Williams[1], D. Qu[5], J. Checkelsky[5], N.P. Ong[5] and R.J. Cava[1]

Because iron is best known as the element that most often leads to high temperature ferromagnetism, the discovery of superconductivity in 2008 [1] in fluorine doped lanthanum iron arsenide oxide (LaFeAsO), with the high onset temperature of 26 K, came as a surprise to the materials physics community. This compound gave rise to a new chemical family of superconductors, based on Fe_2X_2 (X = P,As) layers of edge-sharing FeX_4 tetrahedra, now including oxygen-free systems and complex layered phases of various types. In all cases the materials are difficult to make, and involve reactive, volatile elements whose chemistry is difficult to control. Important discrepancies therefore arise between the formulas that researchers assume their materials have, and those they actually do have.

In the process of investigating these compounds, superconductivity was discovered at 8 K in chemically analogous FeSe in its tetragonal form [2]. The Fe_2Se_2 layers in this compound are analogous to the Fe_2As_2 and Fe_2P_2 layers in the pnictide and oxypnictide superconductors. The initial report attributed the superconductivity to a highly selenium deficient phase, $FeSe_{0.82}$ (*i.e.*, $Fe_{1.22}Se$). This was quickly followed by a structural study that arrived at a composition of $FeSe_{0.92}$ ($Fe_{1.09}Se$) for the superconductor. Both of these formulas fall well outside the narrow composition range, $Fe_{1.01}Se$-$Fe_{1.04}Se$, reported for the tetragonal form of "FeSe" more than thirty years ago [3]. Thus, what appeared at first to be the simplest of the new family of superconductors, holding out the hope that its study might lead to the determination of unambiguous structure-formula-property relations, seemed to be different compounds in different laboratories. It was due to this problem that we took up the case of determining the formula of the "FeSe" superconductor.

Our initial attempts to prepare phase-pure superconducting FeSe employed the methods typically employed in this field, starting with 'freshly cleaned' Fe powder. In agreement with others, we found that a significant amount of iron in excess of the ideal 1:1 ratio, in our case $Fe_{1.06}Se$, was needed to make a sample that appeared to be "phase pure" by laboratory x-ray diffraction (XRD). Our initial neutron powder diffraction (NPD) characterization of these samples on the NIST high resolution powder neutron diffractometer BT-1, showed, however, that they were strongly multiple phase, with a substantial amount of iron oxide present, forcing us to reconsider the synthetic method employed. When prepared from very clean starting materials, specifically taking care to exclude oxygen, to include steps and reactants specifically designed to remove any fortuitous oxygen from the synthetic system, protecting the synthetic system from in-situ oxygen leaks, and quenching the products to avoid low temperature decomposition, we found in contrast to the materials physics researchers that the formula of single phase material is $Fe_{1.01}Se$.

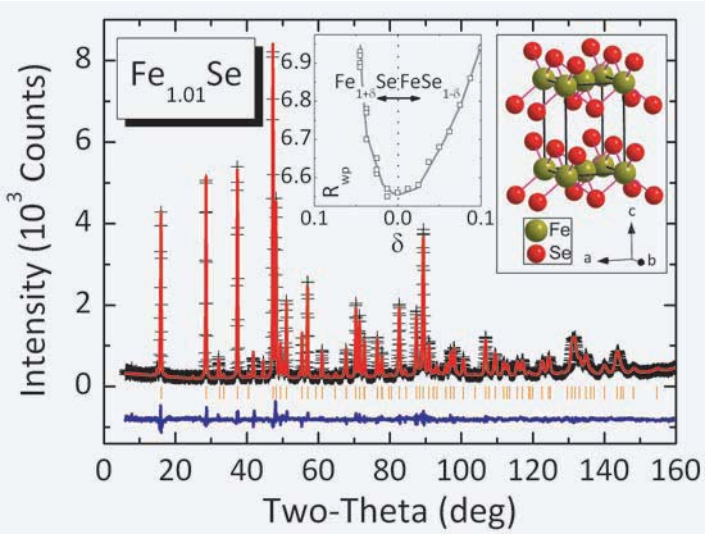

FIGURE 1: Rietveld refinement of 298 K BT-1 powder neutron diffraction data of $Fe_{1.01}Se$ annealed at 300 °C. The left inset shows the fit statistic R_{wp} plotted versus Fe-interstitals (left) and Se-vacancies (right). From these data it is not possible to determine the origin of the 1 % non-stoichiometry, but this shows that the formula of superconducting "FeSe" must be within ≈ 2 % of stoichiometric. The right inset shows the structure of the superconducting phase.

The formula of the superconducting FeSe phase was confirmed to be nearly stoichiometric by Rietveld refinements of the NPD data collected on BT-1. When freely refined, the composition of the superconducting phase is nearly stoichiometric, in agreement with our chemical equilibrium studies. To best determine the

[1]Department of Chemistry, Princeton University, Princeton NJ 08544
[2]NIST Center for Neutron Research, National Institute of Standards and Technology, Gaithersburg MD 20899
[3]Institut für Anorganische Chemie und Analytische Chemie, Johannes Gutenberg-Universität, Staudinger Weg 9, D-55099, Mainz, Germany
[4]Department of Nanoscience, TU Delft, The Netherlands
[5]Department of Physics, Princeton University, Princeton NJ 08544

stoichiometry and to see if we could locate the origin of any non-stoichiometry, we performed free fits to the data as a function of fixed doping levels, with excess iron in interstitial sites and with selenium vacancies. The refinement agreement statistics R_{wp} (minimum for the best agreement) for those refinements as a function of hypothetical stoichiometry are plotted in the inset to Fig. 1. The best agreement is centered at the stoichiometric FeSe composition, with the breadth of the minimum indicating a composition of $Fe_{1.01\pm0.02}Se$. Thus, although these measurements do not have sufficient sensitivity to determine the stoichiometry to better than ± 0.02, the nearly ideal formula of the superconducting FeSe phase is clearly confirmed.

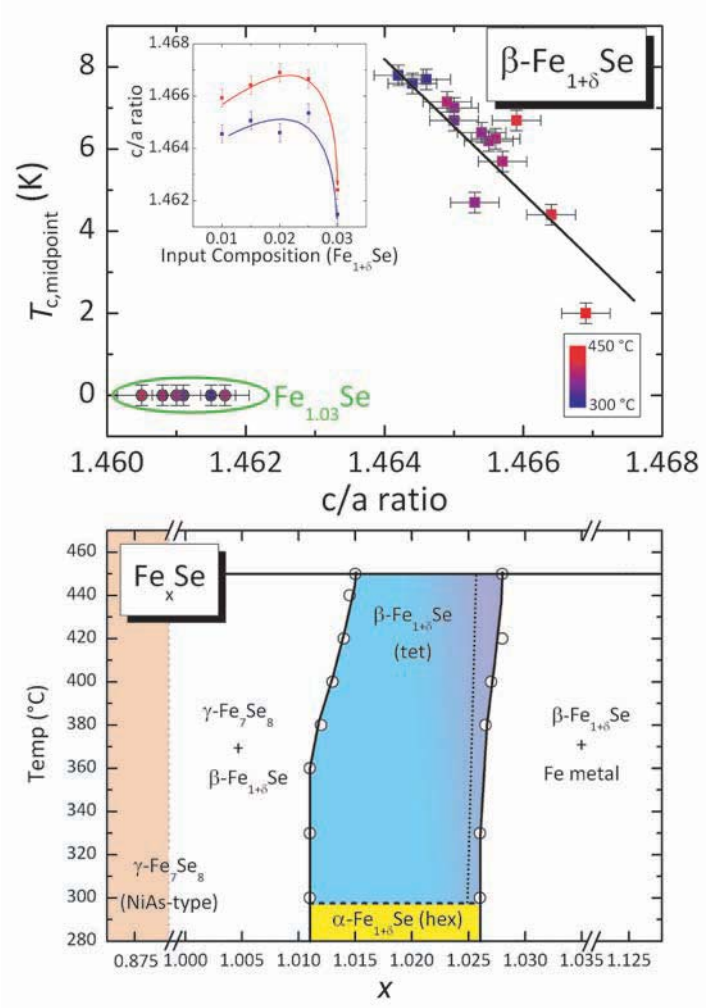

FIGURE 2: (a) Dependence of superconducting transition temperature (T_c) on the crystallographic *c/a* ratio. The inset shows the dependence of *c/a* ratio on synthesis temperature and nominal composition. (b) Phase diagram derived from the samples shown in (a) and others (not shown). Actual compositions of the samples were estimated from the fraction of impurity phases present (Fe_7Se_8 and Fe metal) by XRD and/or room temperature *M(H)* curves. Below 300 °C, the tetragonal form of $Fe_{1+\delta}Se$, within which superconductivity occurs, slowly converts to the hexagonal NiAs form, which is not superconducting.

Further detailed synthesis and analysis studies indicate that the superconductivity, the formula, the synthesis conditions, and the crystal structure are correlated in the "FeSe" phase in an extremely sensitive manner. Fig. 2(a) shows the superconducting transition temperature T_c versus the crystallographic *c/a* ratio (the ratio of intraplane and interplane lattice parameters) for a number of the samples in this system. Several features are evident. Samples prepared at lower temperatures or with lower iron content display *c/a* ratios just above 1.464 and also display the highest superconducting transition temperatures. Higher iron contents or higher synthesis temperatures yield larger *c/a* ratios and reduced T_c's. Samples prepared with the highest iron content, $Fe_{1.03}Se$, show no superconductivity to 0.6 K, irrespective of the synthesis temperature. These samples also display abnormally small c/a ratios, near 1.461. Two distinct structure/superconductivity regions are therefore clearly seen in Fig. 2(a). The inset of Fig. 2(a) shows the dependence of the *c/a* ratio on starting composition for two representative preparation temperatures. In both cases, *c/a* initially rises with increasing Fe content, but by the composition $Fe_{1.03}Se$ the *c/a* ratio is much reduced. We postulate that this peculiar dependence of *c/a* ratio on iron content and the accompanying dramatic disappearance of superconductivity for $Fe_{1.03}Se$ are due to a change in how the non-stoichiometry is accommodated in the phase. Subtle differences in the structure therefore indicate that there is likely a difference in defect chemistry between superconducting and non-superconducting compositions. On the basis of these experiments, we construct the detailed phase diagram for the Fe-Se system near the 1:1 stoichiometry in Fig. 2(b).

The extreme sensitivity of structure and properties to the formula of the "FeSe" superconductor likely extends to other members of this family, and may explain conflicting reports about the properties in other much more problematic members of this superconducting family. Our study clearly shows that careful solid state chemistry and structural analysis can play an important role in the study of the structure/property relations in complex materials.

References

[1] Y. Kamihara, T. Watanabe, M. Hirano, and H. Hosono, Journal of the American Chemical Society **130**, 3296 (2008).

[2] F. C. Hsu, J. Y. Luo, K. W. Yeh, T. K. Chen, T. W. Huang, P. M. Wu, Y. C. Lee, Y. L. Huang, Y. Y. Chu, D. C. Yan, and M. K. Wu, Proceedings of the National Academy of Sciences **105**, 14262 (2008).

[3] W. Schuster, H. Mikler, and K. L. Komarek, Monatshefte Fur Chemie **110**, 1153 (1979).

[4] T.M. McQueen, Q. Huang, V. Ksenofontov, C. Felser, Q. Xu, H. Zandbergen, Y.S. Hor, J. Allred, A.J. Williams, D. Qu, J. Checkelsky, N.P. Ong, R.J. Cava, Phys. Rev. B **79**, 01452 (2009).

Iron-Arsenide Superconductors Under Pressure: The Unusual Case of $CaFe_2As_2$

A. Kreyssig[1], D.K. Pratt[1], S. Nandi[1], Y.B. Lee[1], G.D. Samolyuk[1], N. Ni[1], S.L. Bud'ko[1], B.N. Harmon[1], P.C. Canfield[1], R.J. McQueeney[1], A.I. Goldman[1], M.A. Green[2], P. Zajdel[2], Y. Chen[2], J.B. Leão[2], S.J. Poulton[2], J.W. Lynn[2], K. Prokeš[3], S.A.J. Kimber[3], D.N. Argyriou[3], M.S. Torikachvili[4]

Two recently discovered families of high transition temperature (high T_c) superconductors originate from the parent systems RFeAsO (R = rare earth) and AFe$_2$As$_2$ (A = alkaline earth metal). The parent compounds are not superconducting at ambient pressure, while chemical doping results in a superconducting transition as high as 55 K in RFeAsO$_{1-x}$F$_x$ and 38 K in A_{1-x}K$_x$Fe$_2$As$_2$. Much of the excitement surrounding these new superconductors is that they offer yet another route to high superconducting transition temperatures, because the ubiquitous copper-oxygen planes found in the older high T_c superconductors, the cuprates, are absent. The RFeAsO and AFe$_2$As$_2$ families are tetragonal at room temperature but undergo an orthorhombic distortion in the range 100 K to 220 K that is associated with the onset of antiferromagnetic order (see Fig. 1). Tuning the system via element substitution or oxygen deficiency suppresses the magnetic order and structural distortion in favor of superconductivity, with a phase diagram strikingly similar to the high-T_c copper oxide family of superconductors. In particular, strong magnetic correlations persist in the superconducting regime, and a magnetic resonance forms below T_c, demonstrating that magnetism is intimately tied to the superconducting state.

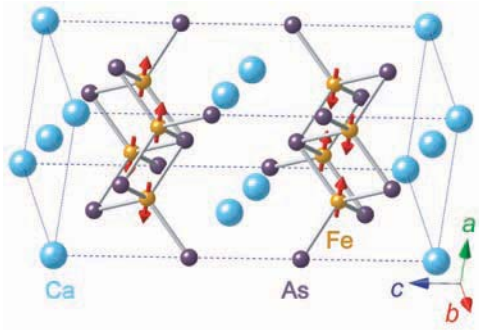

FIGURE 1: Illustration of the crystal structure of $CaFe_2As_2$, and the antiferromagnetic structure below the structural/magnetic transition. The magnetic unit cell is the same as the orthorhombic chemical unit cell. The Fe moments are oriented along the orthorhombic *a* axis.

In the AFe$_2$As$_2$ (A=Ba,Sr,Ca) family it was reported that the parent compounds themselves become superconducting with T_c as high as 28 K in BaFe$_2$As$_2$ and SrFe$_2$As$_2$, and 12 K in $CaFe_2As_2$ [1]. The application of pressure can have significant effects on the enhancement or suppression of superconductivity. Particularly striking is the case of $CaFe_2As_2$ where the onset of superconductivity was observed for pressures of only 0.2 GPa, a very low value indeed. Our powder (BT-1) and single crystal (BT-7) diffraction studies were carried out to detect any changes in the structure that might be associated with the onset of superconductivity, and these investigations discovered dramatic changes in the structure and magnetism of $CaFe_2As_2$ under pressure.

It is important to first describe the different ways that one can apply pressure to a sample for such experiments. The basic pressure cell arrangement consists of a sample immersed in a medium, such as a gas or liquid, and the force applied to that medium by a set of anvils is transmitted undiminished to the sample. In the *hydrostatic* limit, the entire sample experiences the same pressure. However, depending on the properties of the medium itself, *nonhydrostatic* effects can be realized. For example, at low temperatures liquid media typically solidify and the hydrostatic limit cannot be realized. This is not an issue for He-gas pressure cells for temperatures and pressures above the freezing line and, so, they are capable of reaching the hydrostatic limit over a much wider range of temperatures and pressures. The application of hydrostatic pressure in these studies proved to be key in understanding the nature and behavior of $CaFe_2As_2$ under pressure.

Figure 2 shows BT-1 powder diffraction scans in a He-gas pressure cell through the nuclear (0 0 2) [panel (a)], $(2\,2\,0)_T$ [panel (b)], and antiferromagnetic $(1\,2\,1)_{OR}$ [panel (c)] Bragg peaks (indices are either the tetragonal unit cell or the low temperature, ambient pressure orthorhombic unit cell) at selected temperatures and pressures [2]. At 50 K and ambient pressure (A), the splitting of the tetragonal $(2\,2\,0)_T$ into the $(400)_{OR}/(040)_{OR}$ peaks, together with the observation of the magnetic $(1\,2\,1)_{OR}$ magnetic peak (Fig. 2(c)), signals that the sample has transformed to the orthorhombic phase (Fig. 2(b)). Then with increasing pressure, dramatic changes take place in the measured diffraction patterns between 0.24 GPa and 0.35 GPa. Above 0.35 GPa (Fig. 2(c))

[1]Ames Laboratory, USDOE and, Iowa State University, Ames, IA 50011
[2]NIST Center for Neutron Research, National Institute of Standards and Technology, Gaithersburg, MD 20899
[3]Helmholtz-Zentrum Berlin für Materialien und Energie, Glienicker Straße 100, 14109 Berlin, Germany
[4]San Diego State University, San Diego, CA 92182

the magnetic peak is absent and the orthorhombic structure has transformed to a tetragonal phase, similar to the high-temperature ambient-pressure structure, but with extraordinarily different lattice parameters. This is most evident from the huge shift in the positions of the (0 0 2) and (2 2 0) peaks at (B) in Figs. 2(a) and 2(b), respectively. We found an astonishing 9.5 % reduction in the *c*-lattice parameter with respect to the orthorhombic phase in this pressure-induced "collapsed" tetragonal (*cT*) phase, and a nearly 5 % decrease in the unit-cell volume. There is a small increase in *a*, which produces an even more striking reduction of the *c*/*a* ratio by nearly 11 %, a key parameter for bond geometries in the iron arsenides. With the pressure maintained at 0.63 GPa, an isostructural transition between the low temperature *cT* phase and the high temperature tetragonal structure was observed.

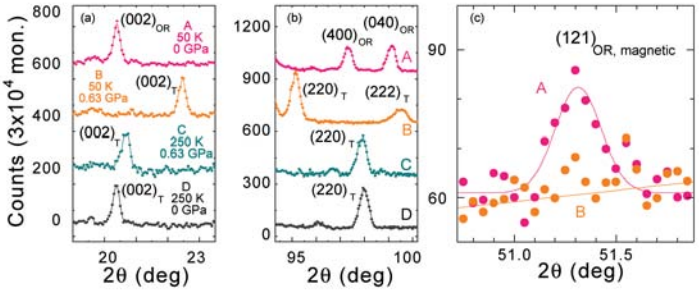

FIGURE 2: Scans through [(a) and (b)] nuclear and (c) magnetic peaks in neutron-diffraction pattern at selected temperatures and pressures. Note that the diffraction peaks change position dramatically due to the huge changes in the lattice parameters. In (c), the magnetic $(1\ 2\ 1)_{OR}$ magnetic diffraction peak for point A is clearly observed above the background taken at B. No new magnetic peaks for B and C were observed.

The dramatic structural transition to the *cT* phase was a surprise, but was then confirmed by spin-polarized total-energy calculations that revealed that the collapsed phase is indeed the most stable phase for the measured 5 % volume collapse [2]. Perhaps most intriguing was the prediction that the *cT* phase is nonmagnetic—the iron moment is quenched. Indeed, no magnetic order or spin fluctuations have been observed in this phase.

Is the *cT* phase in $CaFe_2As_2$ then responsible for superconductivity? Here is where the story takes an interesting twist. The original resistivity measurements [1] on $CaFe_2As_2$ were taken in a conventional pressure cell using a liquid→solid pressure medium. It is worth noting here that $CaFe_2As_2$ is an extremely soft material, and because of the highly anisotropic nature of the change in the structure, the pressure realized in the collapsed phase was also highly anisotropic. When these resistivity measurements were repeated using a He-gas pressure cell, no trace of superconductivity for pressures below 0.7 GPa was found [3]. It appears that superconductivity only occurs in samples subject to a nonhydrostatic pressure component, perhaps due to phase separation, the appearance of some new as yet unidentified phase, or grain boundaries in a multiphase sample.

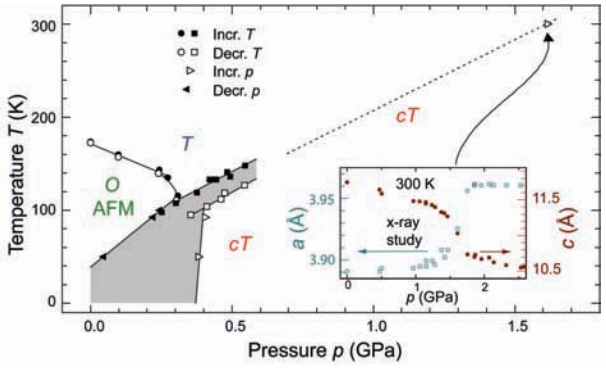

FIGURE 3: Pressure-temperature phase diagram of $CaFe_2As_2$ under hydrostatic pressure determined from neutron and high-energy x-ray diffraction measurements. Filled and open circles (squares) denote phase boundaries determined upon heating and cooling at a set of pressures, respectively. Filled and open triangles denote phase boundaries determined upon decreasing and increasing pressure at a fixed temperature, respectively. The shaded area denotes the hysteretic region. The inset shows the change in lattice constants at the *T*-*cT* transition at 300 K.

To further elucidate the nature of the *p*-*T* phase diagram we turned to single crystal neutron diffraction measurements on BT-7 at NIST, along with high energy x-ray data at Sector 6 of the Advanced Photon Source, and on the E4 diffractometer at the Helmholtz-Zentrum Berlin für Materialien und Energie in Berlin [4]. The results of are summarized in Fig. 3,which clarifies the phase boundaries between the tetragonal, orthorhombic and *cT* phases. Perhaps most interesting is the observation of an extremely broad range of phase coexistence at the pressure/temperatures of transitions between these phases. Under hydrostatic conditions sharp first-order transitions between the phases were observed. Subsequent clamp cell measurements revealed a very broad transition and coexistence region, confirming that there are important differences in behavior between hydrostatic and nonhydrostatic pressure. While these measurements have clarified the nature of the magnetic and crystal structures under pressure, the search for the superconducting phase fraction in $CaFe_2As_2$ under nonhydrostatic pressure conditions continues.

References

[1] M. S. Torikachvili, *et al.*, Phys. Rev. Lett. **101**, 057006 (2008).
[2] A. Kreyssig, *et al.*, Phys. Rev. B **78**, 184517 (2008).
[3] W. Yu, *et al.*, Phys. Rev. B **79**, 020511(R) (2009).
[4] A.I. Goldman, *et al.*, Phys. Rev B **79**, 024513 (2009).

Key Role of Iron-magnetism in High-temperature Fe-pnictide Superconductors

T. Yildirim[1]

High-temperature superconductivity (high-T_c) discovered in 1986 remains one of the great unsolved problems of condensed matter physics. The phenomenon was first found in a class of Cu-O-based compounds (cuprates). Although no explanation is yet completely satisfactory, the current belief is that the magnetic moments of the Cu ions in some manner play a major role in the superconductivity in cuprates. Thus the situation has stood, until the recent discovery of an entirely new class of high-T_c superconductors featuring FeAs (iron pnictide) layers that are analogous to the CuO planes, the major structural feature in the cuprates.

The key question now becomes: what is the mechanism of the superconductivity in these Fe-pnictide systems? The answer to this question is expected to shed light on the long-standing question of the mechanism of high-T_c superconductors in general. Here, we present a brief review of our first principles studies which clearly show that the Fe-spin is the key factor controlling many physical properties of the pnictide systems, including atomic positions, crystal cell size, structural phase transitions, and lattice vibrations, and which provide a strong clue about the superconducting mechanism. In particular, we show how giant magneto-elastic coupling (*i.e.*, a large response of structure to a small change in the magnetization of its atoms) arises, and suggest that this enormous sensitivity of the structure to the Fe-spin may be a key ingredient in the mechanism of high-T_c superconductivity in Fe-pnictides.

From accurate all-electron density functional calculations we showed [1] that there are strong and competing magnetic interactions in these systems that explain both the observed spin-pattern and the structural phase transition. Our theory also predicted the sign of the lattice distortion which was later confirmed experimentally. Similarly, our prediction of very large magnetic exchange interactions (*i.e.,* J_1 and J_2) [1] has recently been confirmed by measurements of spin-waves up to 120 meV, which is almost the same energy scale as spin-waves in the cuprates [2].

When the iron magnetism is ignored, the calculations explain neither structure nor lattice vibration energies (*i.e.*, phonons), resulting in large discrepancies between theory and experiment. In particular, as shown in Fig. 1, when the Fe-spin is turned off [3], the system basically collapses, resulting in a 12 % reduction in the distance between FeAs-layers for the case of $CaFe_2As_2$. The response of the lattice to the change in magnetic moment of its atoms is called magneto-elastic coupling and its magnitude is usually tiny, hardly measurable by x-ray or neutron scattering. However for the case of Fe-pnictide, this effect is enormous. To the best of our knowledge, such a giant coupling of the lattice to its atom-spin state has not been seen before. In our recent study [3] we traced the origin of this c-axis collapse to the large As-As interaction between adjacent FeAs layers.

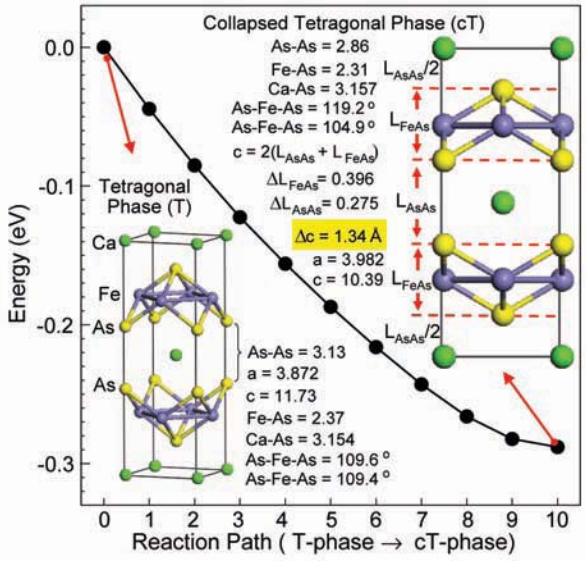

FIGURE 1: Total energy along a reaction path, showing that the $CaFe_2As_2$ tetragonal (T) phase goes directly to collapsed-tetragonal (cT) phase during structural optimization without Fe-magnetism. The insets show the initial (T-Phase) and final (cT-phase) $CaFe_2As_2$ structures with relevant bond-distances (in Å) and angles (in degrees). Note that in the cT-phase the change in the height of the FeAs layer and the change in the distance between FeAs layers are comparable, indicating a uniform compression of the whole lattice.

In order to demonstrate that there is large hybridization between As ions in the $CaFe_2As_2$ system, we show the contour plots of the relevant orbitals in Fig. 2. It is very clear that the As ion below the top Fe-plane makes a bond (or hybridizes) with the arsenic ion which is above the lower Fe-plane. In the collapsed-phase the As-As bonding along the c-axis gets significantly stronger. According

[1]NIST Center for Neutron Research, National Institute of Standards and Technology, Gaithersburg MD 20899

to bond-population analysis, the bond strength increases by a factor of two. Due to close proximity of the As ions in adjacent Fe-layers, the observation of the As-As interaction is probably not that surprising. What is surprising is to see that there is almost the same type of hybridization between two arsenic ions in the *same* FeAs-layer as shown in the bottom panel of Fig. 2. The mechanism by which the *c*-axis shrinks is the strengthening of the bonding of the As ions above and below a given Fe plane as a consequence of the weakening Fe-As interaction with decreasing Fe-moment.

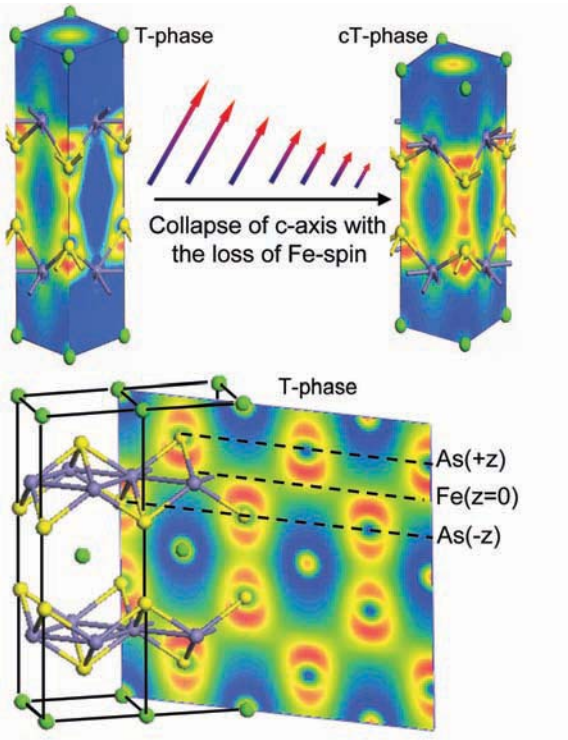

FIGURE 2: Contour plot of one of the orbitals that is responsible for the discovered As-As covalent bonding for the T-phase (top-left) and the cT-phase (top-right), respectively. Note that the As-As bonding present in both phases is much more significant in the cT-phase. The bottom panel shows another orbital on a slice along (110) plane, indicating clear hybridization between intra-layer As atoms below and above the Fe-plane in the T-phase.

So far we have shown that the inclusion of Fe-spin in calculations accounts for lattice parameters and internal atomic coordinates. Below we show that this inclusion also resolves most of the outstanding issues in the observed phonon modes in pnictides, as shown in Fig. 3. Our phonon calculations are done using the direct finite displacement technique, as described in Ref. [2]. The main advantage of this technique over standard linear response theory is that we treat the magnetism and phonon displacements equally and self-consistently. We have already seen that the Fe-magnetic moment is very sensitive to the As-*z* position and therefore it is not a good approximation to assume that the spins are fixed as the atoms move according to a given phonon mode. In our approach, this direct and strong interplay of magnetism and structure is treated self-consistently.

As shown in Fig. 3, including the Fe-spin contribution to the atomic forces [2] allows us to accurately predict the positions of the measured peaks in the lattice vibrational density of states (DOS). Turning on the Fe-spin softens two particular phonon modes (namely, As-atoms vibrating along a line between planes, and in-plane Fe-Fe stretching modes), as observed experimentally, and therefore, through fluctuations of the Fe-spin state, these modes could have very large electron-phonon coupling. This large coupling may be related to the observed high-*T*c. We are currently investigating this possibility.

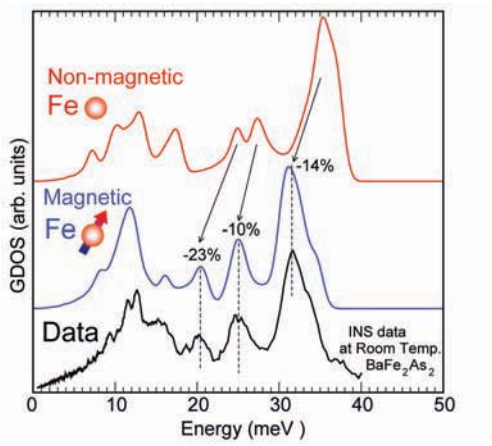

FIGURE 3: Generalized Phonon DOS measured by inelastic neutron scattering at room temperature for $BaFe_2As_2$ (bottom black curve) [4] and the calculated GDOS with (middle blue) and without (top red) Fe-magnetism. Note that including the Fe-spin in the calculations softens the Fe-Fe in-plane and As c-phonons by about 10 % and 23 % and results a DOS that is in excellent agreement with the room temperature data (*i.e.*, well above T_N = 140 K).

In conclusion, we presented several examples which demonstrate that almost all of the observed structural and dynamical properties of Fe-pnictides can be explained in detail, provided that Fe-magnetism is always present in Fe-pnictide systems, even at temperatures well above T_N. The iron magnetism could be in the form of fluctuating spin-density wave type small magnetic domains or it could be at the atomic limit of paramagnetic Fe ions. Further work is required to have a better understanding of the Fe-magnetism in these systems. From the results presented here it is clear that iron-magnetism in the Fe-pnictides is the key factor that controls atomic positions, lattice parameters, structural phase transition, phonon energies, and most probably the superconducting properties as well.

References

[1] T. Yildirim, Phys. Rev. Lett. **101**, 057010 (2008).
[2] T. Yildirim, Physica C (special issue on Fe-pnictides), **469**, 425 (2009).
[3] T. Yildirim, Phys. Rev. Lett. **102**, 037003 (2009).
[4] M. Zbiri, *et al.*, Phys. Rev. B **29**, 064511 (2009).

How Does Cardiac Myosin Binding Protein C Help to Maintain a Healthy Heart Beat?

A.E. Whitten[1], C.M. Jeffries[2], S.P. Harris[3], J. Trewhella[2]

Cardiac myosin binding protein-C (cMyBP-C) is a modular protein that fine tunes the regulation of heart muscle contractions and is linked to the inherited heart disease known as familial hypertrophic cardiomyopathy (FHC) [1]. Up to 1 in 500 adolescents and young adults are affected by FHC [2], which presents as a gradual thickening of the ventricle walls of the heart and is a correlated with increased risk of heart failure. A large number of the gene mutations linked to clinical cases of FHC are in a region that codes for the first four 'regulatory' modules of cMyBP-C. There is increasing evidence that these modules affect their regulatory role through interactions with the thin filaments of heart muscle. We therefore undertook to characterize the structure of these modules and of the assembly they form with actin in order to understand the molecular basis for cMyBP-Cs regulatory role. With this foundational knowledge, we can determine how FHC-linked mutations disrupt that role and cause disease.

Heart muscle is one of the 'striated' muscles, so called because of the stripes it reveals under the microscope arising from inter-digitated thick and thin filaments, the primary components of which are the proteins myosin and actin, respectively. Muscle contraction and relaxation occurs as the filaments slide past each other via the cyclic action of cross bridges formed by the myosin heads that extend from the thick filament to bind to specific sites along the actin thin filament. These actomyosin interactions generate the force required to drive the sliding motion and are regulated by the thin filament accessory proteins troponin and tropomyosin. In response to calcium binding to troponin, tropomyosin moves to unveil the cross-bridge binding sites on the thin filament. Cardiac myosin binding protein-C, first identified as a thick filament accessory protein, appears to provide an additional regulatory layer to the contractile cycle, with biochemical and physiological data implicating the four regulatory modules of cMyBP-C in modulating the myosin cross bridge interactions; the modules are designated C0-C1-m-C2, or C0C2).

Using small-angle x-ray scattering, we first demonstrated that equimolar mixtures of C0C2 and actin form a large molecular assembly. To determine the arrangement of actin and C0C2 within this assembly we used small-angle neutron scattering with contrast variation [1] (Fig. 1a). Differentiation of the C0C2 from the actin was achieved by using C0C2 that had been produced by bacterial expression from cultures grown on D_2O to yield a deuterated protein (^{D}C0C2). The ^{D}C0C2 has a different the neutron scattering-length density than the non-deuterated actin. The relative contributions to the total scattering ($I(q)$) of the ^{D}C0C2 and actin can therefore be modulated by systematic variation of the solvent deuterium content. In solutions containing ≈ 40 % mole fraction D_2O the scattering-length density of actin matches that of the solvent and only ^{D}C0C2 contributes significantly to the scattering, while ^{D}C0C2 is solvent matched between 90 % to 100 % D_2O.

The scattering data revealed that the assembly had F-actin at its core, with the ^{D}C0C2 decorating its exterior (Fig. 1b). As the length of the assembly was beyond the resolution of our data to determine, we analyzed the data initially in terms of the distribution of scattering density in the cross-section. We had previously developed

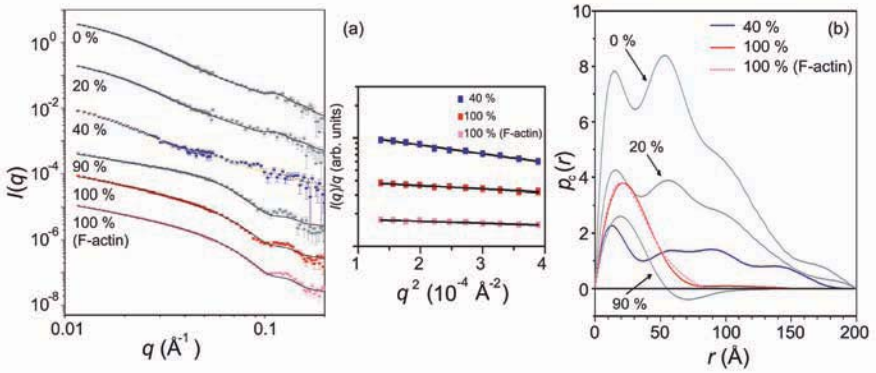

FIGURE 1: (a) Neutron contrast variation data on assemblies of ^{D}C0C2 with actin, solid lines are the fits of the model in Fig. 2 to the data. (b) Probable frequency distribution of distances between scattering centers in the cross-sectional area of the rod-like assembly. The profiles for the 40 % and 100 % data are dominated by the ^{D}C0C2 and actin components, respectively. Comparison of the 100 % profile with that from pure F-actin shows the core is F-actin, while the ^{D}C0C2 extends to ≈ 200 Å, significantly beyond the ≈ 75 Å F-actin diameter.

[1]Bragg Institute , Australian Nuclear Science and Technology Organisation, Lucas Heights, NSW 2234, Australia
[2]University of Sydney, Sydney, NSW 2006, Australia
[3]University of California at Davis, Davis, CA 95616

a structural model for the four-module C0C2 based on NMR structures and homology models for each module and small-angle x-ray scattering data for the intact C0C2 [2]. Using this model, and the fact that we were able to demonstrate that the assembly had approximate two-fold symmetry in its cross-section and thus decorated the F-actin in a regular manner, we were able to complete a comprehensive search of model space and determine a three-dimensional structure of the assembly (Fig. 2, *left*) reveals C0C2 bound at specific actin binding, decorating the fiber in a regular fashion. This structure fits all of the scattering data with nearly ideal fit parameters (Fig. 1a).

Our model shows C0 and C1 interacting with the two neighboring actin molecules along the fiber (Fig. 2, *middle*), explaining the unexpected preservation of a filamentous C0C2-actin assembly in solution conditions that normally support only monomeric actin. In muscle, the stoichiometry of cMyBP-C to actin is much lower than in this saturated assembly and so we confine further interpretation to the details of the C0C2-actin binding interface and implications this has for muscle regulatory mechanisms.

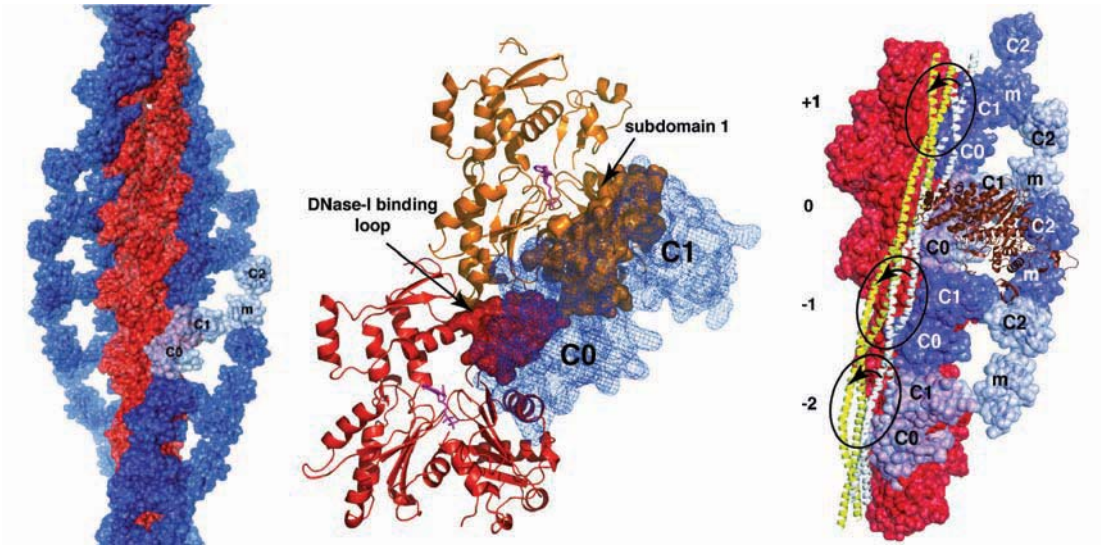

FIGURE 2: *Left* Model structure of C0C2 (blue) decorated actin (red) filaments based on the neutron scattering data. *Middle* Detailed view showing the C0 and C1 modules (blue) binding to neighbouring actin monomers (red and orange) in the filament. *Right* The actin filament (red) with a set of bound C0C2 molecules with the Ca^{2+} on (yellow) and off (white) positions of tropomyosin depicted. Note the strong steric clashes for the Ca^{2+} off tropomyosin position.

Our model suggests cMyBP-C can fine tune the regulation of heart muscle contractions via interactions with tropomyosin and/or myosin cross-bridges, thereby influencing the activation state of the thin filament (Fig. 2, *right*). Our structure predicts significant steric clashes with tropomyosin, especially under conditions of low Ca^{2+} when tropomyosin normally occupies a position that blocks myosin cross-bridge binding to the thin filament. If C0 and C1 displace tropomyosin away from this blocked configuration under relaxed (low Ca^{2+}) conditions, then cMyBP-C could effectively prime thin filament activation by uncovering myosin binding sites in the absence of Ca^{2+}. If C0 and C1 preferentially bind to activated thin filaments, then relaxation (following a decline in Ca^{2+}) could be slowed. These observations suggest the molecular basis for observations in physiological data that suggest how C0C2 can 'buffer' the effects of Ca^{2+} in motility assays; facilitating some motility in the absence of Ca^{2+} and slowing motility in the presence of Ca^{2+}. Intriguingly, the position of C0 and C1 on actin is also predicted to overlap with myosin cross-bridge, which could explain observations that cMyBP-C and myosin-S1 directly compete for actin binding. Our scattering experiments also demonstrate that the intact cMyBP-C must form a linkage between the thick and thin filaments of cardiac muscle providing a means by which the dynamics of the thick and thin filament spacings could be influenced during the contractile cycle which is important for healthy heart function.

Neutron contrast variation with deuterium labeling provides us with the means to extract structural data on the individual components in a protein assembly without bulky labeling or other less benign modification. As these assemblies are too lage for NMR analysis and typically resistant to crystallization, the ability to extract the level of detail obtained here provides an important pathway to critical evidence for determining the molecular mechanism underlying the function of this protein. Further work is underway to use neutron contrast variation to characterize the effects of phosphorylation and FHC-linked mutations on the interactions of cMyBP-C with actin and other heart muscle proteins in order to fully elucitdate its critical role in regulating a healthy heart beat.

References

[1] A. E. Whitten, C. M. Jeffries, S. P. Harris, J. Trewhella, Proc. Natl Acad. Sci. U.S.A. **105**, 18360 (2008).

[2] C. M. Jeffries, A. E. Whitten, S. P. Harris, J. Trewhella, J. Mol. Biol. **377**, 1186 (2008).

How Do Lipid Membranes Accommodate Voltage-sensing Domains of Ion Channels?

M. Mihailescu[1], D. Krepkiy[2], J.A. Freites[1,4], E. Schow[4], D.L. Worcester [5,1,3], K. Gawrisch[6], D. Tobias[4], S.H. White[1] and K.J. Swartz[2]

Electrical signals in the nervous system propagate between neurons along axons via electric potentials that are generated by proteins that reside within the cell membranes. Known as voltage-gated ion channels, these proteins allow ions to pass through the cell membrane in a controlled manner. In the voltage-gated potassium, sodium, and calcium channels found in neurons and muscle cells, a special part of the protein, called the voltage-sensing domain (VSD), moves inside the membrane in response to changes in the membrane potential and drives the ion conduction pore open or closed (gating) [1] (Fig. 1). Until a few years ago, it was thought that VSDs were unique to voltage-gated ion channels. This view has changed radically with the discovery of new families of proteins that use VSD constructs for purposes other than ion channel gating [2]. There is tremendous interest in the structure and function of such proteins. Researchers want to elucidate the mechanism of ion gating in ion channels. Moreover, the portability of VSDs across the genomes of different organisms can provide important clues about evolutionary pathways.

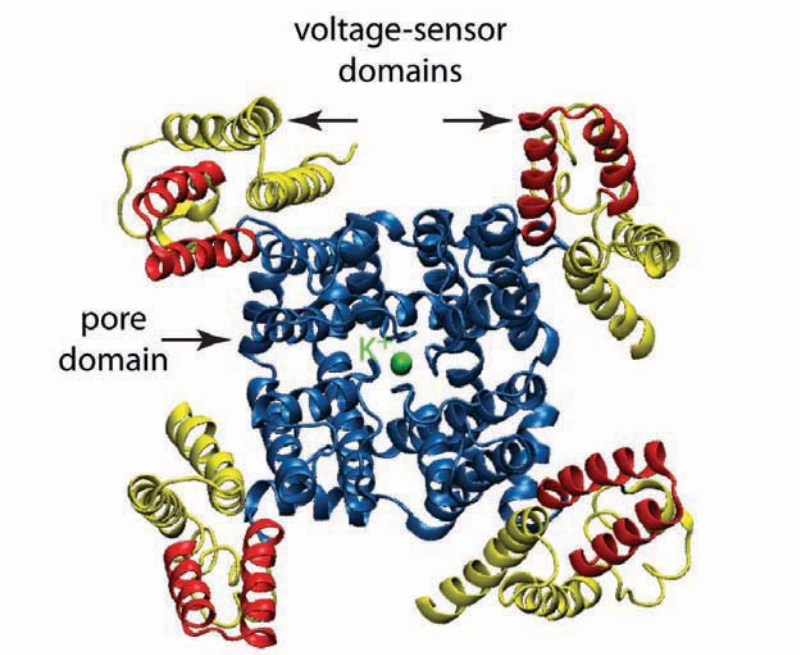

FIGURE 1: Top view (from above the surface of a lipid membrane) of a voltage-gated potassium channel.

Crystallographic studies using x-ray diffraction on voltage-gated potassium channels have revealed the atomic structure of the VSD in crystallized channels and identified regions that move in response to changes in the membrane electric field [3,4]. However, none of those studies were able to demonstrate the structure and conformation of the voltage-sensor domain in its native lipid environment. A picture of the topology of the VSD in a lipid membrane was needed in order to understand the role of the lipid in the protein stability and function, and ultimately, in the voltage-gating mechanism. We have developed an approach that employs neutron diffraction to obtain the image of functional voltage sensor domains in lipid membranes.

We focused our efforts on the voltage-sensing domain of KvAP, an archaebacterial channel from *Aeropyrum pernix* [5], because this domain can be robustly expressed, stably purified, and reconstituted into lipid membranes. The voltage-sensing domains were expressed in *E. coli*, purified, and transferred to lipid vesicles (reconstitution of the VSDs into proteoliposomes). Lipid multilayer samples were prepared by deposition of aqueous dispersions of proteoliposomes on cover glass slides. They were allowed to dry and rehydrated from water phase at 93 % relative humidity throughout the diffraction experiments. Samples containing a few thousands lipid bilayers with incorporated VSDs were measured and strong lamellar diffraction patterns were observed (Fig. 2) and used to generate one dimensional, absolute-scale, scattering-length density profiles normal to the plane of the lipid bilayer. We have determined the protein distribution using contrast variation between protonated and deuterated VSDs. The voltage-sensing domain of KvAP was uniformly deuterated to 74 %

[1]University of California, Irvine, Irvine, CA 92697
[2]National Institute of Neurological Disorders and Stroke, National Institutes of Health, Bethesda, MD 20892
[3]NIST Center for Neutron Research, National Institute of Standards and Technology, Gaithersburg, MD 20899
[4]University of California, Irvine, Irvine, CA 92697
[5]University of Missouri, Columbia MO 65211
[6]National Institute of Alcohol Abuse and Alcoholism, National Institutes of Health, Bethesda, MD 20892

and multilayers were formed with either protonated or deuterated protein at the same protein:lipid ratio and lipid composition. Fourier transformation of the diffraction data to obtain scattering length density profiles and subtraction of the individual profiles for the labeled and unlabeled protein reveals the distribution of the protein across the bilayer (Fig. 3a; red).

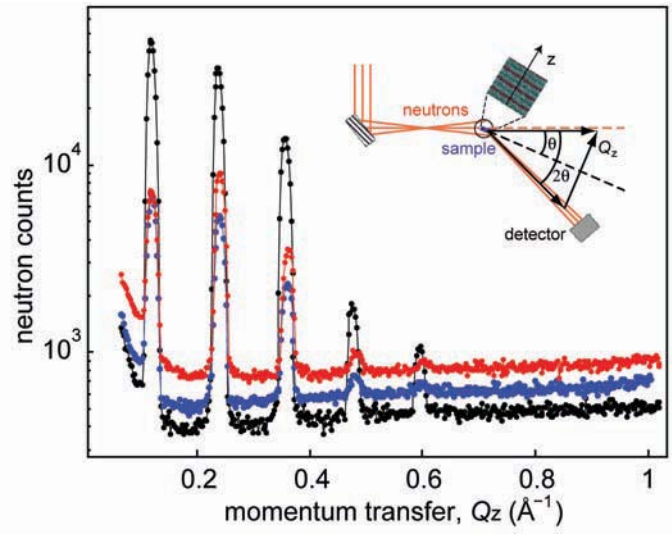

FIGURE 2: Neutron diffraction data collected at the AND/R (NCNR) for lipid multilayers samples with incorporated VSDs: Data displayed are for neat lipid (black), unlabeled VSD in lipid (blue) and deuterated VSD in lipid (red). The inset is a schematic illustration of the experimental setup.

The profile is presented with its uncertainty band derived from the standard deviation of the measured data. Maxima in the density distribution are observed in the headgroup region of the bilayer and minima in the inter-bilayer space. These findings firmly establish that voltage-sensing domains adopt a transmembrane topology, with the four helices oriented roughly normal to the membrane plane. Moreover, the protein distribution (Fig. 3a; red) exhibits extensive overlap with the water distribution (Fig. 3a; blue) within the confines of the lipid membrane, suggesting that the voltage-sensing domains are highly hydrated within the bilayer.

Because neutron diffraction reflects an average distribution of atoms, atomic details in the bilayer structure close to the VSD are not easily revealed in the experiment. To explore details in the protein, lipid and water distribution we employed molecular dynamics simulation for VSDs embedded in lipid bilayers. The simulation results (Fig. 3b) are in qualitative agreement with the experiment regarding the trans-membrane disposition of the four helical segments of the VSD and the overlap with the water distribution. Additionally, the simulations predict that about 4 % all water in the system is intimately associated with the VSDs, and that the lipid layers in contact with the protein are perturbed to a much greater extent than lipids several layers away from the protein (Fig. 3b).

Our results provide direct evidence that voltage sensors domain topology in a membrane environment and will be relevant for other important classes of membrane proteins. They show that the voltage-sensing domains of voltage-gated ion channels interact profoundly with the surrounding membrane and water, in a manner that facilitates their movement and function within the lipid membrane.

References

[1] K. J. Swartz, Nature **456**, 891 (2008).
[2] Murata Y. *et al.*, Nature **435**, 1239 (2005).
[3] Y. Jiang, *et al.*, Nature **423**, 33 (2003).
[4] S. B. Long, *et al.*, Nature **450**, 376 (2007).
[5] V. Ruta, *et al.*, Nature **422**, 180 (2003).

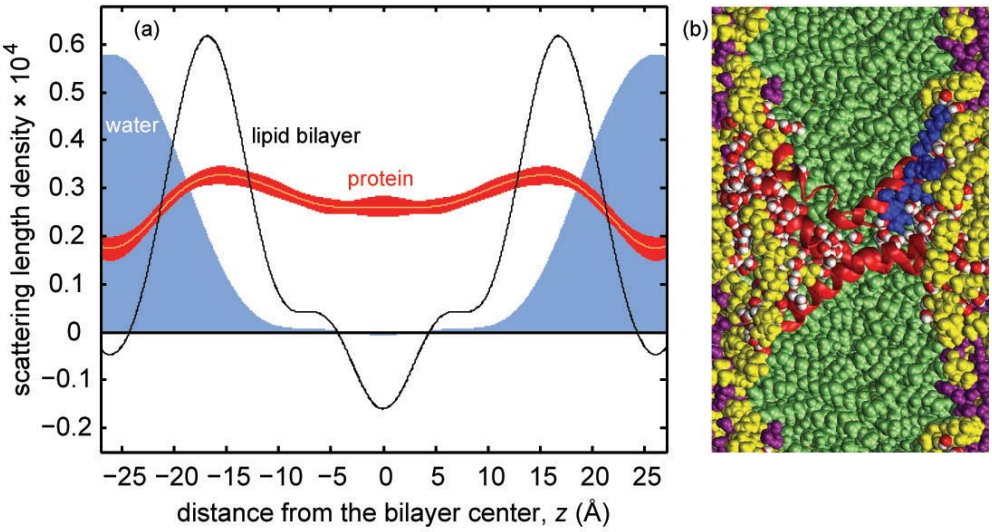

FIGURE 3: Distribution of the protein in lipid membranes: (a) Neutron diffraction results. Trans-bilayer distribution of the protein (red), water (blue) and lipid bilayer (black). (b) Molecular dynamics simulation results. Snapshot of the region in the vicinity of a voltage-sensing domains. Waters within 6 Å of protein are shown as red/white spheres while all other waters are colored purple. Phosphocholine headgroups are colored yellow and the acyl chains are colored light green.

Control of Protein Structure and Function by Hydrodynamic Shear

S. Neelamegham[1], I. Singh[1], E. Themistou[1], L. Porcar[2]

Can fluid shear in the flow of blood alter the structure of blood proteins? The question is relevant to medicine and hematology as well as biophysics. Many biochemical studies suggest that the function of the largest protein in blood, Von Willebrand Factor (VWF), is regulated by fluid or hydrodynamic shear. Using a combination of small angle neutron scattering (SANS) and fluorescence spectroscopy, we studied if, when and how fluid shear promotes changes in the conformation of this blood protein [1], and here we highlight our results.

VWF occurs in circulating blood at concentrations of 10 μg/mL to 20 μg/mL. It exists both as a dimer with molecular weight of 500 kDa and as a linear multimer with molecular weight ranging from 1 MDa to 20 MDa (Fig. 1). Previously, using SANS, we showed that this protein resembles a loosely packed ellipsoidal molecule in which intra-molecular interactions within the protein stabilize its solution structure [2]. By acting as a bridge/adaptor molecule that aids the binding of platelets to sites where the inner lining of the blood vessel has been injured, VWF plays a critical role in regulating platelet clot formation in narrowed arteries. The binding of VWF to human blood platelets is necessary to stop bleeding but it also contributes to blood-clotting events in arteries that lead to heart attacks and strokes.

Many of the functions of VWF are regulated by fluid shear. Among these, it is known that VWF supports platelet adhesion only above a minimum/ threshold shear rate. Lower shear rates do not efficiently support efficient platelet tethering and rolling interactions. A blood protease called ADAMTS-13 cleaves VWF in solution, and in normal human physiology this cleavage only takes place in the presence of fluid shear [3]. Cleavage of VWF by ADAMTS-13 dynamically regulates protein multimer distribution in circulation. Additionally, fluid shear regulates VWF size dynamically by the process of protein self-association [4].

For the current study, we purified VWF from blood plasma cryoprecipitate obtained from human donors. Shear was applied to this purified protein using a quartz Couette cell [5]. Protein conformation was measured in real-time using SANS at the 30 m NG-3 instrument. The length scales studied varied from 2 nm to 140 nm and the maximum applied shear rate was 3000 s^{-1} (Fig. 2A). These SANS experiments show prominent changes in VWF scattering at length scales < 10 nm (scattering vector, q, range > 0.6 nm^{-1}) (Fig. 2B). The control protein, Bovine Serum Albumin (BSA), does not display such alteration in scattering upon shear application.

Computer modeling was performed with the goal of suggesting potential mechanisms that can account for the observed changes in VWF scattering at high q upon shear application. Both the protomer/dimer VWF, and the multimeric VWF were simulated. Since the length scales where structural changes are more prominent occur at < 10 nm, we focused on simulations that change the arrangement of individual VWF domains located within the globular head section of the protein (Fig. 2C). The semi-quantitative agreement of these simulation

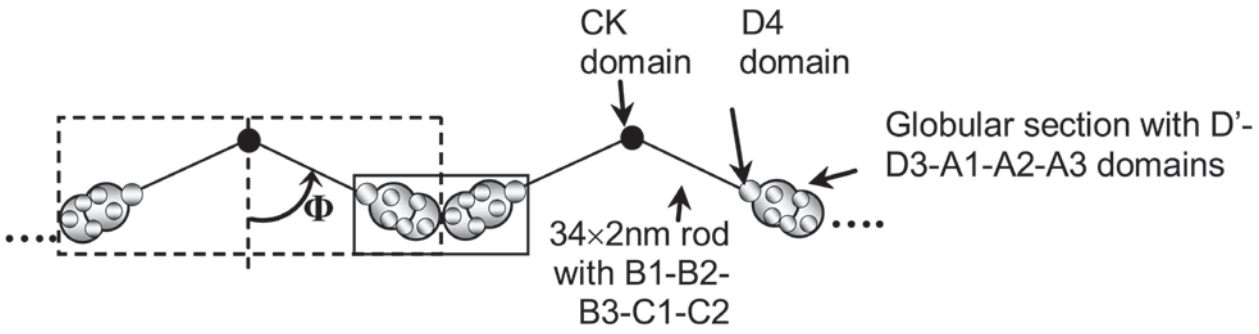

FIGURE 1: VWF structure: Schematic of linear multimeric VWF protein based on electron microscopy studies. A dimer unit with molecular weight of 500 kDa is shown in the dashed box.

[1]State University of New York, Buffalo, NY 14260
[2]NIST Center for Neutron Research, National Institutes of Standards and Technology, Gaithersburg, MD 20899

results (Fig. 2D) with experimental data (Fig. 2B) suggest that structural changes in the VWF globular head section may occur at small length scales upon application of low shear rates < 3000 s^{-1}.

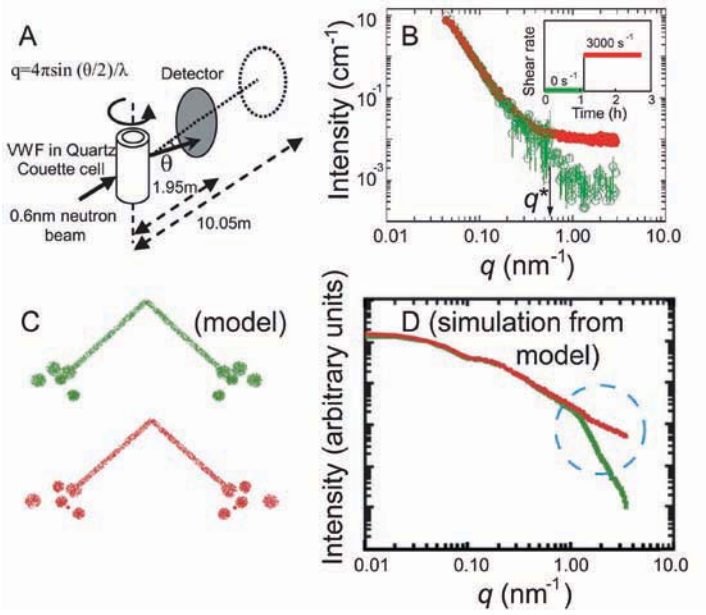

FIGURE 2: VWF subjected to fluid shear: A. Setup for shear-SANS experiments. 0.6 nm neutrons are scattered by a protein sample placed in a Couette cell. Area detectors placed at either 1.95 m or 10.05 m detect scattered neutrons. B. *I*(*q*) versus *q* plot for a representative experiment. Scattering intensity prior to shear is shown by empty green circles and during shear (3000 s^{-1}) by filled red circles. The inset shows the applied shear profile. Changes in scattering intensity suggest that structural changes in VWF occur at $q^* > 0.6$ (corresponding to a length scale < 10 nm). C. Potential scattering profile changes due to protomer VWF was modeled. Here, we examined the effect of changing the arrangement of domains in the globular-section of VWF. D. Alterations in domain level features result in a decrease in scattering intensity slope in the VWF protomer at high *q* (> 0.6 nm^{-1}, green to red). Changes in scattering intensity in this panel of simulated results qualitatively resemble the experimental data in panel B.

In order to extend the shear rate from physiological flow (< 3000 s^{-1} to 5000 s^{-1}) to shear rates that can occur during pathological flow (> 5000 s^{-1}), we examined alternative strategies to quantify protein structure changes. In these investigations, VWF was sheared in a cone and plate viscometer at shear rates up to 9600 s^{-1}, and protein structure was assayed by measuring the binding of a fluorescent probe: 4,4'-Bis (1-anilinonaphthalene 8-sulfonate) (bis-ANS) to hydrophobic pockets exposed in the sheared protein. As seen in Fig. 3, while bis-ANS exhibits low fluorescence signal in solution, the binding of this dye to VWF both increased fluorescence and caused a shift in peak emission wavelength to lower values. Application of shear at shear rates > 2300 s^{-1} further augmented the binding of bis-ANS to VWF. The measured absolute fluorescence signal was ≈ 110 % and ≈ 220 % higher than no-shear control at 6000 s^{-1} and 9600 s^{-1}, respectively.

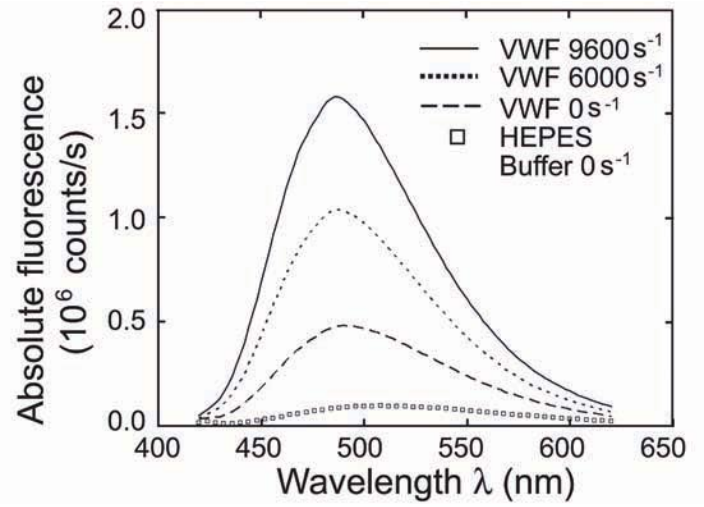

FIGURE 3: Fluorescence spectroscopy using bis-ANS: Representative spectra for experiments performed with 60 µg/mL VWF. Bis-ANS binding to VWF increases absolute fluorescence by 5-fold to 10-fold over HEPES buffer signal (squares). Application of shear for 5 min at 6000 s^{-1} or 9600 s^{-1} further increased absolute bis-ANS signal by 110 % to 220 % compared to no-shear control (0 s^{-1}).

Overall, SANS studies suggest that VWF may undergo conformation change under physiological flow conditions. These changes occur at small length scales. Studies with bis-ANS demonstrate marked increase in bis-ANS binding at shear rates > 2300 s^{-1}. Together, the data suggest that local rearrangements at the domain level may precede changes at larger length scales that accompany exposure of protein hydrophobic pockets. It is likely that changes in VWF conformation described here regulate protein function in blood circulation.

References

[1] I. Singh, E. Themistou, L. Porcar, S. Neelamegham, Biophys J. **96**, 2313 (2009).

[2] I. Singh, H. Shankaran, M.E. Beauharnois, Z. Xiao, Alexandridis P, Neelamegham S., J Biol Chem. **281**, 38266 (2006).

[3] H. M. Tsai, I. I. Sussman, R. L. Nagel, Blood **83**, 2171 (1994).

[4] H. Shankaran, P. Alexandridis, S. Neelamegham, Blood. **101**, 2637 (2003).

[5] L. Porcar, W.A. Hamilton, P.D. Butler. Review of Scientific Instruments **73**, 2345 (2002).

Neutron Measurements of Preferred Orientation and the Prediction of Forming Properties in Automotive Sheet Materials

T. Gnäupel-Herold[1], T. Foecke[2], A. Creuziger[2], M. Iadicola[2]

A substantial part of manufacturing is involved with sheet metal forming for producing panels, covers, or automotive bodies. Currently, the automotive industry is experiencing a shift to light weight, high strength materials to promote fuel economy. Both trends—thinner, higher strength steels and lighter, Al or Mg-based alloys—bring about enormous problems related to the accurate prediction of forming properties such as springback, forming limits and surface quality. It is now widely recognized that polycrystal plasticity modeling together with better materials property data for forming-like conditions can improve the accuracy of overall modeling with the goal to predict the stress-strain state at any given location in the formed part. These efforts are illustrated in this work.

The underlying microscopic process of sheet metal forming is the plastic deformation of constituent grains. For a single grain, this process takes place as a slip on certain crystallographic planes in specific crystal directions, thus leading to a change in the orientation and the shape of the grain. A sheet as a whole consists of many grains in different orientations which, due to their mutual interactions and depending on the applied stresses, develop distinctive distributions of grain orientations (texture). However, texture is not only an effect of deformation, it is also a crucial property setting limits for further deformation (hence the necessity for a "good" starting texture in the sheet before forming). This view of texture is currently seeing a new level of complexity from the introduction of TRIP steels (TRansformation Induced Plasticity), a relatively new class of advanced high strength steels that show both high strength and high ductility due to the stabilization of the austenite phase and strain-induced deformation from the retained austenite into the martensite phase. Thus, the challenge for modeling this three phase system is to elucidate not only the texture evolution of each phase but also the shifting phase content. The texture response for three basic deformation modes in TRIP590 is shown in Fig. 1 for the principal directions of the initial sheet RD (rolling direction) and TD (transverse to RD).

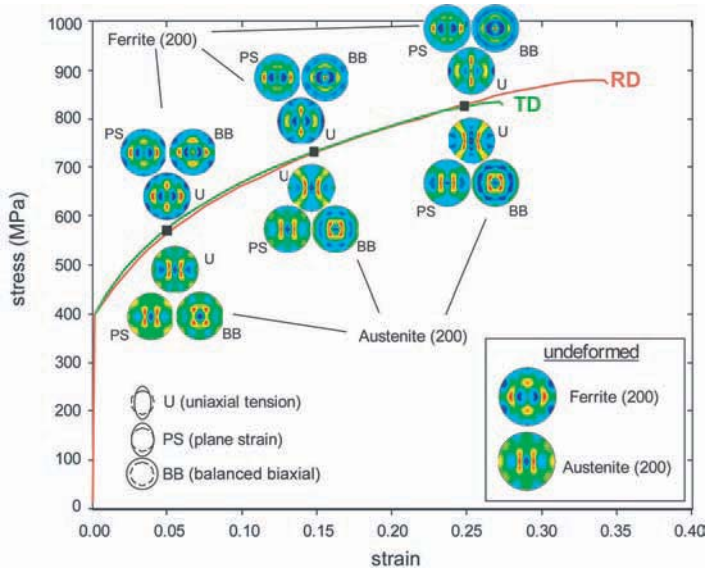

FIGURE 1: Uniaxial stress-strain curve of TRIP 590 (in RD and in TD) together with pole figures for the (200) planes of ferrite (majority phase, bcc structure) and austenite (minority phase, fcc structure) for the three different deformation modes: uniaxial tension (U) in RD, plane strain in the rolling direction (PS, no shrinking in TD) and balanced biaxial (equal strain in RD and TD). The meaning of each mode is shown on the bottom, left indicating the shape change of a circle mark on the sample surface.

It is remarkable that for austenite the texture change is rather subtle which means that this phase participates in the deformation not just through slip and grain rotation but increasingly through transformation to martensite. The consequence is that the texture exhibits strengthening but no change in the main components. Ferrite is the majority phase and it has no such transformation available. However, the ferrite grains are surrounded to an increasing extent by the 'hard' martensite phase, thus leading to a composite-like strengthening in ferrite where the martensite grains act as obstacles for dislocations. The martensite phase in TRIP 590 is difficult to observe because of the complete overlap with ferrite peaks but its content can be determined indirectly through the retained austenite fraction. The determination of the retained austenite content receives a new treatment here. A commonly practiced method is the comparison of a large number of ferrite/austenite reflections. Only limited orientation averaging is applied to individual reflections; the texture effect is dealt with through the number of different reflections (hkl). The approach used here is based on the premise that the pole figure data for ferrite (overlap

[1]University of Maryland, Department of Materials Science and Engineering, College Park, MD 20742, and
NIST Center for Neutron Research, National Institute of Standards and Technology, Gaithersburg MD 20899-6102
[2]Metallurgy Division, National Institute of Standards and Technology, Gaithersburg MD 20899-8553

with the martensite phase) and austenite allow the integration of the diffracted intensities over all orientations, thus removing the texture effect completely. The comparison with the theoretical intensities allows the calculation of the volume fractions (Fig. 2). It is noteworthy that the austenite volume fractions decrease to very low levels (< 1 % for BB) for which both the texture and the volume fraction could still be reliably determined.

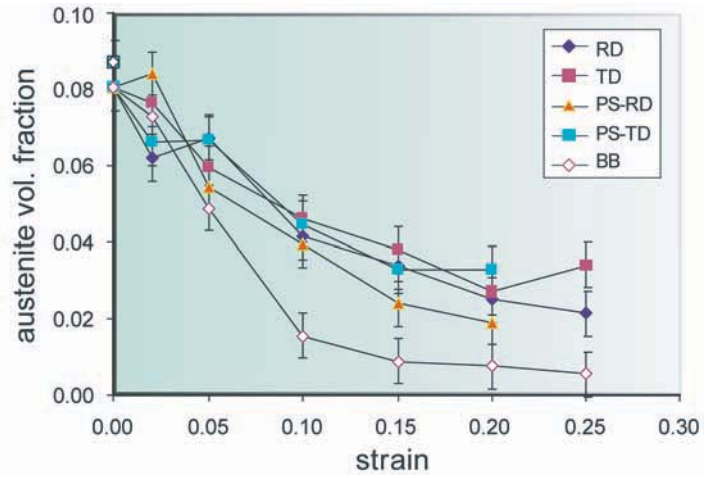

FIGURE 2: Retained austenite content for TRIP 590 in uniaxial tension (RD, TD), plane strain (PS-RD, PS-TD) and balanced biaxial (BB). The errors were estimated from repeated measurements on undeformed samples.

The transformation from austenite to martensite is a well known and studied transformation. Using the lattice parameters of austenite and martensite, it is possible to predict not only the planes on which the transformation will occur, but also the driving energy of the transformation, referred to as a transformation potential. Using the crystallographic theory of martensite (CTM), transformation potentials were calculated as a function of texture (orientation of austenite grains) and the applied stress state (Fig. 3).

The transformation potential calculation predicts that both the uniaxial and plane strain RD samples will have higher transformation potential values than the uniaxial and plane strain TD samples for orientations found in the measured pole figures. The balanced biaxial samples have a uniformly high transformation potential, but the values are lower than the peak plane strain RD values. From these data, the balanced biaxial loading condition (BB) should cause the most transformation, followed by plane strain RD and uniaxial RD, plane strain TD and uniaxial TD. High transformation potentials indicate a higher rate of transformation austenite to martensite, thus resulting in a lower volume fraction as confirmed by the experimentally determined retained austenite in Fig. 2.

The effects of texture, orientation and stress state on the austenite to martensite phase transformation in TRIP steel were investigated in this work. The crystallographic texture was determined for ferrite and austenite in various deformation modes, and the retained austenite fractions were obtained down to levels < 1 %. The austenite-martensite transformation was simulated using the crystallographic theory of martensite. This allowed the prediction of transformation potentials for different stress states/deformation modes. From these data, the texture components that are typical in as-processed TRIP steels were found to correspond to low values of the transformation potential. Grains aligned with these orientations would require higher stresses to transform than other orientations, thus leaving the austenite texture relatively stable but with increased intensity by the transformation of grains in orientations with high transformation potential.

References

[1] A. Creuziger, T. Foecke, submitted to Acta. Mater.

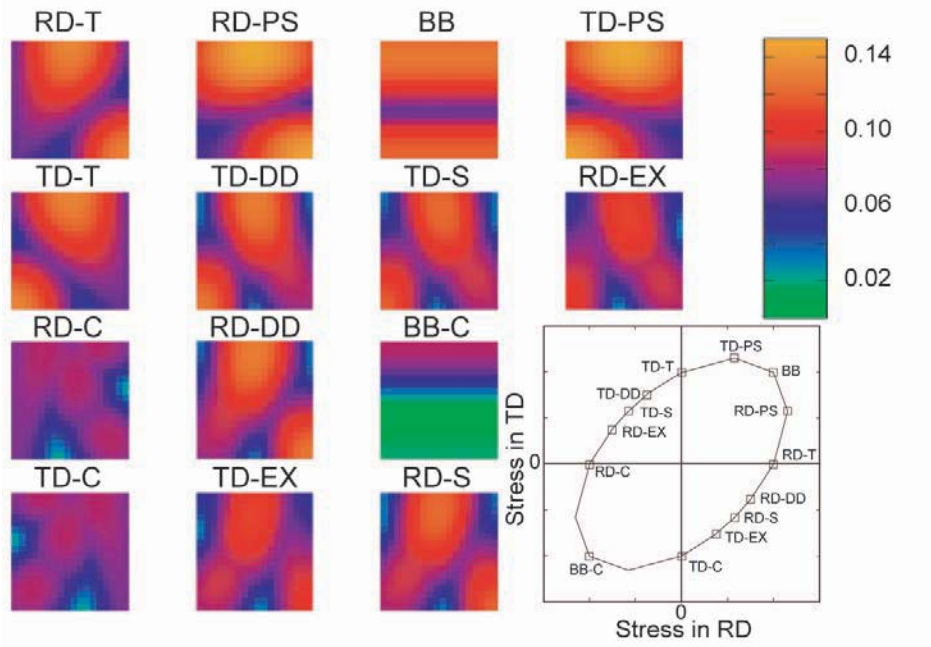

FIGURE 3: Transformation potential in a section of Euler space for the stresses indicated in the bottom, right for combinations of stress directions and sign (+/-). A point in these graphs corresponds to a specific austenite grain orientation. Key to notation: Uniaxial tension in RD (RD-T), plane strain in RD (RD-PS), balanced biaxial tension (BB), plane strain along TD (TD-PS), uniaxial tension along TD (TD-T), deep drawing in TD (TD-DD), pure shear along +TD (TD-S), extrusion in RD (RD-EX), compression in RD (RD-C), balanced biaxial compression (BB-C), compression in TDs (TD-C), extrusion along TD (TD-EX), pure shear in +RD (RD-S), deep drawing in RD (RD-DD).

Water Dynamics in Hydrophobic Confinement

A. Faraone[1], K.-H. Liu and C.-Y. Mou[2], and Y. Zhang and S.-H. Chen[3]

Water is often found confined in nanoscopic pores or on both hydrophilic and hydrophobic surfaces. For example, in proteins water is exposed to both hydrophilic and hydrophobic moieties. In order to better understand how the behavior of water is affected near a hydrophobic surface, we have investigated the dynamics of water confined in a hydrophobically modified nanoporous silica matrix, MCM-41-SM1-18 [1]. MCM-41-SM1-18 is a chemically treated form of hydrophilic-nanopored MCM-41-S to make the pore surfaces partially (42 %) hydrophobic [1]. In so doing the pore size is reduced from 18 Å to ≈ 15 Å. Using a confinement matrix with ≈ 15 Å pore dimension, it was possible to avoid the crystallization of water even below the homogeneous nucleation temperature T_H ≈ 235 K, allowing measurements over a temperature range from 300 K to 210 K. This is relevant because it is believed that the anomalous behavior of water, such as the density maximum at 277 K or the tendency of the thermal expansion coefficient, the isobaric specific heat, and the isothermal compressibility to diverge at a temperature somewhat below T_H, can be understood only by probing water in deeply supercooled states.

The neutron scattering cross section of hydrogen atoms is much larger than silicon or oxygen. Hence, neutron spectroscopy is useful in studying the dynamics of water confined in silica matrices. Since incoherent scattering of neutrons from hydrogen is much stronger than coherent scattering, experiments on hydrogenated samples give information on the single particle dynamics of the hydrogen atoms in the system, simplifying the modeling of the data. Moreover, neutron scattering provides information on the geometry of the investigated motion at the nanometer scale. Thus, measuring the broadening of the elastic line (quasielastic neutron scattering: QENS) arising from the relaxation dynamics of the system yields both spatial and temporal information on the diffusive motion of the H atoms. To follow the slowing down of water confined in MCM-41-SM1-18 in the temperature range from 300 K to 210 K, we have collected data on three NCNR spectrometers, namely the Disk Chopper Spectrometer (DCS), the High Flux Backscattering Spectrometer (HFBS), and the Neutron Spin Echo (NSE) spectrometer. Together these instruments cover a dynamic range from picoseconds to nanoseconds over length scales from fractions of an Angstrom to several Angstroms.

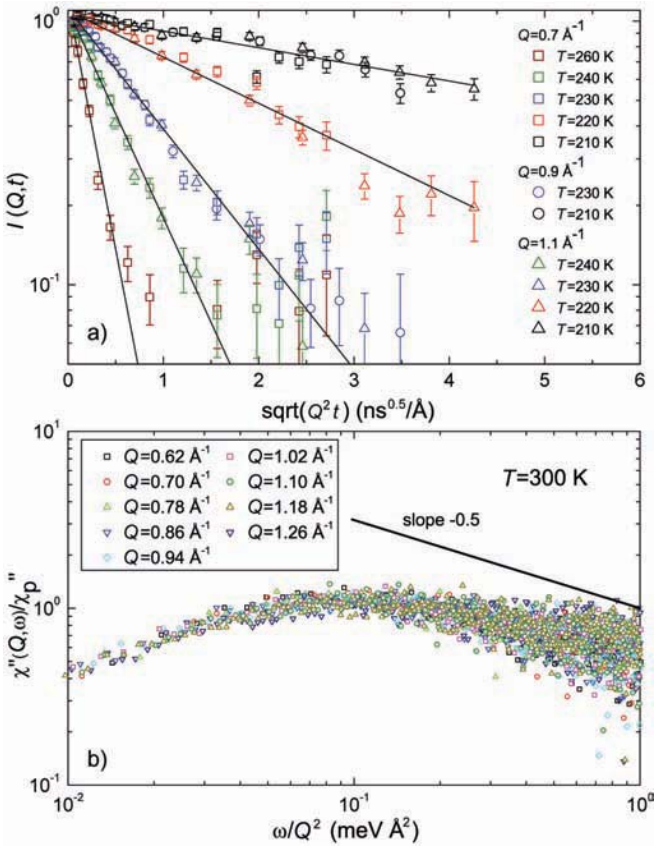

FIGURE 1: a) Values of the intermediate scattering function measured by NSE plotted semilogarithmically as a function of $\sqrt{Q^2 t}$ follow straight lines whose slope depends only on temperature. b) Scaling plot of the susceptibility obtained from the DCS data. By plotting χ''/χ''_p as a function of ω/Q^2 all the curves at the same temperature collapse onto the same master curve, which in the limit of high ω/Q^2 lies parallel to the straight black line with slope -0.5, confirming that, as found by NSE, $\beta = 0.5$ and $\Gamma \sim Q^2$.

The data collected on the three spectrometers show that the self Intermediate Scattering Function (ISF) of the hydrogen atoms in the system can be described by a stretched exponential function, $I(Q,t)=\exp\{-[\Gamma t]^{\beta}\}$. Over the range of investigated momentum transfers, Q, (from ≈ 0.2 Å^{-1} to ≈ 1 Å^{-1}, where the ISF reflects

[1]NIST Center for Neutron Research, National Institute of Standards and Technology, Gaithersburg, MD 20899 and University of Maryland, College Park, Maryland 20742
[2]National Taiwan University, Taipei 106, Taiwan
[3]Massachusetts Institute of Technology, Cambridge, Massachusetts 02139

mostly the water center of mass translational dynamics), the stretching exponent $\beta = 0.5$. The Q dependence of the relaxation rate (Γ) is quadratic as can be seen in a semilog plot of $I(Q,t)$ versus $\sqrt{Q^2 t}$, as measured using NSE (Fig. 1a), as well as by a log-log plot of the susceptibility, $\chi'' = \omega S_H^{self}(Q, \omega)$, obtained from the DCS data versus ω/Q^2 (Fig. 1b). This finding clearly indicates that the heterogeneous scenario applies: the system displays a distribution of relaxation times, probably related to the different microscopic environments experienced by the water molecules. The diffusive behavior of the individual molecules is retained, with an average diffusion coefficient, $\langle D \rangle = \Gamma/(2Q^2)$. In Fig. 2 the values obtained for $\langle D \rangle$ are shown together with the results measured for bulk water by NMR (red curve). Remarkable agreement is found in the results from the three spectrometers. At high temperature the $\langle D \rangle$ values of water confined in MCM-41-SM1-18 tend to be similar to those reported for bulk water. However, it seems plausible that at temperatures ($T > 300$ K), higher than those investigated in this work, the dynamics of bulk water is slightly slower than that of water confined in the hydrophobically modified matrix. On the other hand, in the deeply supercooled region, the diffusion coefficient of bulk water tends to decrease with the lowering of the temperature much faster than water confined in MCM-41-SM1-18. This is not surprising because it is well known that, in bulk water, the inverse of D seems to diverge at $T \approx 228$ K. Such a singularity might be due to the effect of the second critical point of water [2] or to the effect of the hydrogen bond network [3]. While, the divergence is not directly observable in bulk water, we found that the singularity is avoided by the dynamic crossover of water in confined systems [4]. Overall, in the investigated temperature range, the geometric confinement slows down the dynamics of water as compared to the bulk.

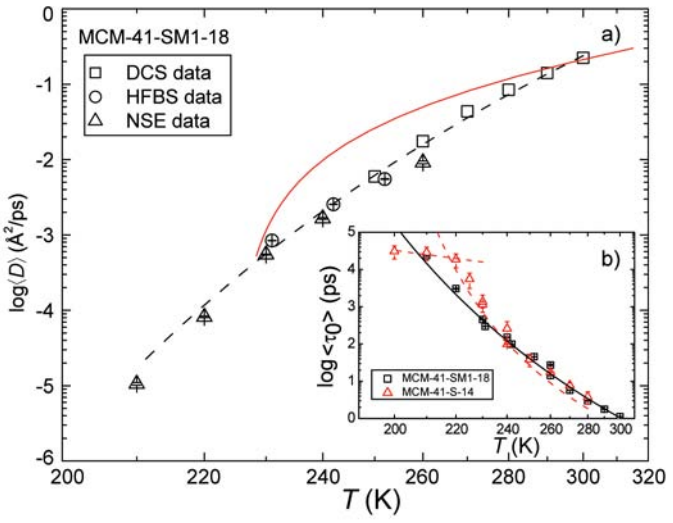

FIGURE 2: a) the temperature dependence of <D> in hydrophobic MCM-41-SM1-18. The continuous red line represents the values obtained for bulk water. The dashed black line is the fit to the data with a VFT law. Inset b) compares the average characteristic translational relaxation times of water in MCM-41-SM1-18 with that of water in hydrophilic MCM-41-S-14.

The $\langle D \rangle$ data have been fitted using a Vogel-Fulcher-Tammann (VFT) law, which is commonly used to analyze the temperature dependence of the transport coefficients in fragile glass forming fluids: $\langle D \rangle = D_0 \exp[-D_f T_0/(T-T_0)]$. D_0 is the diffusion coefficient in the infinite temperature limit. We obtain that the fragility parameter, D_f, is 13.8 ± 0.3, whereas the temperature of the ideal glass transition, T_0, is (121 ± 1) K. D_f in this case is higher than that reported for water in hydrophilic MCM-41-S with similar pore size [4], indicating that water in hydrophobic confinement behaves as a stronger glass-former. The result obtained for T_0 is not very different from the commonly accepted value of the glass transition temperature of water, 135 K.

The inset b) of Fig. 2 shows the average characteristic relaxation time $\langle \tau_0 \rangle$ for water confined in a hydrophilic MCM-41-S sample with a pore diameter of ≈ 14 Å, compared to that in MCM-41-SM1-18. The comparison of the dynamics of water in these two similar confining media, differing only by the hydrophilic or hydrophobic characters of their walls, highlights the effect of the interaction with the confining surface in contrast to purely geometric effects. At high temperature both samples have the same relaxation time. Around room temperature, therefore, the water molecules have enough kinetic energy to overcome the interaction with the confining wall. In the deeply supercooled region, like supercooled bulk water, H_2O molecules confined in hydrophilic sieves show a much stronger dependence of relaxation time on temperature. This finding suggests that water confined in a hydrophilic matrix is qualitatively more similar to bulk water than to water confined by hydrophobic walls. This finding can be related to a more extensive disruption of the hydrogen bond network formation in the hydrophobic confinement. The dynamic crossover, from a non-Arrhenius to an Arrhenius behavior, was not observed in this work. This could be due to the fact that hydrophobic confinement lowers the crossover temperature, as in the case of DWNT [5].

References

[1] A. Faraone, K.-H. Liu, C.-Y. Mou, Y. Zhang, and S.-H. Chen, J. Chem. Phys., **130**, 134512 (2009).

[2] P.H. Poole, F. Sciortino, U. Essmann, and H.E. Stanley, Nature, **360**, 324 (1992).

[3] R.J. Speedy and C.A. Angell, J. Chem. Phys., **65**, 851 (1976).

[4] A. Faraone, L. Liu, C.-Y. Mou, C.-W. Yen, and S.-H Chen, J. Chem. Phys., **121**, 10843 (2004).

[5] X.-C. Chu, A.I. Kolesnikov, A.P. Moravsky, V. Garcia-Sakai, and S.-H. Chen, Phys. Rev. E, **76**, 021505 (2007).

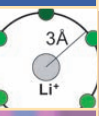

Toward an Improved Understanding of Hydrogen Interactions with Coordinated Metals

C.M. Brown[1], W. Zhou[1,2], Y. Liu[1,2], H. Wu[1,2], T. Yildirim[1], V.K. Peterson[3], C. Kepert[4]

Understanding how hydrogen interacts with high surface area materials, particularly those that are strong absorbers, is a requirement for the rational design and subsequent synthesis of new materials that could one day be used to safely store large amounts hydrogen. The long-term view is that this combination could be a potential replacement for the gasoline engine when coupled with fuel cells to power the automotive drive train using electric motors. While there are promising mechanisms for storing large amounts of hydrogen in solid materials that take up much less space than the equivalent amount of gas, there remain several roadblocks to practical use. When stored on high surface area materials, hydrogen is weakly bound and generally requires low temperatures to achieve significant storage capacities. To be able to increase the storage capacity at room temperature it has been suggested that increasing the interaction energy of hydrogen with the surface to (15 to 25) kJmol^{-1} would be necessary [1] and that one potential mechanism could be to use favorable interactions of hydrogen with metal ions. The combined work shown here indicates that the interaction with the metal center can be well understood and quantified with a general set of trends that depend on simple physical characteristics of the metal embedded in the metal-organic framework (MOF).

The ability to control the H_2 binding energy that governs the adsorption in materials ranging from microporous solids to metal hydrides is key to making hydrogen storage a reality for vehicular use and as such is the focus of much research. In this regard, MOFs, comprised of metal ions linked via organic ligands into porous three-dimensional solids can provide the flexibility of being able to control not only the surface area and pore geometry but also the accessibility of gas to interact with the coordinated metal ions.

Our previous research has shown that hydrogen binds directly to the unsaturated metal coordination sites within certain classes of MOF materials. Along with exhibiting amongst the highest observed enthalpies [2] of hydrogen adsorption known in physisorption systems, there is an overall increase in the areal density of the adsorbed hydrogen on the surface [3] that is a direct consequence of the attraction of hydrogen to these Coordinately Unsaturated Metal Centers (CUMC). Despite the significant progress, there is still uncertainly as to how the metal is binding the hydrogen and giving rise to the increased enthalpy, and what is the best choice of metal to optimize this binding.

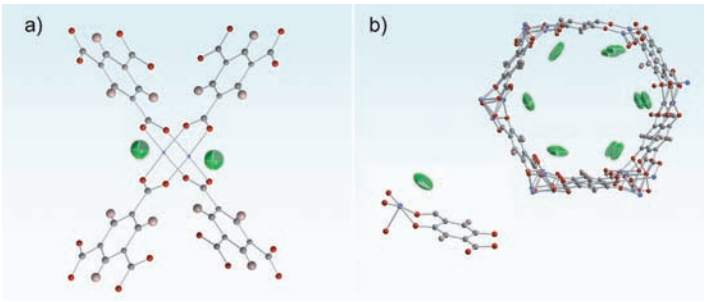

FIGURE 1: The local coordination environment of adsorbed hydrogen with different metal centers in MOFs as determined from neutron powder diffraction. (a) D_2 binding close to the Cu^{2+} metal in the HKUST-1 paddlewheel, (b) and D_2 adsorbed in the pore of Zn-MOF-74 with a close-up view (bottom left). Thermal ellipsoids for the deuterium molecule are green, carbon atoms are gray, oxygen atoms red, and hydrogen on the ligands are pink.

The porous structure of HKUST-1 has several different sized cavities that are available to the adsorbed gases, but the primary 77 K adsorption site for H_2 is at the M^{2+} cation. Figure 1a shows the local paddlewheel coordination environment around the copper ions with available coordination sites along the Cu-Cu axis. For the 1-dimensional pores of MOF-74 the metal cations are bonded to five oxygen atoms in a square-pyramid coordination environment, leaving the cation in the center of the square plane open and accessible to the adsorbed gas molecule (Fig. 1b). For Zn-MOF-74 gas adsorption studies indicate a rather large hydrogen enthalpy of adsorption of -8.8 kJ/mol, and a relatively large excess hydrogen uptake capacity of 2.8 % mass fraction for the modest surface area of 870 m^2/g. In contrast the adsorption in HKUST-1 is typically characterized by an enthalpy of adsorption of -6 kJ/mol, and a relatively large excess hydrogen uptake capacity of ≈ 4 %.

To experimentally clarify exactly how it is the di-hydrogen binds to the copper center we used inelastic neutron scattering to probe the quantum transitions of the associated H_2. Detailed rotational spectra as a function of increasing H_2 loading were taken using the FANS spectrometer and the characteristic spectrum of hydrogen

[1]NIST Center for Neutron Research, National Institute of Standards and Technology, Gaithersburg, MD 20899
[2]Department of Materials Science and Engineering, University of Maryland, College Park, MD 20742
[3]The Bragg Institute, Australian Nuclear Science and Technology Organisation, Menai, N.S.W. 2234, Australia.
[4]School of Chemistry, The University of Sydney, N.S.W. 2006, Australia

transitions from the lowest rotational ground state when adsorbed in HKUST-1 are shown in Fig. 2(a). To obtain the momentum transfer (q) dependence of the lowest energy transition and confirm its rotational nature, we used the DCS spectrometer and fit the resulting intensities to the model for a free rotor (Fig. 2b). While the model includes a variable for the H-H bond distance, we found it unnecessary to vary this from the ideal value of 0.74 Å, and extracted a small mean-squared displacement of 0.175(1) Å^2 for H_2 at the Cu^{2+}-site compared to ≈ 0.3 Å^2 at the weaker ligand-associated sites.

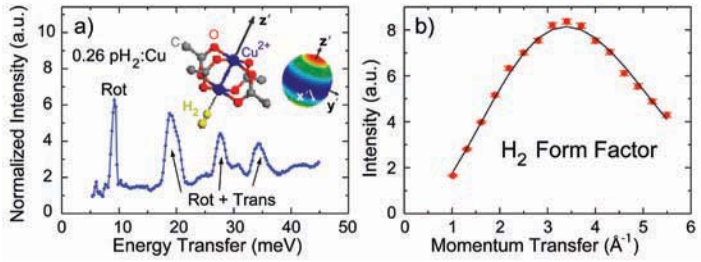

FIGURE 2: (a) Inelastic neutron scattering data for the H_2 adsorbed only at the Cu^{2+} site in HKUST-1. Assignments of rotation (Rot) or translation (Trans) are made based both on experiment and with the aid of calculations. Inset: The local coordination for a classical DFT calculation as a function of the hydrogen rotation results in the orientational potential (perpendicular to the Cu-Cu axis (blue) is favorable; parallel orientation (red) is 78 meV less so). Solving for the rotational levels indicates that the transitions to the split first-level should appear around 9.6 meV and 37 meV. Calculated phonon energies x´ = 9.56 meV, y´ = 13.44 meV, and z´ = 22.87 meV. (b) The assignment to a quantum rotational transition of the ≈ 9.5 meV peak is determined from a separate measurement of the momentum transfer dependent intensity using the DCS spectrometer.

First-principles calculations were performed on the 3-D crystal as a function of the hydrogen orientation with respect to the Cu-dimer axis (Fig. 2a, inset, which shows an H_2 and a portion of the paddlewheel). The resulting potential is shown as a globe in the figure and is dominated by a Coulombic interaction where the di-hydrogen prefers to lay flat against the CUMC (by ≈ 78 meV) and experiences almost negligible electron transfer. Further analysis predicts the rotational and translational frequencies that allow us to completely assign the vibrational spectrum [4] in Fig. 2(a).

Since we are able to understand the interactions of H_2 with a specific CUMC, it is of interest to observe how these properties trend across an isostructural series of differing transition metal ions and compare this to experimental properties related to their hydrogen storage capacities [5]. The existing MOF-74 series was useful for this purpose, though we were also successful in extending this family of compounds making observed trends more apparent. Coupling the physical measurements to specific elemental characteristics required *ab initio* calculations. Select parameters that exhibit strong correlations are detailed in Fig. 3. Of particular note is how the calculated total binding energy for the MOF-74-D_2 system varies in parallel to the experimental isosteric heat of adsorption. The isosteric heat is also anti-correlated with how close the H_2 molecule is calculated to approach the CUMC, or how small the CUMC is. Experimental validation of the calculations comes from neutron powder diffraction measurements of select MOF-74-D_2 systems that show excellent agreement.

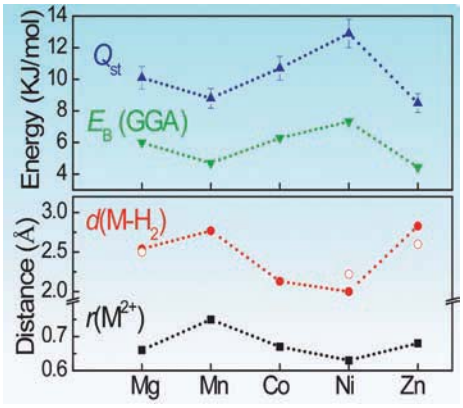

FIGURE 3: In the upper panel the experimental isosteric heat of adsorption (Q_{st}, blue triangles) and the calculated GGA binding energy (E_B(GGA) green triangles) of the isostructural series of MOF-74 compounds are found to behave similarly. In the lower panel the empirical transition metal ion radius (r, black squares) and calculated M-H_2 distance (d, red filled circles) correlate well with d(M-H_2) extracted from neutron powder diffraction data (red circles, filled white).

In these studies, we have measured the interaction strength between a CUMC and di-hydrogen. For this Cu-H_2 interaction the hydrogen is strongly attached to the metal center as evidenced from the small value of the mean-squared displacement parameter as compared to hydrogen frozen in the bulk solid. The form-factor of the scattering is well described by the ideal free-rotor value without any elongation of the H-H bond. Calculations indicate that Coulomb forces dominate the interaction and that the hydrogen prefers to lie perpendicular to the Cu-Cu axis of the paddlewheel and behave like a quasi-2-dimensional rotor. A strong correlation between the size of the exposed CUMCs in isostructural MOF-74 framework structures and the resulting physical characteristics of interest for hydrogen storage are further developed. These observations provide insight in to which metals are preferable for incorporating into MOFs for hydrogen storage.

References

[1] S.K. Bhatia, A.L. Myers, Langmuir 22, 1688 (2006).

[2] M. Dincă, A. Dailly, Y. Liu, C.M. Brown, D.A. Neumann, J.R. Long, J. Am. Chem. Soc. **128**, 16876 (2006).

[3] Y. Liu, H. Kabbour, C.M. Brown, D.A. Neumann, C.C. Ahn, Langmuir, **24**, 4472 (2008).

[4] C. M. Brown, Y. Liu, T. Yildirim, V. K. Peterson, and C. J. Kepert, Nanotechnology, **20**, 4025 (2009).

[5] W. Zhou, H. Wu, T. Yildirim, J. Am. Chem. Soc. **130**, 15268, (2008).

Molecular Mobility and Ion Transport in Solid Polymer Electrolytes For Lithium Batteries

S.K. Fullerton Shirey and J.K. Maranas[1]

Would you like to use a lighter laptop, or a mechanically-flexible portable music player? Unfortunately, the lithium-ion batteries used to power these devices prevent a light and flexible design. The liquid-phase electrolyte requires a rigid casing, making the battery bulky, heavy and inflexible. Replacing the liquid electrolyte with a solid polymer electrolyte (SPE) would eliminate these drawbacks; however, the lithium-ion (Li^+) mobility through the SPE (quantified as the ionic conductivity) is insufficient to power a portable device. Polyethylene oxide (PEO) is used as the polymer because multiple ether oxygen atoms on the PEO backbone can coordinate with Li^+ ions. Ion mobility occurs when Li^+ moves from one set of ether oxygens to the next. SPEs based on PEO can contain both amorphous and crystalline regions, and it is generally accepted that ion mobility is maximized in the amorphous regions because polymer mobility is faster. However, conductivity through *fully crystalline* SPEs can be greater than the amorphous equivalent, owing to the formation of cylindrical PEO channels that direct ion transport [1]. The cylindrical structure is formed by two PEO chains wrapped around a column of Li^+ ions. Anions are required for charge neutrality, and they are located between the PEO/Li^+ channels. This structure is referred to as $(PEO)_6$:LiX, where X is the anion. The channels are highly conductive at low PEO molecular weight where the SPE is a powder. When the molecular weight is increased to create a flexible solid, the crystalline channels misalign and the conductivity plummets. Small remnants of the channels persist in the high molecular weight sample at temperatures above the melting point [2]. Together, these results suggest that structure could be important for achieving high conductivity in SPEs, and that portions of the conductive channels are retained in the high molecular weight sample. We use quasi-elastic neutron scattering (QENS) to learn more about the molecular-level mobility of the $(PEO)_6$:LiX remnants [3].

We measure PEO/$LiClO_4$ over a range of Li^+ concentrations where conductivity is the highest: ether oxygen to lithium ratios of 8:1, 10:1 and 14:1. Measurements are made at 75 °C where all samples are amorphous, and 50 °C where the 8:1 and 10:1 samples are amorphous. The 14:1 sample is semi-crystalline at 50 °C, and the crystalline phase is pure PEO. This phase does not contain Li^+ ions, and is therefore non-conductive. We use the disc-chopper spectrometer (DCS) and the high-flux backscattering spectrometer (HFBS) to measure the mobility of PEO, and transform the data to the self-intermediate scattering function, $S(q,t)$ (Fig. 1). The DCS data (time shorter than 50 ps) and the HFBS data (time longer than 200 ps) are combined in Fig. 1 to form a single curve.

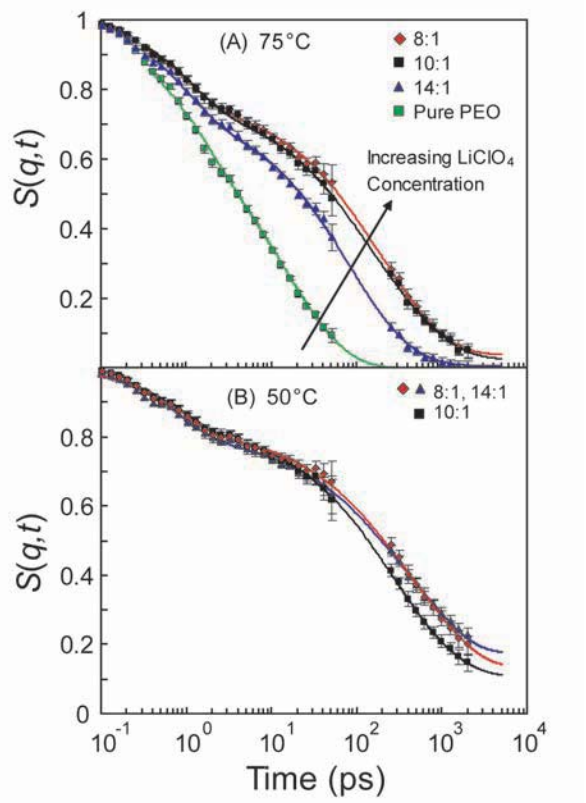

FIGURE 1: Self-intermediate scattering function at q = 1.04 Å^{-1}, (A) 75 °C, and (B) 50 °C. The lines through the data are fits to the Kohlrausch-Williams-Watts (KWW) expression.

We focus on the data at times longer than 2 ps, because mobility on this timescale is associated with the polymer mobility that drives Li^+ transport. At 75 °C, polymer mobility decreases with increasing $LiClO_4$ concentration, because the ether oxygens are slowed by their coordination with Li^+ ions. At 50 °C, the 8:1 and

[1]The Pennsylvania State University, University Park, PA 16802

14:1 samples have the same mobility, because the crystallization of pure PEO in the 14:1 sample increases the Li^+ concentration to 8:1 in the amorphous regions. We fit the data at times longer than 2 ps with a stretched exponential equation, and the fit parameters include the relaxation time (τ), the distribution of relaxation times (β), and the elastic incoherent structure factor (EISF). The data cannot be fit to one process, and we examine each process separately.

The relaxation times for the first process (Figs. 2A and 2B) depend on the spatial scale in a way characteristic of the segmental mobility that drives Li^+ transport ($\tau \sim q^{-2/\beta}$). In contrast, the relaxation times for the second process are independent of spatial scale (Figs. 2C and 2D), signifying a rotational process. Although a rotation would not be observed in pure PEO because it has no side groups, the addition of Li^+ gives rise to a structure where rotation could occur: the $(PEO)_6$:$LiClO_4$ remnants. The protons may rotate on a circle, where the center of the circle is the axis of the cylinder (Fig. 2D). A second process is always reported in SPEs where the $(PEO)_6$:LiX structure can form [4,5].

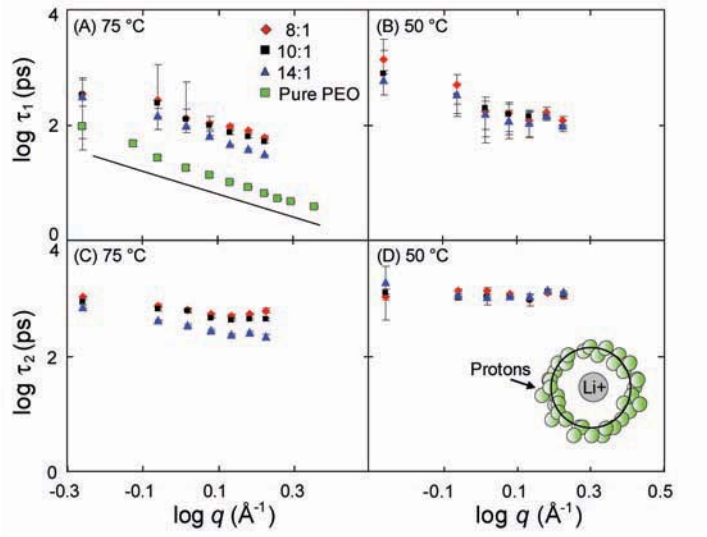

FIGURE 2: Relaxation times for the first (A and B) and second (C and D) processes at 75 °C and 50 °C. The line in (A) represents $\tau_1 \sim q^{-2}$.

To characterize the geometry of motion, we examine the spatial dependence of the EISF for the second process. We evaluate the data at 50 °C because pure rotation is captured at this temperature, whereas an additional motion enters the window of the instrument at 75 °C (*i.e.*, τ_2 has a weak q-dependence). The fit lines for the second process (Fig. 3A) represent fits to a model that describes rotation with a non-uniform distribution, and the angular distribution is provided in Fig. 3B [6]. If the rotation results from protons wrapped around and coordinated with Li^+ ions in the $(PEO)_6$:$LiClO_4$ remnants, then we would expect proton rotation to be restricted due to PEO chain connectivity and coordination with the Li^+ ions. Further support is provided by the agreement between the radius returned by our fit, and the radius of the $(PEO)_6$:$LiClO_4$ structure measured by neutron diffraction (3Å) [2].

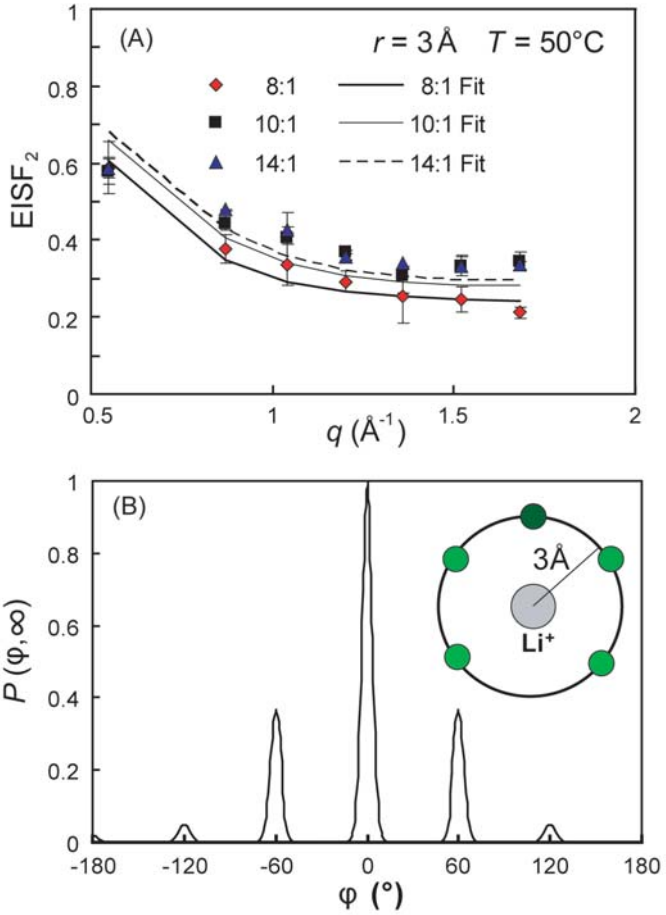

Fig. 3: (A) EISF versus spatial scale for the second process (B) angular probability distribution. The cartoon in (B) represents the probable locations of a proton on the circle, where the shading of the proton becomes more intense with increasing probability.

We have used QENS to measure the mobility of PEO in PEO/$LiClO_4$, and attribute the second dynamic process to the restricted rotation of protons within remnants of $(PEO)_6$:$LiClO_4$. High conductivity has been reported through the $(PEO)_6$:LiX crystal structure, and it is possible that the restricted rotation of the remnants reflects the local reorganization of ether oxygens to accommodate Li^+ transport from one set of ether oxygens to the next. Understanding transport through the channels is important for designing a SPE with adequate conductivity to operate at room temperature.

References

[1] Z. Gadjourova, *et al.*, Nature **412**, 520 (2001).

[2] G. Mao, *et al.*, Europhysics Letters **54**, 347 (2001).

[3] S.K. Fullerton-Shirey, J.K. Maranas, Macromolecules **42**, 2142 (2009).

[4] G.M. Mao, *et al.*, Nature **405**, 163 (2000).

[5] A. Triolo, *et al.*, Physica B. **301**, 163 (2001).

[6] M. Bée, *Quasielastic Neutron Scattering - Principles and Applications in Solid State Chemistry, Biology and Materials Science*; IOP Publishing Ltd: Great Britain (1988).

Film Morphology of Polymer-based Solar Cells

J.W. Kiel[1], M.E. Mackay[1], B.J. Kirby[2], B.B. Maranville[2], and C.F. Majkrzak[2]

Polymer-based solar cells are a potential source to convert solar radiation to electric power due to, among other benefits, their ease of fabrication, mechanical flexibility, light weight and low cost. Their performance is dictated by the nanoscopic morphology developed within a thin (≈ 200 nm) film. In all solar cells, incident photons lift electrons into excited states, leaving behind a positively charged vacancy called a hole. These two opposite but equally charged particles are initially bound to each other through a Coulomb interaction and are collectively referred to as an exciton. For standard inorganic solar cells this binding force between the charges is reduced by the high dielectric constant of the material, thus reducing the binding energy and allowing the exciton to dissociate readily into a "geminate pair" and the separated charges to flow to electrical contacts for extraction.

Organic solar cells are different. Light absorbing polymers in these cells, such as poly(3-hexylthiophene) (P3HT) are poor conductors and have low dielectric constants. Low dielectric constants lead to tightly bound excitons which, coupled with the poor conductivity of the polymer, allow the excitons to thermalize and recombine before the charge carriers can be separated to flow to the boundaries of the cell. While polymers such as P3HT absorb almost all incoming photons within their band gap, the inability to separate and extract the created charge carriers is disastrous for solar cell performance. For polymer solar cells, this problem can be combated by the addition of strong electron acceptors such as C_{60} derivative nanoparticles, e.g., phenyl-C61-butyric acid methyl ester (PCBM), that promote rapid exciton dissociation into geminate pairs. The dispersion of acceptors is critical for cell performance, as each exciton needs an acceptor nearby (≈ 10 nm), while the overall acceptor concentration needs to be low enough to facilitate carrier transport through the solar cell.

Despite its obvious importance, little reliable information exists about the dispersion of acceptor nanoparticles in organic solar cell films. For example, in the very widely studied organic solar cell system spin-coated PCBM nanoparticles in P3HT, it is well established that a 1:1 mass ratio of the two components leads to optimum cell efficiency, but it is not known why that ratio is ideal or if an ideal dispersion is achieved. Techniques commonly used for studying the morphology of thin films such as transmission electron microscopy and x-ray reflectometry are totally unsuitable for the PCBM:P3HT system, as there is virtually no contrast between the nanoparticles and the polymer host, and the microscopy in particular is much more sensitive to local variations in crystallinity than to variations in nanoparticle concentration. Neutrons however, see strong contrast between the two components, as PCBM has roughly a factor of five larger scattering length density (SLD) than does P3HT. Thus, neutron reflectometry (NR) which is sensitive to the depth-dependent scattering length density profiles of thin films is a powerful technique for studying the distribution of acceptor nanoparticles. With this in mind we have spin-coated 1:1 PCBM:P3HT films onto Si substrates, and studied them with NR.

Measurements were conducted at the NG-1 Reflectometer, using a silicon "wet cell" sample holder that allows for different backing layers to be adjacent to the sample surface. Figure 1 shows the wavevector (Q) dependent NR spectra for a PCBM:P3HT film spin coated at 41.7 s^{-1} (2500 rpm), measured against a backing layer of air (green) and D_2O (pink). The compositional depth profiles of films are commonly determined by fitting a sample's reflectivity to a scattering length density model (using the formalism of Parratt [2], for example). However, there is a significant ambiguity associated with this approach; although the depth profile can be uniquely determined from the complex reflection amplitude, the measured reflectivity is actually the square of that reflection amplitude. This "phase problem" can be overcome by conducting two otherwise identical NR measurements with different backing environments, providing enough information to allow an exact phase-sensitive neutron reflectometry (PSNR) determination of the scattering length depth profile. Alternatively, simultaneous fitting of the same two data sets to a common model is virtually guaranteed to provide a non-ambiguous result.

[1]University of Delaware, Newark, Delaware 19716
[2]NIST Center For Neutron Research, National Institute of Standards and Technology, Gaithersburg, Maryland 20899

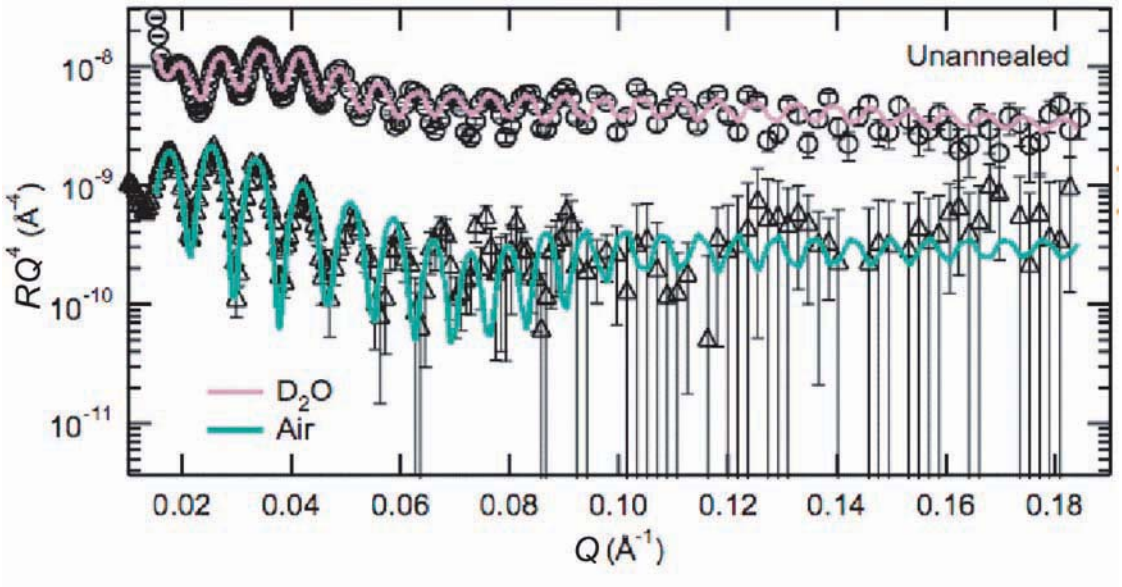

FIGURE 1: Neutron reflectivities for the sample next to a D_2O fronting (pink) and an air fronting (green). Lines are fits corresponding to the (Sim. Fit) profiles in Fig. 2.

In Fig. 2, we show the results of all three approaches (Parratt modeling of the "air" data, simultaneous modeling, and PSNR determination) to analyze the NR data shown in Fig. 1. The agreement among methods is remarkable, as the scattering length density profiles determined by the three techniques each show profiles with spikes in scattering length density near the surface and substrate interfaces. These spikes indicate a profoundly inhomogeneous distribution of PCBM (depicted in Fig. 3), with approximately 50 % volume fraction PCBM through the bulk of the film, increasing to approximately 80 % volume fraction PCBM at the interfaces.

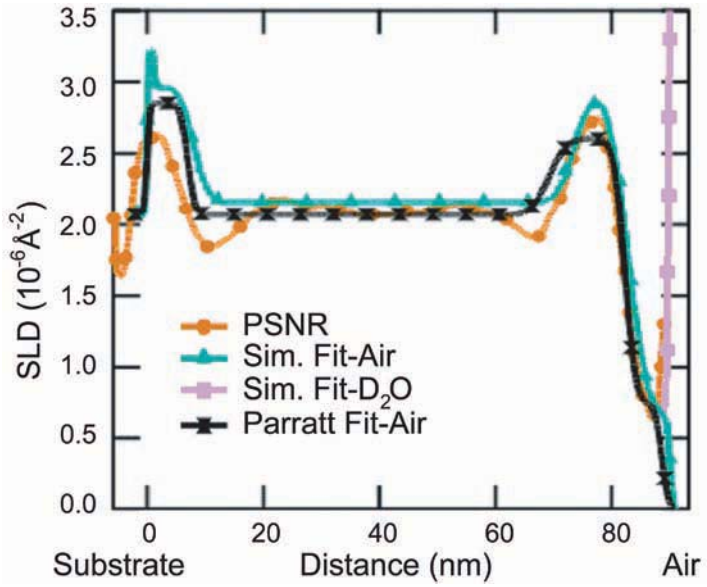

FIGURE 2: Sample depth profile determined from PSNR (orange), simultaneous fitting (green and pink), and Parratt modeling of the "air" data (black).

This result [1] clearly demonstrates that the acceptor dopant concentration in "optimally" prepared PCBM:P3HT is far from ideal, and suggests that striving towards better fabrication techniques could result in significantly improved performance for this system.

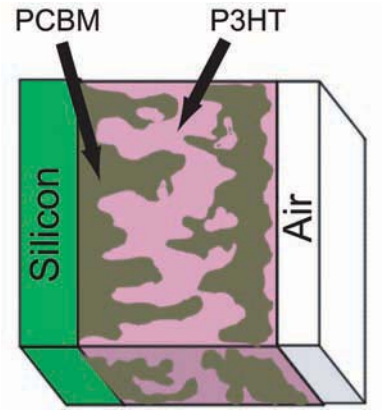

FIGURE 3: Cartoon depiction of the PCBM-rich interface model determined from NR. Such an inhomogeneous distribution of PCBM is not optimal for solar cell performance.

References

[1] J. W. Kiel, B. J. Kirby, C. F. Majkrzak, B. B. Maranville, and M. E. Mackay, submitted to Nature Nanotechnology, 2009.
[2] L.G. Parratt. Phys. Rev. **95**, 359 (1954).

Engineering Protein Electrophoresis With the Aid of SANS

D. Pozzo and M. Ospinal[1]

The identification of proteins at low concentrations or with similar molecular weights in biological settings is very challenging. Scientists routinely aim to separate and quantify the presence of low abundance proteins in mixtures that may contain several thousands of other biomolecules at much larger concentrations. There is a pressing need to significantly improve the resolution, speed and detection sensitivity of protein separations that is motivated by developments in the analysis for proteins (proteomics) in cells and biological samples such as serum and saliva. The identification of low abundance proteins in complex mixtures is critical for the development of technologies such as the early diagnosis of cancer. This need motivates the continued engineering of new materials and technologies for proteomic separations so that these may be applied routinely, accurately and reproducibly to samples of increasing complexity. One essential separation technique is electrophoresis, and small angle neutron scattering (SANS) can be a great tool to understand and re-design this technology.

Electrophoresis is the motion of particles relative to a fluid under the influence of a uniform electric field. The motion allows a mixture of particles to separate over time along the path of motion according to their speeds of migration. Electrophoretic separations are well established and their value to the natural sciences and medical research is widely recognized. Of all electrophoretic techniques, sodium dodecyl sulfate polyacrylamide gel electrophoresis (SDS-PAGE) is by far the most commonly used. In SDS-PAGE, an electric field is applied to protein-surfactant complexes that navigate through a polymeric sieving matrix and separate. This electrophoretic mobility is controlled by a variety of molecular parameters including the size and conformation of the proteins, the size and geometry of the sieving matrix and the mode of transport that molecules use to navigate through obstacles (*e.g.*, reptation). In SDS-PAGE proteins are primarily separated by differences in molecular weight.

In SDS-PAGE, a protein mixture is exposed to heat in the presence of the surfactant sodium dodecyl sulfate (SDS) and a reducing agent that breaks all disulfide bridges in the proteins, opening them out and attaching "pearls" of SDS along the resulting chain. This creates a protein-surfactant complex that acquires the shape of a "pearl necklace" with surfactant micelles decorating the polypeptide backbone (Fig. 1). The solution structure of SDS-protein complexes has been previously investigated with SANS [1]. However, the structure and conformation of these complexes under actual electrophoretic conditions had not been examined and remained unknown. SANS can effectively help in investigating the true molecular conformation of proteins under the application of electric fields.

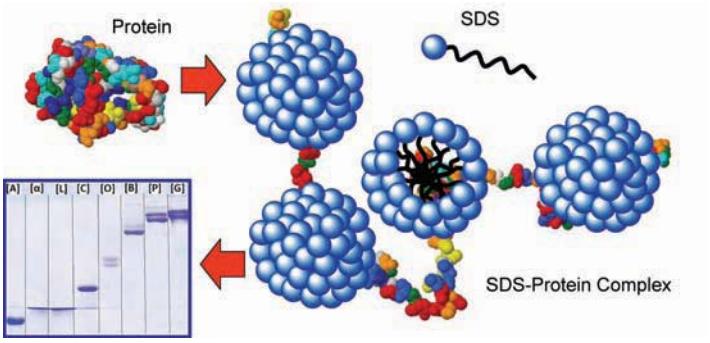

FIGURE 1: Denatured protein-SDS complexes form 'pearl-necklace' structures with discrete surfactant micelles decorating the polypeptide backbone. In SDS-PAGE protein surfactant complexes are driven through a polyacrylamide network by the application of an external electric field. Proteins are separated by molecular weight (blue bands in the gel) because small peptides are able to navigate through the gel at a faster rate than longer ones.

Recent developments at the NCNR using contrast variation SANS through new sample cells that permit probing of SDS-protein complexes under external electric fields (electrophoresis SANS) have allowed exploration of the conformation of SDS-protein complexes inside crosslinked polyacrylamide gels. In these experiments, the polymer matrix is contrast-matched through the use of a mixture of hydrogenated and deuterated monomers. The electrophoresis SANS technique was recently applied to the analysis of complexes formed with bovine serum albumin (BSA) and sodium dodecyl sulfate (SDS) in crosslinked polyacrylamide gels (PAG) with a total monomer concentration of 5 % mass fraction. The scattering of BSA-SDS complexes in free solution is shown in Fig. 2. Analysis is performed using indirect Fourier transformation methods with newly developed DANSE software

[1]University of Washington, Seattle, WA 98195

[3]. From the scattering in solution, the 'pearl necklace' geometry was confirmed and the structural parameters of the protein surfactant complex were accurately measured. The technique may easily be extended to the study of other biomolecules such as DNA and RNA as well as to alternative surfactants and polymeric matrices.

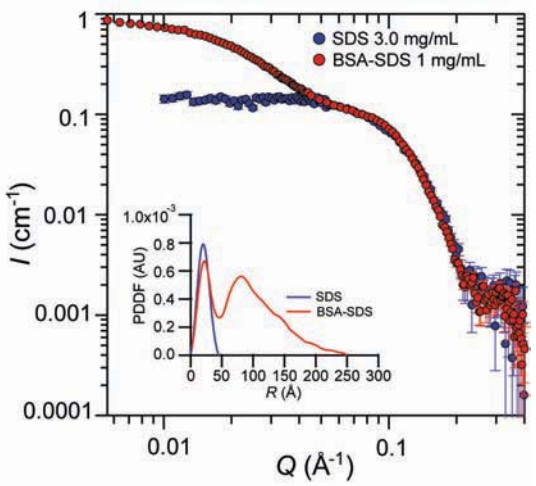

FIGURE 2: SANS is used to confirm the 'pearl-necklace' structure of bovine serum albumin (BSA) proteins in solution. At high *Q*, the scattering of the BSA-SDS complex is identical to that of free SDS micelles. Inset: the pair distance distribution function (PDDF) after indirect Fourier transformation provides a direct measurement of the micelle diameter (40 Å), the average separation between micelles (80 Å) and the extension of the complex (250 Å).

We are now able to probe the transport and conformation of biomolecules in real electrophoretic conditions [2]. An electric field of 10 V/cm was applied across a polyacrylamide gel that separated two reservoirs containing BSA-SDS complexes in solution. Figure 3 shows the scattering of the BSA-SDS complexes as the total electrophoresis time elapsed and they entered the gel. The SANS profiles at short times are similar to those of complexes in buffer solutions (compare the white symbol curve to the red one in Fig. 2). However, as the electrophoresis time elapsed and more proteins enter the gel, the formation of a correlation peak indicated the existence of significant interparticle interactions. Contrast variation of the surfactant was used to ensure that these correlations are only due to BSA-SDS complexes and not affected by any 'free' micelles.

The SANS results show that, at these gel concentrations, the migration of BSA-SDS complexes occurs primarily through a limited fraction of the gel volume that contains relatively large pores. This causes a local enrichment of the BSA-SDS complexes and the subsequent formation of correlation peaks in the scattering. Preferential transport through a fraction of the gel volume is a result of heterogeneities or defects that are known to occur in crosslinked polyacrylamide hydrogels [4]. Interestingly, the scattering of the BSA-SDS samples did not show any sign of angular anisotropy when the electric field was applied. This suggests that the orientation of the complexes at any instant in time is randomized and there is no preferential alignment of proteins in the direction of the electric field. Probing of electrophoresis at other conditions is necessary to determine if orientation occurs when larger monomer concentrations and/or higher electric fields are used. These developments enable a more complete understanding of the electrophoretic transport mechanisms of denatured proteins and provide information to guide the rational development of new surfactant and polymeric materials for proteomic separations.

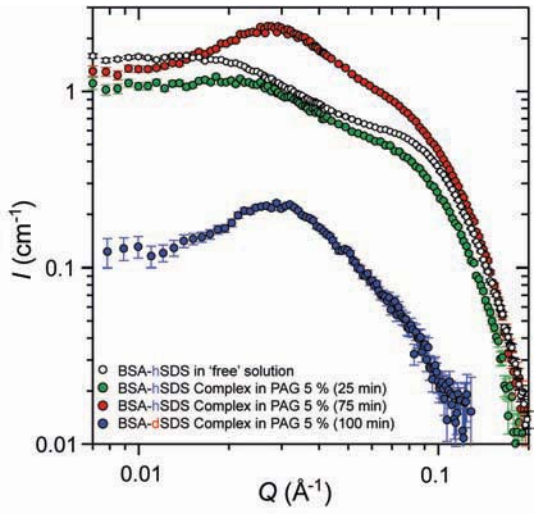

FIGURE 3: The structure factor peaks in SANS profiles of BSA-SDS complexes during electrophoresis indicate the existence of significant interparticle interactions in the polyacrylamide gel. Contrast variation through the use of deuterium labeled surfactants shows that this interaction is due to BSA-SDS complexes and not to 'free' micelles.

This work demonstrates that SANS can be extremely valuable to understand transport mechanisms in gel electrophoresis. These experiments have demonstrated the feasibility and value of this technique. They have also advanced significantly our understanding of molecular transport in the most commonly used electrophoresis system of SDS and polyacrylamide matrices. SANS experiments are now focused on extending this technique to help develop protein separations in which alternative surfactants are used.

References

[1] S.-H. Chen, J. Teixeira, Phys. Rev. Lett. **57**, 2583 (1986).
[2] D.C. Pozzo, Langmuir **25**, 1558 (2009).
[3] PrView SANS analysis package. http://danse.chem.utk.edu/prview.html.
[4] A. M. Hecht, R. Duplessix, E. Geissler, Macromolecules **18**, 2167 (1985).

Organic Semiconductor Polymer Blends For Printable Electronics

D.M. DeLongchamp[1], V.M. Prabhu[1], E. Lin[1], D.Y. Yoon[2]

Organic semiconductors are the most critical element of a new generation of optoelectronic devices that includes printable flexible electronics and photovoltaic devices. The vertical distribution and orientation of crystalline semiconductors in an organic thin film field-effect transistor (OTFT) must be controlled by processing to achieve optimal switching speed and current flow, often for a specific OTFT architecture. Common OTFT architecture variations involve different placements of the contacts and gate dielectric. For large-area flexible displays, many technology developers prefer a bottom-gated OTFT over a top-gated one. Gate placement is critical to device optimization because charge carriers are formed within the semiconductor layer only at its interface with the gate dielectric. Charge transport occurs within the 6 nm to 10 nm adjacent to the gate dielectric, and the composition and orientation of the semiconductor layer at this interface is critical to device performance.

Formulation and processing are key contributors to the character of the organic semiconductor layer at the dielectric interface. Because organic semiconductors can be processed from solution, they offer advantages over inorganic semiconductors such as amorphous silicon, which require vacuum. While synthetic advances in recent years have produced organic semiconductors with performance that matches amorphous silicon, there remain challenges in process development for methods such as ink jet drop-on-demand printing, roll-casting, and spin coating. A processing challenge affecting some of the highest-performing organic semiconductors is that the neat solution viscosity is too low for common coating methods, preventing the formation of high-quality films.

An attractive approach to organic semiconductor formulation was proposed by Brown *et al.*, who blended a high-performance organic semiconductor in solution with an insulating polymer binder [1]. Due to the polymer binder, the blend solution created high-quality conformal films, and the films had charge carrier mobility greater than 0.3 cm^2/Vs in top-gated OTFTs. Because the top-gated mobility was quite high, Brown *et al.* postulated that the semiconducting small molecules were vertically segregated to the top surface of the thin blend film, but no concrete experimental evidence was provided. Although this approach represented a significant advance in formulation, the top-gated architecture is not preferred for large-area displays because the active layer can be damaged by subsequent fabrication steps such as gate electrode patterning and wiring. Instead, the bottom-gate architecture is favored.

We undertook further development of the blend formulation approach to ensure that the semiconducting molecules can also segregate to a bottom dielectric interface. A critical aspect of this development was direct measurement of the vertical composition profile that can be achieved with nanometer resolution using neutron reflectivity (NR). Our model blend formulation included 6,13-bis(triisopropylsilylethynyl)pentacene (TIPS-pentacene) and poly(α-methylstyrene)(PaMS) (Fig. 1) [2]. Specular NR was used to measure the vertical composition profile in films spin-coated onto silicon wafers from solutions of co-dissolved deuterium-labeled TIPS-pentacene and PaMS. These films provide a model OTFT film where the native silicon oxide layer mimics the gate dielectric interface. The segregation characteristics were controlled by adjusting the number-average relative molecular mass of the PaMS.

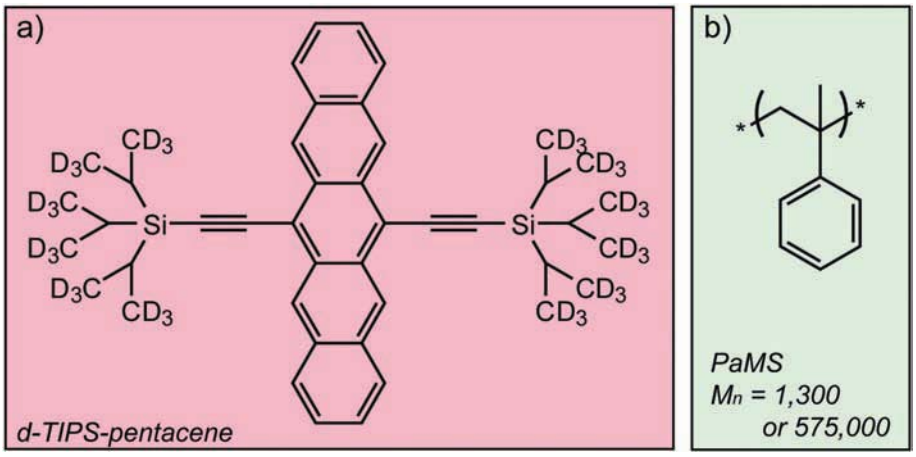

FIGURE 1: Blend formulation materials a) deuterium labeled TIPS-pentacene and b) poly(α-methylstyrene)(PaMS) that are used as the active semiconductor layer in an organic thin film field-effect transistor.

[1]Polymers Division, Materials Science and Engineering Laboratory, National Institute of Standards and Technology, Gaithersburg, MD 20899
[2]Seoul National University, Seoul, Korea

Figure 2a shows the specular NR data for the blend films (50/50 mass ratio) of d-TIPS-pentacene with PaMS of number-average relative molecular mass ($M_{r,n}$) ≈ 1,300 g·mol^{-1}, spin-cast on a thick silicon substrate. In general, the well-defined oscillating reflectivity fringes arise from the interference of the reflected neutrons from the air and the substrate interfaces, such that the period of the fringes is inversely proportional to the film thickness. From the fits to the NR data, the scattering-length density (SLD) profiles were interpreted as d-TIPS-pentacene volume fraction as a function of distance from the substrate using the relation: $\Phi_{d\text{-TIPS}} \times SLD_{d\text{-TIPS}} + (1-\Phi_{d\text{-TIPS}}) \times SLD_{P\alpha MS} = SLD_{blend}$, where $\Phi_{d\text{-TIPS}}$ corresponds to the volume fraction of d-TIPS-pentacene. Reference pure component films provide the values of $SLD_{d\text{-TIPS}}$ and $SLD_{P\alpha MS}$. Insets in Fig. 2 show the depth profiles of d-TIPS-pentacene for the as-cast film that has a mostly uniform distribution of d-TIPS-pentacene with a concentration of 51 % volume fraction throughout the film thickness, except in the two interfacial regions: 11 % excess at the blend/silicon substrate and 20 % excess at the blend/air interface. Annealing induces a further enhanced surface segregation. This segregation feature, quantified by neutron reflectivity, is consistent with the excellent field-effect mobility of this blend active layer in the top-gated OTFT architectures, as reported by Brown *et al.* The bottom interface segregation, however, is relatively modest and not consistent with expectations of high bottom-gated performance as shown by comparing the two basic OTFT device architectures as insets to Fig. 2.

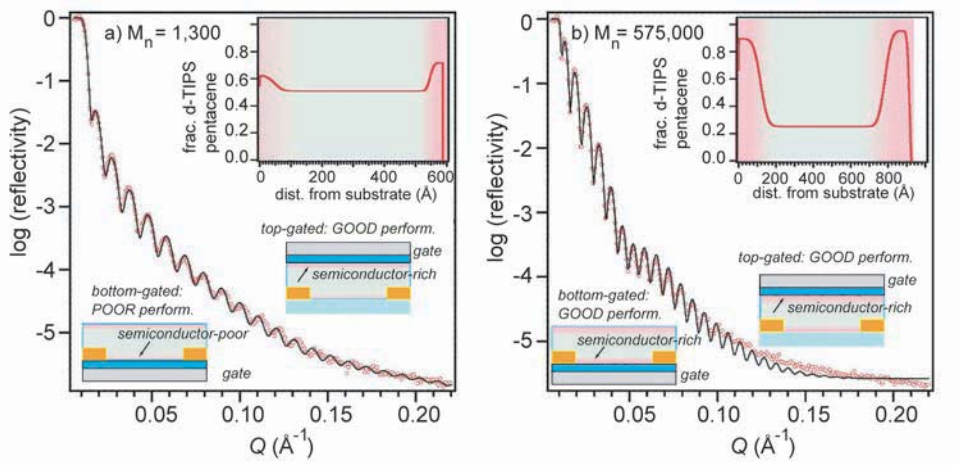

FIGURE 2: Neutron reflectivity and vertical composition profiles (insets) of the TIPS-pentacene semiconductor for two different blend systems with a) low molar mass and b) high molar mass PaMS binder. The relationships among segregations and organic thin film field-effect transistor performances for two contrasting device architectures are provided.

Figure 2b shows the specular NR data for the blend films (50/50 mass fraction) of d-TIPS-pentacene with PaMS of number-average relative molecular mass ($M_{r,n}$) ≈ 570,000 g·mol^{-1}. For this blend with such a high molecular-mass PaMS, a strong interface segregation of TIPS-pentacene occurred in the initial spin-cast film. Moreover, the phase-segregated structure formed a nearly pure TIPS-pentacene layer not only at the air surface, with ≈ 134 Å thickness, but also at the blend/silicon substrate interface with ≈ 117 Å thickness.

Our results confirm that bottom interface semiconductor segregation can indeed be achieved in films cast from blend formulations if the binder molecular mass is correctly chosen. We observed a segregated layer of nearly pure TIPS-pentacene at the blend/silicon substrate interface for high molecular mass PaMS, but not for low molecular mass PaMS. We confirmed by grazing incidence X-ray diffraction that the segregated TIPS-pentacene molecules form a highly crystalline structure with the $\pi-\pi$ stacked molecular layers oriented parallel to the film surface, which is important to their semiconducting performance. Finally, we measured bottom-gated OTFTs to find that the charge carrier mobility, on/off ratio, and threshold voltage of the films cast from the high molecular mass blend were significantly superior to those cast from pure TIPS-pentacene.

Our approach of using specular neutron reflectivity to measure the vertical composition profile in semiconducting blend formulations provides a general paradigm for formulation and process development in organic electronics. Direct measurement of the composition profile identifies processing strategies which permit advantageous segregation to the desired device interface. This paradigm has a key advantage over the common practice of process optimization via solely electrical measurements, because the results are far less ambiguous, and the performance results of process variations can be more correctly assigned to segregation, crystallinity, or other film and device issues [3]. Application of this measurement strategy can accelerate formulation and process development and hasten the introduction of new products from printed, flexible electronics.

References

[1] B.A. Brown, J. Veres, R.M. Anemian, R.T. Williams, S.D. Ogier, S.W. Leeming, In International Application Published Under the Patent Cooperation Treaty, WO 2005/055248 A2, 2005.

[2] J. Kang, N. Shin, D.Y. Jang, V.M. Prabhu and D.Y. Yoon, J. Am. Chem. Soc., **130,** 12273 (2008).

[3] D.M. DeLongchamp *et al.*, Chemistry of Materials, **17** , 5610 (2005).

A Compartmentalized Hydrogel from an ABC Block Terpolymer

R.R. Taribagil, M.A. Hillmyer, T.P. Lodge[1]

An important theme in nanoscience is the search for advanced composite materials endowed with multiple functionalities. The concept of constructing multicompartment assemblies emerged in this context, drawing inspiration from organized biological systems from proteins up to eukaryotic cells [1]. For example, human serum albumins (HSA) encompass multiple sub-domains and combine different environments and functionalities in close proximity. Suitably designed multiblock polymers, such as ABC terpolymers, can spontaneously self-assemble into micellar aggregates or gels, in which separate A and C nanocompartments are dispersed in a matrix of B plus solvent. Potentially, multicompartment assemblies present opportunities for designing sophisticated storage and delivery systems, for example to sequester and release different therapeutic agents in the A and C domains.

Several groups have constructed multicompartment micelles in water by dispersing amphiphilic block copolymers with two mutually incompatible hydrophobic blocks; the mutual incompatibility ensuring well segregated domains inside the core of the micelle [1, 2]. In addition to discrete assemblies such as micelles, it is of equal interest to design multicompartment gels. One route to these novel gels is to hydrate a linear ABC block terpolymer with a long hydrophilic B mid-block and two mutually incompatible, but small hydrophobic end-blocks A and C. In our protoytpe system we examined a solution containing 10 % volume fraction of a linear terpolymer of poly(1,2-butadiene) (PB), poly(ethylene oxide) (PEO) and poly(perfluoropropylene oxide) (PFPO) designated BOF(1.9-26-2.3), where the numbers in the parentheses denote the molecular weights of the three blocks in kg mol^{-1}, respectively. The synthesis of this molecule has been documented elsewhere [3].

Cryogenic scanning electron microscopy (SEM) analysis of the 10 % sample of BOF(1.9-26-2.3) (Fig. 1) revealed a bicontinuous structure with the polymer and water dividing space into two interpenetrating labyrinths. The "pores" (*i.e.*, the previously water-filled chambers) have dimensions in the range 300 nm to 700 nm, consistent with the observed opacity of the solution.

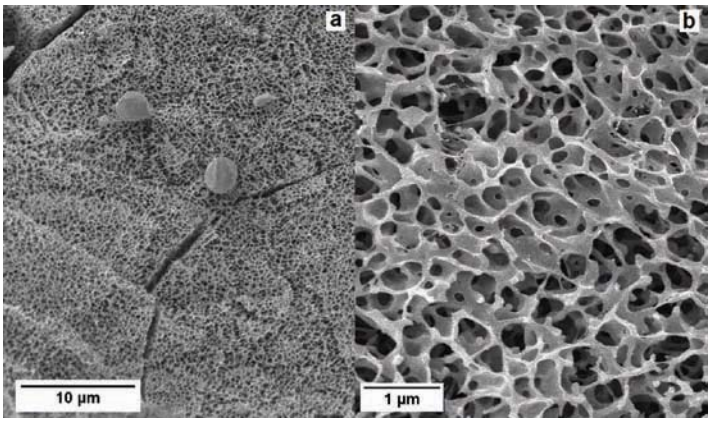

FIGURE 1: Cryo-SEM micrograph for 10 % BOF(1.9-26-2.3) in water at two different magnifications.

It is evident that the bicontinuous structure results from the arrangement of the strongly hydrophobic end blocks (PB and PFPO) into space-spanning sheets with non-preferential curvature, while the PEO chains apparently shield the hydrophobes from water. However, given their appreciably high incompatibility, PB and PFPO are also expected to segregate into different domains. This is subject to the constraint that the volume occupied by PB blocks is almost twice that occupied by the PFPO block; an assembly satisfying this constraint features domains of PFPO dispersed in a PB matrix. From our previous work, where the formation of disk-like fluorodomains was a consistent motif, we proposed the shape of the fluoro-domains in the hydrophobic sheets to be disk-like. The resulting chain packing arrangement is illustrated in the cartoon shown in Fig. 2.

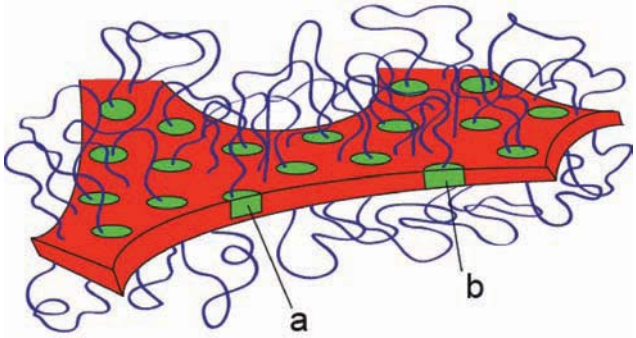

FIGURE 2: Proposed chain packing motif for the compartmentalized network. PB sheet, PFPO disks and PEO chains are represented in red, green and blue, respectively. The PFPO disks could either be (a) thinner than, or (b) extend through the PB sheet.

[1]University of Minnesota, Minneapolis, MN 55455-0431

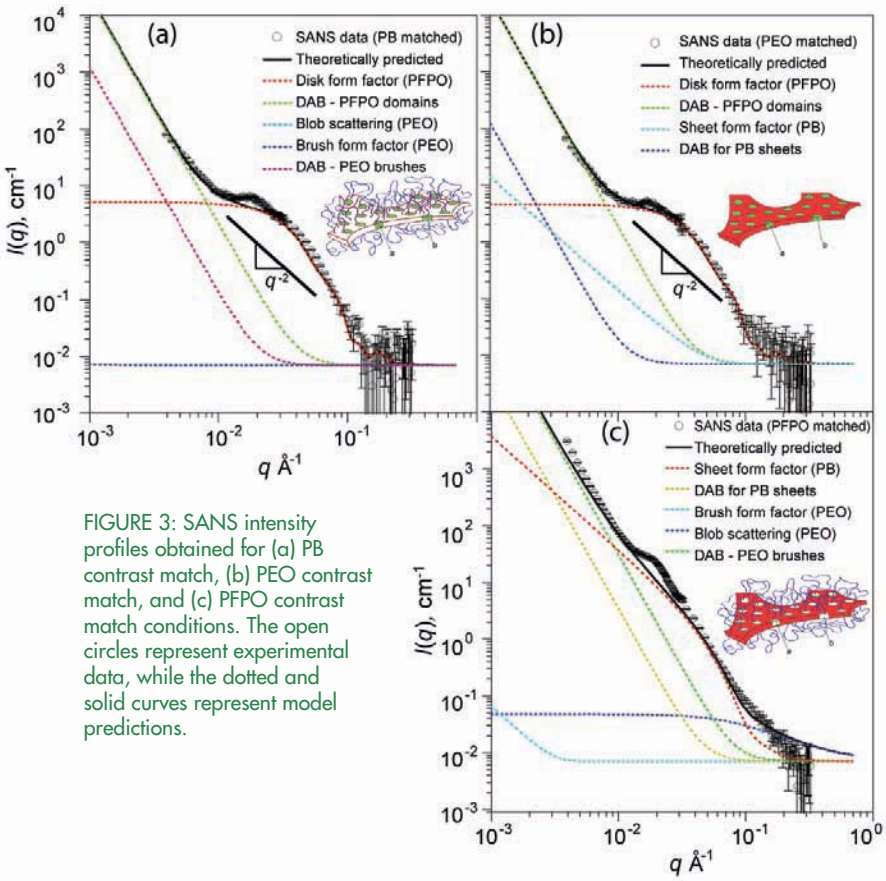

FIGURE 3: SANS intensity profiles obtained for (a) PB contrast match, (b) PEO contrast match, and (c) PFPO contrast match conditions. The open circles represent experimental data, while the dotted and solid curves represent model predictions.

To assess the viability of the microstructure depicted in Fig. 2, we carried out small angle neutron scattering experiments on the NG-7 30 m instrument at the NCNR. Using two different detector settings (1 m and 11 m), we were able to map out the scattering profile over a wide range of scattering wave vector q (0.0039 Å^{-1} to 0.33 Å^{-1}). Using the principle of contrast matching, which involves matching the scattering length density of the solvent (a mixture of H_2O and D_2O) with that of a particular block, thus rendering that block "invisible" to the neutron beam, we were able to isolate the scattering contributions from the different blocks. We estimated the scattering profiles under different contrast match conditions and compared them with the SANS measurements. It is noteworthy that the complexity of the proposed structure, in terms of the number of components present, the inherent irregularity, and the probable polydispersity with respect to the associated length scales (sheet thickness, disk radius and mean spacing, PEO brush thickness, overall pore size) makes precise prediction of the scattering profile impossible. But even a reasonably good fit, in face of the noted complexities, is convincing evidence in support of the proposed structure.

Details of estimating the scattering profile have been presented elsewhere [3]; a brief summary follows. The contributions to the scattering equation are the form factors for the PFPO disks, the PB sheets, and the PEO brushes, as well as an expression to describe the blob scattering from PEO chains. Given the bicontinuity of the structure, the low q scattering should be dominated by the correlations that exist on the length scale of the pore sizes (300 nm to 700 nm) estimated from the cryo-SEM micrographs. We describe this correlation using the single length Debye-Anderson-Brumberger (DAB) model for each component. The individual contributions from the different components as well as the sum of these contributions, marked as theoretical curves, are depicted in Fig. 3. There is reasonable agreement between the model predictions and the experimental data, if 14 nm wide and 5 nm thick PFPO disks are assumed to be embedded in a 5 nm thick PB sheet (Figure 3). A short range spatial correlation between the disks accounts for the peak near 0.02 Å^{-1} in all three profiles.

The confirmation of the presence of fluorocarbon disks from SANS experiments helped us explain the sheet-like morphology in the context of the "Super Strong Segregation Limit" (SSSL), which is accessed when the interfacial tension overwhelms the other contributions to the free energy, leading to the formation of flat interfaces [4]. The high interfacial tension between PEO/water and PFPO encourages formation of flat disks. In an interesting interplay between PB and PFPO, the fluoro-domains surround themselves with PB blocks along the curved surface of the disk to minimize contact with PEO/water (the face of the disk serves as an interface between PFPO and PEO); the incompatibility between PB and PFPO guarantees segregation of both blocks into their respective domains.

In this work we have documented a novel multicompartment morphology, obtained by dispersing a linear ABC terpolymer in water. This serves to highlight the rich structural possibilities that can be obtained from terpolymer gels. The study also highlights the power of contrast matching in small angle neutron scattering, in partnership with microscopy, to probe intricate details of a multicomponent morphology.

References

[1] J. -F. Lutz, A. Laschewsky, Macromol. Chem. Phys. **206**, 813 (2005).
[2] Z. Li, M. A. Hillmyer, T. P. Lodge, Langmuir **22**, 9409 (2006).
[3] R. R. Taribagil, M. A. Hillmyer, T. P. Lodge, Macromolecules **42**, 1796 (2009).
[4] A. N. Semenov, I. A. Nyrkova, A. R. Khokhlov, Macromolecules **28**, 7491 (1995).

Dynamics and Structure of Semiflexible, Self-Assembled Peptide Chain Networks

M.C. Branco[1], J.P. Schneider[2], D.J. Pochan[3], and N.J. Wagner[1]

Hydrogels, three dimensional networks of crosslinked polymer with high water content, are ideal drug delivery vehicles for protein delivery. Their highly porous, aqueous structure provides a biocompatible, solubilizing environment in which proteins can be encapsulated and released with both spatial and temporal control to ensure optimal dosage. Key features of these hydrogels necessary for therapeutic delivery include their mechanical strength (*i.e.*, the elastic modulus), kinetics of assembly, structural stability, and rate of release of the desired therapeutics. We have engineered hydrogels that are comprised of self assembled peptides with great potential for delivery vehicles via the simple modification of the individual peptide sequence [1]. MAX1 and MAX8 are synthetic β-hairpin peptides that undergo triggered nanoscale self-assembly to form a physically crosslinked hydrogel network of fibrils with a defined cross-section, as depicted in Fig. 1.

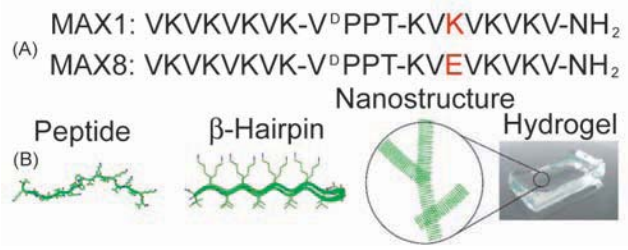

FIGURE 1: (A) Peptide sequence of MAX1 and MAX8. (B) Proposed mechanism: unfolded peptide under external stimulus folds into β-hairpins which self assemble into fibrillar nanostructures that make up the rigid hydrogel.

These peptides are freely soluble in aqueous solutions. However, when a physiological relevant concentration of salt is added at room temperature, the peptides fold into a β-hairpin, and subsequently, self-assemble to form a rigid hydrogel stabilized by non-covalent crosslinks. The sequence of MAX8 is identical to MAX1 with the exception of one single amino acid substitution (Glu replacing Lys at position 15). This reduces the net charge on the peptide and results in faster folding and self assembly kinetics for MAX8 at the same peptide concentration and identical buffer conditions. These faster folding kinetics result in more rigid gels, with the modulus for MAX8 being 2.5 kPa at 1.5 % mass fraction, which is about three times higher than for MAX1 at the same conditions [2].

Transmission electron microscopy (TEM) demonstrates that both peptides form networks of semiflexible fibrils that are composed of a bilayer of hairpins [3]. The fibrils are connected by non-covalent, interfibrillar junctions and entanglements. Imperfections in the self assembly mechanism, in which one hairpin is rotated relative to another hairpin in the bilayer, can give rise to interfibril branching. Therefore, the increased rigidity for MAX8 folded at the same peptide concentration, temperature, and buffer is hypothesized to be a consequence of structural differences either in terms of the topology of the network (*i.e.*, more imperfect branch points in MAX8) or in the compactness of the bilayer (*i.e.*, higher bending constant) [2]. Changes to these structural features can play a large role in the interaction of proteins with the peptide hydrogels and their subsequent delivery from the sterically hindering network, emphasizing the need to fully understand these structural differences between the two peptides.

In this highlight, we report the first neutron spin echo (NSE) measurements of self-assembling peptide hydrogel networks to study their dynamics on nanolength and nanotime scales. These NSE measurements were designed to explore whether these peptide fibrils can be described by the theory of semiflexible chains on length scales smaller than the persistence length of the fibrils. In addition, these studies investigated how the substitution of the Lys at position 15 with a Glu affects the nanoscale dynamics to determine whether the observed increase in viscoelasticity upon peptide substitution is due to a difference in nanoscale fibril rigidity. We follow the procedures and theoretical analysis defined in recent work on self-assembled worm-like surfactants based on the theory of Zilman and Granek [4,5]. Complementary small angle neutron scattering (SANS) measurements of the networks were also performed to assess any differences between the nanoscale structure of the two networks.

NSE measurements of the peptides demonstrate that the self-assembled peptide fibrils can be described as semi-flexible chains on nanolength and nanotime scales [2]. The normalized intermediate scattering functions $I(q,t)/I(q,0)$ obtained from

[1]Department of Chemical Engineering, University of Delaware, Newark, DE 19716
[2]Department of Chemistry and Biochemistry, University of Delaware, Newark, DE 19716
[3]Department of Materials Science and Engineering, University of Delaware, Newark, DE 19716

the NSE measurements are shown in Fig. 2 for the 1.5 % MAX1 (A) and MAX8 (B). These normalized intermediate scattering functions were fitted for all samples to a stretched exponential predicted by the semiflexible chain model, $I(q,t) = I(q,0)\exp(-(\Gamma(q)t)^{\beta})$, with $\Gamma(q) = D_G q^{2\beta}$. An average β value of 0.74 ± 0.08 was measured for the peptide gels, which is consistent with the predicted value of 0.75 [4], further confirming their semi-flexible nature. From the wavevector, q, dependence of the scattering, which followed this equation, the segmental diffusivity D_G decreased upon alteration of the peptide sequence from 1.4×10^{-2} ($nm^{8/3}$ ns^{-1}) for MAX1 to 0.9×10^{-2} ($nm^{8/3}$ ns^{-1}) for MAX8. This difference indicates that the fibrils in the MAX1 network are more mobile on the range of length scales probed, which ranges from the fibril diameters to the characteristic mesh size, as determined from rheology [1]. This difference in segmental diffusivity is consistent with the change in peptide sequence, where the Glu at position 15 in MAX8 adds a salt bridge between peptides in the self-assembled fibril structure that further stabilizes the hairpin structure. However, this difference in mobility is not sufficient to fully explain the significant increase in elasticity, and therefore, we examined the nanostructure of the network itself.

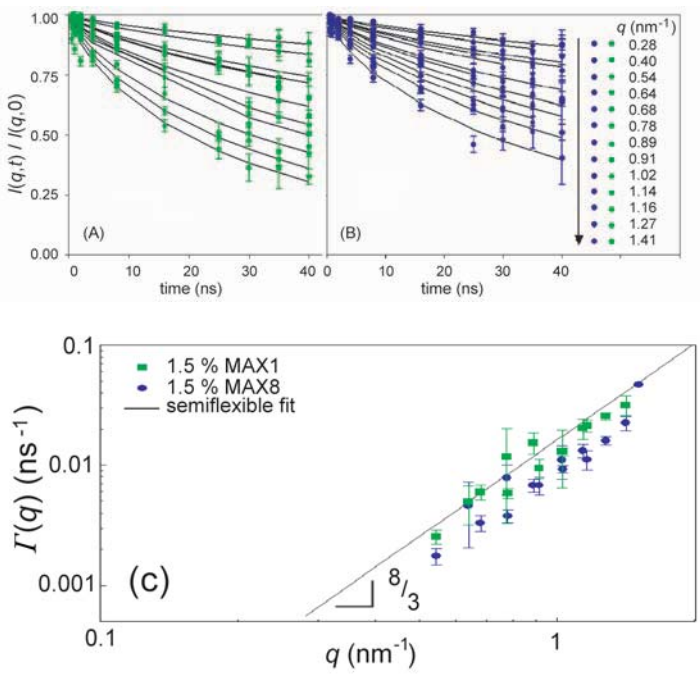

FIGURE 2: Normalized intermediate scattering functions for 1.5 % mass fraction MAX1 (A) and MAX8 (B) in pH 7.4, 50 mmol/L BTP, 150 mmol/L NaCl at 25 °C. Solid lines are fits to a stretched exponential model for semiflexible chains. (C) Relaxation rate ($\Gamma(q)$) as a function of q. The solid line represents the scaling expected for the bending modes of semiflexible chains.

A difference in the number of crosslink junctions between fibrils should manifest as a change in the small angle scattering. A look at SANS data for MAX1 and MAX8 gels supports this assessment [2,6]. As shown in Fig. 3, the scattering for both peptides is the same at high q, corresponding to the length scales of the individual fibril widths. This is expected as both peptides have the same overall length. The spectra differ, however, at lower q, which probes length scales similar to the nanoscale mesh size of the networks. The scattering intensity of MAX8 is significantly greater than MAX1 at the same concentration of peptide. The increased scattering is consistent with a heterogeneous network with a tighter mesh. Indeed, fitting these spectra to Teixeira's model yields apparent fractal dimensions of 1.26 and 1.62 respectively, which correspond with the increase in elastic modulus. This increase in network junctions for MAX8 is consistent with the very rapid rate of self-assembly as compared to MAX1, which is a direct consequence of the peptide substitution that lowers the net peptide charge [2].

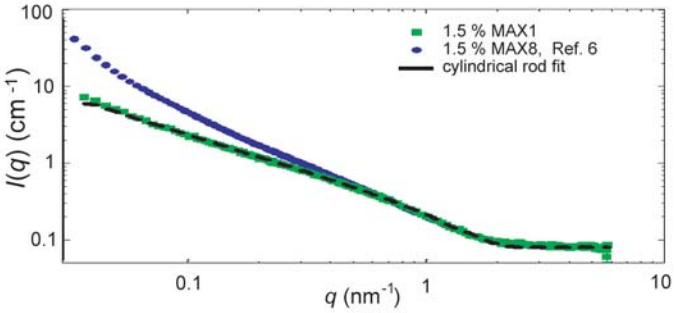

FIGURE 3: SANS intensity $I(q)$ for 1.5 % mass fraction MAX1 and MAX8 (Ref. 6) hydrogels in pH 7.4, 50 mmol/L BTP, 150 mmol/L NaCl, D_2O, 25°C.

In conclusion, combining NSE and SANS measurements yields a physical picture of the nanoscale dynamics and topology of these self-assembled peptide hydrogels that is consistent with a network of entangled and branched semiflexible fibrils. Through controlled modifications of the peptide sequence, we find that the nanoscale dynamics can be altered as well as the network topology itself. These changes in nanoscale dynamics and structure lead to substantial differences in bulk properties, such as the elastic modulus [1-3,6]. As shown, analysis of NSE and SANS data with models developed specifically for semiflexible polymers enables the quantification of the nanoscale properties of these networks and the development of molecular structure-property relations. These relations enable the rational engineering of peptide sequences to synthesize and assemble hydrogels appropriate for specific drug delivery applications.

References

[1] M.C. Branco, *et al.*, Biomaterials **30**, 1339 (2009).

[2]. M.C. Branco, *et al.*, Biomacromolecules **10**, 1374 (2009).

[3] L. Haines-Butterick, *et al.*, Proc. Nat. Acad. Sci. USA **104**, 7791 (2007).

[4] R. Granek, J. Phys. **Ii 7**, 1761 (1997).

[5] F. Nettesheim and N.J. Wagner, Langmuir **23**, 5267 (2007).

[6] R.A. Hule, *et al.*, Faraday Discussions **139**, 251 (2008).

Dynamics of Biomembranes: Effects of Phospholipid Conformations and Presence of Local Anesthetics

Z. Yi[1, 2], M. Nagao[2, 3] and D.P. Bossev[1]

Biomembranes of natural living cells are made of phospholipid molecules stacked together into bilayers. These membranes are subject to thermal fluctuations in shape which are governed by membrane stiffness. When a protein or other molecule is inserted into a membrane to aid it in fulfilling a biological function, the stiffness can be changed, in turn affecting that biological function and others mediated by other molecules. Hence, in understanding biological activity in membranes, it is useful to measure membrane stiffness, which can be characterized by a parameter, κ_c, the bending modulus.

We focus on the effect of a local anesthetic (LA), lidocaine, for two reasons: 1) it is widely used, and 2) it is an example of a small, soluble molecule having hydrophobic and hydrophilic parts which in solution finds a membrane and attaches to it, changing the membrane dynamical properties [1,2]. In this article, we highlight results from neutron spin-echo (NSE), small-angle neutron scattering (SANS), and differential scanning calorimetry (DSC) experiments on bilayers made of phospholipids with different acyl hydrocarbons with and without LA. We have investigated dynamical properties of the membrane as a function of three factors: (*i*) the unsaturation of the acyl chains, (*ii*) the bilayer thickness and (*iii*) the presence of LA.

Membranes made of saturated phospholipids undergo a first-order acyl-chain melting transition, the so-called main transition from the ripple gel (P_{β}') phase to the liquid crystalline (L_{α}) phase, which exists above the freezing point of water. Lower transition temperatures can be achieved either by the introduction of the *cis* double bond or by having shorter acyl-chain hydrocarbon number in saturated lipids [3]. Still unclear is how such phospholipid conformation changes influence the dynamics of bilayers. We have chosen NSE spectroscopy as the most suitable method to determine κ_c, since it is ideal for studies of the thermal fluctuations of biomembranes because its correlation time scale (0.1 ns to 100 ns) and length scale (10 Å to 10^3 Å) overlap those of the cell membrane fluctuations.

Seven synthetic lipids of diacyl-phosphatydilcholine (PC) having chain-lengths varying from 14 to 20 carbon atoms with either zero or one double bond were prepared in the form of large unilamellar vesicles (LUV) to investigate the dynamic properties of model bilayers. Undulating phospholipid bilayers repel each other, so we use the Zilman and Granek single membrane fluctuation model [4] to describe the scattering. Accordingly, the normalized intermediate scattering function $I(Q,t)/I(Q,0)$, observed by NSE has been fitted with the form $I(Q,t)/I(Q,0) = \exp[-(\Gamma t)^{2/3}]$, where Γ is the relaxation rate which is related to the bending elasticity κ_c by

$$\Gamma = 0.025\gamma_k \left(\frac{k_B T}{\kappa_c}\right)^{\frac{1}{2}} \frac{k_B T}{\eta} Q^3 .$$

Here, γ_k is a numerical constant close to unity and η and $k_B T$ are the solvent viscosity and the thermal energy, respectively. All samples were measured in the L_{α} phase at 60 °C, except for 14:1 PC and 16:1 PC which were measured at 30 °C.

From the mechanics of a thin slab of solid material it is known that the bending elasticity κ_c should scale as the area modulus K_A multiplied by the square of the thickness d^2, *i.e.*, $\kappa_c = \beta K_A d^2$ [5], where β is a normalization constant. We speculate that the variations of κ_c in different phospholipid bilayers are due to the differences in bilayer hydrophobic thickness. As shown in Fig. 1 the elastic ratio κ_c/K_A is indeed proportional to the square of hydrophobic thickness d^2. Here, the area modulus K_A and hydrophobic thicknesses d for these seven lipid bilayers were quoted from Ref. 5. The dashed line indicates the best fit result to a linear function and shows that in a broad range of chain lengths (from 14 to 20), either with or without presence of one double bond on the hydrophobic chain, κ_c of lipid bilayers are quadratically dependent on d. The slope β is approximately equal to 1/32.2, which agrees well with the results obtained by micropipette pressurization [5,6].

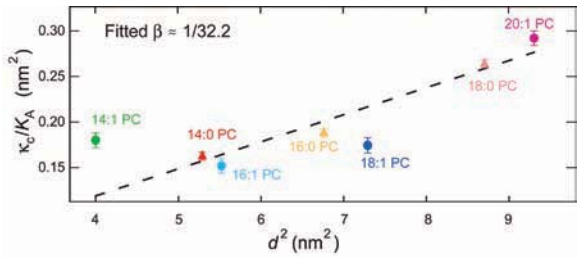

FIGURE 1: The ratio of the bending modulus, κ_c, divided by the area modulus, K_A, plotted against the square of hydrophobic thickness d^2. The labels (*e.g.*, 18:1 PC) refer to the hydrocarbon number (*i.e.*, 18) in PC and the number of double bonds (*i.e.*, 1) in each acyl chain (see Fig. 2).

[1]Physics Department, Indiana University, Bloomington, IN 47405
[2]NIST Center for Neutron Research, National Institute of Standards and Technology, Gaithersburg, MD 20899
[3]Indiana University Cyclotron Facility, Indiana University, Bloomington, IN 47408

LA are weakly amphiphilic bases and may intercalate into the bilayer between phospholipid molecules in membranes. Smith and co-workers have confirmed that the polar parts of LA interact with phospholipid polar fragments and the lipophilic parts of LA insert into the bilayer hydrophobic region [7]. As shown in Fig. 2, the intercalation, or so-called hydrophobic mismatch between the biomembrane and the LA, can induce configurational disorder of membranes. Figure 3 summarizes the results of SANS and DSC measurements on the 14:0 PC bilayers as a function of the molecular ratio R of lidocaine to 14:0 PC. DSC results show that the addition of lidocaine progressively depresses the main transition temperature T_m of the bilayers. The bilayer thickness was calculated from scattering intensities of SANS. The intercalation of LA molecules provides more inter-lipid spaces for lipid hydrophobic chains, and finally results in the decrease of bilayer thickness with the increase of R.

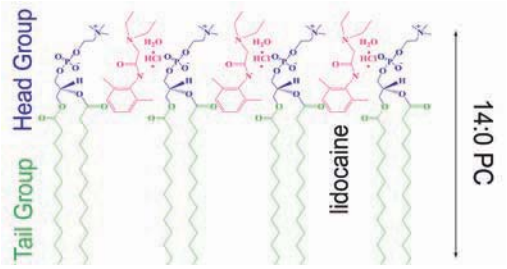

FIGURE 2: Model for the intercalation of lidocaine into 14:0 PC bilayers.

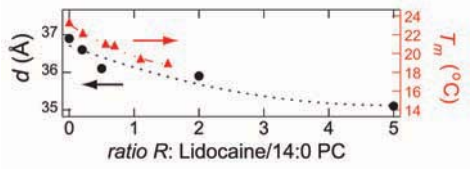

FIGURE 3: Transition temperature T_m (red triangles) and bilayer thickness d (black circles) of 14:0 PC bilayers as a function of lidocaine concentration, R.

NSE has been used to measure the R dependence of $\varkappa_c$ of 14:0 PC bilayers. Figure 4 shows plots of $\varkappa_c$ of these bilayers with R = 0, 0.5 and 2.0 in D_2O as a function of T - T_m. The effect of temperature on $\varkappa_c$ of pure lipid LUVs in D_2O is shown as solid blue circles. For $T >> T_m$, $\varkappa_c$ of the pure 14:0 PC bilayers is nearly independent of temperature, *i.e.*, the temperature has a minimal effect on the properties of the lipid bilayer in the L_α phase. As the temperature approaches T_m from above for this pure case, $\varkappa_c$ becomes slightly larger and then rapidly increases with decreasing temperature in the P_β' phase.

The effect of lidocaine on $\varkappa_c$ in the L_α phase is small compared with its effect on the transition temperature. From our SANS result (not shown), it can be demonstrated that the intercalation of lidocaine causes a lateral expansion of the membrane, so that the tail-tail attractive interaction decreases. The presence of lidocaine is thus expected to make the membrane more flexible because of decreasing the bilayer thickness. On the other hand, the interaction of headgroups increases because of the possible closer packing in hydrophilic parts of 14:0 PC and lidocaine. Under the dual effects on hydrophobic and hydrophilic groups, the bilayers in the L_α phase are slightly more rigid due to the intercalation of lidocaine. At T_m, $\varkappa_c$ for R = 0 was found to be 6 times of that in the L_α phase. By comparison, $\varkappa_c$ was estimated to increase only by a factor of 1 to 3 at T_m for R = 0.5 and R = 2.0. The presence of lidocaine disorders the alignment of hydrophobic parts of phospholipid bilayers, thus preventing "gelling" at lower temperatures. As shown in Fig. 4, below T_m the bending elasticities vary with different slopes in a lidocaine-dose-dependent manner. In the P_β' phase, the $\varkappa_c$ value is found to be fluctuating from (114.4 to 151.0)k_BT and seems to be independent of R. This means that the lipid molecules in the gel phase are substantially better ordered than in the L_α phase, which leads to a significant stiffening of the lipid bilayers. At very low temperatures, the thermal undulations of bilayers are greatly suppressed and the difference caused by the presence of LA is negligible.

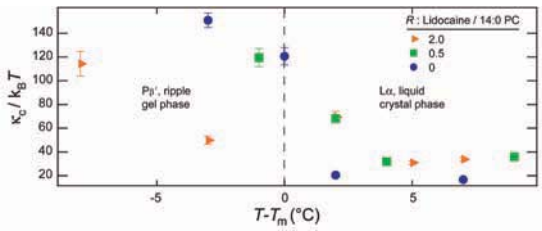

FIGURE 4: κ_c of a 14:0 PC bilayer with lidocaine concentration R = 0, 0.5 and 2.0 plotted against T - T_m.

In conclusion, using DSC, SANS and NSE we have examined the relationship of bending elasticity $\varkappa_c$ and hydrophobic thickness d of pure bilayers, $\varkappa_c = \beta K_A d^2$. Furthermore, we have investigated the influence of LA on the structure and dynamics of 14:0 PC bilayers. Our results confirmed that LA loosens the packing of the membrane constituent lipids and induces lateral membrane expansion. The intercalation of LA molecules provides more inter-molecular space for the lipid hydrophobic chains and results in decrease of the bilayer thickness, a decrease of the main transition temperature from L_α to P_β' phase, and a slight increase of the bending elasticity in L_α phase.

References

[1] Z. Yi, M. Nagao, and D.P. Bossev, J. of Phys: Condens. Matt., **21**, 155104 (2009).

[2] Z. Yi, M. Nagao, and D.P. Bossev, (submitted to Biophys. J.).

[3] G. Cevc, Biochemistry, **30**, 7186 (1991).

[4] A. Zilman, and R. Granek, Chem. Phys., **284**,195 (2002).

[5] W. Rawicz, K.C. Olbrich, et al., Biophys. J., **79** 328 (2000).

[6] H. Bermudez, et al., Langmuir, **20**, 540 (2004).

[7] I.C.P. Smith, M. Auger, H.C. Jarrell., Annals of the New York of Academy of Sci., **625**, 668 (1991).

Probing the Interface of Bedrock and Soil Using Scattered Neutrons

S.L. Brantley[1], L. Jin[1], G. Rother[2], D. Cole[2], A. Navarre-Sitchler[1,3]

Despite the importance of soil in sustaining human society, little is known about how low-porosity bedrock alters to high-porosity soil. This transformation includes physical, chemical and biological weathering processes that create the partly altered rock material—regolith—that blankets Earth's surface (Fig. 1). Regolith develops when bedrock, equilibrated chemically at depth in the crust, is exhumed at the surface and exposed to water, atmospheric gas, and biological organisms. Such exposure allows oxygen, water, acids and organic molecules to react with minerals in the rock. These reactions then drive dissolution, fracturing, and disaggregation, allowing penetration of more reactants into bedrock. As a result, the bedrock-regolith interface moves downward at rates of millimeters to nanometers per year. To understand rates of weathering, we need to understand the nature of the nano- to macro-scale pores, fractures, and rock fragments that comprise this interface (Fig. 1). To probe the advance of the weathering front, we collected rock fragments that span from unaltered bedrock up into the weathered zone in three localities, cut them into sections hundreds of micrometers thick, and scattered neutrons through the sections.

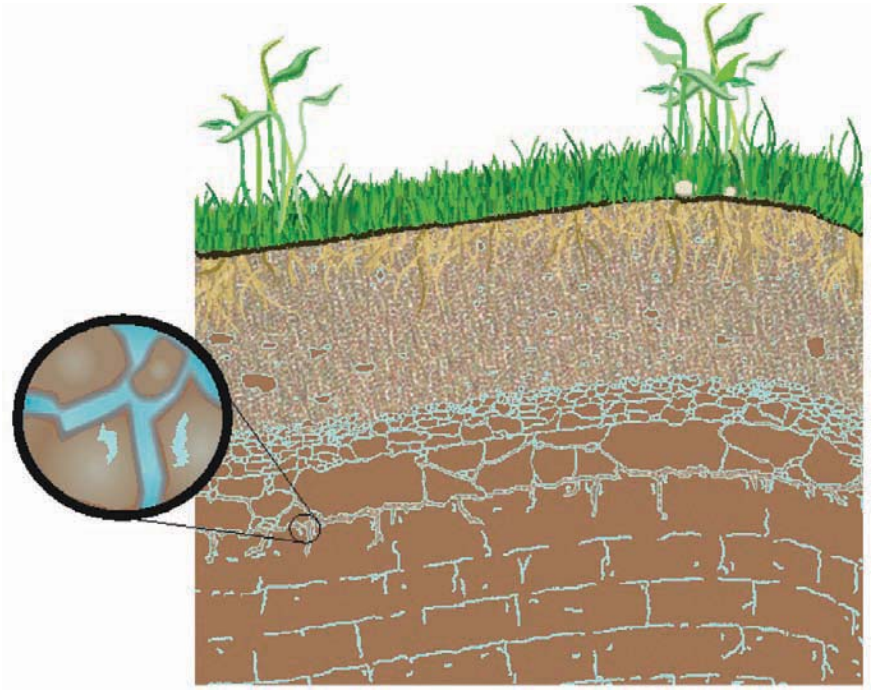

FIGURE 1: This schematic of the interface between bedrock and soil demonstrates the complexity of regolith—the altered material that blankets bedrock at the Earth's surface. Porosity in bedrock is manifested across the scale from large fractures to sub-nanometer-sized pores. We are probing the nanoporosity in unaltered bedrock and in rock fragments collected from within the weathered zone to understand the weathering interface.

Neutrons scatter at an interface if two phases differ in scattering length density. Therefore, geologists can use Small-Angle Neutron Scattering (SANS) and Ultra Small-Angle Neutron Scattering (USANS) to investigate rock features that range from 10 Å to 10 mm in size [1]. Although rocks contain grains of many different compositions—*i.e.*, minerals—neutron scattering in rocks is largely due to the interface between pores and mineral grains. Rocks are thus modeled as random two-phase systems. Furthermore, the different scattering lengths of H and D can be exploited in contrast-matching experiments by mixing a solution of H_2O and D_2O to match the scattering length density of the rock. The rock fragment is then submerged in the contrast-matching H_2O/D_2O mixture during a scattering experiment, and the resultant neutron scattering documents only the unconnected pores, *i.e.*, the pores that are not filled by H_2O/D_2O.

We investigated porosity and internal surface area developed at the bedrock-regolith interface in three of the most common rock types on Earth—granite, basalt, and shale. These silicate rocks differ in composition (from Na-Ca rich granite to Mg-Fe rich basalt to Al-rich shale) and grain size (from several tens of micrometers in diameter in granite to the micrometer-sized grains in basalt and shale). The most abundant mineral in the granite and basalt is Na,Ca-feldspar, whereas the shale is dominated by illite and chlorite clays. In the investigation we explored three types of samples. The granite was sampled across a fractured weathering front on bedrock in Puerto Rico [2]; the sample of basalt was the

[1]Penn State University, State College, PA 16802
[2]Oak Ridge National Laboratory, Oak Ridge, TN 37831
[3]University of Wyoming, Laramie, WY 82071

alteration rind on one rock specimen weathered in Costa Rica [3]; and the samples of shale were chips recovered from drilled bedrock and a soil profile in Pennsylvania [4].

Scattering patterns from granite and basalt are observed to be isotropic while scattering from shale is generally not (Fig. 2). Azimuthally symmetric scattering spectra in the igneous rocks are consistent with random two-phase systems. In contrast, for the shale, the anisotropic scattering pattern is consistent with cylindrical pores lying within the bedding planes where the shale's clay particles are aligned.

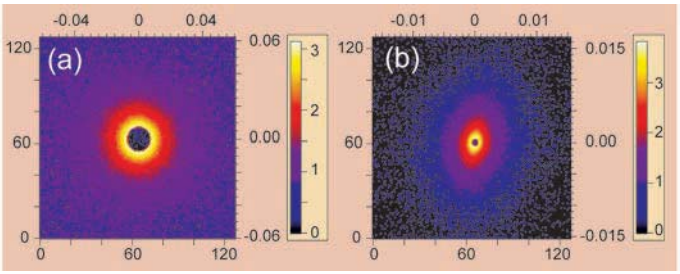

FIGURE 2: Plots of neutron intensity contours from SANS data for (a) granite and (b) shale, with brighter colors depicting higher count rates. These figures show that scattering is isotropic for the granite and anisotropic for the shale. This effect is attributed to roughly equal-sized non-aligned pores in the granite and roughly cylindrical and aligned pores in the shale. Scattering from basalt thin sections produces intensities that are similar to granite.

For unweathered granite and basalt, the porosity calculated from neutron scattering is ≈1.3 % and the surface area is (1 to 3) m^2/g. For both rocks, the porosity (Fig. 3) and surface area increase by a factor of about 10 across the reaction front where the feldspar dissolves. In the reaction zone on the basalt, the porosity that is connected increases from ≈ 0.02 % to 1 %. The thickness across the zone of feldspar dissolution is ≈ 40 cm in the granite and ≈ 2 mm in the basalt.

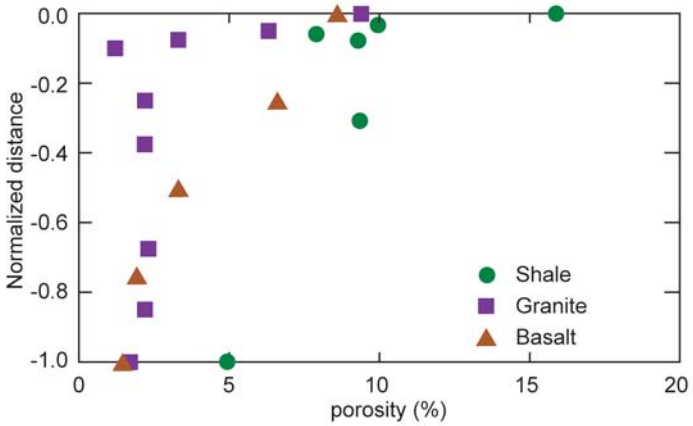

FIGURE 3: Calculated porosity based on SANS and USANS of samples from three rock types collected as a function of position within zones of intense weathering. Changes in porosity document the extent of weathering reactions such as dissolution of feldspars and clay mineral transformations. The position within the weathering interface has been normalized to 1 to enable all data to be plotted together (unaltered rock plots at -1, most altered rock plots at 0).

In contrast, the shale has about 4 % porosity when unweathered, and this increases to 15 % in rock fragments near the land surface (Fig. 3). D_2O/H_2O contrast matching shows that less than 5 % of these pores are connected in the bedrock but 50 % are connected in rock fragments in the soil. As weathering proceeds, the specific surface area increases five-fold, but in the most highly weathered samples near the land surface, the specific surface area decreases back toward parent rock values.

For all three rock types, the scattering intensity varies with the size of the scattering object and is consistent with power-law size distributions of scattering objects. In both the unweathered granite and basalt, the data for scattering intensity versus size of scattering object are consistent with two populations of objects, each described by a fractal dimension over a wide range in length scale. As weathering progresses, the intensity of scattering increases but the power-law size distributions do not change markedly. Eventually, however, weathering-induced fractures with relatively smooth surfaces form in the granite and change the power-law size distributions. In contrast, weathering of the basalt and shale are not characterized by fractures but are dominated by growth and coalescence of pores. Pores in the shale that are probed by SANS and USANS are inferred to be pores that are within and between clay particles. Trends in surface area and fractal dimensions inferred from scattering plots are attributed to coalescence of smaller pores into larger pores as well as smoothing of surfaces.

In this research, neutron scattering is revealing for the first time the nanoscale character of the interface where bedrock transforms to soil. This interface is not a Euclidean plane but is instead characterized by rock fragments and mineral grains that are bathed in porefluids as well as nanometer-sized pores that are largely unconnected in the unaltered bedrock but connected in weathered samples (Fig. 1). The weathering interface can be characterized by a fractal dimension, and these characteristics change as porosity increases during weathering. Conceptual and numerical models are now needed to describe how this developing surface controls the rates of weathering advance into bedrock.

References

[1]A.P. Radlinski, Ch. 14 in *Reviews in Mineralogy and Geochemistry*, vol. 63, Neutron Scattering in Earth Sciences, H.-R. Wenk, Ed., Mineralogical Society of America, c. 2006.

[2] H.L. Buss, P.B. Sak, S.M. Webb, and S.L. Brantley, Cosmochim. Acta **72**, 4488 (2008).

[3] A. Navarre-Sitchler, C.I. Steefel, L. Yang, and S.L. Brantley, J. Geophys. Res. **114**, F02016 (2009).

[4] L. Jin, R. Ravella, B. Ketchum, P. Heaney, S.L. Brantley, Geochim. Cosmochim. Acta, Submitted.

MACS -The Multi-Axis Crystal Spectrometer

J.A. Rodriguez-Rivera[1,3], D.M. Adler[3], P.C. Brand[3], C. Broholm[2,3], J.C. Cook[3], C. Brocker[3], R. Hammond[2], Z. Huang[3], P. Hundertmark[3], J. W. Lynn[3], N.C. Maliszewskyj[3], J. Moyer[3], J. Orndorff[2], D. Pierce[3], G. Scharfstein[2], S.A. Smee[2], R.Vilaseca[3] and Y. Zhao[2]

Through an optimized beam delivery system and a multi-channel detector, the new Multi-Axis-Crystal-Spectrometer (MACS) provides an unprecedented data rate for low energy inelastic neutron scattering at NIST. In a matter of hours MACS can acquire fixed energy transfer scattering data through a slice of momentum space. Such data determine the atomic scale structure of fluctuating condensed matter and can for example reveal the effective dimensionality and critical wave vector of new magnetic materials. Multiple slices can also be assembled to map a volume of *Q-E* space. Alternatively, for low dimensional systems, a high resolution *Q-E* slice can rapidly be obtained by pointing the dispersive directions towards the focusing monochromator and acquiring data versus E_i and $2q$. The unprecedented data rate on MACS offers a unique new capability for probing low energy dynamic correlations in condensed matter.

MACS presently enjoys a direct view of the NIST cold source through the NG-0/CTW beam tube resulting in 5×10^8 neutrons/cm^2/s on the sample at 5 meV (Fig. 1). During the shutdown to implement the NIST Expansion, MACS will move to BT-9 where a new dedicated cold source will be brighter and smaller, resulting in lower background with similar neutron flux. Down-stream from the source a rotary beam shutter offers three aperture options and is followed by a temporary cooled beryllium filter. This filter will eventually be replaced by a cryo-filter exchange system that will allow cooled beryllium and graphite filters to be positioned between the beam shutter and the monochromating system. To control energy resolution, two radial collimators are placed after the filters. These function as effective horizontal apertures at the source. The overall beam divergence is controlled by vertical and horizontal beam apertures immediately after the collimators.

The heart of MACS is the doubly focusing monochromator (DFM) which consists of an array of 357 PG crystals attached to thin aluminum blades which rotate and bend to focus horizontally and vertically [1,2]. The monochromator moves along the reactor beam to vary the incident energy while minimizing the corresponding motion of the large detector system. The Monochromatic Beam Transport system (MBT) employs m = 3.5 Ni-Ti supermirrors to guide the monochromatic beam to the sample. The MBT channel can be adjusted to accommodate the varying projected width of the monochromator and sample, and increases the flux on the sample by up to 25 % [3]. Immediately before the sample are vertical and horizontal slits to shape the incident beam and two LiF single crystal attenuators with transmission factors of 1/10 and 1/100. The sample table is designed for use with high field magnet systems with a mass of up to 400 kg.

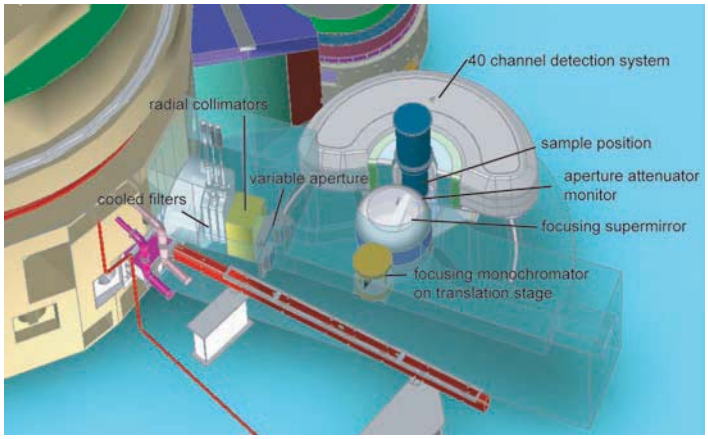

FIGURE 1: Overview of MACS. The monochromating system includes two radial collimators, three filters, a variable beam aperture and a doubly focusing monochromator for optimization of Q-resolution, energy resolution, and intensity.

The detection system consists of 20 identical channels surrounding the sample and separated by 8 degrees in the horizontal scattering plane. Defined by a cast structure formed from B_4C in polyurethane, each channel contains a vertically focusing double crystal analyzer (DXAL). Each of the two analyzer blades consists of 9 PG (002) crystals mounted to form the surface of a cylinder with a 50 cm radius. By rotating a single axis for each DXAL, the selected energy can be varied from 2.3 meV to 15 meV. There are two detectors in each of the twenty channels. The so-called diffraction detector, which views the sample directly, is placed behind the first analyzer blade. The spectroscopic detector views the second blade, detecting neutrons that satisfy the DXAL Bragg condition. Now in procurement, a semi-annular cryostat will

[1]University of Maryland, College Park, MD
[2]The Johns Hopkins University, Baltimore, MD 21218
[3]NIST Center for Neutron Research, National Institute of Standards and Technology, Gaithersburg, MD 20899

provide cooled Be, BeO, or PG post sample filters. Four different collimation options (60′, 90′, 36′, and open) will furthermore be available for each channel via Soller collimators.

Quasi-two-dimensional Magnetism in $TeVO_4$

On the very first day of scattering experiments on MACS, magnetic Bragg peaks corresponding to commensurate long range antiferromagnetic order were discovered in $TeVO_4$. Apart from its structure, which indicated the possibility of quasi-one-dimensional quantum magnetism, very little was previously known about $TeVO_4$ [4]. The rings of inelastic scattering in the (hk0) zone and lines along the [1,0,-2] direction detected on MACS (Fig. 2) however revealed that $TeVO_4$ is a quasi-two-dimensional magnet with weakly interacting ferromagnetic sheets perpendicular to (1,0,-2). The experiment illustrates that MACS is a powerful tool for an overview of spin correlations in novel materials.

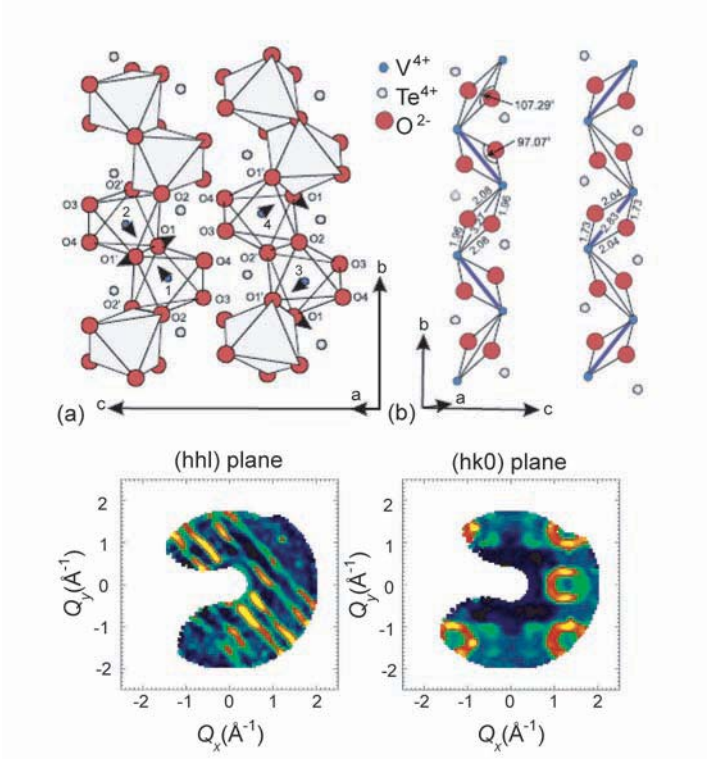

FIGURE 2: Upper figure: $TeVO_4$ structure from Ref. 4. Lower figure: Inelastic Q maps at energy transfer $\hbar\omega$ = 2.5 meV. With its twenty detection channels and high neutron flux MACS allows such data acquisition in hours rather than days.

Quantum Criticality in Spin ½ Chains

MACS can also provide interesting new details in well known materials. Figure 3 shows *Q-E* slices of inelastic scattering from the quasi-one-dimensional spin-½ chain CuPzN [5] at three temperatures. High *Q*-resolution is maintained by pointing the spin chains towards the focusing monchromator. Even at low temperatures, inelastic scattering in this crystalline material is detected through an area of *Q-E* space rather than along a sharp trajectory and this is evidence of a multi-particle neutron scattering process. The efficiency of MACS allows each of these data sets to be acquired with less than 3.5 h of neutron counting time so the full pattern of quantum critical scattering can be probed versus temperature.

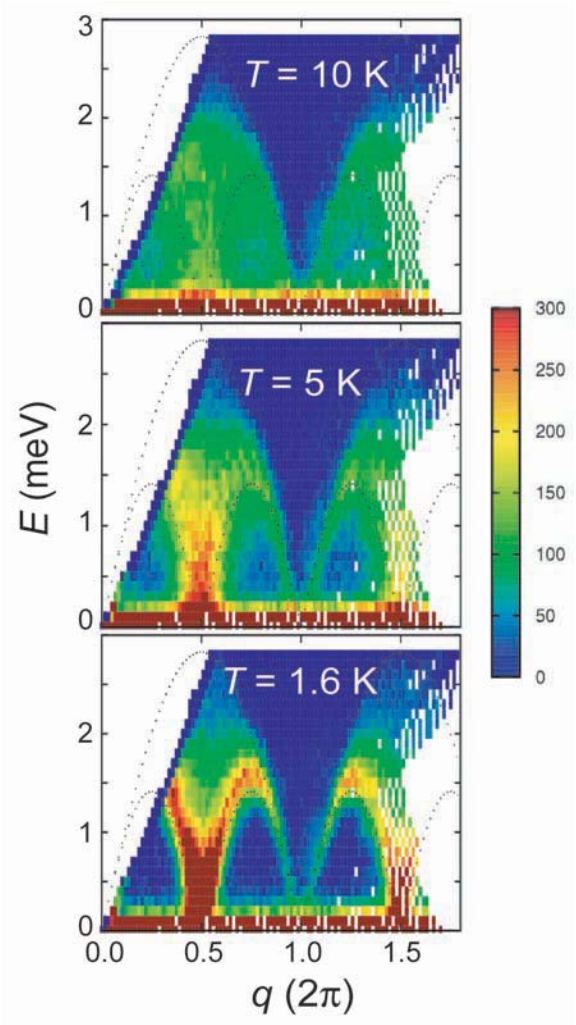

FIGURE 3: Maps of inelastic scattering from the quasi-one-dimensional spin- ½ chain CuPzN [5] at three temperatures. Each data set required just 3.5 h of neutron counting.

After a long period of planning, designing, engineering, manufacturing, and assembly, these two first successful experiments clearly indicate that an exciting new tool for condensed matter physics has been created in MACS.

References

[1] C. Broholm, Nucl. Instrum. Methods. Phys. Res., Sect. A **369**, 169 (1996).

[2] S.A. Smee, *et al.*, Nucl. Instrum. Methods. Phys. Res., Sect. A **446**, 513 (2001).

[3] J.A. Rodriguez, *et al.*, Meas. Sci. Technol. **19**, 034023 (2008).

[4] V. Gnezdilov, *et al.*, Phys. Rev. B. **78**, 184407 (2008).

[5] M. B. Stone, *et al.*, Phys. Rev. Lett. **91**, 037205 (2003).

Are There Benefits to Multiple Beam Neutron Spectrometers?

N.F. Berk[1,2] and C.F. Majkrzak[2]

A primary concern in elastic neutron scattering instrumental design is to put as many neutrons as possible on the sample in order to minimize statistical counting errors. On the other hand, the need for sufficient measurement resolution generally means "throwing away" valuable neutrons by tight collimation. It appears to be commonly believed that these competing requirements can be mutually accommodated by defining a number of well-collimated beams simultaneously incident on the sample at different angles, so that the scattering is measured simultaneously at different angles (*i.e.*, at different wavevectors for a common neutron wavelength). For the general case of non-specular scattering, however, this means that neutrons counted at a given angle may well "belong" to different incident beams, thus requiring a means of sorting out the overlapping reflections in each detector element. (For ease of presentation, we now will assume reflection geometry, in particular, and refer to the desired data as properly normalized reflectivities, *i.e.*, the ratios of reflected to incident intensities.)

Say there are N incident beams in the multiplex. Then the ambiguities of overlapping reflections can be mathematically resolved by repeating the measurements N times with different sets of incident intensities, leading to N differently weighted (or "modulated") sums, which can be unwound by solving the resulting N linear algebraic equations in the N unknown reflectivities, assuming that the $N \times N$ matrix (we call it B) representing the modulated beams is nonsingular. Since a computer can perform the inversion essentially instantaneously, the mathematical aspect of the scheme might appear to be trivial. And since there is an apparent statistical benefit to collecting a sum of sums at each angle, the multiple beam strategy would seem to produce the desired effect of combining high resolution with reduced counting error relative to performing N single-beam experiments with the same total number of incident neutrons.

But is this really so? While the summed data in each detector benefit from the usual law-of-large-number effect, retrieving the contributing reflectivities is not innocuous: because of the counting errors attached to the actual reflected intensities from each incident beam, every one of the N N-beam measurements introduces N unknown (*i.e.*, uncertain) reflectivities, so the algebraic problem actually is one of N equations for N^2 unknowns, which has no unique solution. More precisely, a multiplexed experiment consists of N measurements with N simultaneously incident beams. In the m^{th} measurement, a specific detector records the sum $S_m = \sum_{s=1}^{N} B_{ms} R_{ms}$ for $m = 1, 2, \ldots, N$, where B_{ms} is the intensity of the s^{th} incident beam in the m^{th} measurement and R_{ms} is the noisy reflectivity associated with beam B_{ms}. A nominal inversion of the vector $S = \{S_m\}$ is sensibly defined by following our nose and *defining* the solution as $\hat{R}(r) = (B^{-1}S)_r = \sum_{m,s=1}^{N} (B^{-1})_{rm} B_{ms} R_{ms}$, for $r = 1, 2, \ldots, N$. In the absence of shot noise, $R_{ms} = R_{0s}$, the "true" reflectivities, independent of m, and then $\hat{R}(r)_s = R_{0s}$.

To analyze propagation of shot noise, let us define random input (shot noise) and output (results) "errors", $\Delta_{ms} = R_{ms} - R_{0s}$ and $\hat{\Delta}(r)_s = \hat{R}(r)_s - R_{0s}$, respectively. For an ensemble of like measurements on the same rig, we can also define gross mean square input and output errors, σ_{in} and σ_{out}, respectively, by $\sigma^2 = \overline{\text{var}\,\Delta}$ for the appropriate Δ, where "var" means the ensemble statistical variance and where the overstrike is the average over input and output channels (*i.e.*, input beams and output results). Then, with the usual assumptions about random errors, one can show (with some work) that $\sigma_{out} = \sqrt{\Omega[B]}\,\sigma_{in}$, where the number

$$\Omega[B] = N^{-1} \sum_{m=1}^{N} (BB^{\dagger})_{mm} ((B^{\dagger}B)^{-1})_{mm} \qquad (1)$$

serves as a natural figure of merit for the given beam modulation strategy.

Clearly from (1), $\Omega[B] = 1$ for a diagonal matrix—corresponding to a set of single beam measurements—or for any constant scalar multiple of a unitary (*i.e.*, here, orthogonal) matrix. Since most real unitary matrices have mixtures of positive and negative elements, the latter case might seem inappropriate for intensity–defined modulations. However, by applying two distinct modulations, B_1 and B_2, and considering the differences of measured S_m for each case, the nominal inversion results are those appropriate for the effective modulation, $B_1 - B_2$, and such differential modulation strategies indeed can have matrix elements of either sign. Thus for diagonal and unitary strategies, $\sigma_{out} = \sigma_{in}$, and there is no shot noise error propagation benefit to multiplexing. But can we do better, in terms of error? Are there B for which $\Omega[B] < 1$, so that $\sigma_{out} < \sigma_{in}$? We have proven a theorem to the contrary, *viz.,* that $\Omega[B] \geq 1$, and that $\Omega[B] = 1$ occurs only for the aforementioned matrix classes. Thus, with regard to shot noise propagation, modulated multibeam measurements of reflectivities can do no better then single–beam measurements. Mathematical details and an expanded discussion of consequences and related issues are given in [1].

References

[1] N. F. Berk and C. F. Majkrzak, Langmuir **25**, 4145 (2009).

[1]University of Maryland, College Park, MD 20742
[2]NIST Center for Neutron Research, National Institute of Standards and Technology, Gaithersburg, MD 20899

High Resolution Stress Measurements Using In-house X-ray Diffraction

T. Gnäupel-Herold[1]

This work lays out an x-ray measurement procedure that is able to measure residual stresses with a demonstrated spatial resolution of 1 mm × 0.05 mm. Although surface limited, the technique is able to solve a variety of measurement problems previously reserved for synchrotron x-ray diffraction. The basic principle is the use of finely collimated x-ray beams with standard – and comparatively inexpensive – x-ray diffraction equipment in conjunction with a constant shape and orientation of the beam spot on the sample.

Many engineering problems require the knowledge of residual stress gradients on a length scale of 1 mm or less which happens to be a range very difficult to access nondestructively because of the strict requirements for spatial resolution (typically < 10^{-1} mm). Methods and experimental tools exist – such as neutron diffraction, high-energy synchrotron diffraction and conventional x-ray diffraction in connection with successive layer removal – but all carry with them the disadvantages of high cost and low availability, which effectively prevents a routine acquisition of the large amounts of data that are often necessary to understand the stress effects of a given manufacturing process. However, often overlooked is the fact that for stress problems where one or more stress tensor components are constant over larger length scales (several mm) the stress components of interest are "visible" on the free surface to which they are parallel. In this case the experimental requirements are much less stringent, since no beam penetration is necessary. It was demonstrated in [1] how these conditions can be realized in a simple way with high spatial resolution in only one dimension through the use of conventional x-ray tubes.

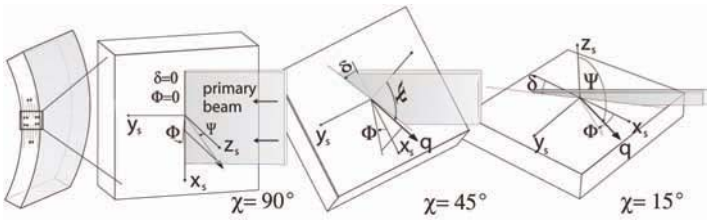

FIGURE 1: Left: Example (schematic) of a through-thickness stress field that can be determined with the technique described in this work. Right: Magnified measurement field with rotation δ of the beam spot as the specimen (left) is tilted and rotated.

Diffraction stress analysis is based on measuring lattice strains in different directions which requires the specimen surface to be tilted and rotated. It is immediately obvious that the x-ray beam spot on the surface changes its area and orientation, depending on the specimen orientation as shown in Fig. 1. If one poses the condition of a constant beam footprint on the sample surface, both in orientation and in size, such that the spatial resolution is constant in the direction where the stresses change, then the problem has a twofold solution: first, a tightly collimated x-ray beam giving the desired spatial resolution is required, and second, a path through orientation space must be chosen along which that resolution remains constant (Fig.1).

A prime application for this technique is found in automotive sheet metal forming where sheet thickness is ≤ 1 mm and residual stresses are a key factor for the magnitude of springback (the hard-to-predict shape change of a part after a forming or stamping operation). What appears to be an arcane side problem actually causes additional costs of over $100 million per year in the US alone for tooling development. It is thought that advances in materials modeling helped by residual stress data will reduce these costs. Figure 2 shows the evolution of stresses of a forward-backward- forward-backward bending sequence with a bending radius of 5.2 mm which is typical for a deep drawing operation using draw beads.

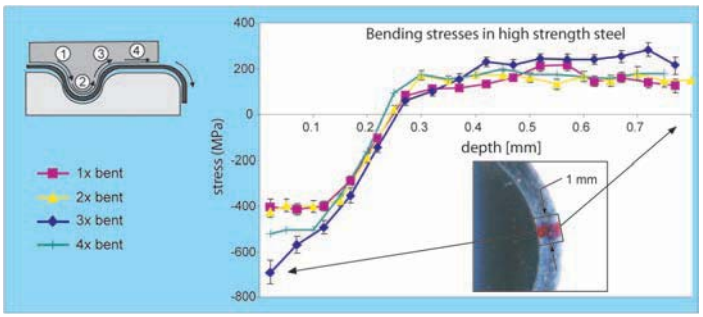

FIGURE 2: Stresses during a bending-backbending sequence on the high strength automotive steel HSLA50. Sheet thickness was 0.8 mm, the height of the measurement field was 1 mm (indicated) and the effective spatial resolution 0.05 mm.

Additionally, the sheet can be tested in under severe compressive strain (≈ 10 %) at the inside of the bent sheet. The level of detail shown in Fig. 2 has rarely been seen before, and important insights about the magnitude of the Bauschinger effect (essentially the non-symmetric distribution of tensile and compressive stresses) become possible.

References

[1] T. Gnäupel-Herold, J. Appl. Cryst. **42**, 19 (2009).

[1]University of Maryland, College Park MD 20742, and
NIST Center for Neutron Research, National Institute of Standards and Technology, Gaithersburg MD 20899

Neutron Tomography for Advanced Energy Storage

D.S. Hussey and D.L. Jacobson[1]

A common topic in energy systems is the mass transport of hydrogen or hydrogenous materials (such as water and electrolyte solutions). Neutron imaging has played a critical role in the understanding of water transport in proton exchange membrane fuel cells (PEMFCs). This is due to the high sensitivity of neutrons to hydrogen, while having relatively small sensitivity to many common materials of construction such as aluminum and carbon. In addition to the PEMFC research, the NIST neutron imaging facility is an ideal location for non-destructive, *in situ*, mass transport research in three dimensions for a variety of energy storage systems, including hydrogen storage beds and a variety of battery chemistries. The intense, highly collimated, thermal neutron beam has high penetration lengths through the metal hydrides and battery chemistries of interest, with sufficient sensitivity to measure changes in the hydrogen distribution. The high beam collimation and high resolution imaging detectors (spatial resolutions ranging from 250 μm to 10 μm) enable resolving features of interest. Two examples of neutron tomography demonstrate the use of the technique, hydrogen uptake in a prototype hydrogen storage bed and the electrolyte distribution in an AA alkaline cell during discharge.

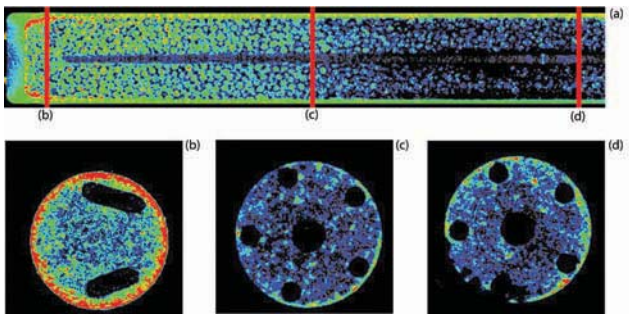

FIGURE 1: Slices through the 3-D image of a hydrogen storage bed after the addition of 12 standard liters of H_2. Red indicates higher concentration of hydrogen, black the absence of hydrogen. (a) Slice along the length of the storage bed, (b)-(d) perpendicular slices from the locations denoted in (a). Hydrogen uptake decreases with increasing temperature which is why hydrogen is seen to preferentially absorb along the outer circumference in (a), and accumulate towards the end of the storage bed.

The metal hydride bed described in detail in Ref. 1 consisted of a ≈ 90 % porous aluminum foam filled with $LaNi_{5-x}Sn_x$ powder. Hydrogen gas was introduced into and removed from the bed via a hollow stainless steel filter tube in the center. Two tomograms of the hydrogen storage bed were acquired. The first was after the bed was heated to 100 °C and evacuated to a pressure below 10^{-6} mbar. The second was after the bed was charged with about 12 standard liters of hydrogen. Comparing the empty bed tomogram to the bed charged with hydrogen, as shown in Fig. 1, reveals that the hydrogen preferentially absorbs along the outer circumference.

In alkaline primary cells, the neutron attenuation is dominated by the aqueous electrolyte. Tomograms (Fig. 2) of two AA alkaline cells were acquired before and after discharge to a cell potential of 0 V achieved by two different current draw conditions, 50 mA and 1 A. The distribution of the electrolyte after the cell potential has fallen to 0 V clearly depends on the discharge rate.

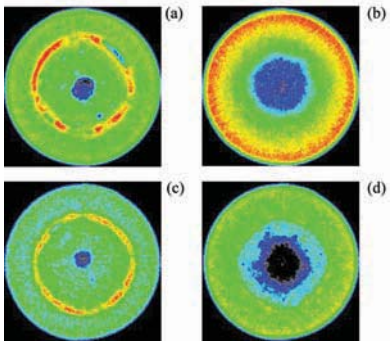

FIGURE 2: Comparison of the changes in an alkaline AA cell where black is low neutron attenuation, red is high neutron attenuation. (a) and (c) Fresh cell before discharge. (b) Discharged cell after operation at 50 mA for 52.5 h. (d) Discharged cell after operation at 1 A for about 70 min. The electrolyte has an initially uniform distribution (green) in the anode (interior) and in the cathode (exterior), and the rayon separator (red/yellow) is clearly visible in (a) and (c). At the end of life, the electrolyte concentration clearly depends on the discharge rate. At lower current, the electrolyte is concentrated at the outer circumference of the cathode. At higher current, there is a clear change in the electrolyte concentration at the separator boundary.

References

[1] R.C. Bowman, Jr., M. Prina, D.S. Barber, P. Bhandari, D. Crumb, A. S. Loc, G. Morgante, J.W. Reiter, and M.E. Schmelzel, Cryocoolers **12** 627 (2003).

[1]Physics Laboratory, National Institute of Standards and Technology, Gaithersburg, MD 20899

A Phase-Inversion Principle for Neutron Specular Reflectometry

N. F. Berk[1,2] and C. F. Majkrzak[1]

Neutron specular reflection probes the laterally averaged scattering length density (SLD) depth profile of thin films. Specular reflection can be cast formally as a one-dimensional scattering problem (along the *x*-axis, say), and the power of the technique ultimately stems from its resulting mathematical coherence, establishing a one-to-one correspondence between the reflection amplitude spectrum $r(k)$ and the SLD $\rho(x)$ that produces it (where *k* is the incident wavevector along *x*). Thus not only is the reflection amplitude unique to its SLD (the "direct" problem) but the SLD is unique to its specular reflection spectrum (the "inverse" problem) for perfect data. Moreover, practical "phase-inversion" methods have been developed for determining the reflection amplitude from one or more reflectivity measurements and then inverting it, providing a means for reliable interpretations of thin film reflection data. We argue that phase-inversion, indeed, sets the limits of informative interpretation.

In more formal terms, the veridical ("true") ρ induces the veridical (or ideal) *r*, according to a prescription that can be operationally denoted by $r = r_{op}\rho$. In a feasible experiment we measure $\hat{r}$, a degraded image of *r*, which, over a large class of ρ, can be represented by $\hat{r} = D_{op}r$, where D_{op}, the degradation operator, encodes the deleterious effects of the measurement and phase reconstruction process, including counting (shot) noise, N_{op}, and data truncation, T_{op}^{K}, at a finite value of $k = K$; if these are the only degradations, then $D_{op} = T_{op}^{K}N_{op}$. For this class, there is an exact solution of the inverse reflection problem, represented by r_{op}^{-1}, such that $r_{op}^{-1}r = \rho$ retrieves the veridical SLD from ideal data. If we apply r_{op}^{-1} to the measured $\hat{r}$, instead, we obtain $r_{op}^{-1}\hat{r} = \hat{\rho}$, a degraded image of ρ. If $\hat{r} \approx r$ in some quantitative sense, then it seems reasonable to expect $\hat{\rho} \approx \rho$ in a similar sense. For example, one such sense is that reverting $\hat{\rho}$ to $\hat{\hat{r}}$, by defining $r_{op}\hat{\rho} = \hat{\hat{r}}$, will produce $\hat{\hat{r}} \approx r$ over the measured *k*-range. In fact, with some important refinements of these ideas, we are led to propose [1] the

Phase-inversion principle: For given $\rho(x) - r(k)$ pair, the $\hat{\rho}(x)$ defined by phase-inversion, $r \rightarrow T_{op}^{L}r_{op}^{-1}D_{op}r_{op}\rho = \hat{\rho}$, is the best estimate of veridical ρ over any set of measurements on the same setup (*i.e.,* for given D_{op}).

Here T_{op}^{L} denotes truncation over the physical support of the film of thickness *L*. Several factors contribute to the substance of the principle. Perhaps the most novel, compared to other methods of data analysis, is the distinction between "in-film" noise, the effect of propagated shot noise on $\hat{\rho}$ over the thickness *L,* and "out-of-film" noise, *viz*., the propagated shot noise in $D_{op}r$ that lands outside the support of ρ and thus is disposable. In effect $T_{op}^{L}r_{op}^{-1}$ acts as a low pass filter, so that the reversion, $\hat{\hat{r}} = T_{op}^{L}r_{op}^{-1}\hat{r}$, is smoother than $\hat{r}$. Another important ingredient of the principle is that data truncation, the component $T_{op}^{K}r$, of $D_{op}r$, represents irretrievably lost information – if one holds to the subsidiary principle that only the data at hand determine verifiable knowledge of ρ. *A priori* knowledge (*i.e*., additional assumptions about ρ) can not inform us about unmeasured data, *viz*., "data" beyond the cutoff *K*.

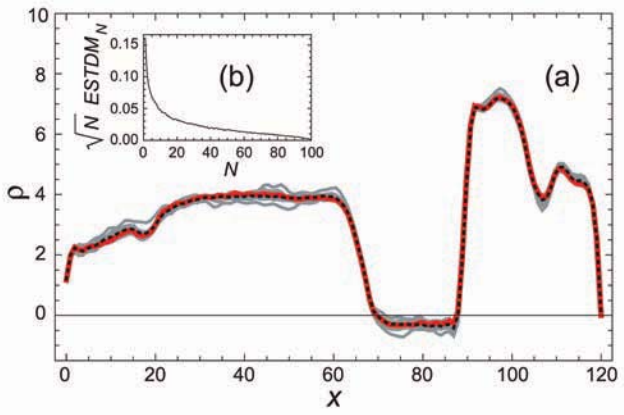

FIGURE 1: (a) Efficient averaging over *N* results $\{\hat{\rho}_m\}_N$, for *N=1,..,100,* for a model film [1]; dotted line, *N* = 100; red line, *N* = 10. (b) Inset: $ESTDM_N$ is the point-wise estimated standard deviation averaged over *x*.

The statistical analysis of phase-inversion is discussed extensively in [1]. Among the more surprising findings is the efficiency of averaging over a set of inversions $\{\hat{\rho}_m\}_N$ for *N* measurements on the same setup. The average $\langle\hat{\rho}\rangle_N$ converges exponentially faster to the true average ($N \rightarrow \infty$) than the expected $1/\sqrt{N}$ rate. Even $\langle\hat{\rho}\rangle_{10}$ is remarkably close to the large-*N* average, as shown in Fig. 1. This accelerated convergence is, in part, a benefit of disposable out-of-film noise and further illuminates the statistical underpinnings of the phase-inversion principle.

References

[1] N. F. Berk and C. F. Majkrzak, Langmuir **25**, 4132 (2009).

[1]University of Maryland, College Park, MD 20742
[2]NIST Center for Neutron Research, National Institute of Standards and Technology, Gaithersburg, MD 20899

Neutron Source Operations

The NIST reactor (NBSR) operated for 244 full power (20 MW) days or 99 % of the scheduled time during FY2009. A typical operating year consists of seven cycles. A cycle has 38 d of continuous full power operation followed by 11 d of shutdown for maintenance, refueling, and startup preparations. This outstanding record of safe and reliable performance of the reactor and cold source lies at the foundation of the success of the neutron scattering, nuclear methods, and neutron physics programs. The Nuclear Regulatory Commission issued a 20 year license renewal on July 2, which permits operation of the reactor to 2029. Some of the activities of the Reactor Operations and Engineering Group are outlined below.

FIGURE 1: Operations Electrical Engineer Dennis Brady inspects the status indicator on a newly installed Motor Control Center.

Facility Improvements

- **Shim Arm Replacement:** The NIST Reactor is controlled by shim arms, which consist of neutron absorbing cadmium, lodged between two supporting aluminum tubular structures. The cadmium gets depleted ("burned") in the process of controlling the reactor, which requires the periodic replacement of the shim arms. This complex project was completed without incident early in the fiscal year. An improved drive mechanism has been designed by the group and a contract has been signed to provide replacement shim arms for the duration of the reactor license.

FIGURE 2: Cask is aligned in a spent fuel transfer operation.

- **Leak Detector Panel:** The reactor's heavy water coolant/moderator is an expensive resource and an extensive detection system monitors for leakage of any water. The original analog panel has been replaced with a computer controlled system which allows the control room operators to more quickly assess the duration and location of potential leakage.
- **Electric Panel Upgrade:** All motor control centers associated with the reactor systems have now been replaced with state of the art units. The new units allow the NCNR increased reliability and several special features including relaying the status of the motor control centers directly to the reactor control room.

New Staff

The Reactor Operations and Engineering Group hired several new staff members this year. One senior reactor operator candidate, Andrew Blazek, is scheduled to be licensed by the summer of 2010. Two experienced nuclear engineers, Daniel Hughes and Sean O'Kelly were also brought on board in 2009. Our group is very pleased to welcome these able new staff members to the NCNR.

FIGURE 3: New Reactor Operations and Engineering staff members Andrew Blazek, senior reactor operator candidate, Dan Hughes, nuclear engineer, and Sean O'Kelly, nuclear engineer.

Facility Development

The NCNR is entering a period of unprecedented activity of facility expansion and upgrades that will deliver long-term gains and satisfy the changing needs of the user community. During the past year construction of the guide hall extension and support buildings has begun and NCNR engineering efforts have focused on integrating the new guide hall with the existing experiment hall and the design, construction, and installation planning for the suite of new guides, new instruments, and a re-optimized instrument layout.

NCNR Expansion

The new guide array (shown schematically in Fig. 1) will view the current liquid hydrogen cold source through the beam port currently occupied by the MACS spectrometer. All the new guides utilize the latest high-reflectivity supermirror coatings and include a curved section at the source end followed by a straight section. The curved sections permit five new beamlines to be extracted from the restricted angle of the beam port and have the added advantage to reduce or eliminate the need for crystal filters upstream typically required in straight guides to remove unwanted short wavelength neutrons and gamma rays.

Installation of the full guide system involves precision alignment of over 350 individual glass guide modules including many with quasi-elliptical cross-sections. To expedite this complex process, facility engineers and technicians have been working on dedicated procedures to utilize state-of-the-art laser tracking alignment systems. Adopting this new technology offers highly accurate alignment of individual guide components in three dimensions during the installation process while promising benefits in future for maintenance and operation. In particular, the laser tracker system allows for easy replacement of guide components and re-verification of their positions in case of ground settlement, and allows remote alignment in areas of potentially elevated radiation.

Design work has been initiated on vSANS – the first of five new instruments in the expansion program. The vSANS instrument will be a highly versatile and unique instrument offering an extended q-range ($2.0 \times 10^{-4} < q < 0.7$ Å^{-1}) thus bridging the gap between conventional SANS and uSANS instruments. The design includes both multiple converging pinhole and multiple converging slit geometries and is optimized to take advantage of the present large neutron guide at NG-6, thus offering appropriate intensity for the measurements.

Progress with existing instrumentation, software, and sample environment equipment at the facility continues to be made in parallel with the expansion activities and recent developments are described below.

Instrument Development

The Multi-Axis Crystal Spectrometer (MACS) is the most recent addition to the suite of advanced cold-neutron instruments provided by NCNR. During the fall of 2008 the MACS

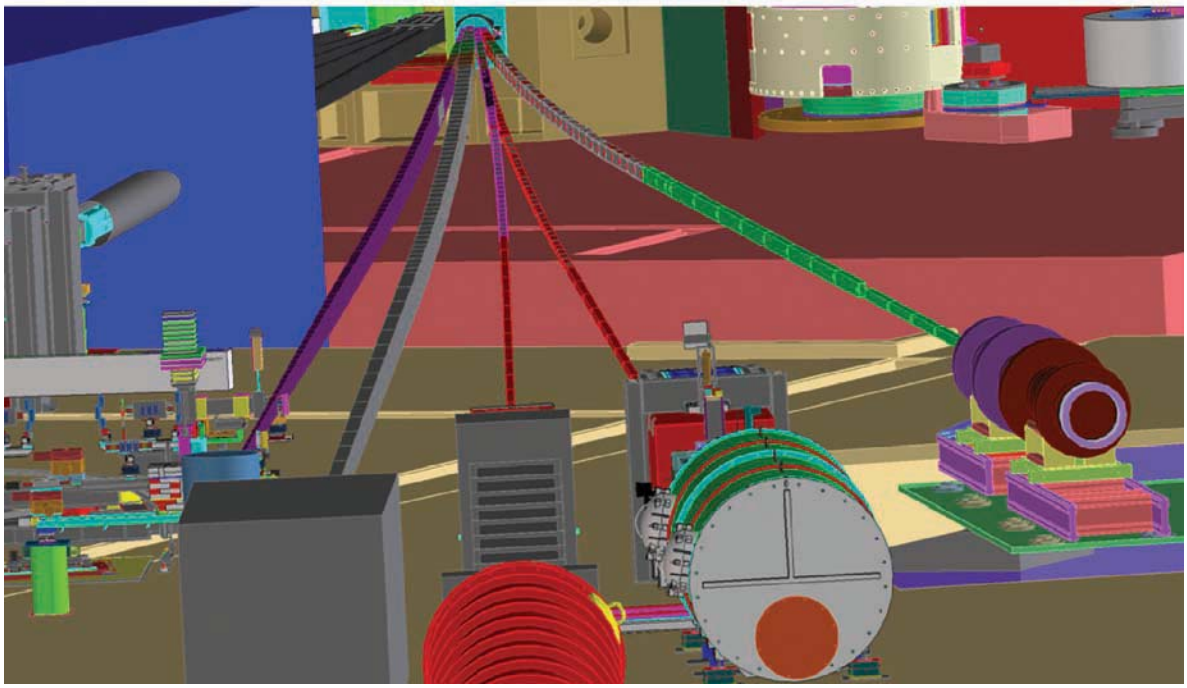

FIGURE 1: Design drawing showing the 5-guide array in the new guide hall viewing upstream to the cold neutron beam port NG-0. The instruments shown are (r-l): NSE; 10 m & 30 m SANS; Physics Station; MAGIK reflectometer.

analyzer was installed at NG-0 and this year has seen the landmark first scattered neutrons to be recorded by the novel detection system comprising twenty independent monochromatic channels. The performance of MACS, in particular the complex analyzer system, is presently being evaluated and optimized as the instrument enters a period of rigorous commissioning activities. Even at this early stage, the unique capabilities of MACS in the area of cold-neutron spectroscopy can be seen (see pp. 48–49) and the new spectrometer has been shown to record publication quality data and outperform traditional triple axis instruments on previously measured specimens. As part of the NCNR expansion program MACS will relocate within the confinement building to BT-9 and view a dedicated new cold source – offering still further increases in cold neutron flux albeit across a smaller beam size. Design and fabrication of the new cold source has now been completed along with successful proof testing of all components.

Progress has also been made with the TISANE project, funded through the Center for High Resolution Neutron Scattering (CHRNS), to develop the new experimental Fourier method of Time dependent SANS Experiments. The technique provides for microsecond time resolution without a major sacrifice in intensity by making use of very large frame overlap and complements recent progress with time resolved small angle x-ray scattering. The fast chopper, pre-requisite for the TISANE technique, was installed on the NG-7 SANS instrument along with timing and control electronics for the detector system. This equipment will permit dynamic studies of phenomena occurring on time scales of 50 μs to 150 ms by time-resolved stroboscopic SANS. Commissioning measurements on a range of optically and magnetically excited systems will begin in late Summer 2009.

Instrument Control and Software Development

This year the NCNR continued a program of instrumentation upgrades intended to bring all NCNR instruments in compliance with facility standards and to prepare them for migration to the Instrument Control Environment (ICE) software system. The ICE software package, currently operating on the triple axis spectrometers BT-7 and MACS, has now been extended and is under release on the SANS instruments NG-3 and NG-7. As part of the migration, both SANS instruments have been recipients of motion controls and histogramming upgrades. Tangible improvements over the legacy VMS controls and software include faster collection times, reduced overhead, real-time detector overcount protection, and greatly increased functionality for data acquisition through scripting.

Given the remarkable reliability record of the NIST reactor and cold source, efforts are continually being made to improve instrument reliability. To this end, the facility infrastructure monitoring system has been upgraded to use readily deployable remote sensing modules so that more monitoring points, for example guide vacuums, chilled water temperature and pressure, and other, instrument-specific quantities, can be accommodated. The new system has enhanced facilities allowing condition monitoring of equipment and fault notification. Using this information in targeted maintenance activities and for rapid fault diagnosis helps minimize instrument down time.

Data Analysis Software Development

DAVE is the NCNR multi-platform software suite, tailored particularly for non-expert users, designed to rapidly and easily view and interpret experimental data. Following the release last year of DAVE 2, designed around the IDL iTools framework, efforts this year have focused on consolidating the application core and taking advantage of the new framework. For example, improved interactions between program modules now enable sophisticated visualizations to be generated with a single mouse click and numerous data manipulation operations are now implemented as self-contained components that are globally available and share a standard interface.

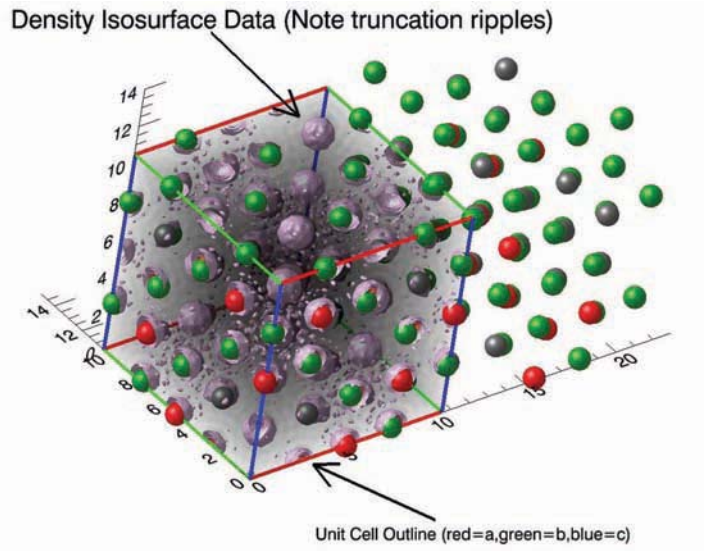

FIGURE 2: DAVE visualization of the Fourier density map (F observed) and corresponding atomic positions for a simple spinel structure.

The development of DAVE continues to be responsive to user requests and new modules are added regularly. A recent example is 3DenPro (see Figure 2) which uses the built-in volume visualization capabilities to display unit cell information computed from crystallography experiments; the application module displays the atoms and bonds, unit cell outlines, and Fourier densities.

Sample Environment

NCNR personnel support a diverse range of ancillary sample environment equipment and promote development activity in a number of areas. In response to user demand, a bottom-loading close-cycle refrigerator (CCR) operating over an extended temperature range from 25 K and up to 900 K has been commissioned for general use across the facility. The CCR also boasts a rapid cool down from ambient to base operating temperature allowing for more efficient use of beam time. New high-pressure cells have also been acquired in response to significant growth in experimental programs utilizing the recently commissioned 1.36 MPa helium gas intensifier system. The aluminum and stainless steel cells reliably and routinely operate down to low temperature and up to pressures of 0.65 MPa and 1.00 MPa, respectively.

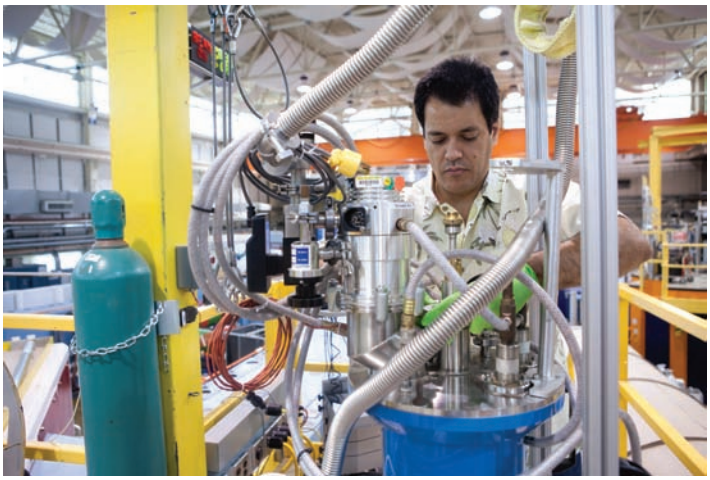

FIGURE 3: NCNR's Juscelino Leão prepares a complicated sample environment installation for a DCS experiment.

New equipment introduced this year includes a low-temperature 10-postion sample changer designed for the SANS instruments and capable of operating down to approximately 200 K. Options for low-temperature SANS experiments have been enhanced further with the outfitting of a liquid helium cryostat dedicated for specific use on the SANS instruments.

In late 2009, the facility will take delivery of a new dilution refrigerator and cryostat assembly operating down to 20 mK. The new refrigerator will increase both the capacity and also reliability of low-temperature operations and is primarily for use supporting user programs on the triple-axis and spin echo instruments. Delivery of a new rheometer for the SANS user program is also expected and will update and expand significantly the capability for rheology using this technique.

A major focus of development activity continues on ^{3}He neutron spin filters (NSFs). This program, run in collaboration with the Physics Laboratory at NIST, has provided ^{3}He NSFs that are now in routine use for polarized beam experiments on the thermal neutron triple-axis spectrometer BT-7 in addition to small-angle neutron scattering instruments and reflectometers. Neutron spectrometers present some challenging spatial constraints for the spin filter setup and there is a constant drive towards miniaturization of the apparatus. This year the team has successfully produced a reduced length "Magic Box" for use on BT-7 and NG-3. This device is the magnetostatic cavity that provides a homogenous magnetic field over the ^{3}He cell while providing shielding from stray fields thus promoting longer polarization ^{3}He lifetimes. By introducing compensation sections tuned to limit end effects of the box the new devices meet a length constraint on key NCNR instruments of 29 cm compared with 37 cm of previous designs while retaining the large, 10 x 15 cm^2, cross-sections required by the cells.

A further challenge being addressed is to develop a compact system for wide-angle polarization analysis for use on MACS: here the polarizer, analyzer and any spin flippers must fit within a region surrounding the sample of only 40 cm diameter while also accommodating a typical cryostat tail of 13 cm diameter. An unshielded solenoid wound with aluminum wire, dimensioned for the MACS sample stage, has now been produced to provide the uniform field for the ^{3}He cells and serve as the guide field for the polarized neutrons. A miniature, radio-frequency shielded solenoid has also been constructed that enables efficient inversion of the ^{3}He polarization in the polarizer without affecting the analyzer. To cover the full detector angular range on MACS, two fused quartz analyzer cells, on opposite sides relative to the incident neutron beam will be used to cover a total angular range of 240 °. The analyzer cells, as well as the simple polarizer cell, are polarized off-line using the well-established spin-exchange optical pumping (SEOP) method prior to installation on the beamline. Offline tests of this novel apparatus have shown promising results and polarized beam experiments on MACS are keenly anticipated as part of the instrument commissioning program.

User Laboratories

The program to improve and renovate the NCNR laboratories used by both visitors and staff continues. This year saw the acquisition of a thermal gravimetric analyzer and refurbishment of laboratory space in support primarily of research programs on hydrogen storage materials. The TGA was purchased through a DOE grant awarded to the hydrogen storage group at the NCNR.

Serving the Science and Technology Community

The mission of the NIST Center for Neutron Research is to assure the availability of neutron measurement capabilities to meet the needs of U.S. researchers from industry, academia and from other U.S. government agencies. To carry out this mission, the NCNR uses several different mechanisms to work with participants from outside NIST, including a competitive proposal process, instrument partnerships, and collaborative research with NIST.

Proposal System

Most of the time on NCNR instruments is made available through a competitive, peer-review proposal process. The NCNR issues calls for proposals approximately twice a year. Proposals are reviewed at several different levels. First, expert external referees evaluate each proposal on merit and provide us with written comments and ratings. This is a very thorough process where several different referees review each proposal. Second, the proposals are evaluated on technical feasibility and safety by NCNR staff. Third, we convene our Beam Time Allocation Committee (BTAC) to assess the reviews and to allocate the available instrument time. Using the results of the external peer review and their own judgment, the BTAC makes recommendations to the NCNR Director on the amount of beam time to allocate to each approved experiment. Approved experiments are scheduled by NCNR staff members in consultation with the experimenters.

The current BTAC members are:

- Andrew Allen (NIST Ceramics Division)
- Collin Broholm (Johns Hopkins University)
- Ken Chen (Sandia National Laboratories)
- Kalina Hristova (Johns Hopkins University)
- Young Lee (Massachusetts Institute of Technology)
- Raul Lobo (University of Delaware)
- Robert Leheny (Johns Hopkins University)
- Lee Magid (University of Tennessee, Knoxville)
- Janna Maranas (The Pennsylvania State University)
- Alan Nakatani (Rohm and Haas Company)
- Stephan Rosenkranz (Argonne National Laboratory)
- Dawn Sumner (University of California Davis)
- Michael Toney (Stanford Synchrotron Radiation Laboratory)
- Lynn Walker (Carnegie-Mellon University)

Partnerships

The NCNR may form partnerships with other institutions to fund the development and operation of selected instruments. These partnerships, or "Participating Research Teams", may have access to as much as 75 % of the available beam time on the instrument depending on the share of total costs born by the team. A minimum of 25 % of the available beam time is always made available through the NCNR proposal program to all users. Partnerships are negotiated for a fixed period (usually three years) and may be renewed if there is mutual interest and a continued need. These partnerships have proven to be an important and effective way to expand the research community's access to NCNR capabilities and have been very successful in developing new instruments.

Collaboration with NIST

Some time on all instruments is available to NIST staff in support of our mission. This time is used to work on NIST research needs, instrument development, and promoting the widespread use of neutron measurements in important research areas, particularly by new users. As a result of these objectives, a significant fraction of the time available to NIST staff is used collaboratively by external users, who often take the lead in the research. Access through such collaborations is managed through written beam time requests. In contrast to proposals, beam time requests are reviewed and approved internally by NCNR staff. We encourage users interested in exploring collaborative research opportunities to contact an appropriate NCNR staff member.

Research Participation at the NCNR

The NCNR continued its strong record of serving the U.S. research community this year. Over the 2009 fiscal year, 2290 research participants benefited from use of the NCNR. (Research participants include users who come to the NCNR to use the facility as well as active collaborators, including co-proposers of approved experiments, and co-authors of publications resulting from work performed at the NCNR.) Research participants represented 220 external institutions, including 142 U.S. universities, 32 national laboratories, and 46 U.S. industries. The NCNR is a national facility, with participants from 41 states, DC, and Puerto Rico.

FIGURE 1: Research participants at the NCNR 1987- 2009

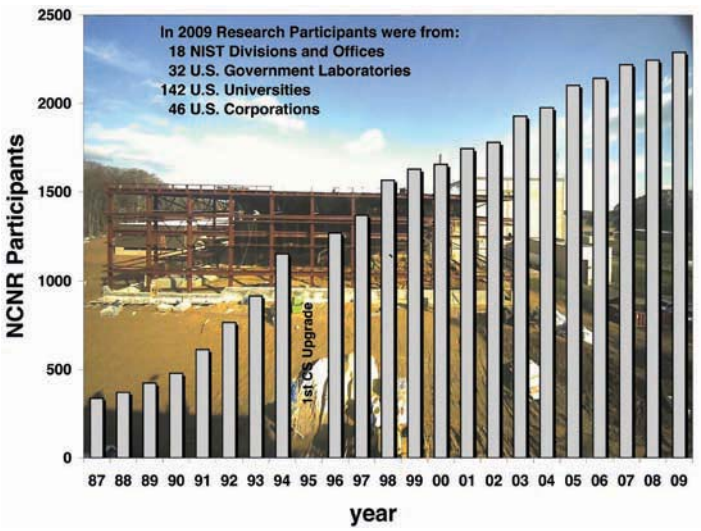

2009 NCNR Proposal Program

Two calls in the past year resulted in the submission of 680 proposals, a record number, of which 418 were approved and received beam time.

The oversubscription, *i.e.,* the ratio of days requested on all proposals to the days available, was 2.1 on the average, but as high as 3.3 for specific instruments in one call. Proposal demand has grown constantly since the NCNR first began accepting proposals in 1991, and has doubled in the past seven years. The following table shows the data for several instrument classes.

Instrument class	Proposals	Days requested	Days allocated
SANS and USANS	261	977	466
Reflectometers	107	814	418
Spectrometers	270	1831	820
Diffraction	21	78	58
Imaging	31	147	68
Total	698	3847	1830

User Group Plans Third Election

The NCNR Users Group (NUG) provides an independent forum for all facility users to raise issues to NCNR management, working through its executive officers to carry out this function. In early 2007, it conducted a comprehensive online survey of user satisfaction and concerns, eliciting 260 responses with many useful comments on areas such as instrument quality and problems, sample environment, data analysis software, and user laboratories. The survey input is being used as a guide to make some significant improvements in user support. In December 2009, the NUG will conduct its third online election of officers. The current NUG Executive Committee members are Stephan Rosenkranz (Argonne National Laboratory, chair), Mark Dadmun (University of Tennessee, Knoxville, vice-chair), Kalina Hristova (Johns Hopkins University), Moon Jeong Park (University of California, Berkeley), Tonya Kuhl (University of California, Davis), Robert Leheny (Johns Hopkins University), and Lynn Walker (Carnegie-Mellon University).

Panel of Assessment

The major organizational components of NIST are evaluated periodically for quality and effectiveness by the National Research Council (NRC), the principal operating agency of both the National Academy of Sciences and the National Academy of Engineering. A panel appointed by the NRC reported on the NIST Center of Neutron Research in January 2008 and again in January 2009. The findings from a 2008 assessment are summarized in a document that may be viewed online at http://www.nap.edu/catalog.php?record_id=12495. The panel members included Tonya Kuhl of the University of California, Davis (chair), Frank Bates, University of Minnesota, Stuart Bush, Rohm and Haas Corporation, Donald Engelmann, Yale University, Christopher Gould, North Carolina State University, Alexander Grosberg, New York University, Sunil Sinha, University of California, San Diego, and Barbara Wyslouzil, the Ohio State University.

The Center for High Resolution Neutron Scattering (CHRNS)

The CHRNS is a national user facility that is jointly funded by the National Science Foundation and the NCNR. Its primary goal is to maximize access to state-of-the-art neutron scattering instrumentation for the research community. It operates six neutron spectrometers and diffractometers at the NCNR, enabling users from around the nation and the world to observe dynamical phenomena involving energies from ≈ 30 neV to ≈ 100 meV, and to obtain structural information on length scales from 1 nm to ≈ 10 μm. A more detailed account of CHRNS activities may be found on pp. 60–61 of this report.

Partnerships for Specific Instruments

NG-7 SANS Consortium

A consortium that includes NIST, the Industrial Partnership for Research in Interfacial and Materials Engineering (IPRIME) led by the University of Minnesota, and the ExxonMobil Research and Engineering Company, operates, maintains, and conducts research at the NG-7 30 m SANS instrument. The consortium uses 65 % of the beam time on this instrument, with the remaining 35 % allocated to the general scientific community through the NCNR's proposal system. Consortium members conduct independent research programs primarily in the area of large-scale structure in soft matter. For example, ExxonMobil has used this instrument to deepen their understanding of the underlying nature of ExxonMobil's products and processes, especially in the fields of polymers, complex fluids, and petroleum mixtures.

NIST / General Motors – Neutron Imaging

An ongoing partnership between General Motors and NIST has resulted in an exciting collaboration employing neutron imaging to visualize the operation of fuel cells for automotive vehicle applications. Neutron imaging is an ideal method for observing the movement and behavior of water in proton exchange membrane fuel cells, a key to developing hydrogen-powered cars that employ such cells instead of internal combustion engines as their central power source. In the past year, the spatial resolution of the technique has been improved yet again to a value approaching 10 m. Experiments were performed to understand and optimize fuel cell performance at temperatures approaching -40 °C, a necessary advance towards development of robust fuel cell vehicles.

Interagency Collaborations

The Center for Food Safety and Applied Nutrition, U.S. Food and Drug Administration (FDA), directs and maintains a facility at the NCNR that provides agency-wide analytical support for food safety and food defense programs. Neutron activation (instrumental, neutron-capture prompt-gamma, and radiochemical), x-ray fluorescence spectrometry, and low-level gamma-ray detection techniques provide diverse multi-element and radiological information about foods and related materials. Ongoing work includes studies of cryogenic homogenization of foods, *improved detection capabilities for toxic and nutritional elements in foods*, and rapid screening of food products for dangerous levels of cadmium, lead, and mercury in beverages and residual bromine in baked goods. Recent studies include the preparation and characterization of a swordfish in-house reference material.

The Smithsonian Institution's Nuclear Laboratory for Archeological Research is part of the Anthropology Department at the National Museum of Natural History. It has had a productive 32 year partnership with the NCNR, during which time it has chemically analyzed over 39,000 archaeological artifacts by Instrumental Neutron Activation Analysis (INAA), drawing extensively on the collections of the Smithsonian, as well as on those of many other institutions in this country and abroad. Such chemical analyses provide a means of linking these diverse collections together in order to study continuity and change involved in the production of ceramic and other artifacts.

The Center for High Resolution Neutron Scattering (CHRNS)

CHRNS is a national user facility that is jointly funded by the National Science Foundation, through its Division of Materials Research (grant number DMR-0454672), and by the NCNR. The primary purpose of this partnership is to maximize access to state-of-the-art neutron scattering instrumentation for the research community through the NCNR's proposal system. Proposals to use the CHRNS facilities are critically reviewed on the basis of scientific merit and/or technological importance.

The core mission of CHRNS is fourfold: (i) to develop and operate neutron scattering instrumentation, with broad application in materials research, for use by the general scientific community; (ii) to promote the effective use of the CHRNS instruments by having an identifiable staff whose primary function is to assist users; (iii) to conduct research that advances the capabilities and utilization of CHRNS facilities; and (iv) to contribute to the development of human resources through educational and outreach efforts.

Scattering Instruments and Research

CHRNS currently operates six instruments: the 30-meter Small Angle Neutron Scattering (SANS) instrument at NG-3, the Ultra-Small Angle Neutron Scattering (USANS) instrument at BT-5, the Spin-Polarized Inelastic Neutron Scattering (SPINS) spectrometer at NG-5, the Disk Chopper Spectrometer (DCS) at NG-4, the High Flux Backscattering Spectrometer (HFBS) at NG-2, and the Neutron Spin-Echo (NSE) spectrometer at NG-5.

The small angle scattering instruments supported by CHRNS provide structural information over length scales from ≈ 1 nm to ≈ 10 μm. The spectrometers collectively yield dynamical information over time scales from ≈ 3×10^{-14} s to ≈ 10^{-7} s (energy scales from ≈ 100 meV to ≈ 30 neV). These wide ranges of accessible distances and times support a very diverse scientific program, allowing researchers in materials science, chemistry, biology, and condensed matter physics to investigate materials such as polymers, metals, ceramics, magnetic materials, porous media, fluids and gels, and biological molecules.

In the most recent Call for Proposals, 246 of the 359 proposals received were for the six CHRNS-operated instruments. One hundred and twenty-eight of the 256 were awarded beam time. Of the 1291 days requested, the Beam Time Allocation Committee approved 569. Roughly half of the users of neutron scattering techniques at the NCNR use CHRNS-funded instruments, and more than one third of NCNR publications (see the "Publications" section on p. 64) over the current one-year period are based on research performed using these instruments. In 2008 more than twenty Ph.D. theses were completed using results from CHRNS-sponsored instruments. Two of these received awards (Matthew Helgeson (University of Delaware) from the Neutron Scattering Society of America for Outstanding Student Research, and Susan Fullerton Shirey (Penn State University) from the American Physical Society was selected for the Frank J. Padden, Jr. award for Excellence in Polymer Physics Research.)

Scientific Support Services

An important ingredient of the CHRNS operation is its support of staff whose responsibility is to provide services that are essential to the success of neutron scattering investigations. One such service is the provision and operation of an expanding range of sample environment equipment. The sample environment team often takes on projects to expand the range of existing equipment, enhance its safety, improve its reliability, and even develop entirely new capabilities. For example, a top-loading closed-cycle refrigerator has been specifically designed for use on the NSE spectrometer.

Other services include the maintenance of several well-equipped user laboratories, and the development, documentation and maintenance of data reduction, visualization, and analysis software through the DAVE project. DAVE is a suite of programs that enables users to rapidly reduce, examine and display their experimental data. It may be downloaded free of charge from the website http://www.ncnr.nist.gov/dave/, either as a binary executable with an embedded runtime license or as the complete source code. Recent work has focused on upgrading existing capabilities and adding new tools that extend the analysis and visualization functionalities. Windows and Linux are now supported on 64-bit hardware machines in order to better cope with very large datasets such as those generated at the Spallation Neutron Source (Oak Ridge).

Education and Outreach

One of the missions of the CHRNS program is to contribute to the development of human resources through education and outreach, thereby fostering future generations of scientists and neutron scatterers.

FIGURE 1: NCNR 2009 Summer School participants

This was the 15th annual CHRNS sponsored neutron scattering summer school. The 2009 school, devoted to spectroscopy, attracted 90 applicants for the 35 available places. The CHRNS summer schools are very effective in educating potential new users of neutron scattering as more than 70 % of the participants return to the NCNR for their own research. Course materials have been placed on the Web.

We also offered a series of tutorial demonstrations based on the experiments and lectures presented at the 2008 Summer School on Small Angle Neutron Scattering and Reflectometry. Fifty-one participants, from US universities and from twenty-one NIST divisions other than the NCNR, attended the tutorials. Course materials will be placed on the Web.

FIGURE 2: The 2009 SURF students

CHRNS once again participated in NIST's Summer Undergraduate Research Fellowship (SURF) program, hosting nine undergraduate students who worked with staff members studying materials that included hydrogen storage systems, magnetic nanoparticle films for data storage applications, and disordered protein structures. The students enthusiastically agreed that their summer research experiences were productive and worthwhile, and their advisors benefited from their efforts, expanding their understanding of the scientific process.

2009 was the third year that NIST organized a "Summer Institute" for middle school science teachers. Eighteen teachers from three Maryland counties participated this year. They toured the NCNR and attended lectures and demonstrations that described how neutrons are used to probe matter. They were also provided the opportunity to interact with facility users, SURF students and the scientific staff. The neutron scattering component of the Summer Institute gave teachers a greater appreciation of what can be accomplished using neutron scattering.

FIGURE 3: Middle school science teachers and NCNR/CHRNS staff

This was the second year that high school students worked on research projects with an NCNR staff member. Mr. Vikas Bhatia from Gaithersburg High School worked with his advisor Dr. Jasmine Millican on the synthesis and characterization of Yttrium Cerium Titanium Oxide. Mr. Pavan Bhargava and his advisor Dr. Joseph Dura worked on the production of novel Nafion thin films for the development of lipid bilayers.

Other education and outreach activities included "Bring your Kids to Work Day", and tours for middle school and high school students. During the "Bring your Kids to Work Day," held every year in the month of April, NIST opens its doors to more than 250 students ranging from 6th through 12th grades. Within this site-wide yearly program, NCNR prepares tours of the facility, lectures and demonstrations specially designed for middle school age children on how neutrons are used to probe matter.

Awards 2009

Craig Brown of the NCNR has been chosen to receive a **Presidential Early Career Award for Scientists and Engineers** (PECASE) at the White House this year. The PECASE Awards are intended to recognize some of the finest scientists and engineers who, while early in their research careers, show exceptional potential for leadership at the frontiers of scientific knowledge during the twenty-first century. Dr. Brown is being recognized for his pioneering work on hydrogen storage materials.

Michihiro Nagao, guest researcher at the NCNR, will receive the **2009 Young Scientist Award** of the **Physical Society of Japan** in the area of Soft Matter Physics. He is being recognized for his paper entitled *"Concentration dependence of shape and structure fluctuations of droplet microemulsions investigated by neutron spin echo spectroscopy,"* work carried out at NCNR's Neutron Spin Echo instrument where Dr. Nagao is an instrument scientist.

Richard Lindstrom, retired from NIST and currently guest scientist with the Analytical Chemistry Division at the NCNR has been selected to receive the **Hevesy Medal Award 2009** *"for his exceptional and comprehensive contributions to radioanalytical measurement science, namely prompt gamma-ray activation analysis and gamma-ray spectrometry, and for his educational and organizational activities."* The George Hevesy Medal Award is the premier international award of excellence in radioanalytical and nuclear chemistry.

Sungdae Ji, postdoctoral appointee at the University of Virginia and guest researcher at the NCNR has been chosen for the **2008 Young Researcher Science Award** from the **Korean Synchrotron Radiation User's Association.**

Susan T. Krueger of the NCNR was awarded the **DOC Bronze Medal** *"for research in the basic biological science of viral protein structures."*

Paul A. Kienzle of the NCNR was awarded the **DOC Bronze Medal** for *"development of the Reflpak software package"* which has had a major impact on the usefulness of neutron reflectometry research.

Dona M. Hanak, secretary at the NCNR, has been recognized with a NIST **Eugene Casson Crittenden Award** for *"her willingness to accept extra work and perform new administrative assignments benefiting the NCNR."*

NIST Standards Alumni Association Portrait Gallery of Distinguished Alumni 2009 has added NCNR's **Tawfik Raby** *"for contributions to NIST and national goals through his leadership of the Reactor Operations and Engineering Group to create the most reliable and cost-effective major research reactor in the world."*

Taner Yildirim has been appointed **Fellow of the American Physical Society.** Yildirim's citation reads: *"For combining analytic theory, first-principles computations, and neutron scattering measurements to design, discover, and understand new materials with novel physics."*

Dan Neumann of the NCNR has been appointed **Fellow** of the **American Physical Society.** Neumann's citation reads: *"for seminal studies of the structure and dynamics of new carbon-based materials and critical leadership serving the U.S. neutron scattering community."*

Jeff Nico of the Ionizing Radiation Division at the NCNR has been appointed **Fellow** of the **American Physical Society.** *"In recognition of his contributions and leadership in precision measurements and fundamental symmetry tests using cold neutrons, and his contributions to radiochemical determinations of the p-p fusion solar neutrino flux."*

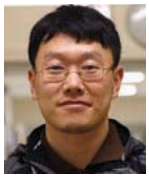

Jae-Hyuk Her of the NCNR was selected by the NIST chapter of **Sigma Xi** for a **2009 outstanding poster award** for his presentation: *"Structural Studies on Various Hydrogen Storage Materials: MIL-53, $K_2Zn_3[Fe(CN)_6]_2$ and $Li_2B_{12}H_{12}$."*

Jason Simmons of the NCNR was selected by the NIST chapter of **Sigma Xi** for a **2009 outstanding poster award** for his presentation: *"Nanoporous Carbons and Coordination Polymers for Energy-related Applications: Alternative Fuels and Carbon Capture."*

Winnie K. Wong-Ng of the NIST Ceramics Division was awarded a **DOC Bronze Medal** for leading a multiyear team *"project resulting in accurate phase diagrams for the entire class of high-temperature superconducting ceramic materials."*


Marcus T. Cicerone and **Christopher L. Soles**, both of the NIST Polymers Division, were awarded a **DOC Bronze Medal** for *"the seminal discovery that nanosecond molecular dynamics are critical in determining"* the *"viability of freeze-dried biopharmaceuticals."* Several key experiments in this work were performed using inelastic scattering instruments at the NCNR.

Tiffany Santos of Argonne National Laboratory has been selected for a **L'Oreal USA Fellowship for Women in Science** for her work in transition metal oxides at the Center for Nanoscale Materials at Argonne. Awardees each receive $60,000 grants to be used toward independent scientific research and career development. Her plans include the use of NCNR neutron facilities to pursue her oxide work, and also to support an undergraduate student through the course of a short-term research project under her guidance.

Prof. Frank Bates of the University of Minnesota is part of a team of five researchers that was chosen for the **2008 Cooperative Research Award in Polymer Science and Engineering** *"for their highly productive and sustained collaborative efforts in the area of poly(cyclohexylene) block copolymers."* The UM shares a PRT operating the NG-7 SANS instrument where many of Prof. Bates' experiments were carried out.

Prof. Steven White of the University of California at Irvine was selected for the **Avanti Award in Lipids** by the **Biophysical Society** *"for his novel findings in the areas of membrane structure and protein insertion into membranes."* Prof. White and his group have conducted their reflectometry measurements at the NCNR's AND/R instrument.

Prof. Valery Kiryukhin of Rutgers University was selected for a **Friedrich Wilhelm Bessel Research Award** from the **Alexander von Humboldt Foundation in Germany.** Award winners are honored *"for their outstanding research record and invited to spend a period of up to one year cooperating on a long-term research project with specialist colleages at a research institution in Germany."* Prof. Kiryukhin recently spent sabbatical time at the NCNR, performing measurements at the BT-9 spectrometer.

Prof. Jeffrey Thomas of Northwestern University was selected for the **2008 Brunauer Award** by the **American Ceramic Society** for his paper *"A New Approach to Modeling the Nucleation and Growth Kinetics of Tricalcium Silicate Hydration."* Prof. Thomas's group uses SANS and inelastic scattering instruments at the NCNR.

Susan Fullerton Shirey, recent doctoral recipient from Prof. Janna Maranas group at Penn State University, was selected to receive the **2009 Frank J. Padden, Jr. Award** from the **American Physical Society** for *"excellence in polymer physics research."* Her work appears as a highlight in this issue on pp. 32–33.

Jinsheng Wen, a graduate student at University of Stony Brook working at Brookhaven National Laboratory, was chosen for a **Margaret C. Etter Student Lecturer Award** at the 2009 Annual Meeting of the **American Crystallographic Association.** The neutron measurements in his paper *"Magnetic Field Effect on Charge Order in the New Multiferroic $LuFe_2O_4$"* were made at the NCNR.

Monica Branco, recent doctoral student at the University of Delaware, was invited to speak at the 2009 **American Chemical Society** meeting in recognition of her **Excellence in Graduate Polymer Research.** Her paper was entitled *"Neutron scattering analysis of the dynamics and structure of semiflexible, self-assembled peptide chain networks."* Her work appears as a highlight in this issue on pp. 42–43.

Prof. James Eckert of Harvey Mudd College was the recipient of the **2009 Prize for a Faculty Member for Research in an Undergraduate Institution** awarded by the **American Physical Society.** *"For the significant contributions he has made to the understanding of the complex exchange biasing mechanism crucial to spin-valve sensors used in the read-write heads of hard disks and for his skilled and enthusiastic inclusion of undergraduates in physics research."* Prof. Eckert's student, Stephanie Moyerman, an APS Apker award winner in 2006, conducted neutron reflectometry work at the NCNR.

Publications: August 1, 2008 to July 31, 2009

Acosta, E.J., Szekeres, E., Harwell, J.H., Grady, B.P., Sabatini, D.A., "Morphology of Ionic Microemulsions: Comparison of SANS Studies and the Net-Average Curvature (NAC) Model," Soft Matter **5** (3), 551 (2009).

Akcora, P., Liu, H., Kumar, S.K., Moll, J., Li, Y., Benicewicz, B.C., Schadler, L.S., Acehan, D., Panagiotopoulos, A.Z., Pryamitsyn, V., Ganesan, V., Ilavsky, J., Thiyagarajan, P., Colby, R.H., Douglas, J.F., "Anisotropic Self-Assembly of Spherical Polymer-Grafted Nanoparticles," Nat. Mater. **8** (4), 354 (2009).

Akgun, B., Uğur, G., Jiang, Z., Narayanan, S., Song, S., Lee, H., Brittain, W.J., Kim, H., Sinha, S.K., Foster, M.D., "Surface Dynamics of 'Dry' Homopolymer Brushes," Macromol. **42** (3), 737 (2009).

Alinger, M.J., Odette, G.R., Hoelzer, D.T., "On the Role of Alloy Composition and Processing Parameters in Nanocluster Formation and Dispersion Strengthening in Nanostuctured Ferritic Alloys," Acta Mater. **57** (2), 392 (2009).

Allen, A.J., Hackley, V.A., Jemian, P.R., Ilavsky, J., Raitano, J.M., Chan, S.-W., "*In Situ* Ultra-Small-Angle X-Ray Scattering Study of the Solution-Mediated Formation and Growth of Nanocrystalline Ceria," J. Appl. Crystallogr. **41** (5), 918 (2008).

Alsmadi, A.M., Alyones, S., Mielke, C.H., McDonald, R.D., Zapf, V., Altarawneh, M.M., Lacerda, A., Chang, S., Adak, S., Kothapalli, K., Nakotte, H., "Radio-Frequency Measurements of UNiX Compounds (X=Al, Ga, Ge) in High Magnetic Fields," J. Mag. Mag. Mater., in press.

Amoretti, G., Caciuffo, R., Carretta, S., Guidi, T., Magnani, N., Santini, P., "Inelastic Neutron Scattering Investigations of Molecular Nanomagnets," Inorg. Chim. Acta **361** (14), 3771 (2008). **(CHRNS)**

Anderson, D.L., "Analytical Capabilities of Anticoincidence INAA for Biological Materials," J. Radioanal. Nucl. Chem., in press.

Anderson, D.L., "Determination of Bromine in Regulated Foods with a Field-Portable X-Ray Fluorescence Analyzer," J. AOAC Int. **92** (2), 502 (2009).

Anderson, D.L., "Screening of Foods and Related Products for Toxic Elements with a Portable X-Ray Tube Analyzer," J. Radioanal. Nucl. Chem., in press.

Anderson, D.L., "Use of L-Cysteine for Minimization of Inorganic Hg Loss During Thermal Neutron Irradiation," J. Radioanal. Nucl. Chem., in press.

Araos, M.U., Warr, G.G., "Structure of Nonionic Surfactant Micelles in the Ionic Liquid Ethylammonium Nitrate," Langmuir **24** (17), 9354 (2008). **(CHRNS)**

Arif, M., Hussey, D.S., Jacobson, D.L., "Neutron Imaging for the Hydrogen Economy," Neutron Imaging and Applications **11**, 191 (2009).

Atakan, V., Chen, C.-W., Paul, R., Riman, R.E., "Quantification of Hydroxyl Content in Ceramic Oxides: A Prompt γ Activation Analysis Study of $BaTiO_3$," Anal. Chem. **80** (17), 6626 (2008).

Bao, W., Gasparovic, Y.C., Lynn, J.W., Ronning, F., Bauer, E.D., Thompson, J.D., Fisk, Z., "Commensurate Magnetic Structure of $CeRhIn_{4.85}Hg_{0.15}$," Phys. Rev. B **79** (9), 092415 (2009).

Bao, W., Qiu, Y., Huang, Q., Green, M.A., Zajdel, P., Fitzsimmons, M.R., Zhernenkov, M., Chang, S., Fang, M., Qian, B., Vehstedt, E.K., Yang, J., Pham, H.M., Spinu, L., Mao, Z.Q., "Tunable ($\delta\pi$, $\delta\pi$)-Type Antiferromagnetic Order in α-Fe(Te,Se) Superconductors," Phys. Rev. Lett. **102** (24), 247001 (2009). **(CHRNS)**

Barker, J.G., Mildner, D.F.R., Rodriguez, J.A., Thiyagarajan, P., "Neutron Transmission of Single-Crystal Magnesium Fluoride," J. Appl. Crystallogr. **41** (6), 1003 (2008). **(CHRNS)**

Belik, A.A., Huang, Q., Takayama-Muromachi, E., Lynn, J.W., "Neutron Powder Diffraction Study of the Magnetic and Crystal Structures of $SrFe_2(PO_4)_2$," J. Solid State Chem. **181** (9), 2292 (2008).

Berk, N.F., Majkrzak, C.F., "Analysis of Multibeam Data for Neutron Reflectivity," Langmuir **25** (7), 4145 (2009).

Berk, N.F., Majkrzak, C.F., "Statistical Analysis of Phase-Inversion Neutron Specular Reflectivity," Langmuir **25** (7), 4132 (2009).

Bianchi, A., Carretta, S., Santini, P., Amoretti, G., Guidi, T., Qiu, Y., Copley, J.R.D., Timco, G., Muryn, C., Winpenny, R.E.P., "Rotational Bands in Open Antiferromagnetic Rings: A Neutron Spectroscopy Study of Cr_8Zn," Phys. Rev. B **79** (14), 144422 (2009). **(CHRNS)**

Blackburn, E., Goodkind, J., Sinha, S.K., Broholm, C., Copley, J.R.D., Erwin, R., "Neutron Scattering Study of the Excitation Spectrum of Solid Helium at Ultra-Low Temperatures," PRAMANA J. Phys. **71** (4), 673 (2008). **(CHRNS)**

Borup, R.L., Mukundan, R., Davey, J., Spendelowa, J., Hussey, D.S., Jacobson, D.L., and Arif, M., "In Situ PEM Fuel Cell Water Measurements," ECS Trans. **17** (1), 263 (2008).

Branco, M.C., Nettesheim, F., Pochan, D.J., Schneider, J.P., Wagner, N.J., "Fast Dynamics of Semiflexible Chain Networks of Self-Assembled Peptides," Biomacromol. **10** (6), 1374 (2009). **(CHRNS)**

Bridges, C.A., Krishnamurthy, V.V., Poulton, S., Paranthaman, M.P., Sales, B.C., Myers, C., Bobev, S., "Magnetic Order in $CaMn_2Sb_2$ Studied via Powder Neutron Diffraction," J. Mag. Mag. Mater., in press.

Brown, C.M., Liu, Y., Neumann, D.A., "Neutron Powder Diffraction of Metal-Organic Frameworks for Hydrogen Storage," PRAMANA J. Phys. **71** (4), 755 (2008).

Brown, C.M., Liu, Y., Yildirim, T., Peterson, V.K., Kepert, C.J., "Hydrogen Adsorption in HKUST-1: A Combined Inelastic Neutron Scattering and First-Principles Study," Nanotech. **20** (20), 204025 (2009). **(CHRNS)**

Bumrongjaroen, W., Livingston, R.A., Neumann, D.A., Allen, A.J., "Characterization of Fly Ash Reactivity in Hydrating Cement by Neutron Scattering," J. Mater. Res. **24** (7), 2435 (2009). **(CHRNS)**

Cabrera, I., Kenzelmann, M., Lawes, G., Chen, Y., Chen, W.C., Erwin, R., Gentile, T.R., Leão, J.B., Lynn, J.W., Rogado, N., Cava, R.J., Broholm, C., "Coupled Magnetic and Ferroelectric Domains in Multiferroic $Ni_3V_2O_8$," Phys. Rev. Lett., in press.

Cai, J., Zhang, L., Liu, S., Liu, Y., Xu, X., Chen, X., Chu, B., Guo, X., Xu, J., Cheng, H., Han, C.C., Kuga, S., "Dynamic Self-Assembly Induced Rapid Dissolution of Cellulose at Low Temperatures," Macromol. **41** (23), 9345 (2008).

Cao, H., Bai, F., Li, J., Viehland, D., Lograsso, T.A., Gehring, P.M., "Structural Studies of Decomposition in Fe-*x* at.%Ga Alloys," J. Alloys Compd. **465** (1), 244 (2008).

Cao, H., Gehring, P.M., Devreugd, C.P., Rodriguez-Rivera, J.A., Li, J., Viehland, D., "Role of Nanoscale Precipitates on the Enhanced Magnetostriction of Heat-Treated Galfenol ($Fe_{1-x}Ga_x$) Alloys," Phys. Rev. Lett. **102** (12), 127201 (2009).

Cao, H., Stock, C., Xu, G., Gehring, P.M., Li, J., Viehland, D., "Dynamic Origin of the Morphotropic Phase Boundary: Soft Modes and Phase Instability in $0.68Pb(Mg_{1/3}Nb_{2/3})O_3$-$0.32PbTiO_3$," Phys. Rev. B **78** (10), 104103 (2008).

Cao, L., Bindel, R., "The Use of Webcam for Neutron Imaging," Trans. Am. Nucl. Soc. **100**, 243 (2009).

Cao, L.R., Hattrick-Simpers, J.R., Bindel, R., Tomlin, B.E., Zeisler, R., Paul, R., Bendersky, L.A., Downing, R.G., "Combinatorial Study of Thin Film Metal Hydride by Prompt Gamma Activation Analysis," J. Radioanal. Nucl. Chem., in press.

Cao, L.R., Hattrick-Simpers, Oguchi, H., Paul, R., Bendersky, L., Downing, R.G., "The Study of Thin Film Metal Hydride with Prompt Gamma Activation Analysis," Trans. Am. Nucl. Soc. **99**, 268 (2008).

Cappelletti, R.L., editor, "2008 NIST Center for Neutron Research Accomplishments and Opportunities," NIST SP 1089 (2008).

Cetinkol, M., Wilkinson, A.P., Lee, P.L., "Structural Changes Accompanying Negative Thermal Expansion in $Zr_2(MoO_4)(PO_4)_2$," J. Solid State Chem. **182** (6), 1304 (2009).

Chatjaroenporn, K., Baker, R.W., FitzGerald, P.A., Warr, G.G., "Structure Changes in Micelles and Adsorbed Layers During Surfactant Polymerization," J. Colloid Inter. Sci. **336** (2), 449 (2009).

Chaudhury, R.P., Lorenz, B., Wang, Y.Q., Sun, Y.Y., Chu, C.W., Ye, F., Fernandez-Baca, J., Mook, H., Lynn, J., "Re-Entrant Spiral Magnetic Order and Ferroelectricity in $Mn_{1-x}Fe_xWO_4$ (x=0.035)," J. Appl. Phys. **105** (7), 07D913 (2009).

Chen, C., Maranas, J.K., "A Molecular View of Dynamic Responses When Mixing Poly(Ethylene Oxide) and Poly (Methyl Methacrylate)," Macromol. **42** (7), 2795 (2009). **(CHRNS)**

Chen, H., Ren, Y., Qiu, Y., Bao, W., Liu, R.H., Wu, G., Wu. T., Xie, Y.L., Wang, X.F., Huang, Q., Chen, X.H., "Coexistence of the Spin-Density-Wave and Superconductivity in the $Ba_{1-x}K_xFe_2As_2$," EPL **85** (1), 17006 (2009).

Chen, J.-H., Chang, C.-S., Chang, Y.-X., Chen, C.-Y., Chen, H.-L., Chen, S.-A., "Gelation and Its Effect on the Photophysical Behavior of Poly(9,9-dioctylfluorene-2,7-diyl) in Toluene," Macromol. **42** (4), 1306 (2009). **(CHRNS)**

Chen, S.-H., Zhang, Y., Lagi, M., Chong, S.-H., Baglioni, P., Mallamace, F., "Evidence of Dynamic Crossover Phenomena in Water and Other Glass-Forming Liquids: Experiments, MD Simulations and Theory," J. Phys.: Condens. Mat., in press.

Chen, S.-H., Zhang, Y., Lagi, M., Chu, X., Liu, L., Faraone, A., Fratini, E., Baglioni, P., "The Dynamic Response Function $\chi_T(Q,t)$ of Confined Supercooled Water and its Relation to the Dynamic Crossover Phenomenon," Z. Phys. Chem., in press. **(CHRNS)**

Chen, W.C., Erwin, R., McIver III, J.W., Watson, S., Fu, C.B., Gentile, T.R., Borchers, J.A., Lynn, J.W., Jones, G.L., "Applications of ^{3}He Neutron Spin Filters at the NCNR," Physica B, in press. **(CHRNS)**

Chen, Y., Lynn, J.W., Li, J., Li, G., Chen, G.F., Luo, J.L., Wang, N.L., Dai, P., dela Cruz, C., Mook, H.A., "Magnetic Order of the Iron Spins in NdFeAsO," Phys. Rev. B **78** (6), 064515 (2008).

Chen, Y., Ueland, B.G., Lynn, J.W., Bychkov, G.L., Barilo, S.N., Mukovskii, Y.M., "Polaron Formation in the Optimally Doped Ferromagnetic Manganites $La_{0.7}Sr_{0.3}MnO_3$ and $La_{0.7}Ba_{0.3}MnO_3$," Phys. Rev. B **78** (21), 212301 (2008).

Cheng, G., Graessley, W.W., Melchenko, Y.B., "Polymer Dimensions in Good Solvents: Crossover from Semidilute to Concentrated Solutions," Phys. Rev. Lett. **102** (15), 157801 (2009). **(CHRNS)**

Cheng, G., Melnichenko, Y.B., Wignall, G.D., Hua, F., Hong, K., Mays, J.W., "Small Angle Neutron Scattering Study of Conformation of Oligo(Ethylene Glycol)-Grafted Polystyrene in Dilute Solutions: Effect of the Backbone Length," Macromol. **41** (24), 9831 (2008). **(CHRNS)**

Chi, S., Adroja, D.T., Guidi, T., Bewley, R., Li, S., Zhao, J., Lynn, J.W., Brown, C.M., Qiu, Y., Chen, G.F., Lou, J.L., Wang, N.L., Dai, P., "Crystalline Electric Field as a Probe for Long-Range Antiferromagnetic Order and Superconducting State of $CeFeAsO_{1-x}F_x$," Phys. Rev. Lett. **101** (21), 217002 (2008). **(CHRNS)**

Cho, J.Y., Millican, J.N., Capan, C., Sokolov, D.A., Moldovan, M., Karki, A.B., Young, D.P., Aronson, M.C., Chan, J.Y., "Crystal Growth, Structure, and Physical Properties of Ln_2MGa_{12} (Ln = La, Ce; M = Ni, Cu)," Chem. Mater. **20** (19), 6116 (2008).

Chokshi, U., Selvam, P., Porcar, L., da Rocha, S.R.P., "Reverse Aqueous Emulsions and Microemulsions in HFA227 Propellant Stabilized by Non-Ionic Ethoxylated Amphiphiles," Int. J. Pharm. **369** (1-2), 176 (2009). **(CHRNS)**

Christensen, M., Abrahamsen, A.B., Christensen, N.B., Juranyi, F., Andersen, N.H., Lefmann, K., Andreasson, J., Bahl, C.R.H., Iversen, B.B., "Avoided Crossing of Rattler Modes in Thermoelectric Materials," Nat. Mater. **7**, 811 (2008).

Chu, X.-Q., Faraone, A., Kim, C., Fratini, E., Baglioni, P., Leao, J.B., Chen, S.-H., "Proteins Remain Soft at Lower Temperatures under Pressure," J. Phys. Chem. B **113** (15), 5001 (2009). **(CHRNS)**

Chung, J.-H., Chung, S.J., Lee, S., Kirby, B.J., Borchers, J.A., Cho, Y.J., Liu, X., Furdyna, J.K., "Carrier-Mediated Antiferromagnetic Interlayer Exchange Coupling in Diluted Magnetic Semiconductor Multilayers $Ga_{1-x}Mn_xAs$/GaAs:Be," Phys. Rev. Lett. **101** (23), 237202 (2008).

Chung, J.-H., Lim, J.-H., Shin, J., Kang, J.-S., Jaiswal-Nagar, D., Kim, K.H., "Possible Charge Disproportionation in 3R-$AgNiO_2$ Studied by Neutron Powder Diffraction," Phys. Rev. B **78** (21), 214417 (2008).

Clancy, J.P., Ruff, J.P.C., Dunsiger, S.R., Zhao, Y., Dabkowska, H.A., Gardner, J.S., Qiu, Y., Copley, J.R.D., Jenkins, T., Gaulin, B.D., "Revisiting Static and Dynamic Spin-Ice Correlations in $Ho_2Ti_2O_7$ with Neutron Scattering," Phys. Rev. B **79** (1), 014408 (2009). **(CHRNS)**

Clerici, C., Gu, X., Sung, L., Forster, A.M., Ho, D.L., Stutzman, P., Nguyen, T., Martin, J.W., "Effect of Pigment Dispersion on Durability of a TiO_2 Pigmented Epoxy Coating During Outdoor Exposure," in "Service Life Prediction for Polymeric Materials: Global Perspectives," edited by Martin, J.W., Ryntz, R.A., Chin, J., and Dickie, R., (Springer US) Chap. 31, 475 (2009).

Cleveland IV, T.E., Hussey, D.S., Chen, Z.-Y., Jacobson, D.L., Brown, R.L., Carter-Wientjes, C., Cleveland, T.E., Arif, M., "The Use of Neutron Tomography for the Structural Analysis of Corn Kernels," J. Cereal Sci. **48**, 517 (2008).

Cole, D.R., Mamontov, E., Rother, G., "Structure and Dynamics of Fluids in Microporous and Mesoporous Earth and Engineered Materials," in "Neutron Applications in Earth, Energy and Environmental Sciences," edited by Liang, L., Rinaldi, R., Schober, H., (Springer US) Chap. 19, 547 (2009). **(CHRNS)**

Comoletti, D., Grishaev, A., Whitten, A.E., Taylor, P., Trewhella, J., "Characterization of the Solution Structure of a Neuroligin/β-Neurexin Complex," Chem. Biol. Interact. **175** (1-3), 150 (2008).

Contescu, C.I., Bhat, V.V., Gallego, N.C., "Hydrogen Spillover: Its 'Diffusion' From Catalysis to Hydrogen Storage Community," ACS Div. Fuel Chem. **54** (1), 382 (2009).

Contescu, C.I., Brown, C.M., Liu, Y., Bhat, V.V., Gallego, N.C., "Detection of Hydrogen Spillover in Palladium-Modified Activated Carbon Fibers During Hydrogen Adsorption," J. Phys. Chem. C **113** (14), 5886 (2009).

Cook, J.C., "Design and Estimated Performance of a New Neutron Guide System for the NCNR Expansion Project," Rev. Sci. Instrum. **80** (3), 023101 (2009).

Cooper, J.W., Coplan, M.A., Hughes, P.P., "The Detection of Lyman Alpha Radiation Formed by the Slowing Down of Protons and Tritons Produced by the He-3 (n,tp) Reaction - A Model Study," J. Res. Natl. Inst. Stand. Technol. **114** (3), 185 (2009).

Copley, J.R.D., Brown, C.M., Qiu, Y., "Time-of-Flight Spectroscopy at the NIST Center for Neutron Research," Neutron News **20** (2), 28 (2009). **(CHRNS)**

Cui, H., Muraoka, T., Cheetham, A., Stupp, S.I., "Self-Assembly of Giant Peptide Nanobelts," Nano Lett. **9** (3), 945 (2009). **(CHRNS)**

Dai, P., Wilson, S.D., Li, S., Wen, H.-H., "Nature of the Quantum Spin Correlations Through the Superconducting-Normal Phase Transition in Electron-Doped Superconducting $Pr_{0.88}LaCe_{0.12}CuO_4$," J. Phys. Chem. Solids **69** (12), 3096 (2008).

Dandu, R., Von Cresce, A., Briber, R., Dowell, P., Cappello, J., Ghandehari, H., "Silk–Elastinlike Protein Polymer Hydrogels: Influence of Monomer Sequence on Physicochemical Properties," Polymer **50** (2), 366 (2009).

Davey, J., Mukundan, R., Spendelow, J., Hussey, D.S., Jacobson, D., Arif, M., Borup, R.L., "Water Dynamics in a PEM Fuel Cell: Effect of Current and Humidity Transients," ECS Trans. **16** (2), 329 (2008).

Doe, C., Choi, S.-M., Kline, S.R., Jang, H.-S., Kim, T.-H., "Charged Rod-Like Nanoparticle Assisted Single-Wall Carbon Nanotube Dispersion in Water," Adv. Func. Mater. **18**, 2685 (2008). **(CHRNS)**

Doe, C., Jang, H.-S., Kline, S.R., Choi, S.-M., "Subdomain Structures of Lamellar and Reverse Hexagonal Pluronic Ternary Systems Investigated by Small Angle Neutron Scattering," Macromol. **42** (7), 2645 (2009).

Dowling, M.B., Lee, J.-H., Raghavan, S.R., "pH-Responsive Jello: Gelatin Gels Containing Fatty Acid Vesicles," Langmuir, in press.

Dunsiger, S.R., Zhao, Y., Gaulin, B.D., Qiu, Y., Bourges, P., Sidis, Y., Copley, J.R.D., Kallin, A., Mazurek, E.M., Dabkowska, H.A., "Diagonal and Collinear Incommensurate Spin Structures in Underdoped $La_{2-x}Ba_xCuO_4$," Phys. Rev. B **78** (9), 092507 (2008). **(CHRNS)**

Dura, J.A., LaRock, J., "A Molecular Beam Epitaxy Facility for *In Situ* Neutron Scattering," Rev. Sci. Instrum. **80** (7), 073906 (2009).

Dura, J.A., Murthi, V.S., Hartman, M., Satija, S.K., Majkrzak, C.F., "Multilamellar Interface Structures in Nafion," Macromol. **42** (13), 4769 (2009).

Ehlers, G., Mamontov, E., Zamponi, M., Kam, K.C., Gardner, J.S., "Direct Observation of a Nuclear Spin Excitation in $Ho_2Ti_2O_7$," Phys. Rev. Lett. **102** (1), 016405 (2009).

ElMassalami, M., Rapp, R.E., Chaves, F.A.B., Moreno, R., Takeya, H., Ouladdiaf, B., Lynn, J.W., Huang, Q., Freitas, R.S., Oliveria Jr., N.F., "Synthesis and Magnetic Characterization of $TmCo_2B_2C$," J. Phys.: Condens. Mat. **21** (4), 046007 (2009).

Emery, S.B., Wells, B.O., "Properties of Phase-Separated, Super-Oxygenated $La_{2-x}Sr_xCuO_{4+y}$," J. Supercond. Nov. Magn. **22** (1), 33 (2009).

Faraone, A., Fratini, E., Todea, A.M., Krebs, B., Müller, A., Baglioni, P., "Dynamics of Water in Voids Between Well-Defined and Densely Packed Spherical Nanocages Acting as Polyprotic Inorganic Acids," J. Phys. Chem. C **113** (20), 8635 (2009). **(CHRNS)**

Faraone, A., Liu, K.-H., Mou, C.-Y., Zhang, Y., Chen, S.-H., "Single Particle Dynamics of Water Confined in a Hydrophobically Modified MCM-41-S Nanoporous Matrix," J. Chem. Phys. **130** (13), 134512 (2009). **(CHRNS)**

Ferguson, M.L., Prasad, K., Boukari, H., Sackett, D.L., Krueger, S., Lafer, E.M., Nossal, R., "Clathrin Triskelia Show Evidence of Molecular Flexibility," Biophys. J. **95** (4), 1945 (2008). **(CHRNS)**

Fischbach, E., Buncher, J.B., Jenkins, J.H., Krause, D.E., Lindstrom, R.M., Mattes, J.J., "Possibility of a Self-induced Contribution to Nuclear Decays," Trans. Am. Nucl. Soc. **100**, 223 (2009).

Foster, B., Cosgrove, T., Hammouda, B., "Pluronic Triblock Copolymer Systems and Their Interactions with Ibuprofen," Langmuir **25** (12), 6760 (2009).

Frounfelker, B.D., Kalur, G.C., Cipriano, B.H., Danino, D., Raghavan, S.R., "Persistence of Birefringence in Sheared Solutions of Wormlike Micelles," Langmuir **25** (1), 167 (2009). **(CHRNS)**

Fullerton-Shirey, S.K., Maranas, J.K., "Effect of $LiClO_4$ on the Structure and Mobility of PEO-Based Solid Polymer Electrolytes," Macromol. **42** (6), 2142 (2009). **(CHRNS)**

Gagliardo, J.J., Owejan, J.P., Trabold, T.A., Tighe, T.W., "Neutron Radiography Characterization of an Operating Proton Exchange Membrane Fuel Cell with Localized Current Distribution Measurements," Nucl. Instr. Meth. A **605** (1), 115 (2009).

Garcia Sakai, V., Mamontov, E., Neumann, D., "A Background Suppression Chopper for the High-Flux Backscattering Spectrometer at NIST," J. Neutron Res., in press. **(CHRNS)**

Gasser, U., Sierra-Martin, B., Fernandez-Nieves, A., "Crystal Structure of Highly Concentrated, Ionic Microgel Suspensions Studied by Neutron Scattering," Phys. Rev. E **79** (5), 051403 (2009).

Gawrisch, K., Soubias, O., Mihailescu, M., "Insights From Biophysical Studies on the Role of Polyunsaturated Fatty Acids for Function of G-Protein Coupled Membrane Receptors," Prost. Leuk. Essent. Fatty Acids **79** (3), 131 (2008).

Gehring, P.M., Hiraka, H., Stock, C., Lee, S.-H., Chen, W., Ye, Z.-G., Vakhrushev, S.B., Chowdhuri, Z., "Reassessment of the Burns Temperature and its Relationship to the Diffuse Scattering, Lattice Dynamics, and Thermal Expansion in Relaxor $Pb(Mg_{1/3}Nb_{2/3})O_3$," Phys. Rev. B **79** (22), 224109 (2009). **(CHRNS)**

Giblin, S.R., Champion, J.D.M., Zhou, H.D., Wiebe, C.R., Gardner, J.S., Terry, I., Calder, S., Fennell, T., Bramwell, S.T., "Static Magnetic Order in $Tb_2Sn_2O_7$ Revealed by Muon Spin Relaxation with Exterior Muon Implantation," Phys. Rev. Lett. **101** (23), 237201 (2008).

Gnäupel-Herold, T., "Techniques for Neutron Stress Determination with High Spatial Resolution," J. Nondestructive Evaluation, in press.

Gnäupel-Herold, T., Iadicola, M.A., Foecke, T., "Residual Stresses in Numisheet Benchmark 3 Panels," in "Material Property Data for More Effective Numerical Analysis," edited by Levy, B.S., Matlock, D.K., Van Tyne, C.J., (IDDRG Conf. Proc.) 7 (2009).

Gnäupel-Herold, T., "Formalism for the Determination of Intermediate Stress Gradients Using X-Ray Diffraction," J. Appl. Crystallogr. **42** (2), 192 (2009).

Gogotsi, Y., Portet, C., Osswald, S., Simmons, J.M., Yildirim, T., Laudisio, G., Fischer, J.E., "Importance of Pore Size in High-Pressure Hydrogen Storage by Porous Carbons," Int. J. Hydrogen Energy, in press.

Goldman, A.I., Kreyssig, A., Prokeš, K., Pratt, D.K., Argyriou, D.N., Lynn, J.W., Nandi, S., Kimber, S.A.J., Chen, Y., Lee, Y.B., Samolyuk, G., Leão, J.B., Poulton, S.J., Bud'ko, S.L., Ni, N., Canfield, P.C., Harmon, B.N., McQueeney, R.J., "Lattice Collapse and Quenching of Magnetism in $CaFe_2As_2$ Under Pressure: A Single-Crystal Neutron and X-Ray Diffraction Investigation," Phys. Rev. B **79** (2), 024513 (2009).

Green, M.A., "When Small is Better," Nature **8**, 450 (2009).

Guidi, T., Carretta, S., Santini, P., Amoretti, G., Caciuffo, R., Hiess, A., Copley, J.R.D., Qiu, Y., Timco, G., Winpenny, R.E.P., "Quantum Oscillations of the Total Spin in a Heterometallic Antiferromagnetic Ring," Not. Neutroni Luce Sinc. **13** (2), 4 (2008). **(CHRNS)**

Gupta, S., Muralikiran, M., Farmer, J., Cao, L.R., and Downing, R.G., "The Effect of Boron Doping and Gamma Irradiation on the Structure and Properties of Microwave Chemical Vapor Deposited Boron-Doped Diamond Films," J. Mater. Res. **24** (4), 1498 (2009).

Hamill, A.C., Lee Jr, C.T., "Photocontrol of β-Amyloid Peptide (1–40) Fibril Growth in the Presence of a Photosurfactant," J. Phys. Chem. B **113** (17), 6164 (2009). **(CHRNS)**

Han, X., Hristova, K., "Viewing the Bilayer Hydrocarbon Core Using Neutron Diffraction," J. Memb. Biol. **227**, 123 (2009).

Hanley, H.J.M., Payne, T.E., "Adsorption of a Jet Fuel on a Model Organic-Clay Soil: Application of Small Angle Neutron Scattering," Can. J. Chem. Eng. **36** (3), 559 (2009).

Hansen, F.Y., Taub, H., "Decomposition of Molecular Motions Into Translational, Rotational, and Intramolecular Parts by a Projection Operator Techniques," Comm. Comp. Phys., in press.

Hassan, P.A., Hodgdon, T.K., Sagasaki, M., Fritz-Popovski, G., and Kaler, E.W., "Phase Behavior and Microstructure Evolution in Aqueous Mixtures of Cetyltrimethylammonium Bromide and Sodium Dodecyl Tri-Oxyethylene Sulfate," Comptes Rendus Chimie **12** (1), 18 (2009).

Heinrich, F., Ng, T., Vanderah, D.J., Shekhar, P., Mihailescu, M., Nanda, H., Lösche, M., "A New Lipid Anchor for Sparsely Tethered Bilayer Lipid Membranes," Langmuir **25** (7), 4219 (2009).

Heitfeld, K.A., Schaefer, D.W., "Structure-Property Relationships in Flavour-Barrier Membranes with Reduced High-Temperature Diffusivity," Soft Matter **5** (1), 156 (2009). **(CHRNS)**

Helgeson, M.E., Vasquez, P.A., Kaler, E.W., Wagner, N.J., "Rheology and Spatially Resolved Structure of Cetyltrimethylammonium Bromide Wormlike Micelles Through the Shear Banding Transition," J. Rheol. **53** (3), 727 (2009). **(CHRNS)**

Her, J.-H., Kennon, B.S., Shum, W.W., Stephens, P.W., Miller, J.S., "Structure and Magnetic Properties of $Ln^{III}[Ru_2(CO_3)_4]\bullet 8H_2O$," Inorg. Chim. Acta **361** (12-13), 3462 (2008).

Her, J.-H., Stephens, P.W., Ribas-Ariño, J., Novoa, J.J., Shum, W.W., Miller, J.S., "Structure and Magnetic Interactions in the Organic-Based Ferromagnet Decamethylferrocenium Tetracyanoethenide, $[FeCp^*_2]^{\bullet+}[TCNE]^{\bullet-}$," Inorg. Chem. **48** (8), 3296 (2009).

Her, J.-H., Yousufuddin, M., Zhou, W., Jalisatgi, S.S., Kulleck, J.G., Zan, J.A., Hwang, S.-J., Bowman Jr., R.C., Udovic, T.J., "Crystal Structure of $Li_2B_{12}H_{12}$: A Possible Intermediate Species in the Decomposition of $LiBH_4$," Inorg. Chem. **47** (21), 9757 (2008).

Her, J.-H., Zhou, W., Stavila, V., Brown, C.M., Udovic, T.J., "Role of Cation Size on the Structural Behavior of the Alkali-Metal Dodecahydro-*closo*-Dodecaborates," J. Phys. Chem. C **113** (16), 11187 (2009).

Hernández, Y., Brown, C.M., "User Facilities: The Education of New Neutron Users," in "8th International Conference on Methods and Applications of Radioanalytical Chemistry: MARC-VIII," edited by Zeisler, R., Ünlü, K., Heller-Zeisler, S., (AIP Conf. Proc.), in press.

Heuser, B.J., Udovic, T.J., Ju, H., "Vibrational Density of States Measurement of Hydrogen Trapped at Dislocations in Deformed $PdH_{0.0008}$," Phys. Rev. B **78** (21), 214101 (2008).

Hodges, C.S., Biggs, S., Walker, L., "Complex Adsorption Behavior of Rodlike Polyelectrolyte–Surfactant Aggregates," Langmuir **25** (8), 4484 (2009).

Holt, S.A., Le Brun, A.P., Majkrzak, C.F., McGillivray, D.J., Heinrich, F., Lösche, M., Lakey, J.H., "An Ion-Channel-Containing Model Membrane: Structural Determination by Magnetic Contrast Neutron Reflectometry," Soft Matter **5** (13), 2567 (2009).

Hong, T., Garlea, V.O., Zheludev, A., Fernandez-Baca, J.A., Manaka, H., Chang, S., Leao, J.B., Poulton, S.J., "Effect of Pressure on the Quantum Spin Ladder Material IPA-$CuCl_3$," Phys. Rev. B **78** (22), 224409 (2008). **(CHRNS)**

Horkay, F., "Biopolymer Gels: Nanostructure and Macroscopic Properties," Prog. Colloid Polym. Sci. **135**, 10 (2008). **(CHRNS)**

Horkay, F., Basser, P.J., "Ionic and pH Effects on the Osmotic Properties and Structure of Polyelectrolyte Gels," J. Polym. Sci., Part B: Polym. Phys. **46** (24), 2803 (2008). **(CHRNS)**

Horkey, F., Basser, P.J., "Ion Sensitivity of DNA Gel Structure," Polym. Prepr. **49** (1), 438 (2008).

Hsieh, D., Qian, D., Berger, R.F., Cava, R.J., Lynn, J.W., Huang, Q., Hasan, M.Z., "Magnetic Excitations in Triangular Lattice $NaCrO_2$," J. Phys. Chem. Solids **69** (12), 3174 (2008).

Huang, E.-W., Liaw, P.K., Porcar, L., Liu, Y., Liu, Y.-L., Kai, J.-J., Chen, W.-R., "Study of Nanoprecipitates in a Nickel-Based Superalloy Using Small-Angle Neutron Scattering and Transmission Electron Microscopy," Appl. Phys. Lett. **93** (16), 161904 (2008).

Huang, Q., Qiu, Y., Bao, W., Green, M.A., Lynn, J.W., Gasparovic, Y.C., Wu, T., Wu, G., Chen, X.H., "Neutron-Diffraction Measurements of Magnetic Order and a Structural Transition in the Parent $BaFe_2As_2$ Compound of FeAs-Based High-Temperature Superconductors," Phys. Rev. Lett. **101** (25), 257003 (2008).

Huang, Q., Zhao, J., Lynn, J.W., Chen, G.F., Lou, J.L., Wang, N.L., Dai, P., "Doping Evolution of Antiferromagnetic Order and Structural Distortion in $LaFeAsO_{1-x}F_x$," Phys. Rev. B **78** (5), 054529 (2008).

Hubbard Jr., F.P., Abbott, N.L., "A Small Angle Neutron Scattering Study of the Thicknesses of Vesicle Bilayers Formed from Mixtures of Alkyl Sulfates and Cationic Bolaform Surfactants," Soft Matter **4** (11), 2225 (2008).

Huber, M.G., Arif, M., Black, T.C., Chen, W.C., Gentile, T.R., Hussey, D.S., Pushin, D.A., Wietfeldt, F.E., Yang, L., "Precision Measurement of the n-^{3}He Incoherent Scattering Length Using Neutron Interferometry," Phys. Rev. Lett. **102** (20), 200401 (2009).

Hudson, S.D., Hutter, J.L., Nieh, M.P., Pencer, J., "Characterization of Anisotropic Poly(Vinyl Alcohol) Hydrogel by Small- and Ultra-Small-Angle Neutron Scattering," J. Chem. Phys. **130** (3), 034903 (2009). **(CHRNS)**

Hyett, G., Green, M.A., Parkin, I.P., "An Investigation of Titanium-Vanadium Nitride Phase Space, Conducted Using Combinatorial Atmospheric Pressure CVD," Chem. Vap. Deposition **14** (9), 309 (2008).

Hyett, G., Green, M.A., Parkin, I.P., "Ultra-Violet Light Activated Photocatalysis in Thin Films of the Titanium Oxynitride, $Ti_{3-\delta}O_4N$," J. Photochem. Photobiol. A **203** (2), 199 (2009).

Ikedo, Y., Nozaki, H., Harada, M., Sugiyama, J., Sato, T.J., Matsuo, Y., Nishiyama, K., Lord, J.S., Qiu, Y., Copley, J.R.D., "Study of Hydrogen Diffusion in Superprotonic Ionic Conductors, MH_xO_4, by μ^+SR and QENS," Nucl. Instr. Meth. A **600** (1), 316 (2009). **(CHRNS)**

Inderhees, S.E., Borchers, J.A., Green, K.S., Kim, M.S., Sun, K., Strycker, G.L., Aronson, M.C., "Manipulating the Magnetic Structure of Co Core/CoO Shell Nanoparticles: Implications for Controlling the Exchange Bias," Phys. Rev. Lett. **101** (11), 117202 (2008).

Jackson, A.J., Li, P.X., Dong, C.C., Thomas, R.K., Penfold, J., "Structure of Partially Fluorinated Surfactant Monolayers at the Air - Water Interface," Langmuir **25** (7), 3957 (2009).

Jacques, D.A., Langley, D.B., Jeffries, C.M., Cunningham, K.A., Burkholder, W.F., Guss, J.M., Trewhella, J., "Histidine Kinase Regulation by a Cyclophilin-Like Inhibitor," J. Mol. Biol. **384**, 422 (2008). **(CHRNS)**

Janik, J.A., Zhou, H.D., Jo, Y.J., Balicas, L., MacDougall, G.J., Luke, G.M., Garrett, J.D., McClellan, K.J., Bauer, E.D., Sarrao, J.L., Qiu, Y., Copley, J.R.D., Yamani, Z., Buyers, J.L., Wiebe, C.R., "Itinerant Spin Excitations Near the Hidden Order Transition in URu_2Si_2," J. Phys.: Condens. Mat. **21** (19), 192202 (2009). **(CHRNS)**

Jha, A.K., Hule, R.A., Jiao, T., Teller, S.S., Clifton, R.J., Duncan, R.L., Pochan, D.J., Jia, X., "Structural Analysis and Mechanical Characterization of Hyaluronic Acid-Based Doubly Cross-Linked Networks," Macromol. **42** (2), 537 (2009). **(CHRNS)**

Ji, S., Lee, S.H., Broholm, C., Koo, T.Y., Ratcliff, W., Cheong, S.W., Zschack, P., "Spin-Lattice Order in Frustrated $ZnCr_2O_4$," Phys. Rev. Lett. **103** (3), 037201 (2009).

Jiang, J., Li, C., Lombardi, J., Colby, R.H., Rigas, B., Rafailovich, M.H., Sokolov, J.C., "The Effect of Physiologically Relevant Additives on the Rheological Properties of Concentrated Pluronic Copolymer Gels," Polymer **49** (16), 3561 (2008). **(CHRNS)**

Jo, Y.J., Lee, S., Choi, E.S., Yi, H.T., Ratcliff, W., Choi, Y.J., Kiryukhin, V., Cheong, S.W., Balicas, L., "3:1 Magnetization Plateau and Suppression of Ferroelectric Polarization in an Ising Chain Multiferroic," Phys. Rev. B **79** (1), 012407 (2009).

Johnson, M.E., Malardier-Jugroot, C., Murarka, R.K., Head-Gordon, T., "Hydration Water Dynamics Near Biological Interfaces," J. Phys. Chem. B **113** (13), 4082 (2009). **(CHRNS)**

Kadowaki, H., Motoya, K., Sato, T.J., Lynn, J.W., Fernandez-Baca, J.A., Kikuchi, J., "Quantum Phase Transition in the Itinerant Antiferromagnet $(V_{0.9}Ti_{0.1})_2O_3$," Phys. Rev. Lett. **101** (9), 096406 (2008).

Kalman, D.P., Wagner, N.J., "Microstructure of Shear-Thickening Concentrated Suspensions Determined by Flow-USANS," Rheol. Acta, in press. **(CHRNS)**

Kamazawa, K., Louca, D., Morinaga, R., Sato, T.J., Huang, Q., Copley, J.R.D., Qiu, Y., "Field-Induced Antiferromagnetism and Competition in the Metamagnetic State of Terbium Gallium Garnet," Phys. Rev. B **78** (6), 064412 (2008). **(CHRNS)**

Kang, J., Shin, N., Jang, D.Y., Prabhu, V.M., Yoon, D.Y., "Structure and Properties of Small Molecule–Polymer Blend Semiconductors for Organic Thin Film Transistors," J. Am. Chem. Soc. **130** (37), 12273 (2008).

Kang, S., Prabhu, V.M., Soles, C.L., Lin, E.K., and Wu, W.-L., "Methodology for Quantitative Measurements of Multilayer Polymer Thin Films with IR Spectroscopic Ellipsometry," Macromol. **42** (14) 5296 (2009).

Karul, A., Tan, K.T., White, C.C., Hunston, D.L., Marshall, S.T., Akgun, B., Satija, S.K., Soles, C.L., Vogt, B.D., "Impact of Polymer Modulus/Chain Mobility on Water Accumulation at Polymer/Metal Oxide Interfaces," Polymer **50** (14), 3234 (2009).

Keally, C., Sokolova, A., Kearley, G., Kemner, E., Russina, M., Faraone, A., Hamilton, W., Gilbert, E., "Dynamical Transition in a Large Globular Protein: Macroscopic Properties and Glass Transition," Biochim. Biophys. Acta, in press. **(CHRNS)**

Kennon, B.S., Her, J.H,. Stephens, P.W., Miller, J.S., "Diruthenium Tetracarbonate Trianion, $[Ru^{II/III}_2(O_2CO)_4]_3^-$, Based Molecule-Based Magnets: Three-Dimensional Network Structure and Two-Dimensional Magnetic Ordering," Inorg. Chem. **48** (13), 6117 (2009).

Kent, M.S., Murton, J.K., Dibble, D.C., Zendejas, F., Banuelos, J.L., Urquidi, J., Hjelm, R., Simmons, B.A., "Effect of Agitation/Flow on the Enzymatic Digestion of Cellulose: A Structural Study by SANS," ACS Chem. Biol., in press.

Kent, M.S., Murton, J.K., Zendejas, F.J., Tran, H., Simmons, B.A., Satija, S., Kuzmenko, I., "Nanosilica Formation at Lipid Membranes Induced by the Parent Sequence of a Silaffin Peptide," Langmuir **25** (1), 301 (2009).

Kepa, H., Majkrzak, C.F., Sipatov, A., Fedorov, A.G., Samburskaya, T.A., Giebultowicz, T.M., "Interlayer Coupling in EuS/SrS, EuS/PbSe and EuS/PbTe Magnetic Semiconductor Superlattices," J. Phys.: Condens. Mat. **21** (12), 124207 (2009).

Khan, A.S., Meredith, C.S., "Thermo-Mechanical Response of Al 6061 with and Without Equal Channel Angular Pressing (ECAP)," Int. J. Plast., in press.

Khoadadadi, S., Pawlus, S., Sokolov, A.P., "Influence of Hydration on Protein Dynamics: Combining Dielectric and Neutron Scattering Spectroscopy Data," J. Phys. Chem. B **112** (45), 14273 (2008). **(CHRNS)**

Kilburn, D., Sokol, P.E., Brown, C.M., "Inelastic Neutron Scattering From Confined Molecular Oxygen," Phys. Rev. B **78** (21), 214304 (2008). **(CHRNS)**

Kim, J.H., Ji, S., Lee, S.H., Lake, B., Yildirim, T., Nojiri, H., Kikuchi, H., Habicht, K., Qiu, Y., Kiefer, K., "External Magnetic Field Effects on a Distorted Kagome Antiferromagnet," Phys. Rev. Lett. **101** (10), 107201 (2008). **(CHRNS)**

Kim, J.H., Lee, S.H., Park, S.I., Kenzelmann, M., Harris, A.B., Schefer, J., Chung, J.H., Majkrzak, C.F., Takeda, M., Wakimoto, S., Park, S.Y., Cheong, S.W., Matsuda, M., Kimura, H., Noda, Y., Kakurai, K., "Spiral Spin Structures and Origin of the Magnetoelectric Coupling in YMn_2O_5," Phys. Rev. B **78** (24), 245115 (2008).

Kim, M.H., Glinka, C.J., "Correlation between Structure and Vapor Sorption in Semicrystalline Linear Polyethylene: One Dimensional Nano-Swelling Measured Using in Situ Vapor Sorption Small Angle Neutron Scattering (iVSANS)," Macromol. **42** (7), 2618 (2009). **(CHRNS)**

Kim, T.H., Kang, S.H., Doe, C., Yu, J., Sim, J.B., Kim, J., Kline, S.R., Choi, S.M., "Highly Ordered Self-Assembly of 1D Nanoparticles in Phospholipids Driven by Curvature and Electrostatic Interaction," J. Am. Chem. Soc. **131** (21), 7456 (2009).

Kim, T.J., Kim, J.R., Sim, C.M., Lee, S.W., Kaviany, M., Son, S.Y., Kim, M.H., "Experimental Approaches for Distribution and Behavior of Water in PEMFC Under Flow Direction and Differential Pressure Using Neutron Imaging Technique," Nucl. Instr. Meth. A **600** (1), 325 (2009).

King, G., Wills, A.S., Woodward, P.M., "Magnetic Structures of Na*L*MnWO$_6$ Perovskites (*L*=La,Nd,Tb)," Phys. Rev. B **79** (22), 224428 (2009).

Kirby, B.J., Kan, D., Luykx, A., Mrakami, M., Kundaliya, D., Takeuchi, I., "Anomalous Ferromagnetism in $TbMnO_3$ Thin Films," J. Appl. Phys. **105** (7), 07D917 (2009).

Kirby, B.J., Watson, S.M., Davies, J.E., Zimanyi, G.T., Liu, K., Shull, R.D., Borchers, J.A., "Direct Observation of Magnetic Gradient in Co/Pd Pressure-Graded Media," J. Appl. Phys. **105** (7), 07C929 (2009).

Kiryukhin, V., Lee, S., Ratcliff, W., Huang, Q., Yi, H.T., Choi, Y.J., Cheong, S.W., "Order by Static Disorder in the Ising Chain Magnet $Ca_3Co_{2-x}Mn_xO_6$," Phys. Rev. Lett. **102** (18), 187202 (2009).

Klimczuk, T., McQueen, T.M., Williams, A.J., Huang, Q., Ronning, F., Bauer, E.D., Thompson, J.D., Green, M.A., Cava, R.J., "Superconductivity at 2.2 K in the Layered Oxypnictide $La_3Ni_4P_4O_2$," Phys. Rev. B **79** (1), 012505 (2009).

Klimczuk, T., Zandbergen, H.W., Huang, Q., McQueen, T.M., Ronning, F., Kusz, B., Thompson, J.D., Cava, R.J., "Cluster-Glass Behavior of a Highly Oxygen Deficient Perovskite, $BaBi_{0.28}Co_{0.72}O_{2.2}$," J. Phys.: Condens. Mat. **21** (10), 105801 (2009).

Knoll, W., Naumann, R., Friedrich, M., Robertson, J.W.F., Lösche, M., Heinrich, F., McGillivray, D.J., Schuster, B., Gufler, P.C., Pum, D., Sleyter, Y.B., "Solid Supported Lipid Membranes: New Concepts for the Biomimetic Functionalization of Solid Surfaces," Biointerph. **3** (2), FA125 (2008).

Kofu, M., Kim, J.H., Ji, S., Lee, S.H., Ueda, H., Qiu, Y., Kang, H.J., Green, M.A., Ueda, Y., "Weakly Coupled S = ½ Quantum Spin Singlets in $Ba_3Cr_2O_8$," Phys. Rev. Lett. **102** (3), 037206 (2009). **(CHRNS)**

Kofu, M., Lee, S.H., Fujita, M., Kang, H.J., Eisaki, H., Yamada, K., "Hidden Quantum Spin-Gap State in the Static Stripe Phase of High-Temperature $La_{2-x}Sr_xCuO_4$ Superconductors," Phys. Rev. Lett. **102** (4), 047001 (2009). **(CHRNS)**

Kofu, M., Qiu, Y., Bao, W., Lee, S.H., Chang, S., Wu, T., Wu, G., Chen, X.H., "Neutron Scattering Investigation of the Magnetic Order in Single Crystalline $BaFe_2As_2$," New J. Phys. **11** (5), 055001 (2009). **(CHRNS)**

Kothapalli, K., Nasreen, F., Peterson, J., Nakotte, H., El-Khatib, S., Vogel, S.C., Llobet, A., Reiche, H., Swainson, I., Brück, E., "Effect of Temperature on Hybridization and Magnetism in UPdSn and UCuSn," J. Appl. Phys. **105** (7), 07E121 (2009).

Kravtsov, E., Haskel, D., te Velthuis, S.G.E., Jiang, J.S., Kirby, B.J., "Complementary Polarized Neutron and Resonant X-Ray Magnetic Reflectometry Measurements in Fe/Gd Heterostructures: Case of Inhomogeneous Intralayer Magnetic Structure," Phys. Rev. B **79** (13), 134438 (2009).

Kreyssig, A., Green, M.A., Lee, Y., Samolyuk, G.D., Zajdel, P., Lynn, J.W., Bud'ko, S.L., Torikachvili, M.S., Ni, N., Nandi, S., Leão, J.B., Poulton, S.J., Argyriou, D.N., Harmon, B.N., McQueeney, Canfield, P.C., Goldman, A.I., "Pressure-Induced Volume-Collapsed Tetragonal Phase of $CaFe_2As_2$ as Seen via Neutron Scattering," Phys. Rev. B **78** (18), 184517 (2008).

Krycka, K.L., Booth, R., Borchers, J.A., Chen, W.C., Conlon, C., Gentile, T., Hogg, C., Ijiri, Y., Laver, M., Maranville, B.B., "Resolving 3D Magnetism in Nanoparticles Using Polarization Analyzed SANS," Physica B, in press. **(CHRNS)**

Krycka, K.L., Maranville, B.B., Borchers, J.A., Castaño, Ng, B.G., Perkinson, J.C., Ross, C.A., "Magnetic Domain Formation within Patterned NiFe/Cu/Co Ellipses," J. Appl. Phys. **105** (7), 07C120 (2009).

Kučerka, N., Nagle, J.F., Sachs, J.N., Feller, S., Pencer, J., Jackson, A.J., Katsaras, J., "Lipid Bilayer Structure Determined by the Simultaneous Analysis of Neutron and X-Ray Scattering Data," Biophys. J. **95** (5), 2356 (2008). **(CHRNS)**

Kumar, R., Raghavan, S.R., "Photogelling Fluids Based on Light-Activated Growth and Zwitterionic Wormlike Micelles," Soft Matter **5** (4), 797 (2009). **(CHRNS)**

Lagi, M., Chu, X., Kim, S., Mallamace, F., Baglioni, P., Chen, S.-H., "The Low-Temperature Dynamic Crossover Phenomenon in Protein Hydration Water: Simulations vs Experiments," J. Phys. Chem. B **112** (6), 1571 (2008).

Lashley, J.C., Shapiro, S.M., Winn, B.L., Opeil, C.P., Manley, M.E., Atalas, A., Ratcliff, W., Park, T., Fisher, R.A., Mihaila, B., Riseborough, P., Salje, E.K., Smith, J.L., "Observation of a Continuous Phase Transition in a Shape-Memory Alloy," Phys. Rev. Lett. **101** (13), 135703 (2008).

Lashley, J.C., Stevens, R., Crawford, M.K., Boerio-Goates, J., Woodfield, B.F., Qiu, Y., Lynn, J.W., Goddard, P.A., Fisher, R.A., "Specific Heat and Magnetic Susceptibilities of the Spinels $GeNi_2O_4$ and $GeCo_2O_4$," Phys. Rev. B **78** (10), 104406 (2008). **(CHRNS)**

Laver, M., Bowell, C.J., Forgan, E.M., Abrahamsen, A.B., Fort, D., Dewhurst, C.D., Mühlbauer, S., Christen, D.K., Kohlbrecher, J., Cubitt, R., Ramos, S., "Structure and Degeneracy of Vortex Lattice Domains in Pure Superconducting Niobium: A Small-Angle Neutron Scattering Study," Phys. Rev. B **79** (1), 014518 (2009).

Law, B.M., Brown, M.D., Marchand, L., Lurio, L.B., Hamilton, W.A., Kuzmenko, I., Gog, T., Satija, S., Watkins, E., Majewski, J., "Adsorption at Liquid Interfaces: A Comparison of Multiple Experimental Techniques," Eur. Phys. J. **167** (1), 127 (2009).

Lawes, G., Kenzelmann, M., Broholm, C., "Magnetically Induced Ferroelectricity in the Buckled Kagomé Antiferromagnet $Ni_3V_2O_8$," J. Phys.: Condens. Mat. **20** (43), 434205 (2008).

Lee, H.J., Soles, C.L., Vogt, B.D., Liu, D.W., Wu, W.L., Lin, E.K., Kim, H.C., Lee, V.Y., Volksen, W., Miller, R.D., "Effect of Porogen Molecular Architecture and Loading on Structure of Porous Thin Films," Chem. Mater. **20** (24), 7390 (2008).

Lee, J.H., Danino, D., Raghavan, S.R., "Polymerizable Vesicles Based on a Single-Tailed Fatty Acid Surfactant: A Simple Route to Robust Nanocontainers," Langmuir **25** (3), 1566 (2009). **(CHRNS)**

Lee, S., Choi, T., Ratcliff, W., Erwin, R., Cheong, S.W., Kiryukhin, V., "Single Ferroelectric and Chiral Magnetic Domain of Single-Crystalline $BiFeO_3$ in an Electric Field," Phys. Rev. B **78** (10), 100101 (2008).

Lee, S., Chung, J.H., Liu, X., Furdyna, J.K., Kirby, B.J., "Ferromagnetic Semiconductor GaMnAs," Mater. Today **12** (14), 14 (2009).

Lee, S., Tirumala, V.R., Nagao, M., Tominaga, T., Lin, E.K., Gong, J.P., Wu, W.L., "Dynamics in Multicomponent Polyelectrolyte Solutions," Macromol. **42** (4), 1293 (2009). **(CHRNS)**

Lee, S.W., Hussey, D.S., Jacobson, D.L., Sim, C.M., Arif, M., "Development of the Grating Phase Neutron Interferometer at a Monochromatic Beam Line," Nucl. Instr. Meth. A **605** (1), 16 (2009).

Leighton, C., Stauffer, D.D., Huang, Q., Ren, Y., El-Khatib, S., Torija, M.A., Wu, J., Lynn, J.W., Wang, L., Frey, N.A., Srikantha, H., Davies, J.E., Liu, K., Mitchell, J.F., "Coupled Structural/Magnetocrystalline Anisotropy Transitions in the Doped Perovskite Cobaltite $Pr_{1-x}Sr_xCoO_3$," Phys. Rev. B **79** (21), 214420 (2009).

Lelong, G., Bhattacharyya, S., Kline, S., Cacciaguerra, T., Gonzalez, M.A., Saboungi, M.-L., "Effect of Surfactant Concentration on the Morphology and Texture of MCM-41 Materials," J. Phys. Chem. C **112** (29), 10674 (2008). **(CHRNS)**

Li, J., Callaway D.J., Bu Z., "Ezrin Induces Long-Range Interdomain Allostery in the Scaffolding Protein NHERF1", J. Mol. Biol., in press. **(CHRNS)**

Li, J., Jensen, T.B.S., Andersen, N.H., Zarestky, J.L., McCallum, R.W., Chung, J.H., Lynn, J.W., Vaknin, D., "Tweaking the Spin-Wave Dispersion and Suppressing the Incommensurate Phase in $LiNiPO_4$ by Iron Substitution," Phys. Rev. B **79** (17), 174435 (2009). **(CHRNS)**

Li, J., Singh, U.G., Schladt, T.D., Stalick, J.K., Scott, S.L., Seshadri, R., "Hexagonal $YFe_{1-x}Pd_xO_{3-\delta}$: Nonperovskite Host Compounds for Pd^{2+} and Their Catalytic Activity for CO Oxidation," Chem. Mater. **20** (20), 6567 (2008).

Li, J., Tian, W., Chen, Y., Zarestky, J.L., Lynn, J.W., Vaknin, D., "Antiferromagnetism in the Magnetoelectric Effect Single Crystal $LiMnPO_4$," Phys. Rev. B **79** (14), 144410 (2009). **(CHRNS)**

Li, S., Chen, Y., Chang, S., Lynn, J.W., Li, L., Luo, Y., Cao, G., Xu, Z., Dai, P., "Spin Gap and Magnetic Resonance in Superconducting $BaFe_{1.9}Ni_{0.1}As_2$," Phys. Rev. B **79** (17), 174527 (2009). **(CHRNS)**

Li, S., de la Cruz, C., Huang, Q., Chen, G.F., Xia, T.L., Luo, J.L., Wang, N.L., Dai, P., "Structural and Magnetic Phase Transitions in $Na_{1-\delta}FeAs$," Phys. Rev. B **80** (2), 020504 (2009).

Li, S., de la Cruz, C., Huang, Q., Chen, Y., Lynn, J.W., Hu, J., Huang, Y.L., Hsu, F.C., Yeh, K.W., Wu, M.K., Dai, P., "First-Order Magnetic and Structural Phase Transitions in $Fe_{1+y}Se_xTe_{1-x}$," Phys. Rev. B **79** (5), 054503 (2009).

Li, T., Hong, K., Porcar, L., Verduzco, R., Butler, P.D., Smith, G.S., Liu, Y., Chen, W.R., "Assess the Intramolecular Cavity of a PAMAM Dendrimer in Aqueous Solution by Small-Angle Neutron Scattering," Macromol. **41** (22), 8916 (2008). **(CHRNS)**

Li, Y.C., Chen, C.Y., Chang, Y.X., Chuang, P.Y., Chen, J.H., Chen, H.L., Hsu, C.S., Ivanov, V.A., Khalatur, P.G., Chen, S.A., "Scattering Study of the Conformational Structure and Aggregation Behavior of a Conjugated Polymer Solution," Langmuir **25** (8), 4668 (2009).

Liberatore, M.W., Nettesheim, F., Vasquez, P.A., Helgeson, M.E., Wagner, N.J., Kaler, E.W., Cook, L.P., Porcar, L., Hu, Y.T., "Microstructure and Shear Rheology of Entangled Wormlike Micelles in Solution," J. Rheol. **53** (2), 441 (2009).

Lin, X., Telepeni, I., Blake, A.J., Dailly, A., Brown, C.M., Simmons, J.M., Zoppi, M., Walker, G.S., Thomas, K.M., Mays, T.J., Hubberstey, P., Champness, N.R., Schröder, M., "High Capacity Hydrogen Adsorption in Cu(II) Tetracarboxylate Framework Materials: The Role of Pore Size, Ligand Functionalization, and Exposed Metal Sites," J. Am. Chem. Soc. **131** (6), 2159 (2009).

Lindstrom, R.M., Fischbach, E., Buncher, J.B., Greene, G.L., Jenkins, J.H., Krause, D.E., Mattes, J.J., and Yue, A., "Does the Half-Life of a Radioactive Sample Depend on its Shape?," Trans. Am. Nucl. Soc. **100**, 225 (2009).

Lindstrom, R.M., Fleming, R.F., "Neutron Self-Shielding Factors for Simple Geometries, Revisited," Chem. Anal. (Warsaw) **53**, 855 (2008).

Lindstrom, R.M., Zeisler, R., Mackey, E.A., Liposky, P.J., Popelka-Filcoff, R.S., Williams, R.E., "Neutron Irradiation in Activation Analysis: A New Rabbit for the NBS," J. Radioanal. Nucl. Chem. **278** (3), 665 (2008).

Liu, D., Yue, M., Zhang, J., McQueen, T.M., Lynn, J.W., Wang, X., Chen, Y., Li, J., Cava, R.J., Liu, X., Altounian, Z., Huang, Q., "Origin and Tuning of the Magnetocaloric Effect in the Magnetic Refrigerant $Mn_{1.1}Fe_{0.9}(P_{0.8}Ge_{0.2})$," Phys. Rev. B **79** (1), 014435 (2009).

Liu, G., Huang, Q., Kaduk, J.A., Yang, Z., Lucas, C., Wong-Ng, W., "X-Ray and Neutron Powder Diffraction Studies of $Ba(Nd_xY_{2-x})CuO_5$," J. Solid State Chem. **181** (12), 3236 (2008).

Liu, H.-T., Gnäupel-Herold, T., Hovanski, Y., Dahl, M.E., "Fatigue Performance Enhancement of AWJ-Machined Aircraft Aluminum with Dry-Grit Blasting," in "Proceedings of the 2009 American WJTA Conference and Expo," edited by Hashish, M. (Am WJTA Conf. Proc.), in press.

Liu, Y., Her, J.H., Dailly, A., Ramirez-Cuesta, A.J., Neumann, D.A., Brown, C.M., "Reversible Structural Transition in MIL-53 with Large Temperature Hysteresis," J. Am. Chem. Soc. **130** (35), 11813 (2008). **(CHRNS)**

Liu, Y., Watson, S.M., Lee, T., Gorham, J.M., Katz, H.E., Borchers, J.A., Fairbrother, H.D., Reich, D.H., "Correlation Between Microstructure and Magnetotransport in Organic Semiconductor Spin-Valve Structures," Phys. Rev. B **79** (7), 075312 (2009).

Livingston, R.A., Bumrongjaroen, W., Allen, A.J., "The Fractal Ratio as a Metric of Nanostructure Development in Hydrating Cement Paste," in "Nanotechnology in Construction 3," edited by Bittnar, Z., Bartos, P.J.M., Němeček, J., Šmilauer, V., Zeman, J., (Springer Berlin Heidelberg), Part 2, 101 (2009).

Luo, J., Xu, H., Liu, Y., Zhao, Y., Daemen, L.L., Brown, C., Timofeeva, T.V., Ma, S., Zhou, H.C., "Hydrogen Adsorption in a Highly Stable Porous Rare-Earth Metal-Organic Framework: Sorption Properties and Neutron Diffraction Studies," J. Am. Chem. Soc. **130** (30), 9626 (2008).

Lynn, J.W., Dai, P., "Neutron Studies of the Iron-Based Family of High T_C Magnetic Superconductors," Physica C **469** (9), 469 (2009).

Ma, S., Simmons, J.M., Li, J.R., Yuan, D., Wang, W., Liu, D.J., Zhou, H.C., "A Nanotubular Metal-Organic Framework with Permanent Porosity: Structure Analysis and Gas Sorption Studies," Chem. Commun. 4049 (2009).

Ma, S., Simmons, J.M., Sun, D., Yuan, D., Zhou, H.C., "Porous Metal-Organic Frameworks Based on an Anthracene Derivative: Syntheses, Structure Analysis, and Hydrogen Sorption Studies," Inorg. Chem. **48** (12), 5263 (2009).

Mackey, E.A., Spatz, R.O., "Assessment of Stability of Trace Elements in Two Natural Matrix Environmental Standard Reference Materials: NIST-SRM 1547 Peach Leaves and NIST-SRM 1566a Oyster Tissue," J. Radioanal. Nucl. Chem. **281** (1), 91 (2009).

Majkrzak, C.F., Berk, N.F., Kienzle, P., Perez-Salas, U., "Progress in the Development of Phase-Sensitive Neutron Reflectometry Methods," Langmuir **25** (7), 4154 (2009).

Mamontov, E., Cole, D.R., Dai, S., Pawel, M.D., Liang, C.D., Jenkins, T., Gasparovic, G., Kintzel, E., "Dynamics of Water in LiCl and $CaCl_2$ Aqueous Solutions Confined in Silica Matrices: A Backscattering Neutron Spectroscopy Study," Chem. Phys. **352** (1), 117 (2008). **(CHRNS)**

Mamontov, E., Vlcek, L., Wesolowski, D.J., Cummings, P.T., Rosenqvist, J., Wang, W., Cole, D.R., Anovitz, L.M., Gasparovic, G., "Suppression of the Dynamic Transition in Surface Water at Low Hydration Levels: A Study of Water on Rutile," Phys. Rev. E **79** (5), 051504 (2009). **(CHRNS)**

Manley, M.E., Sievers, A.J., Lynn, J.W., Kiselev, S.A., Agladze, N.I., Chen, Y., Llobet, A., Alatas, A., "Intrinsic Localized Modes Observed in the High-Temperature Vibrational Spectrum of NaI," Phys. Rev. B **79** (13), 134304 (2009).

Manson, J.L., Lancaster, T., Blundell, S.J., Qiu, Y., Singleton, J., Sengupta, P., Pratt, F.L., Kang, J., Lee, C., and Whangbo, M.H., "Spin Fluctuations and Orbital Ordering in Quasi-One-Dimensional α-$Cu(dca)_2(pyz)$ {dca=Dicyanamide=$N(CN)_2$; pyz=Pyrazine}, a Molecular Analogue of $KCuF_3$," Polyhedron, in press. **(CHRNS)**

Marszalek, J., Pojman, J.A., "Neutron Scattering Study of the Structural Change Induced by Photopolymerization of AOT/D_2O/Dodecyl Acrylate Inverse Microemulsions," Langmuir **24** (23), 13694 (2008). **(CHRNS)**

Mayumi, K., Endo, H., Osaka, N., Yokoyama, H., Nagao, M., Shibayama, M., Ito, K., "Mechanically Interlocked Structure of Polyrotaxane Investigated by Contrast Variation Small-Angle Neutron Scattering," Macromol., in press.

Mayumi, K., Nagao, M., Endo, H., Osaka, N., Shibayama, M., Ito, K., "Dynamics of Polyrotaxane Investigated by Neutron Spin Echo Technique," Physica B, in press. **(CHRNS)**

McGillivray, D.J., Valincius, G., Heinrich, F., Robertson, J.W.F., Vanderah, D.J., Febo-Ayala, W., Ignatjev, I., Lösche, M., Kasianowicz, J.J., "Structure of Functional Staphylococcus Aureus α-Hemolysin Channels in Tethered Bilayer Lipid Membranes," Biophys. J. **96** (4), 1547 (2009).

McIver, J.W., Erwin, R., Chen, W.C., Gentile, T.R., "End-Compensated Magnetostatic Cavity for Polarized ^{3}He Neutron Spin Filters," Rev. Sci. Instrum. **80** (6), 063905 (2009).

McQueen, T.M., Huang, Q., Ksenofontov, V., Felser, C., Xu, Q., Zandbergen, H., Hor, Y.S., Allred, J., Williams, A.J., Qu, D., Checkelsky, J., Ong, N.P., Cava, R.J., "Extreme Sensitivity of Superconductivity to Stoichiometry in $Fe_{1+\delta}Se$," Phys. Rev. B **79** (1), 014522 (2009).

McQueen, T.M., Klimczuk, T., Williams, A.J., Huang, Q., Cava, R.J., "Stoichiometry, Spin Fluctuations, and Superconductivity in LaNiPO," Phys. Rev. B **79** (17), 172502 (2009).

McQueen, T.M., Stephens, P.W., Huang, Q., Klimczuk, T., Ronning, F., Cava, R.J., "Successive Orbital Ordering Transitions in $NaVO_2$," Phys. Rev. Lett. **101** (16), 166402 (2008).

Melnichenko, Y.B., Radlinski, A.P., Mastalerz, M., Cheng, G., Rupp, J.A., "Characterization of the CO_2 Fluid Adsorption in Coal as a Function of Pressure Using Neutron Scattering Techniques (SANS and USANS)," Int. J. Coal Geo. **77** (2), 69 (2009). **(CHRNS)**

Meure, L.A., Knott, R., Foster, N.R., Dehghani, F., "The Depressurization of an Expanded Solution into Aqueous Media for the Bulk Production of Liposomes," Langmuir **25** (1), 326 (2009).

Mikel, S.E., Biernacki, J.J., Gnaeupel-Herold, T., "A Neutron Diffraction-Based Technique for Determining Phase Resolved Strains in Portland Cement," ACI Mater. J., in press.

Millican, J., Phelan, D., Thomas, E.L., Leão, J.B., Carpenter, E., "Pressure-Induced Effects on the Structure of the FeSe Superconductor," Solid State Commun. **149** (17), 707 (2009).

Moore, R.G., Lumsden, M.D., Stone, M.B., Zhang, J., Chen, Y., Lynn, J.W., Jin, R., Mandrus, D., Plummer, E.W., "Phonon Softening and Anomalous Mode Near the x_c=0.5 Quantum Critical Point in $Ca_{2-x}Sr_xRuO_4$," Phys. Rev. B **79** (17), 172301 (2009).

Mühlbauer, S., Pfleiderer, C., Böni, P., Laver, M., Forgan, E.M., Fort, D., Keiderling, U., Behr, G., "Morphology of the Superconducting Vortex Lattice in Ultrapure Niobium," Phys. Rev. Lett. **102** (13), 136408 (2009).

Mukherjee, P.P., Springer, T., Mukundan, Hussey, D.S., Jacobson, D., Arif, M., and Borup, R.L., "Probing Liquid Water Profile in the Polymer Electrolyte Fuel Cell Membrane," ECS Trans. **16** (2), 1027 (2008).

Mukundan, R., Davey, J., Lujan, R., Spendelow, J., Kim, Y.S., Hussey, D.S., Jacobson, D., Arif, M., Borup, R.L., "Performance and Durability of PEM Fuel Cells Operated at Sub-Freezing Temperatures," ECS Trans. **16** (2), 1939 (2008).

Murthi, V.S., Dura, J.A., Satija, S.K., Majkrzak, C.F., "Water Uptake and Interfacial Structural Changes of a Perfluorosulfonic Acid Ionomer Membranes Measured by Neutron Reflectivity for PEM Fuel Cells," ECS Trans. **16** (2), 1471 (2008).

Nagao, M., Seto H., "Full Fitting Analysis of the Relative Intermediate Form Factor Measured by Neutron Spin Echo," Physica B, in press. **(CHRNS)**

Nayak, A., Sorci, M., Krueger, S., Belfort, G., "A Universal Pathway for Amyloid Nucleus and Precursor Formation for Insulin," Proteins **74** (3), 556 (2009).

Nedoma, A.J., Robertson, M.L., Wanakule, N.S., Balsara, N.P., "Measurements of the Composition and Molecular Weight Dependence of the Flory–Huggins Interaction Parameter," Macromol. **41** (15), 5773 (2008). **(CHRNS)**

Nettesheim, F., Liberatore, M.W., Hodgdon, T.K., Wagner, N.J., Kaler, E.W., Vethamuthu, M., "Influence of Nanoparticle Addition on the Properties of Wormlike Micellar Solutions," Langmuir **24** (15), 7718 (2008).

Nieh, M.P., Guiver, M.D., Kim, D.S., Ding, J., Norsten, T., "Morphology of Comb-Shaped Proton Exchange Membrane Copolymers Based on a Neutron Scattering Study," Macromol. **41** (16), 6176 (2008).

Nieh, M.-P., Yamani, Z., Kucerka, N., Katsaras, J., Burgess, D., Breton, H., "Adapting a Triple-Axis Spectrometer for Small Angle Neutron Scattering Measurements," Rev. Sci. Instrum. **79** (9), 095102 (2008).

Odette, G.R., Alinger, M.J., Wirth, B.D., "Recent Developments in Irradiation-Resistant Steels," Annu. Rev. Mater. Sci. **38**, 471 (2008).

Olsen, B.D., Shah, M., Ganesan, V., Segalman, R.A., "Universalization of the Phase Diagram for a Model Rod–Coil Diblock Copolymer," Macromol. **41** (18), 6809 (2008). **(CHRNS)**

Page, K., Li, J., Savinelli, R., Szumila, H.N., Zhang, J., Stalick, J.K., Proffen, T., Scott, S.L., Seshadri, R., "Reciprocal-Space and Real-Space Neutron Investigation of Nanostructured Mo_2C and WC," Solid State Sci. **10** (11), 1499 (2008).

Page, K.A., Park, J.K., Moore, R.B., Garcia Sakai, V., "Direct Analysis of the Ion-Hopping Process Associated with the α-Relaxation in Perfluorosulfonate Ionomers Using Quasielastic Neutron Scattering," Macromol. **42** (7), 2729 (2009). **(CHRNS)**

Page, M.G., Warr, G.G., "Influence of the Structure and Composition of Mono- and Dialkyl Phosphate Mixtures on Aluminum Complex Organogels," Langmuir **25** (15), 8810 (2009). **(CHRNS)**

Park, J., Li, X., Tran, D., Abdel-Baset, T., Hussey, D.S., Jacobson, D.L., Arif, M., "Neutron Imaging Investigation of Liquid Water Distribution in and the Performance of a PEM Fuel Cell," Int. J. Hydrogen Energy **33** (13), 3373 (2008).

Park, J., Watson, S.M., Furjanic, C.M., Draganova, D.K., Chen, C.Y., Borchers, J.A., Carey, M.J., Sparks, P.D., Eckert, J.C., "Probing the Effect of Structural Roughness on Domain Wall Formation in Spin Valves Using Off-Specular Reflectivity Techniques," IEEE Trans. Mag. **44** (11), 2839 (2008).

Park, M.J., Balsara, N.P., Jackson, A., "Order–Disorder Transitions in Block Copolymer Electrolytes at Equilibrium with Humid Air," Macromol., in press. **(CHRNS)**

Park, S., Fitzsimmons, M.R., Majkrzak, C.F., Schultz, B.D., Palmstrøm, C.J., "The Influence of Growth Temperature and Annealing on the Magnetization Depth Profiles Across Ferromagnetic/Semiconductor Interfaces," J. Appl. Phys. **104** (8), 083905 (2008).

Paul, R.L., Lindstrom, R.M., Brocker, C., Mackey, E.A., "Design of a New Instrument for Cold Neutron Prompt Gamma-Ray Activation Analysis at NIST," J. Radioanal. Nucl. Chem. **278** (3), 697 (2008).

Peterson, V.K., Whitten, A.E., "Hydration Processes in Tricalcium Silicate: Application of the Boundary Nucleation Model to Quasielastic Neutron Scattering Data," J. Phys. Chem. C **113** (6), 2347 (2009).

Phelan, D., Louca, D., Ancona, S.N., Rosenkranz, S., Zheng, H., Mitchell, J.F., "Neutron Scattering Study of the Competing Magnetic Correlations in $La_{0.85}Sr_{0.15}CoO_3$," Phys. Rev. B **79** (9), 094420 (2009). **(CHRNS)**

Phelan, D., Millican, J.N., Thomas, E.L., Leão, J.B., Qiu, Y., Paul, R., "Neutron Scattering Measurements of the Phonon Density of States of $FeSe_{1-x}$ Superconductors," Phys. Rev. B **79** (1), 014519 (2009). **(CHRNS)**

Phelan, D., Yu, J., Louca, D., "Jahn-Teller Spin Polarons in Perovskite Cobaltites," Phys. Rev. B **78** (9), 094108 (2008).

Porcar, L., Liu, Y., Hong, K., Butler, P.D., Huang, E.W., Chen, W.R., "Counterion Association and Structural Conformation Change of Charged PAMAM Dendrimer in Aqueous Solutions Revealed by Small Angle Neutron Scattering," Macromol. Symp. **279** (1), 65 (2009). **(CHRNS)**

Porcar, L., Liu, Y., Verduzco, R., Hong, K., Butler, P.D., Magid, L.J., Smith, G.S., Chen, W.R., "Structural Investigation of PAMAM Dendrimers in Aqueous Solutions Using Small-Angle Neutron Scattering: Effect of Generation," J. Phys. Chem. B **112** (47), 14772 (2008). **(CHRNS)**

Pozzo, D.C., "Neutron-Scattering Probe of Complexes of Sodium Dodecyl Sulfate and Serum Albumin During Polyacrylamide Gel Electrophoresis," Langmuir **25** (3), 1558 (2009).

Prabhu, V.M., Rao, A., Kang, S., Lin, E.K., Satija, S.K., "Manipulation of the Asymmetric Swelling Fronts of Photoresist Polyelectrolyte Gradient Thin Films," J. Phys. Chem. B **112** (49), 15628 (2008).

Prodi, A., Gilioli, E., Cabassi, R., Bolzoni, F., Licci, F., Huang, Q., Lynn, J.W., Affronte, M., Gauzzi, A., Marezio, M., "Magnetic Structure of the High-Density Single-Valent e_g Jahn-Teller System $LaMn_7O_{12}$," Phys. Rev. B **79** (8), 085105 (2009).

Psurek, T., Soles, C.L., Page, K.A., Cicerone, M.T., Douglas, J.F., "Quantifying Changes in the High-Frequency Dynamics of Mixtures by Dielectric Spectroscopy," J. Phys. Chem. B **112** (50), 15980 (2008). **(CHRNS)**

Purewal, J.J., Keith, J.B., Ahn, C.C., Fultz, B., Brown, C.M., Tyagi, M., "Adsorption and Melting of Hydrogen in Potassium-Intercalated Graphite," Phys. Rev. B **79** (5), 054305 (2009). **(CHRNS)**

Pushin, D.A., Arif, M., Cory, DG., "Decoherence-Free Neutron Interferometry," Phys. Rev. A **79** (5), 053635 (2009).

Pynn, R., Fitzsimmons, M.R., Lee, W.T., Stonaha, P., Shah, V.R., Washington, A.L., Kirby, B.J., Majkrzak, C.F., Maranville, B.B., "Birefringent Neutron Prisms for Spin Echo Scattering Angle Measurement," Physica B, in press.

Qiu, D., Cosgrove, T., Revell, P., Howell, I., "Poly(ethylene oxide) Adsorption on Polystyrene Latex Particles in the Presence of Poly(styrenesulfonate sodium)," Macromol. **42** (2), 547 (2009).

Qiu, Y., Bao, W., Huang, Q., Yildirim, T., Simmons, J.M., Green, M.A., Lynn, J.W., Gasparovic, Y.C., Li, J., Wu, T., Wu, G., Chen, X.H., "Crystal Structure and Antiferromagnetic Order in $NdFeAsO_{1-x}F_x$ (x = 0.0 and 0.2) Superconducting Compounds From Neutron Diffraction Measurements," Phys. Rev. Lett. **101** (25), 257002 (2008).

Qiu, Y., Bao, W., Zhao, Y., Broholm, C., Stanev, V., Tesanovic, Z., Gasparovic, Y.C., Chang, S., Hu, J., Qian, B., Fang, M., Mao, Z., "Spin Gap and Resonance at the Nesting Wave Vector in Superconducting $FeSe_{0.4}Te_{0.6}$," Phys. Rev. Lett., in press. **(CHRNS)**

Qiu, Y., Kofu, M., Bao, W., Lee, S.-H., Huang, Q., Yildirim, T., Copley, J.R.D., Lynn, J.W., Wu, T., Wu, G., Chen, X.H., "Neutron Scattering Study of the Oxypnictide Superconductor $LaO_{0.87}F_{0.13}FeAs$," Phys. Rev. B **78** (5), 052508 (2008). **(CHRNS)**

Qu, Z., Spinu, L., Yuan, H., Dobrosavljević, V., Bao, W., Lynn, J.W., Nicklas, M., Peng, J., Liu, T., Fobes, D., Flesch, E., Mao, Z.Q., "Unusual Heavy-Mass Nearly Ferromagnetic State with a Surprisingly Large Wilson Ratio in the Double Layered Ruthenates $(Sr_{1-x}Ca_x)_3Ru_2O_7$," Phys. Rev. B **78** (18), 180407 (2008).

Radlinski, A.P., Busbridge, T.L., Gray, E.M.A., Blach, T.P., Cheng, G., Melnichenko, Y.B., Cookson, D.J., Mastalerz, M., Esterle, J., "Dynamic Micromapping of CO_2 Sorption in Coal," Langmuir **25** (4), 2385 (2009). **(CHRNS)**

Rahatekar, S.S., Koziol, K.K., Kline, S.R., Hobbie, E.K., Gilman, J.W., Windle, A.H., "Length-Dependent Mechanics of Carbon-Nanotube Networks," Adv. Mater. **21** (8), 874 (2008).

Ramachandran, R., Beaucage, G., Kulkarni, A.S., "Persistence Length of Short-Chain Branched Polyethylene," Macromol. **41** (24), 9802 (2008). **(CHRNS)**

Ramachandran, R., Beaucage, G., Kulkarni, A.S., McFaddin, D., Merrick-Mack, J., Galiatsatosm V., "Branch Content of Metallocene Polyethylene," Macromol. **42** (13), 4746 (2009).

Ratcliff II, W., Sharma, A.L.L., Gomes, A.M., Gonzalez, J.L., Huang, Q., Singleton, J., "The Magnetic Ground State of $CaMn_2Sb_2$," J. Magn. Magn. Mater., in press.

Rekas, A., Lo, V., Gadd, G.E., Cappai, R., Yun, S.I., "PAMAM Dendrimers as Potential Agents against Fibrillation of -Synuclein, a Parkinson's Disease-Related Protein," Macromol. Biosci. **9** (3), 230 (2009). **(CHRNS)**

Reynolds, P.A., McGillivray, D.J., Jackson, A.J., White, J.W., "Ultra-Small-Angle Neutron Scattering: A Tool to Study Packing of Relatively Monodisperse Polymer Spheres and Their Binary Mixtures," Phys. Rev. E **80** (1), 011301 (2009). **(CHRNS)**

Ricciardo, R.A., Hauser, A.J., Yang, F.Y., Kim, H., Lu, W., Woodward, P.M., "Structural, Magnetic, and Electronic Characterization of Double Perovskites $Bi_xLa_{2-x}MnMO_6$ (M= Ni, Co; x = 0.25, 0.50)," Mater. Res. Bull. **44** (2), 239 (2009).

Rimmer, C.A., Howerton, S.B., Sharpless, K.E., Sander, L.C., Long, S.E., Murphy, K.E., Porter, B.J., Putzbach, K., Rearick, M.S., Wise, S.A., Wood, L.J., Zeisler, R., Hancock, D.K., Yen, J.H., Betz, J.M., NguyenPho, A., Yang, L., Scriver, C., Willie, S., Sturgeon, R., Schaneberg, B., Nelson, C., Skamarack, J., Pan, M., Levanseler, K., Gray, D., Waysek, E.H., Blatter, A., Reich, E., "Characterization of a Suite of Ginko-Containing Standard Reference Materials," Anal. Bioanal. Chem. **389**, 179 (2007).

Roh, J.H., Briber, R.M., Damjanovic, A., Thirumalai, D., Woodson, S.A., Sokolov, A.P., "Dynamics of tRNA at Different Levels of Hydration," Biophys. J. **96** (7), 2755 (2009). **(CHRNS)**

Ross, N.L., Spencer, E.C., Levchenko, A.A., Kolesnikov, A.I., Wesolowski, D.J., Cole, D.R., Mamontov, E., Vlcek, L., "Studies of Mineral-Water Surfaces," in "Neutron Applications in Earth, Energy and Environmental Sciences," edited by Liang, L., Rinaldi, R., Schober, H., (Springer US) Chap. 8, 235 (2009). **(CHRNS)**

Rubinson, K.A., Hubbard, J., "Experimental Compressibilities and Average Intermolecular Distances of Poly(Ethylene Glycol) Molecular Masses 2000–8000 Da in Aqueous Solution," Polymer **50** (12), 2618 (2009).

Ruff, J.P., Clancy, J.P., Bourque, A., White, M.A., Ramazanoglu, M., Gardner, J.S., Qiu, Y., Copley, J.R.D., Johnson, M.B., Dabkowska, H.A., Gaulin, B.D., "Spin Waves and Quantum Criticality in the Frustrated XY Pyrochlore Antiferromagnet $Er_2Ti_2O_7$," Phys. Rev. Lett. **101** (14), 147205 (2008). **(CHRNS)**

Rughani, R.V., Salick, D.A., Lamm, M.S., Yucel, T., Pochan, D.J., Schneider, J.P., "Folding, Self-Assembly, and Bulk Material Properties of a De Novo Designed Three-Stranded β-Sheet Hydrogel," Biomacromol. **10** (5), 1295 (2009). **(CHRNS)**

Rule, K.C., Bonville, P., "Tetragonal Distortion in $Tb_2Ti_2O_7$ Seen by Neutron Scattering," J. Phys.: Conf. Series **145**, 012027-1 (2009). **(CHRNS)**

Russo, D., Teixeira, J., Ollivier, J., "The Impact of Hydration Water on the Dynamics of Side Chains of Hydrophobic Peptides: From Dry Powder to Highly Concentrated Solutions," J. Chem. Phys. **130** (23), 235101 (2009). **(CHRNS)**

Sahoo, P., Adarsh, N.N., Chacko, G.E., Raghavan, S.R., Puranik, V.G., Dastidar, P., "Combinatorial Library of Primaryalkylammonium Dicarboxylate Gelators: A Supramolecular Synthon Approach," Langmuir, in press.

Saines, P.J., Kennedy, B.J., Johannessen, B., Poulton, S., "Phase and Valence Transitions in $Ba_2LnSn_xNb_{1-x}O_{6-\delta}$," J. Solid State Chem. **181** (11), 2994 (2008).

Sakiyama, N., Zaliznyak, I.A., Lee, S.H., Mitsui, Y., Yoshizawa, H., "Doping-Dependent Charge and Spin Superstructures in Layered Cobalt Perovskites," Phys. Rev. B **78** (18), 180406 (2008).

Sakiyama, N., Zaliznyak, I.A., Lee, S.H., Mitsui, Y., Yoshizawa, H., "Spin and Charge Order in Single-Layered Perovskite Cobaltates," J. Korean Phys. Soc. **53** (2), 995 (2008).

Schaefer, D.W., Zhao, J., Dowty, H., Alexander, M., Orler, E.B., "Carbon Nanofibre Reinforcement of Soft Materials," Soft Matter **4** (10), 2071 (2008).

Schexnailder, P., Loizou, E., Porcar, L., Butler, P., Schmidt, G., "Heterogeneity in Nanocomposite Hydrogels from Poly(Ethylene Oxide) Cross-Linked with Silicate Nanoparticles," Phys. Chem. Chem. Phys. **11**, 2760 (2009). **(CHRNS)**

Seah, M.P., Unger, W.E.S., Wang, H., Jordaan, W., Gross, T., Dura, J.A., Moon, D.W., Totarong, P., Krumrey, M., Hauert, R., Zhiqiang, M., "Ultra-Thin SiO2 on Si IX: Absolute Measurements of the Amount of Silicon Oxide as a Thickness of SiO_2 on Si," Surf. Interface Anal. **41** (5), 430 (2009).

Seibell II, H.A., Karen, P., Wagner, T.R., Woodward, P.M., "Synthesis and Characterization of Color Variants of Nitrogen- and Fluorine-Substituted TiO_2," J. Mater. Chem. **19**, 471 (2009).

Seo, P.N., Barrón-Palos, L., Bowman, J.D., Chupp, T.E., Crawford, C., Dabaghyan, M., Dawkins, M., Freedman, S.J., Gentile, T., Gericke, M.T., Gillis, R.C., Green, G.L., Hersman, F.W., Jones, G.L., Kandes, M., Lamoureaux, S., Lauss, B., Leuschner, M.B., Mahurin, R., Mason, M., Mei, J., Mitchell, G.S., Nann, H., Page, S.A., Penttilä, S.I., Ramsay, W.D., Bacci, A.S., Santra, S., Sharma, M., Smith, T.B., Snow, W.M., Wilburn, W.S., Zhu, H., "High-Efficiency Resonant RF Spin Rotator with Broad Phase Space Acceptance for Pulsed Polarized Cold Neutron Beams," Phys. Rev. ST Accel. Beams **11** (8), 084701 (2008).

Sha, H., Ye, F., Dai, P., Fernandez-Baca, J.A., Mesa, D., Lynn, J.W., Tomioka, Y., Tokura, Y., Zhang, J., "Signature of Magnetic Phase Separation in the Ground State of $Pr_{1-x}Ca_xMnO_3$," Phys. Rev. B **78** (5), 052410 (2008).

Sharma, M., Babcock, E., Andersen, K.H., Barrón-Palos, L., Becker, M., Boag, S., Chen, W.C., Chupp, T.E., Danagoulian, A., Gentile, T.R., Klein, A., Penttila, S., Petoukhov, A., Soldner, T., Tardiff, E.R., Walker, T.G., Wilburn, W.S., "Neutron Beam Effects on Spin-Exchange-Polarized ^{3}He," Phys. Rev. Lett. **101** (8), 083002 (2008).

Shibayama, M., Matsunaga, T., Nagao, M., "Evaluation of Incoherent Scattering Intensity by Transmission and Sample Thickness," J. Appl. Crystallogr., in press.

Shlyk, L.V., Kryukov, S.A., De Long, L.E., Schupp-Niewa, B., Niewa, R., Lynn, J.W., Huang, Q., Arenholz, E., Piamonteze, C., "A Novel Class of High-T_C Ferromagnetic Semiconductors: Novel Ferromagnetic Semiconductors," UGIM Symp. Proc., 142 (2008).

Shoenfelt, J., Mitkus, R.A., Zeisler, R., Spatz, R.O., Powell, J., Fenton, M.J., Squibb, K.A., Medvedev, A.E., "Involvement of TLR2 and TLR4 in Inflammatory Immune Responses Induced by Fine and Coarse Ambient Air Particulate Matter," J. Leuk. Biol., in press.

Siegel, J.B., McKay, D.A., Stefanopoulou, A.G., Hussey, D.S., Jacobson, D.L., "Measurement of Liquid Water Accumulation in a PEMFC with Dead-Ended Anode," J. Electrochem. Soc. **155** (11), B1168 (2008).

Singh, D.K., Helton, J.S., Chu, S., Han, T.H., Bonnoit, C.J., Chang, S., Kang, H.J., Lynn, J.W., Lee, Y.S., "Spin Correlations in the Geometrically Frustrated Pyrochlore $Tb_2Mo_2O_7$," Phys. Rev. B **78** (22), 220405 (2008). **(CHRNS)**

Singh, I., Themistou, E., Porcar, L., Neelamagham, S., "Fluid Shear Induces Conformation Change in Human Blood Protein von Willebrand Factor in Solution," Biophys. J. **96** (6), 2313 (2009). **(CHRNS)**

Skripov, A.V., Udovic, T.J., Cook, J.C., Hempelmann, R., Rempel, A.A., Gusev, A.I., "Quasielastic Neutron Scattering Study of Hydrogen Motion in $NbC_{0.71}H_{0.28}$," J. Phys.: Condens. Mat. **21** (17), 175410 (2009). **(CHRNS)**

Skripov, A.V., Wu, H., Udovic, T.J., Huang, Q., Hempelmann, R., Soloninin, A.V., Rempel, A.A., Gusev, A.I., "Hydrogen in Nonstoichiometric Cubic Niobium Carbides: Neutron Vibrational Spectroscopy and Neutron Diffraction Studies," J. Alloys Compd. **478** (1), 68 (2009).

Sokolov, D.A., Aronson, M.C., Erwin, R., Lynn, J.W., Lumsden, M.D., Nagler, S.E., "Neutron Diffraction in a Model Itinerant Metal near a Quantum Critical Point," J. Phys.: Conf. Ser. **150** (4), 042189 (2009).

Spendelow, J., Mukundan, R., Davey, J., Rockward, T., Hussey, D.S., Jacobson, D., Arif, M., Borup R.L., "High Resolution Neutron Radiography Imaging of Operating PEM Fuel Cells: Effect of Flow Configuration and Gravity on Water Distribution," ECS Trans. **16** (2), 1345 (2008).

Spernjak, D., Advani, S.G., Prasad, A.K., "Simultaneous Neutron and Optical Imaging in PEM Fuel Cells," J. Electrochem. Soc. **156** (1), B109 (2009).

Stalick, J.K., Waterstrat, R.M., "The Crystal Structure of Martensitic ZrIr and ZrRh," J. Alloys Compd. **477** (1), 123 (2009).

Stewart, J.R., Gardner, J.S., Qiu, Y., Ehlers, G., "Collective Dynamics in the Heisenberg Pyrochlore Antiferromagnet $Gd_2Sn_2O_7$," Phys. Rev. B **78** (13), 132410 (2008). **(CHRNS)**

Stock, C., Buyers, W.J.L., Rule, K.C., Chung, J.H., Liang, R., Bonn, D., Hardy, W.N., "Magnetic Field Resonantly Enhanced Free Spins in Heavily Underdoped $YBa_2Cu_3O_{6+x}$," Phys. Rev. B **79** (18), 184514 (2009).

Stock, C., Chapon, L.C., Adamopoulos, O., Lappas, A., Giot, M., Taylor, J.W., Green, M.A., Brown, C.M., Radaelli, P.G., "One-Dimensional Magnetic Fluctuations in the Spin-2 Triangular Lattice α-$NaMnO_2$," Phys. Rev. Lett. in press. **(CHRNS)**

Sun, K., Kumar, R., Falvey, D.E., Raghavan, S.R., "Photogelling Colloidal Dispersions Based on Light-Activated Assembly of Nanoparticles," J. Am. Chem. Soc. **131** (20), 7135 (2009). **(CHRNS)**

Sung, L., Gu, X., Clerici, C., Hu, H., Delaurent, V., "Metrologies for Characterizing Optical Properties of Clear and Pigmented Coatings," in "Service Life Prediction for Polymeric Materials: Global Perspectives," edited by Martin, J., Ryntz, R., Chin, J., and Dickie, R., (Springer US) Chap. 17, 257 (2008).

Sung, L., Gu, X., Clerici, C., Hu, H., Loizou, E., Ho, D.L., "Effect of Pigment Dispersion on Optical Properties and Durability of a TiO_2 Pigmented Epoxy Coating," in "Polymer Degradation and Performance," edited by Celina, M.C., Wiggins, J., and Billingham, N., (ACS Publications) ACS Symp. Ser. **1004**, Chap. 23, 276 (2009).

Sung, L., Gu, X., Ho, D.L., Landis, F.A., Nguyen, D., "Effect of Composition and Processing Condition on Surface Morphology and Microstructural Properties of Fluoropolymer/Acrylic Blends," Chin. J. Polym. Sci. **27** (1), 59 (2009).

Swainson, I.P., Stock, C., Gehring, P.M., Xu, G., Hirota, K., Qiu, Y., Luo, H., Zhao, X., Li, J.-F., Viehland, D., "Soft Phonon Columns on the Edge of the Brillouin Zone in the Relaxor $PbMg_{1/3}Nb_{2/3}O_3$," Phys. Rev. B **79** (22), 224301 (2009). **(CHRNS)**

Taherizadeh, A., Ghaei, A., Green, D.E., Altenhof, W.J., "Finite Element Simulation of Springback for a Channel Draw Process with Drawbead Using Different Hardening Models," Int. J. Mech. Sci. **51** (4), 314 (2009).

Tan, K.T., Vogt, B.D., White, C.C., Steffens, K.L., Goldman, J., Satija, S.K., Clerici, C., Hunston, D.L., "On the Origins of Sudden Adhesion Loss at a Critical Relative Humidity: Examination of Bulk and Interfacial Contributions," Langmuir **24** (17), 9189 (2008).

Taribagil, R.R., Hillmyer, M.A., Lodge, T.P., "A Compartmentalized Hydrogel from a Linear ABC Terpolymer," Macromol. **42** (6), 1796 (2009).

Terech, P., Dourdain, S., Bhat, S., Maitra, U., "Self-Assembly of Bile Steroid Analogues: Molecules, Fibers, and Networks," J. Phys. Chem. B **113** (24), 8252 (2009).

Terech, P., Maitra, U., "Structural and Rheological Properties of Aqueous Viscoelastic Solutions and Gels of Tripodal Cholamide-Based Self-Assembled Supramolecules," J. Phys. Chem. B **112** (43), 13483 (2008). **(CHRNS)**

Thomas, E.L., Wong-Ng, W., Phelan, D., Millican, J.N., "Thermopower of Co-Doped FeSe," J. Appl. Phys. **105** (7), 073906 (2009).

Thomas, J.J., Allen, A.J., Jennings, H.M., "Structural Changes to the Calcium–Silicate–Hydrate Gel Phase of Hydrated Cement with Age, Drying, and Resaturation," J. Am. Chem. Soc. **91** (10), 3362 (2008).

Thomas, J.J., Jennings, H.M., Chen, J.J., "Influence of Nucleation Seeding on the Hydration Mechanisms of Tricalcium Silicate and Cement," J. Phys. Chem. C **113** (11), 4327 (2009). **(CHRNS)**

Thompson, S.M., Ma, H.B., Winholtz, R.A., Wilson, C., "Experimental Investigation of Miniature Three-Dimensional Flat-Plate Oscillating Heat Pipe," J. Heat Transfer **131** (4), 043210 (2009).

Tian, W., Li, J., Lynn, J.W., Zarestky, J.L., Vaknin, D., "Spin Dynamics in the Magnetoelectric Effect Compound $LiCoPO_4$," Phys. Rev. B **78** (18), 184429 (2008). **(CHRNS)**

Tomlin, B.E., Zeisler, R., "Improvements in Determinations Using the Cu-64 Annihilation Gamma-Rays," Appl. Radiat. Isot., in press.

Tranquada, J.M., Gu, G.D., Hücker, M., Jie, Q., Kang, H.J., Klingeler, R., Li, Q., Tristan, N., Wen, J.S., Xu, G.Y., Xu, Z.J., Zhou, J., Zimmermann, M.V., "Evidence for Unusual Superconducting Correlations Coexisting with Stripe Order in $La_{1.875}Ba_{0.125}CuO_4$," Phys. Rev. B **78** (17), 174529 (2008). **(CHRNS)**

Tucker, I., Penfold, J., Thomas, R.K., Grillo, I., Mildner, D.F.R., Barker, J.G., "Self-Assembly in Complex Mixed Surfactant Solutions: The Impact of Dodecyl Triethylene Glycol on Dihexadecyl Dimethyl Ammonium Bromide," Langmuir **24** (18), 10089 (2008).

Tucker, I., Penfold, J., Thomas, R.K., Grillo, I., Mildner, D.F.R., Barker, J.G., "Self-Assembly in Mixed Dialkyl Chain Cationic–Nonionic Surfactant Mixtures: Dihexadecyldimethyl Ammonium Bromide–Monododecyl Hexaethylene Glycol (Monododecyl Dodecaethylene Glycol) Mixtures," Langmuir **24** (15), 7674 (2008).

Udby, L., Andersen, N.H., Chou, F.C., Christensen, N.B., Emery, S.B., Lefmann, K., Lynn, J.W., Mohottala, H.E., Niedermayer, C., Wells, B.O., "Magnetic Ordering in Electronically Phase Separated $La_{2-x}Sr_xCuO_{4+y}$: Neutron Diffraction Experiments," Phys. Rev. B **80** (1), 014505 (2009). **(CHRNS)**

Udovic, T.J., Huang, Q., Santoro, A., Rush, J.J., "The Nature of Deuterium Arrangements in YD_3 and Other Rare-Earth Trideuterides," Z. Kristallogr. **223** (10), 697 (2008).

Valincius, G., Heinrich, F., Budvytyte, R., Vanderah, D.J., McGillivray, D.J., Sokolov, Y., Hall, J.E., Lösche, M., "Soluble Amyloid β Oligomers Affect Dielectric Membrane Properties by Bilayer Insertion and Domain Formation: Implications for Cell Toxicity," Biophys. J. **95** (10), 4845 (2008).

Vandoolaeghe, P., Campbell, R.A., Reenie, A.R., Nylander, T., "Adsorption of Intact Cubic Liquid Crystalline Nanoparticles on Hydrophilic Surfaces: Lateral Organization, Interfacial Stability, Layer Structure, and Interaction Mechanism," J. Phys. Chem. C **113** (11), 4483 (2009).

Vandoolaeghe, P., Rennie, A.R., Campbell, R.A., Nylander, T., "Neutron Reflectivity Studies of the Interaction of Cubic-Phase Nanoparticles with Phospholipid Bilayers of Different Coverage," Langmuir **25** (7), 4009 (2009).

VanOudenhove, J., Anderson, E., Krueger, S., Cole, J.L., "Analysis of PKR Structure by Small-Angle Scattering," J. Mol. Biol. **387** (4), 910 (2009). **(CHRNS)**

Verruto, V.J., Kilpatrick, P.K., "Water-in-Model Oil Emulsions Studied by Small-Angle Neutron Scattering: Interfacial Film Thickness and Composition," Langmuir **24** (22), 12807 (2008). **(CHRNS)**

Wang, B., Tchessalov, S., Cicerone, M.T., Warne, N.W., Pikal, M.J., "Impact of Sucrose Level on Storage Stability of Proteins in Freeze-Dried Solids: II. Correlation of Aggregation Rate with Protein Structure and Molecular Mobility," J. Pharm. Sci., in press. **(CHRNS)**

Wang, J.Y., Chen, W., Russell, T.P., "Ion-Complexation-Induced Changes in the Interaction Parameter and the Chain Conformation of PS-b-PMMA Copolymers," Macromol. **41**, 4904 (2008). **(CHRNS)**

Weber, A.Z., Hickner, M.A., "Modeling and High-Resolution-Imaging Studies of Water-Content Profiles in a Polymer-Electrolyte-Fuel-Cell Membrane-Electrode Assembly," Electrochim. Acta **53** (26), 7668 (2008).

Wen, J., Xu, G., Gu, G., Shapiro, S.M., "Magnetic-Field Control of Charge Structures in the Magnetically Disordered Phase of Multiferroic $LuFe_2O_4$," Phys. Rev. B **80** (2), 020403 (2009).

Wen, J., Xu, G., Stock, C., Gehring, P.M., "Response of Polar Nanoregions in $68\%Pb(Mg_{1/3}Nb_{2/3})O_3$-$32\%PbTiO_3$ to a [001] Electric Field," Appl. Phys. Lett. **93** (8), 082901 (2008).

Wen, J., Xu, G., Stock, C., Gehring, P.M., Zhong, Z., Boatner, L.A., Venturini, E.L., Samara, G.A., "Effect of Local Dipole Moments on the Structure and Lattice Dynamics of $K_{0.98}Li_{0.02}TaO_3$," Phys. Rev. B **78** (14), 144202 (2008). (CHRNS)

Wen, J., Xu, Z., Xu, G., Tranquada, J.M., Gu, G., Chang, S., Kang, H.J., "Magnetic Field Induced Enhancement of Spin-Order Peak Intensity in $La_{1.875}Ba_{0.125}CuO_4$," Phys. Rev. B **78** (21), 212506 (2008). (CHRNS)

West, D.V., Huang, Q., Zandbergen, H.W., McQueen, T.M., Cava, R.J., "Structural Disorder, Octahedral Coordination, and 2-Dimensional Ferromagnetism in Anhydrous Alums," J. Solid State Chem. **181** (10), 2768 (2008).

West, D.V., McQueen, T.M., Huang, Q., Cava, R.J., "Structural and Magnetic Properties of Pyrochlore Solid Solutions $(Y,Lu)_2Ti_{2-x}(Nb,Ta)_xO_{7\pm y}$," J. Solid State Chem. **181** (8), 1753 (2008).

West, D.V., McQueen, T.M., Posen, I.D., Ke, X., Huang, Q., Zandbergen, H.W., Williams, A.J., Schiffer, P., Cava, R.J., "The $A^{2+}Mn_5(SO_4)_6$ Family of Triangular Lattice, Ferrimagnetic Sulfates," J. Solid State Chem. **182** (6), 1343 (2009).

West, D.V., Posen, I.D., Huang, Q., Zandbergen, H.W., McQueen, T.M., Cava, R.J., "$PbMn(SO_4)_2$: A New Chiral Antiferromagnet," J. Solid State Chem., in press.

White, J.S., Hinkov, V., Heslop, R.W., Lycett, R.J., Forgan, E.M., Bowell, C., Strässle, S., Abrahamsen, A.B., Laver, M., Dewhurst, C.D., Kohlbrecher, J., Gavilano, J.L., Mesot, J., Keimer, B., Erb, A., "Fermi Surface and Order Parameter Driven Vortex Lattice Structure Transitions in Twin-Free $YBa_2Cu_3O_7$," Phys. Rev. Lett. **102** (9), 097001 (2009).

Whitten, A.E., Jeffries, C.M., Harris, S.P., Trewhella, J., "Cardiac Myosin-Binding Protein C Decorates F-Actin: Implications for Cardiac Function," Proc. Natl. Acad. Sci. USA, **105** (47), 18360 (2008). (CHRNS)

Wong-Ng, W., Yang, Z., Hu, Y.F., Huang, Q., Lowhorn, N., Otani, M., Kaduk, J.A., Li, Q., "Thermoelectric and Structural Characterization of $Ba_2Ho(Cu_{3-x}Co_x)O_{6+y}$," J. Appl. Phys. **105** (6), 063706 (2009).

Wu, H., "Strategies for the Improvement of the Hydrogen Storage Properties of Metal Hydride Materials," Chem. Phys. Chem. **9** (15), 2157 (2008).

Wu, H., Zhou, W., Udovic, T.J., Rush, J.J., Yildirim, T., "Crystal Chemistry and Dehydrogenation Rehydrogenation Properties of Perovskite Hydrides $RbMgH_3$ and $RbCaH_3$," J. Phys. Chem. C, in press.

Wu, H., Zhou, W., Wang, K., Udovic, T.J., Rush, J.J., Yildirim, T., Bendersky, L.A., Gross, A.F., Van Atta, S.L., Vajo, J.J., Pinkerton, F.E., Meyer, M.S., "Size Effects on the Hydrogen Storage Properties of the Nanoscaffolded $Li_3BN_2H_8$," Nanotech. 20, 204002 (2009).

Wu, H., Zhou, W., Yildirim, T., "Alkali and Alkaline-Earth Metal Amidoboranes: Structure, Crystal Chemistry, and Hydrogen Storage Properties," J. Am. Chem. Soc. **130** (44), 14834 (2008).

Wu, H., Zhou, W., Yildirim, T., "High-Capacity Methane Storage in Metal–Organic Frameworks M2(dhtp): The Important Role of Open Metal Sites," J. Am. Chem. Soc. **131** (13), 4995 (2009).

Wu, H., Zhou, W., Yildirim, T., "Methane Sorption in Nanoporous Metal–Organic Frameworks and First-Order Phase Transition of Confined Methane," J. Phys. Chem. C **113** (7), 3029 (2009).

Wu, W., Kiryukhin, V., Noh, H.J., Ko, K.-T., Park, J.H., Ratcliff, W., Sharma, P.A., Harrison, N., Choi, Y.J., Horime, Y., Lee, S., Park, S., Yi, H.T., Zhang, C.L., Cheong, S.W., "Formation of Pancakelike Ising Domains and Giant Magnetic Coercivity in Ferrimagnetic $LuFe_2O_4$," Phys. Rev. Lett. **101** (13), 135203 (2008).

Wu, Y., Yu, B., Jackson, A., Zha, W., Lee, L.J., Wyslouzil, B.E., "Coaxial Electrohydrodynamic Spraying: A Novel One-Step Technique to Prepare Oligodeoxynucleotide Encapsulated Lipoplex Nanoparticles," Mol. Pharmaceutics, in press.

Xue, M., Liu, Y., Schaffino, R.M., Xiang, S., Zhao, X., Zhu, G.S., Qiu, S.L., Chen, B., "New Prototype Isoreticular Metal–Organic Framework $Zn_4O(FMA)_3$ for Gas Storage," Inorg. Chem. **48** (11), 4649 (2009).

Yager, K.G., Berry, B.C., Page, K., Patton, D., Karim, A., Amis, E.J., "Disordered Nanoparticle Interfaces for Directed Self-Assembly," Soft Matter **5** (3), 622 (2009).

Yamada, N.L., Endo, H., Osaka, N., Kawabata, Y., Nagao, M., Takeda, T., Seto, H., Shibayama, M., "Detector Area Expansion at iNSE Neutron Spin Echo Spectrometer," Physica B, in press.

Yamaura, K., Huang, Q., Takayama-Muromachi, E., "Superconductivity and Structure of η-Mo_3C_2," Physica C **468** (15), 1135 (2008).

Yang, H., Shin, K., Tae, G., Satija, S.K., "Structure of a Monolayer of Poly(ethylene glycol) End-Capped with a Fluoroalkyl Group and its Relationship with Protein Adsorption at the Aqueous Interface," Soft Matter, in press.

Ye, F., Ren, Y., Fernandez-Baca, J.A., Mook, H.A., Lynn, J.W., Chaudhury, R.P., Wang, Y.Q., Lorenz, B., Chu, C.W., "Magnetic Switching and Phase Competition in the Multiferroic Antiferromagnet $Mn_{1-x}Fe_xWO_4$," Phys. Rev. B **78** (19), 193101 (2008).

Yeon, S.H., Osswald, S., Gogotsi, Y., Singer, J.P., Simmons, J.M., Fischer, J.E., Lillo-Rodenas, M.A., Linares-Solano, A., "Enhanced Methane Storage of Chemically and Physically Activated Carbide-Derived Carbon," J. Power Sources **191**, 560 (2009).

Yi, Z., Nagao, M., Bossev, D.P., "Bending Elasticity of Saturated and Monounsaturated Phospholipid Membranes Studied by the Neutron Spin Echo Technique," J. Phys.: Condens. Mat. 21 (15), 155104 (2009). (CHRNS)

Yildirim, T., "Frustrated Magnetic Interactions, Giant Magneto-Elastic Coupling, and Magnetic Phonons in Iron-Pnictides," Physica C **469** (9-12), 425 (2009).

Yildirim, T., "Origin of the 150-K Anomaly in LaFeAsO: Competing Antiferromagnetic Interactions, Frustration, and a Structural Phase Transition," Phys. Rev. Lett. **101** (5), 057010 (2008).

Yildirim, T., "Strong Coupling of the Fe-Spin State and the As-As Hybridization in Iron-Pnictide Superconductors from First-Principle Calculations," Phys. Rev. Lett. **102** (3), 037003 (2009).

Yildirim, T., Vergara, L.I., Íñiguez, J., Musfeldt, J.L., Harris, A.B., Rogado, N., Cava, R.J., Yen, F., Chaudhury, R.P., Lorenz, B., "Phonons and Magnetoelectric Interactions in $Ni_3V_2O_8$," J. Phys.: Condens. Mat. **20** (43), 434214 (2008).

Yoonessi, M., Seikel, E., Pender, M.J., "Characterization and Modeling of Stable Colloids of Organically Surface Tailored Gold Nanoparticle Liquids," Langmuir **25** (6), 3369 (2009).

Yousufuddin, M., Her, J.-H., Zhou, W., Jalisatgi, S.S., Udovic, T.J., "Crystal Structure, Neutron Vibrational Spectroscopy, and DFT Calculations of $Li_2B_{12}H_{12} \cdot 4H_2O$," Inorg. Chim. Acta **362** (9), 3155 (2009).

Yun, S.I., Gadd, G.E., Lo, V., Gauthier, M., Munam, A., "Temperature-Responsive Supramolecular Assembly and Morphology of Arborescent Copolymer Micelles with a Solvophilic Core–Solvophobic Shell Structure," Macromol. **41** (19), 7166 (2008). (CHRNS)

Zeisler, R., Greenberg, R.R., Mackey, E.A., Murphy, K.E., Spatz, R.O., Tomlin, B.E., "Challenges and Successes in the Use of Neutron Activation Analysis Procedures for Value Assignment of Animal Serum and Bovine Liver Standard Reference Materials", J. Radioanal. Nucl. Chem. **281** (1), 11 (2009).

Zeisler, R., Heller-Zeisler, S., Ünlü, K., Williamson, C., "Current Status, Trends, and Needs in Radiochemical Education: The US and Abroad," in "8th International Conference on Methods and Applications of Radioanalytical Chemistry: MARC-VIII," edited by Zeisler, R., Ünlü, K., Heller-Zeisler, S., (AIP Conf. Proc.), in press.

Zeisler, R., James, W.D., Mackey, E.A., Spatz, R.O., Greenberg, R.R., "NAA Characterization of the New Bovine Liver SRM," J. Radioanal. Nucl. Chem. **278** (3), 783 (2008).

Zeisler, R., Lindstrom, R.M., Tomlin, B.E., "Development of Quality Assessment Tools for Activation Analysis Software," Trans. Am. Nucl. Soc. 99, 59 (2008).

Zeisler, R., Paul, R.L., Spatz, R.O., "Reproducible Elemental Analyses of Single-Walled Carbon Nanotubes by Neutron Activation Analysis," Trans. Am. Nucl. Soc. 100, 247 (2009).

Zhang, X., Berry, B.C., Yager, K.G., Kim, S., Jones, R.L., Satija, S., Pickel, D.L., Douglas, J.F., Karim, A., "Surface Morphology Diagram for Cylinder-Forming Block Copolymer Thin Films," ACS Nano **2** (11), 2331 (2008).

Zhang, Y., Lagi, M., Liu, D., Mallamace, F., Fratini, E., Baglioni, P., Mamontov, E., Hagen, M., Chen, S.H., "Observation of High-Temperature Dynamic Crossover in Protein Hydration Water and its Relation to Reversible Denaturation of Lysozyme," J. Chem. Phys. **130** (13), 135101 (2009).

Zhao, J., Huang, Q., de la Cruz, C., Li, S., Lynn, J.W., Chen, Y., Green, M.A., Chen, G.F., Li, G., Li, Z., Luo, J.L., Wang, N.L., Dai, P., "Structural and Magnetic Phase Diagram of $CeFeAsO_{1-x}F_x$ and its Relation to High-Temperature Superconductivity," Nat. Mater. 7, 953 (2008).

Zhao, J., Huang, Q., de la Cruz, C., Lynn, J.W., Lumsden, M.D., Ren, Z.A., Yang, J., Shen, X., Dong, X., Zhao, Z., Dai, P., "Lattice and Magnetic Structures of PrFeAsO, $PrFeAsO_{0.85}F_{0.15}$, and $PrFeAsO_{0.85}$," Phys. Rev. B **78** (13), 132504 (2008).

Zhao, J., Ratcliff, W., Lynn, J.W., Chen, G.F., Luo, J.L., Wang, N.L., Hu, J., Dai, P., "Spin and Lattice Structures of Single-Crystalline $SrFe_2As_2$," Phys. Rev. B **78** (14), 140504 (2008).

Zhao, J., Yao, D.X., Li, S., Hong, T., Chen, Y., Chang, S., Ratcliff, W., Lynn, J.W., Mook, H.A., Chen, G.F., Luo, J.L., Wang, N.L., Carlson, E.W., Hu, J., Dai, P., "Low Energy Spin Waves and Magnetic Interactions in $SrFe_2As_2$," Phys. Rev. Lett. **101** (16), 167203 (2008). (CHRNS)

Zhou, H.D., Wiebe, C.R., Balicas, L., Yo, Y.J., Qiu, Y., Copley, J.R.D., Gardner, J.S., "Intrinsic Spin-Disordered Ground State of the Ising Garnet $Ho_3Ga_5O_{12}$," Phys. Rev. B **78** (14), 140406 (2008). **(CHRNS)**

Zhou, H.D., Wiebe, C.R., Janik, J.A., Balicas, L., Yo, Y.J., Qiu, Y., Copley, J.R.D., Gardner, J.S., "Dynamic Spin Ice: $Pr_2Sn_2O_7$," Phys. Rev. Lett. **101** (22), 227204 (2008). (CHRNS)

Zhou, H.D., Wiebe, C.R., Jo, Y.J., Balicas, L., Urbano, R.R., Lumata, L.L., Brooks, J.S., Kuhns, P.L., Reyes, A.P., Qiu, Y., Copley, J.R.D., Gardner, J.S., "Chemical Pressure Induced Spin Freezing Phase Transition in Kagomé Pr Langasites," Phys. Rev. Lett. **102** (6), 067203 (2009). (CHRNS)

Zhou, H.D., Wiebe, C.R., Yo, Y.J., Balicas, L., Takano, Y., Case, M.J., Qiu, Y., Copley, J.R.D., Gardner, J.S., "Nanoscale Freezing of the 2D Spin Liquid $Pr_3Ga_5SiO_{14}$," Meas. Sci. Technol. **19** (3), 34023 (2008). (CHRNS)

Zhou, W., Wu, H., Yildirim, T., Simpson, J.R., Hight Walker, A.R., "Origin of the Exceptional Negative Thermal Expansion in Metal-Organic Framework-5 Zn_4O(1,4-benzenedicarboxylate)$_3$," Phys. Rev. B **78** (5), 054114 (2008). (CHRNS)

Zhou, W., Wu, H., Udovic, T.J., Rush, J.J., Yildirim, T., "Quasi-Free Methyl Rotation in Zeolitic Imidazolate Framework-8," J. Phys. Chem. A **112** (49), 12602 (2008). (CHRNS)

Zhou, W., Wu, H., Yildirim, T., "Enhanced H_2 Adsorption in Isostructural Metal–Organic Frameworks with Open Metal Sites: Strong Dependence of the Binding Strength on Metal Ions," J. Am. Chem. Soc. **130** (46), 15268 (2008).

Instruments and Contacts

Instruments and Contacts: (name, tel. 301-975-xxxx, email)

High Resolution Powder Diffractometer (BT-1):
- Judy Stalick, 6223, judith.stalick@nist.gov
- Qingzhen Huang, 6164, qing.huang.@nist.gov
- Mark Green, 4297, mark.green@nist.gov

Residual Stress Diffractometer (BT-8):
- Thomas Gnaeupel-Herold, 5380, tg-h@nist.gov

30-m SANS Instrument (NG-7):
- Yun Liu, 6235, yun.liu@nist.gov
- Paul Butler, 2028, paul.butler@nist.gov
- Jeff Krzywon, 6650, jkrzywon@nist.gov

30-m SANS Instrument (NG-3) (CHRNS):
- Boualem Hammouda, 3961, hammouda@nist.gov
- Steve Kline, 6243, steven.kline@nist.gov
- Susan Krueger, 6734, susan.krueger@nist.gov
- Cedric Gagnon, 2020, cedric.gagnon@nist.gov

USANS, Perfect Crystal SANS (BT-5) (CHRNS):
- Andrew Jackson, 3146, andrew.jackson@nist.gov
- David Mildner, 6366, david.mildner@nist.gov
- Paul Butler, 2028, paul.butler@nist.gov

Reflectometer, Vertical Sample, Polarized Beam Option (NG-1):
- Brian Kirby, 8395, brian.kirby@nist.gov
- Julie Borchers, 6597, julie.borchers@nist.gov
- Chuck Majkrzak, 5251, cmajkrzak@nist.gov

AND/R, Advanced Neutron Diffractometer/Reflectometer (NG-1):
- Joe Dura, 6251, joseph.dura@nist.gov
- Brian Maranville, 6034, brian.maranville@nist.gov

Reflectometer, Horizontal Sample (NG-7):
- Sushil Satija, 5250, satija@nist.gov
- Bulent Akgun, 6469, bulent.akgun@nist.gov

Double-focusing Triple Axis Spectrometer (BT-7):
- Songxue Chi, 4570, songxue.chi@nist.gov
- Jeff Lynn, 6246, jeff.lynn@nist.gov

Triple-axis Spectrometer (BT-9):
- William Ratcliff, 4316, william.ratcliff@nist.gov
- Ross Erwin, 6245, rerwin@nist.gov
- Jeff Lynn, 6246, jeff.lynn@nist.gov

SPINS, Spin-polarized Triple-axis Spectrometer (NG-5) (CHRNS):
- Sung Chang, 8369, sung.chang@nist.gov
- Deepak Singh, 4863, deepak.singh@nist.gov

MACS, Multi-Analyzer Crystal Spectrometer (NG-0)
- Jose Rodriguez, 6019, jose.rodriguez@nist.gov
- Collin Broholm, 5179, collin.broholm@nist.gov

FANS, Filter-analyzer Neutron Spectrometer (BT-4):
- Terry Udovic, 6241, tudovic@nist.gov
- Juscelino Leão, 8867, juscelino.leao@nist.gov

DCS, Disk-chopper Time-of-flight Spectrometer (NG-4) (CHRNS):
- John Copley, 5133, jcopley@nist.gov
- Yiming Qiu, 3274, yiming.qiu@nist.gov
- Craig Brown, 5134, craig.brown@nist.gov

HFBS, High-flux Backscattering Spectrometer (NG-2) (CHRNS):
- Madhusudan Tyagi, 2046, mtyagi@nist.gov
- Tim Jenkins, 8396, timothy.jenkins@nist.gov

NSE, Neutron Spin Echo Spectrometer (NG-5) (CHRNS):
- Antonio Faraone, 5254, antonio.faraone@nist.gov
- Jason Gardner, 8396, jason.gardner@nist.gov
- Michi Nagao, 5505, michihiro.nagao@nist.gov

Cold Prompt-gamma Neutron Activation Analysis (NG-7):
- Rick Paul, 6287, rpaul@nist.gov

Thermal Prompt-gamma Neutron Activation Analysis (VT-5):
- Liz Mackey, 5149, liz.mackey@nist.gov

Other Activation Analysis Facilities:
- Greg Downing, 3782, gregory.downing@nist.gov

Cold Neutron Depth Profiling (NG-1):
- Greg Downing, 3782, gregory.downing@nist.gov

Neutron Imaging Station (BT-2):
- David Jacobson, 6207, david.jacobson@nist.gov
- Dan Hussey, 6465, daniel.hussey@nist.gov
- Muhammad Arif, 6303, muhammad.arif@nist.gov

Neutron Interferometer (NG-7):
- Muhammad Arif, 6303, muhammad.arif@nist.gov
- Dave Jacobson, 6207, david.jacobson@nist.gov
- Dan Hussey, 6465, daniel.hussey@nist.gov

Fundamental Neutron Physics Station (NG-6):
- NG-6M: Scott Dewey, 4843, mdewey@nist.gov
- NG-6U: Pieter Mumm, 8355, pieter.mumm@nist.gov
- NG-6: Jeff Nico, 4663, nico@nist.gov

Theory and Modeling:
- Taner Yildirim, 6228, taner@nist.gov
- Joseph Curtis, 3959, joseph.curtis@nist.gov

Sample Environment:
- Julia Scherschligt, 5328, julia.scherschligt@nist.gov
- Juscelino Leão, 8867, juscelino.leao@nist.gov

NIST CENTER FOR NEUTRON RESEARCH CONTACTS

Copies of annual reports, facility information, user information, And research proposal guidelines are available electronically.

Please vist our website: http://www.ncnr.nist.gov

For a paper copy of this report:

Ron Cappelletti
301-975-6221
ron.cappelletti@nist.gov

For general information on the facility:

Rob Dimeo
301-975-6210
robert.dimeo@nist.gov

Dan Neumann
301-975-5252
dan.neumann@nist.gov

For information on visiting the facility and/or user access questions:

User Office:
Mary Ann FitzGerald
301-975-8200
maryann.fitzgerald@nist.gov

For information on performing research at the facility:

Bill Kamitakahara
301-975-6878
william.kamitakahara@nist.gov

Facility address:

NIST Center for Neutron Research
National Institute of Standards and Technology
100 Bureau Drive, Mail Stop 6100
Gaithersburg, MD 20899-6100
USA

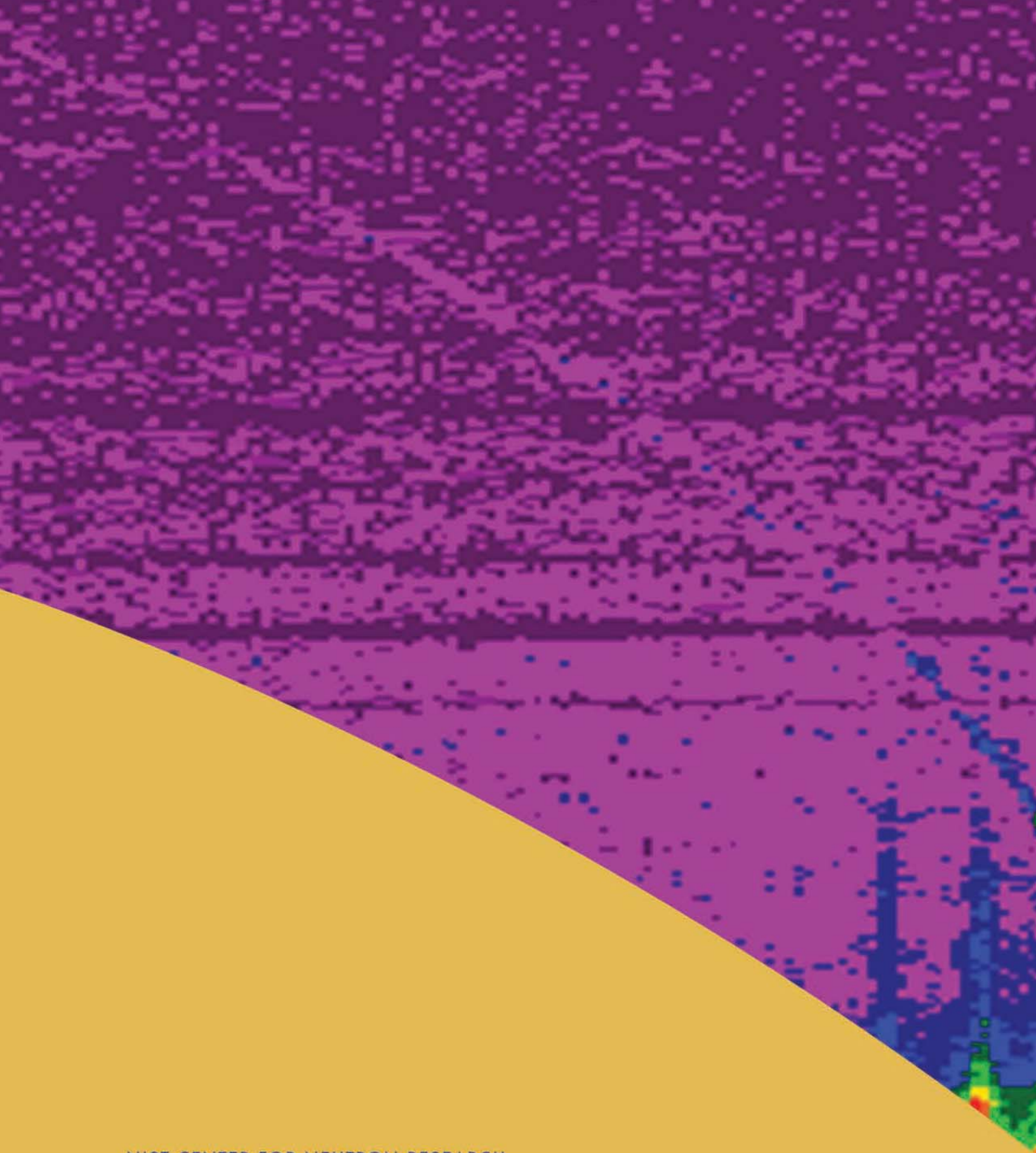

NIST CENTER FOR NEUTRON RESEARCH
National Institute of Standards and Technology
100 Bureau Drive, MS 6100
Gaithersburg, MD 20899-6100

www.ncnr.nist.gov